3-2020

Modeling Hybrid Composites Using Tsai-Wu and Hashin Failure Criterion

Candice R. Roberts

MODELING HYBRID COMPOSITES USING TSAI-WU AND HASHIN FAILURE CRITERION

THESIS

Candice R. Roberts, Second Lieutenant, USAF

AFIT-ENY-MS-20-M-278

DEPARTMENT OF THE AIR FORCE
AIR UNIVERSITY

AIR FORCE INSTITUTE OF TECHNOLOGY

Wright-Patterson Air Force Base, Ohio

AFIT-ENY-MS-20-M-278

MODELING HYBRID COMPOSITES USING TSAI-WU AND HASHIN FAILURE CRITERION

THESIS

Presented to the Faculty

Department of Aeronautics and Astronautics

Graduate School of Engineering and Management

Air Force Institute of Technology

Air University

Air Education and Training Command

In Partial Fulfillment of the Requirements for the

Degree of Master of Science in Aeronautical Engineering

Candice R. Roberts, BS

Second Lieutenant, USAF

March 2020

AFIT-ENY-MS-20-M-278

MODELING HYBRID COMPOSITES USING TSAI-WU AND HASHIN FAILURE CRITERION

Candice R. Roberts, BS

Second Lieutenant, USAF

Committee Membership:

Dr. Anthony Palazotto
Chair

Dr. Marina Ruggles-Wren
Member

Maj. Ryan Kemnitz
Member

AFIT-ENY-MS-20-M-278

Abstract

Hybrid composites require further study and testing for future use in various fields. This study focuses on simulating a Hybrid Composite using IM7-977-3 laminae with steel foils in Abaqus under bolt loading by using Hashin and Tsai-Wu failure criterion. Initial simulations contain only the IM7-977-3 composite with cohesive layers. Foil samples were then tested for accurate material properties from which the simulations were then updated to include steel foils. The two models show that Tsai-Wu failure criterion, while great for anisotropic material in tension, does not prove accuracy around the hole of the composite material which is in compression. Hashin shows failure in compression for the matrix and portions of the fibers for the material long before Tsai-Wu indicates any failure is forthcoming. Each layer is analyzed for differing results between the two failure criterion.

Acknowledgments

I would like to express my sincere appreciation to my faculty advisor, Dr. Anthony Palazotto for his guidance and support throughout the course of this thesis effort. The insight and experience were certainly appreciated. I would, also, like to thank Maj Brewer for his help in the initial modeling of the composite material using Hashin and for his willingness to give me the MatLAB code used in determining the yield stress and Modulus of Elasticity for the steel foil specimen.

Candice R. Roberts

Table of Contents

Page

List of Figures

List of Tables

Page

MODELING HYBRID COMPOSITES USING TSAI-WU AND HASHIN FAILURE CRITERION

Chapter 1

I. Introduction

Carbon fiber materials are strong and desirable when it comes to making better performing structures. Carbon fiber polymers are lighter and possess a higher strength-to-weight ratio than the monolithic materials that are typically used in the manufacturing of aircraft, automobiles, and other structures. However, the notch sensitivity of carbon fiber materials is incredibly high due to the brittleness of the matrix and the low strain to failure. This high sensibility makes the composites undesirable when a hole is required in the material. The solution to this problem of high sensitivity is to reinforce the carbon fiber with a monolithic material that does not possess such high notch sensitivity. This thesis focuses on modeling a hybrid carbon fiber material under an axial load using Tsai-Wu and Hashin theory. Two models are generated using the requirements for each theory and then regenerated with the addition of a steel foil in order to calculate and determine the characteristics each theory shows for the material.

As technology advances and increasing demands are made from aircraft, manufacturers look toward new materials in order to maintain the strength and capability of current aerospace structures while simultaneously increasing functionality. Engineered composite materials typically provide lower density with increased strength and thermal properties; however, the current materials are not easily replaced with composite structures due to the limits of the materials and present knowledge. While a desire to

increase the use of composite materials in aerospace structures, the work and intensive study into their failures for damage protection and mitigation is greatly needed.

Carbon fiber composites and the study of their strength began in 1956 when Roger Bacon delved into the study of carbon fiber and produced high performance of the material two years later [1]. Since that time, the grandeur of using carbon fiber increased along with the knowledge and information regarding the strength of those materials. Though due to the complexity and various variations of composites, there is still more information and knowledge to be gained from studying these materials. Composite materials can be used to make ductile material stiffer or weaker material stronger with the right combination of materials and procedures to combine the materials [2]. In some cases, the composite will be lighter but stronger than most metals. Their higher strength to weight ratio makes them ideal in many facets of industry, particularly aerospace engineering.

The drawbacks of composites make them less than ideal for bolting or extensive use. Composites, when cracked, become significantly weaker and break quickly once that small crack appears. Noticing the crack before imminent destruction of the structure is highly unlikely and could lead to catastrophes. These drawbacks led scientists to further look into reinforcing composites and making them even better for commercial and everyday use. One such use was the metal matrix composites. Metal matrix composites designed early in the 1970's for the space race made carbon fibers reinforced with a metal and were used in various space components [3]. These MMCs consisted "of fibres or particles surrounded by a matrix of metal." [4]. They generated benefits for the

materials such as better abrasion resistance, creep resistance, high temperature resistance, and non-flammability [4].

Metal Matrix Composites reinforcing constituent is typically ceramic, but occasionally metal will be used. There are primarily three different forms of MMCs: mono-filament, whiskers, and particulate [5]. Each form of reinforcement encourages the composite to increase in certain factors. Table 1 shows how the micro-structural material affects the composite. The arrows indicate whether the added matrix material increases or decreases a certain parameter within the carbon fiber material as compared to a typical polymer reinforced matrix. Not only does the increase in certain characteristics make the MMCs better, but the fact that they require few monetary funds also made them a better candidate to investigate for aerospace and automotive industries [6]. The success and better situation involving MMCs led to further study into various matrices being used with carbon fiber or other composite material.

Table 1: Effects of Micro-structural Material on Composites

Microstructural feature	Composite property					
	α_{axial}	E_{axial}	Tensile YS (0.2% PS)	Work hardening rate	Creep resistance	Toughness (ductility)
Ceramic content f	⇓ § 5.1.2	⇑ §3.6	⇑ §4.1.1	⇑ §4.3.1	⇑ §5.2.3	⇓ §7.3.3
Fibre aspect ratio s	⇓ §5.1.2	⇑ §3.6	⇑ or ⇓ §4.1.1	⇑ §4.3.1	⇑ §5.2.3	⇑ or ⇓ §7.4.2
Misalignment $g(\theta)$	⇑ §5.1.2	⇓ §3.6	⇑ or ⇓ §7.1.2	⇓ §4.3.1	⇓ §5.2.3	⇑ or ⇓ §7.4.2
Fibre diameter d	–	–	⇓ §4.2	⇓ §4.3.2	⇑ §5.2.3	⇑ §7.4.3
Inhomogeneity of f	–	–	–	–	⇓ §5.2.3	⇓ §7.4.5
Bond strength τ_i	⇓	⇑ §6.1.4	⇑	⇑ §4.4.2	⇑ §5.2.3	⇑ or ⇓ §6.1.4
Reaction layer t	⇑ or ⇓	⇓ §6.3.2	⇓ §6.1.4	⇓ §6.1.4	⇓ §5.2.3	⇓ §6.1.4
$\Delta\alpha\,\Delta T$ stresses	–	–	⇓ §4.1.2	⇓ §4.1.2	⇓ §5.2.3	⇓ §7.2.2
Matrix porosity	⇓ §5.1.1	⇓ §3.6	⇓	⇓	⇓	⇓ §7.3.3
Matrix YS	–	–	⇑ §4.2	⇑ §4.3.2	⇑ §5.2.3	⇓ §7.4.6

The next form of composite to come as a result of MMCs was composites possessing ceramic matrices instead of metal or polymer [3]. Although MMCs included ceramic matrices, the MMC would typically consist of two materials being embedded into the matrix while a Ceramic Matrix Composite (CMC) consisted of only ceramic fibers being placed into the composite matrix [7]. The desire for a different matrix came from the fact that in an MMC, the metal does increase the weight, and this drawback gave birth to the CMC gaining a foothold in being further developed [7]. This new form of composites produced different results that were useful at high temperature, but the material would be more brittle than normal [8]. However, the new material gained significance for being able to withstand high temperatures making them useful when building engines [9]. The idea of different matrices introduced the fact that composite materials possessed a plethora of forms that could be explored and provide various results

depending on each factor. Adding the fact that certain parameters could be changed for the better, meant scientists would investigate more forms of composites to try and achieve the material characteristics that they desired.

Scientists further explored composites due to the revelation of the plethora of characteristics that a material could bring out. The next form of composites scientists discovered received its inspiration from nature. The idea of combining organic and inorganic material to generate a stronger substance became the focal point for hybrid composites [3]. This new form of reinforcing a carbon material happens at the molecular level by combining materials. As seen in Figure 1, thin sheets of each material are laid in secession with the metal material layers being separated from one another. The combination of materials typically happens using epoxy or adhesive layer. The process involved depends on which materials are being united, but autoclave is the usual way for combining the different materials into one. While combining and buying hybrid composites is more expensive, the weight savings when compared to monolithic materials would be worth the price [10].

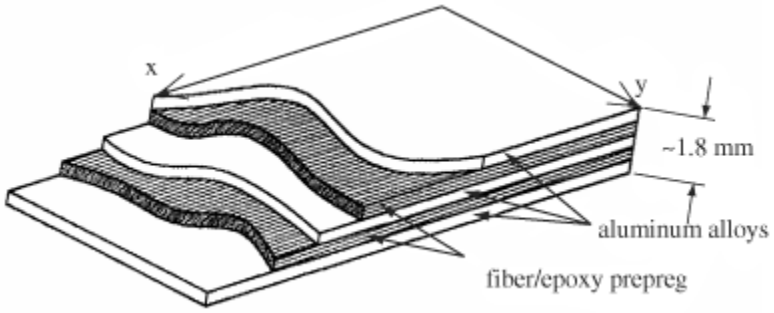

Figure 1: Hybrid Composite Lay-up

Of those hybrid composites, one being extensively considered for a plethora of aerospace functions are Carbon Fiber Reinforced Polymers (CFRPs) [11]. CFRPs are

carbon inlaid with another material, for example: steel, titanium, or glass. A composite is made up of a specific number of layers with each one laying a specific direction. With CFRPs, one or more of the layers within the composite are a specific material: metal or even glass. As seen in Figure 2, a CFRP inlaid with titanium is pictured. The titanium in this case only occupies one layer of the composite but adds some benefit to the entire layer.

The carbon fiber helps to improve the strength while lessening the weight of the entire object while still maintaining some of the properties of the material inlaid within the carbon fiber. While the properties of the materials are strengthened, there is a primary drawback which needs further understanding for CFRPs to become more prominent in

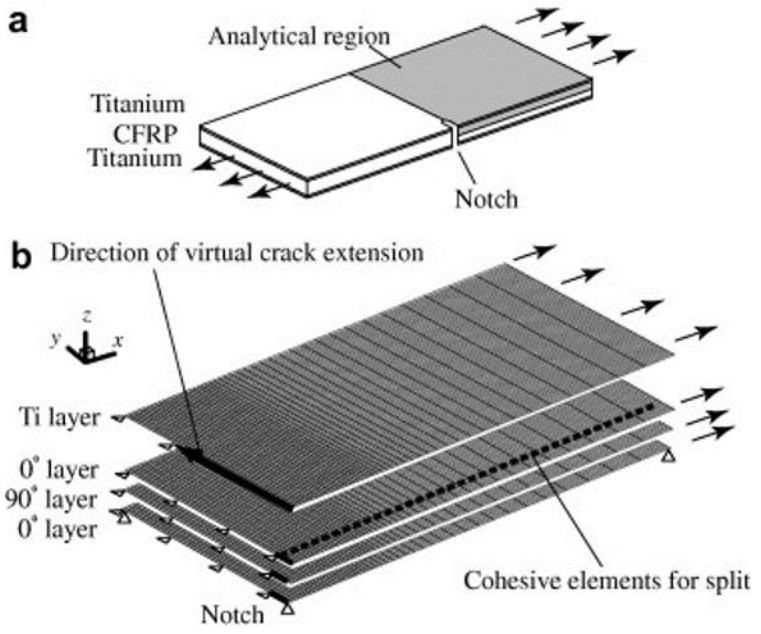

Figure 2: Lay-up of CFRP with Titanium

any field of industry: brittle failure. Typically, when a carbon fiber composite becomes damaged in any way, shape, or form, the failure is imminent, and catastrophe may occur. In order to mitigate the problems associated with brittle failure, extensive research is

desired to understand and provide more information concerning the failure of composites with different variations of lay-ups, orientations, and materials.

One of the first ways people implemented carbon fiber materials and other composite materials, including CFRPs, into structures is by using them to reinforce the current building material and even automotive structures [1]. Their superior strength would help provide a longer future for the item, but since carbon fiber composites are relatively new, there is work and research into how they perform over great lengths of time and in various environments [2]; and since they are still being tested for longevity, there is much research to be done on how they will perform as the main material instead of just a reinforcer to the current material. Research is being conducted with CFRPs in static loading with simple bolt holes in order to determine and come up with a good model for depicting the lifespan in these situations.

Issues exist currently with bolting composite materials together as introducing a hole within the composite brings local damage to the area where the hole is placed [12]. One possible solution is thickening the composite and adding more layers to the material in order to overcome the local damage introduced; however, thickening the material itself can cause many problems including additional weight. The light weight of a composite is one of the most sought-after qualities in engineering, so the thickening and additional weight diminishes the positive aspects seen by the lightweight, strong material. Another solution that also solves the issue of local damage introduced by a hole is to strengthen the composite material by introducing metals [12]. Metals may add weight, but the possible benefits outweigh the negative aspects. CFRPs, or hybrid composites, look at the pros and cons of metal being added to a composite material. However, these materials are

still new and need testing in order to determine strengths and weaknesses. The plethora of tests needed to determine the capabilities and characteristics of such materials is extensive, but modeling may be able to perform the same calculations and predictions as testing with less intensive physical work.

Testing and modeling various composite loads and depictions will give an indication as to how that specific material will perform under given circumstances. When modeling any structure, it is important to note the strength and material properties of every item under loading. Calculating composite material properties is arduous and requires individual information of each part of the composite coming together: the volume percentage for the fiber, polymer, and matrix, the weights of each individual part, and the modulus of elasticity for each material combined within the composite. The Law or Rule of Mixtures for each ply is then used to determine the modulus of elasticity for the entire material [13]. Once the modulus is found, the yield strength is then determined in order to find where the first layer or material will break within the composite. The process is then completed with the rest of the remaining layers and materials until the final layer is broken and the object or material failed entirely. Unlike normal materials, composites posses a modulus of elasticity that varies as the load increases due to different layers breaking and bending at various strengths. In Figure 3, the stress-load diagram for steel is shown. In Figure 4, the stress-load diagram for various polymers is depicted. As can be seen in the differences between the two figures, the steel possesses a straight forward and constant modulus that is somewhat ductile whereas the carbon fiber shows that the modulus can be high, but the material is often extremely brittle. The deformation or displacement of a composite material is calculated similarly: the entire material is

taken account in order to find out the stiffness or ductility of the material. One part of the composite may react differently than another layer or piece but combining the entire reaction of the materials helps determine how the object deforms [14]. Euler-Bernoulli's hypothesis is sometimes used in order to find stress and from stress, the strain may be calculated [15]. These curves may help determine the deformation and reaction of composite materials under known loading conditions.

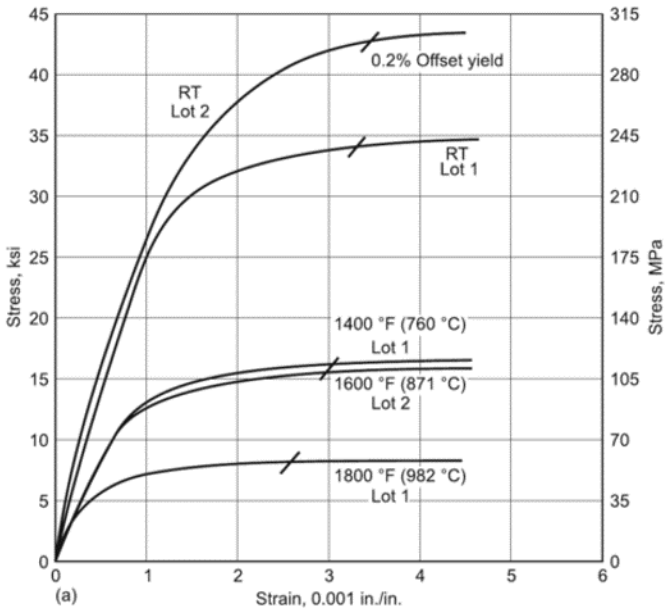

Figure 3: Stress-strain Curve for Steel at Various Temperatures [16]

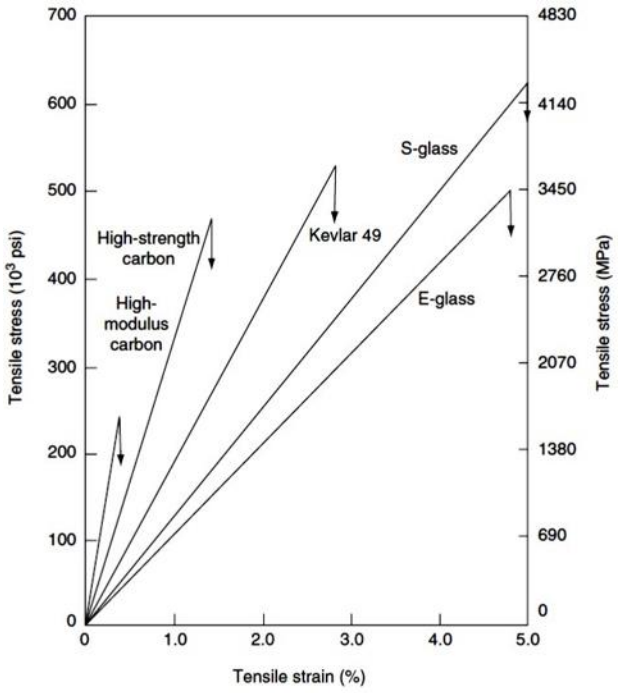

Figure 4: Stress-strain Curve for Various Polymers [17]

The extreme brittleness of a polymer in composites makes gaining the knowledge of their failures even more important. If a person can understand and know when a composite material may fail, then he can plan and prevent a catastrophe from happening. This becomes even more important when working in a field that affects human life: aerospace, automobile, and even construction. Understanding the failure of composite materials helps design and create models of various structures under different loading conditions. If the model shows a deformation in a costly area, before implementation, the construction of the material can have reinforcement in that spot or even change the percentage of a certain layer in that area.

Modeling composites is no easy feat and requires testing in order to truly determine the failure load of a material, but if the testing proves the model to be accurate then the model may prove to be useful in determining other factors for that specific

material design, such as where the material will ultimately fail and how it will fail. With modeling, a person can change the lay-up of the composite before manufacturing the material which in turn helps with the cost of buying all the necessary items. These models can tell the engineer where the weakest point in the composite lies and then the engineer can try a different lay-up easily if the specifications do not match the desired outcome. One way the composites are reinforced is using CFRPs. CFRPs help strengthen the structure of a carbon fiber material while still maintaining most of the benefits obtained by both materials. The use of a material with carbon fiber, such as steel, adds weight to the whole material, but the steel offers other benefits that need to be investigated. Additional weight within the material may cause lower strength to weight ratio, but the added material may also help with fatigue growth and prevent a catastrophic failure from immediately happening in a structure.

While the CFRPs may increase the overall strength now, the timeline of such a material may remain a mystery unless further investigated. The CFRPs need to be tested for longevity and environmental factors if they are to be a future prospect in the aerospace engineering field. The benefits of such materials are fantastic, but the brittle failure could cause tremendous damage if not properly studied and mitigated for future use. Currently, CFRPs are primarily being tested in standard conditions with various bolt-holes cut into the material in order to determine how and when the CFRP will break. A model is being introduced that will determine the failure mode and yield strength of certain CFRPs when loaded under countersunk measures.

Table 2: Material Strength for Steel and Carbon Fiber

Material Type		Density ρ (kg/m^3)	Tensile Strength σ_u (GPa)	Elastic Modulus E (GPa)	Breaking Length $\sigma_u/(\rho g)$ (km)
Carbon Fiber	Standard	1760	3.53	230	205
	High Strength	1820	7.06	294	396
	High Modulus	1870	3.45	441	188
Steel	S355	7850	0.50	210	6
	Wire	7850	1.77	210	23

This thesis investigates a specific carbon fiber material reinforced with steel under a bolt loading. Table 2 shows the material properties for steel and carbon fiber. If the density of carbon fiber is combined with strength of steel, the resulting structural material would possess tremendous strength-to-weight ratio. A form of this material exists, and this thesis explores modeling, with Abaqus, the material under axial loading using two different failure theories: Hashin and Tsai-Wu. These two theories are implemented in two different models of the nine-ply material. The first two models consist of only carbon fiber plys, but the next two models incorporate the steel foil into the design. Characteristics for the steel foil are determined through testing under quasi-static loading. The results from these tests are then used in the modeling.

Chapter 2

II. Theory

Tsai-Wu

The Tsai-Wu failure criterion was generated in 1970 by Stephen W. Tsai and Edward M. Wu. Their failure criterion is based upon strength in anisotropic materials which makes the criterion applicable for composite laminates [18]. The theory starts by assuming that there exists some strength failure in the stress-space with the below equation:

$$f(\sigma_k) = F_i\sigma_i + F_{ij}\sigma_i\sigma_j \quad (1)$$

where i,j=1,2...6, and F_i and F_{ij} are strength tensors. This equation is automatically invariant and each stress component shows an independent material property [18]. The independent nature of the failure criterion means that each component does not rely upon one another which is part of the usefulness and uniqueness for using this equation to determine failure. Another reason this equation is useful for composite laminates is the fact that the strength components are shown as tensors. These tensors can then be transformed easier into the different fiber directions for a specific layer. Along with rotating the strength tensor, the stress can also be easily transformed in order to determine or study the off-axis properties [18].

While the tensors provide an overabundance of features, one of the main ideas is that stability is incorporated within the strength tensors. This means that the magnitude of the interaction terms is defined by the inequality:

$$F_{ii}F_{jj} - {F_{ij}}^2 \geq 0 \tag{2}$$

with the emphasis that the repeated indices are not summations but simply one of the diagonal terms within the tensor matrix. This inequality ensures that the failure will intercept each axis of a shear-stress graph without generating a hyperbolic function. Rather the function generated and encompassed by the inequality and failure criterion is an ellipse as depicted in Figure 5 [18]. Each plane axis in the envelope generated by the Tsai-Wu failure criterion creates an ellipse that shows the boundaries of a material's strength within shear and stress. While Equation 2 defines the shape of the envelope, all terms in the inequality must be positive for the shape to remain ellipsoidal.

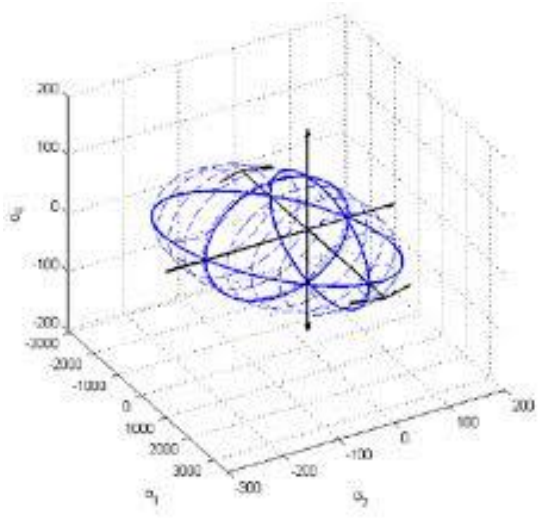

Figure 5: Three Dimensional Failure Envelope for Tsai-Wu Failure Criterion

Along with the strength tensor being positive, Tsa-Wu criterion also assumes that the strength tensors are symmetric. This assumption reduces the number of independent components to 6 and 21 for F_i and F_{ij} respectively. Since assuming a symmetric strength tensor, the criterion can also then reduce the number of independent components again by

assuming that the change in sign of a shear stress does not affect this failure. This leaves 3 and 9 components for F_i and F_{ij} respectively.

Additionally, for composite materials, assuming a state of plane stress, the strength tensors can further be reduced to:

$$F_i = \begin{pmatrix} F_1 \\ F_2 \\ F_6 \end{pmatrix} \tag{3}$$

$$F_{ij} = \left(\begin{bmatrix} F_{11} & F_{12} & F_{16} \\ F_{12} & F_{22} & F_{26} \\ F_{16} & F_{26} & F_{66} \end{bmatrix} \right) \tag{4}$$

where there is a total of 9 independent material components. When dealing with orthotropic materials, however, F_6=F_{16}=F_{26}=0.This reduces the total number of independent material components to 6. All these assumptions can then be plugged back into Equation 1 producing:

$$I_F = F_1\sigma_{11} + F_2\sigma_{22} + F_{11}{\sigma_{11}}^2 + +F_{22}{\sigma_{22}}^2 + F_{66}{\sigma_{12}}^2 + 2F_{12}\sigma_{11}\sigma_{22} < 1.0 \tag{5}$$

which is the simplified form of the Tsai-Wu failure criterion. Using the relationship between engineering strengths and strength tensors, each component of Equation 5 can be defined by the material strength as follows:

$$F_1 = \frac{1}{X_t} + \frac{1}{X_c} \tag{6a}$$

$$F_2 = \frac{1}{Y_t} + \frac{1}{Y_c} \tag{6b}$$

$$F_{11} = \frac{-1}{X_t X_c} \tag{6c}$$

$$F_{22} = \frac{1}{Y_t Y_c} \tag{6d}$$

$$F_{66} = \frac{1}{S^2} \tag{6e}$$

where X_t and X_c are tensile and compressive limits in the 1-direction; Y_t and Y_c are tensile and compressive limits in the 2-direction. These variables are typically obtained through experimental data by performing uniaxial testing in each direction [18]. This leaves one variable left to determine: F_{12}, which is called the interaction coefficient. There two different ways to determine F_{12}:

$$F_{12} = \frac{1}{2{\sigma_{biax}}^2}\left[1 - \left(\frac{1}{X_t} + \frac{1}{X_c} + \frac{1}{Y_t} + \frac{1}{Y_c}\right)\sigma_{biax} + \left(\frac{1}{X_t X_c} + \frac{1}{Y_t Y_c}\right){\sigma_{biax}}^2\right] \tag{7}$$

Or

$$F_{12} = f^* \sqrt{F_{11} F_{22}} \tag{8}$$

where σ_{biax} is the equibiaxial stress at failure and $1.0 \geq f^* \leq 1.0$. F_{12} is a critical number and can be very sensitive. This component is the primary driver of the Tsai-Wu failure criterion and is typically determined through experimentation. The equibiaxial stress is preferred when using the Tsai-Wu failure criterion, but if no equibiaxial stress is known for the given material then Equation 8 is used. In the case where both variables are known, the equibiaxial stress will be used. Other people in the past tried to define F_{12} by proportionality factors, but this does not ensure internal consistency nor uniformity under transformation which could lead to instability [18].

Hashin

The Hashin Failure Criteria generated in 1980 by Zvi Hashin separates the failure of a composite by the tension and compression of the fiber and matrix making four

different equations by which the material can fail [19]. Back in 1973, it was noted that composites fail in more ways than metals. Composites can have the fibers fracture and break or the matrix in a composite material may break down first causing the material to fail altogether. The idea of different failure methods led to experimentation on how composites fail led to the discovery tension and compression failure methods depending on the angle of the composite direction [20]. Hashin proposed a criteria for four different ways a composite may fail due to a state of stress in a piecewise smooth function rather than an all simplifying equation [19].

Hashin proposed to consider a quadratic function in order to try and create a better envelope for the failure of a composite material. He proposes that since all unidirectional fibers are transversely isotropic that the failure functions must consist of stress variants under rotation of the x_2 and x_3 around x_1, where x_1 is the fiber direction [19]. This would make the invariants (I_i):

$$I_1 = \sigma_{11} \tag{9a}$$

$$I_2 = \sigma_{22} + \sigma_{33} \tag{9b}$$

$$I_3 = {\sigma_{23}}^2 - \sigma_{23} - \sigma_{22}\sigma_{33}, \qquad \text{or} \qquad I_3 = \frac{1}{4}(\sigma_{22} - \sigma_{33})^2 + {\sigma_{23}}^2 \tag{9c}$$

$$I_4 = {\sigma_{12}}^2 + {\sigma_{13}}^2 \tag{9d}$$

$$I_5 = 2\sigma_{12}\sigma_{23}\sigma_{13} - \sigma_{22}{\sigma_{13}}^2 - \sigma_{33}{\sigma_{12}}^2 \tag{9e}$$

Since quadratic formulation was preferred in order to generate this failure criteria, Equation 9e is not used in further assumptions. This makes the general approximation form for transversely isotropic material:

$$A_1 I_1 + B_1 {I_1}^2 + A_2 I_2 + B_2 {I_2}^2 + C_{12} I_1 I_2 + A_3 I_3 + A_4 I_4 = 1 \quad (10)$$

Which follows that the combined Equations 9 and 10 for shear are:

$$A_3 = \frac{1}{{\tau_T}^2} \quad (11a)$$

$$A_4 = \frac{1}{{\tau_A}^2} \quad (11b)$$

As stated earlier, a unidirectional fiber material may fail in two primary modes: fiber and matrix. A fiber mode failure is when the fibers of a material rupture because of tension or compression, and matrix mode failure is when a plane parallel in a composite crack [19]. Assuming a failure plane is identifiable and cause by shear and normal stresses then it is approximately in the $x_2 x_3$ plane, and σ_{11} does not enter into the equation with matrix mode failure because it is a planar fracture [19]. Combining these two assumptions with Equations 10 and 11 makes the two failure criteria mode equations:

Fiber Mode

$$A_f \sigma_{11} + B_f {\sigma_{11}}^2 + \frac{1}{{\tau_A}^2}({\sigma_{12}}^2 + {\sigma_{13}}^2) = 1 \quad (12)$$

Matrix Mode

$$A_m(\sigma_{22}+\sigma_{33})+B_m(\sigma_{22}+\sigma_{33})^2+\frac{1}{{\tau_T}^2}({\sigma_{23}}^2-\sigma_{22}\sigma_{33})+\frac{1}{{\tau_A}^2}({\sigma_{12}}^2+{\sigma_{13}}^2)=1 \quad (13)$$

Unlike metals, composites fail differently in tension and compression and therefore the failure modes require further refinement for tension and compression generating the four different failure modes of Hashin.

In tensile fiber failure mode σ_{11}>0. An assumption is made to estimate the failure mode involving generating an ellipsoidal quadrant of ${\sigma_A}^+$ and τ_A with the axes [19]. This reduces Equation 12 to:

$$\frac{\sigma_{11}}{{\sigma_A}^+}+\frac{1}{{\tau_A}^2}({\sigma_{12}}^2+{\sigma_{13}}^2)=1 \quad (14)$$

or the maximum stress criterion may be used:

$$\sigma_{11}={\sigma_A}^+ \quad (15)$$

On the opposite end for fiber mode failure σ_{11}<0. Since not too much information is known or given regarding this mode of failure, the simplified equation becomes:

$$\sigma_{11}=-{\sigma_A}^- \quad (16)$$

Matrix mode failure is more complicated to identify and generate equations, so a simple choice based upon σ_{nn}, σ_{ni}, and σ_{in} is

$$f(\sigma_{nn},\sigma_{ni},\sigma_{in}) = (\frac{\sigma_{nn}}{{\sigma_T}^+})^2 + (\frac{\sigma_{ni}}{\tau_T})^2 + (\frac{\sigma_{in}}{\tau_A})^2 = 1 \quad (17)$$

Tensile mode for matrix mode failure is where σ_{nn} >0 and ${\sigma_{ni}}^m$=${\sigma_T}^+$ which when combined with Equation 13 makes:

$${A_m}^+{\sigma_T}^+ + {B_m}^+{\sigma_2}^{+2} = 1 \quad (18)$$

Then using similar assumptions to Equation 14 results in the failure criterion with the following equation:

$$\frac{1}{{\sigma_T}^{+2}}(\sigma_{22}+\sigma_{33})^2 + \frac{1}{{\tau_T}^2}({\sigma_{12}}^2 + {\tau_{13}}^2) = 1 \quad (19)$$

Conversely for compression mode, σ_{nn}<0 where the simple equation ${\sigma_{22}}^m$= -${\sigma_T}^-$ is combined with equation 13 to become:

$$-{A_m}^-{\sigma_T}^- + {B_m}^-{\sigma_2}^{-2} = 1 \quad (20)$$

The resulting failure criterion is then determined by the argument that σ_{22}=σ_{33}=-σ and σ ≫ ${\sigma_T}^-$ which makes:

$$\frac{1}{{\sigma_T}^-}\left[\left(\frac{{\sigma_T}^-}{2\tau_T}\right)^2 - 1\right](\sigma_{22}+\sigma_{33}) + \frac{1}{4{\tau_T}^2}(\sigma_{22}+\sigma_{33})^2 + \frac{1}{{\tau_T}^2}({\sigma_{23}}^2 - \sigma_{22}\sigma_{33}) + \frac{1}{{\tau_A}^2}({\sigma_{12}}^2 + {\sigma_{13}}^2) = 1 \quad (21)$$

The failure modes produce so far may be further reduced when incorporating plane stress. Assume σ_{11} is the fiber direction stress, σ_{22} is the stress in transverse

direction, and σ_{12} is in-plane or axial shear. All other stresses vanish when considering plane stress. The four-failure mode criterion become:

Tensile Fiber Mode

$$(\frac{\sigma_{11}}{\sigma_A{}^+})^2 + (\frac{\sigma_{12}}{\tau_A})^2 = 1, \qquad \sigma_{11} > 0 \tag{22}$$

Fiber Compressive Mode

$$\sigma_{11} = -\sigma_A{}^-, \qquad \sigma_{11} < 0 \tag{23}$$

Tensile Matrix Mode

$$(\frac{\sigma_{22}}{\sigma_T{}^+})^2 + (\frac{\sigma_{12}}{\tau_T})^2 = 1, \qquad \sigma_{22} > 0 \tag{24}$$

Matrix Compressive Mode

$$(\frac{\sigma_{22}}{2\tau_T})^2 + \left[\left(\frac{\sigma_T{}^-}{2\tau_T}\right)^2 - 1\right]\frac{\sigma_{22}}{\sigma_T{}^-} + (\frac{\sigma_{12}}{\tau_A})^2 = 1, \qquad \sigma_{22} < 0 \tag{25}$$

Abaqus

The Abaqus explicit modeling is based upon time and integration methods. The equations of motion used are the following:

$$\dot{u}^{(i+\frac{1}{2})} = \dot{u}^{(i-\frac{1}{2})} + \frac{\Delta t^{(i+1)} + \Delta t^{(i)}}{2}\ddot{u}^{(i)} \tag{26}$$

$$u^{(i+1)} = u^{(i)} + \Delta t^{(i+1)}\dot{u}^{(i+\frac{1}{2})} \tag{27}$$

where $\dot{u}$ signifies velocity and $\ddot{u}$ means acceleration. The superscript (i) represents the increment number in reference to the model time. Initial times are automatically set equal to zero unless otherwise specified [21]. Further time increment measurements are then

determined using Equations 26 and 27. Along with determining the time increments, Abaqus also calculates the internal forces in the model using the following equation:

$$\int B^T \sigma dV \tag{28}$$

Where B^T is the transpose of the strain displacement matrix.

Within Abaqus, there are a multitude of ways to express the properties of different materials used in the model. For the steel foil within the later models, the material properties are determined through experimentation where the 0.02% yield offset method, otherwise known as just the offset method, is used to determine yield strength for the model. The 0.02% offset includes initially determining the Modulus of Elasticity by the elastic portion of the Stress-strain curve. Then, a line is generated to start at 0.02 strain with the same slope as the elastic portion of the curve (yield stress). Where the new line meets on the curve is the yield stress point for the material.

Chapter 3

III. Methodology

Machine Testing

The following method for determining and calculating the strain values are not accurate, however, for the purpose of this work, the estimated strain values suffice. The thickness of the foil samples did not allow for extensometers, so a method was developed to determine strain values based upon the displacement given by the machine (similar to ASTM E345 paragraph 4.7). Taking the displacement data generated by the Mechanical Testing System (MTS), strain would be calculated using the basic definition of engineering strain:

$$\varepsilon = \frac{\delta}{l_o} \tag{29}$$

Where δ is the displacement of the actuator and l_o is the distance between the upper and lower grips of the MTS. The estimated strains were then used to determine an estimated strain rate by the follow equation:

$$\dot{\varepsilon} = \frac{\dot{\delta}}{l_o} \tag{30}$$

Before gathering data, stainless steel foils were shaped into dog bone structures in order to be tested at varying displacement rates to ensure the modulus of elasticity and yield stress were consistent. Once the specimen were ready to be tested, the testing area would then be prepared for the foil samples. A Mechanical Testing System (MTS Landmark Servohydraulic Test System) as depicted in Figure 6 was used in order to find the loads and displacement that would be calculated into estimated strains and stress to determine the yield strength and modulus of elasticity for the steel foils used in the modeling of a hybrid composite for this thesis. Preparing for testing initiated by opening the Station Manager depicted in Figure 7 and turning the hydraulic pressure of the MTS grips on. Under displacement control, the procedure editor would then be opened and modified for each test according to the displacement rates specified in Table 3.

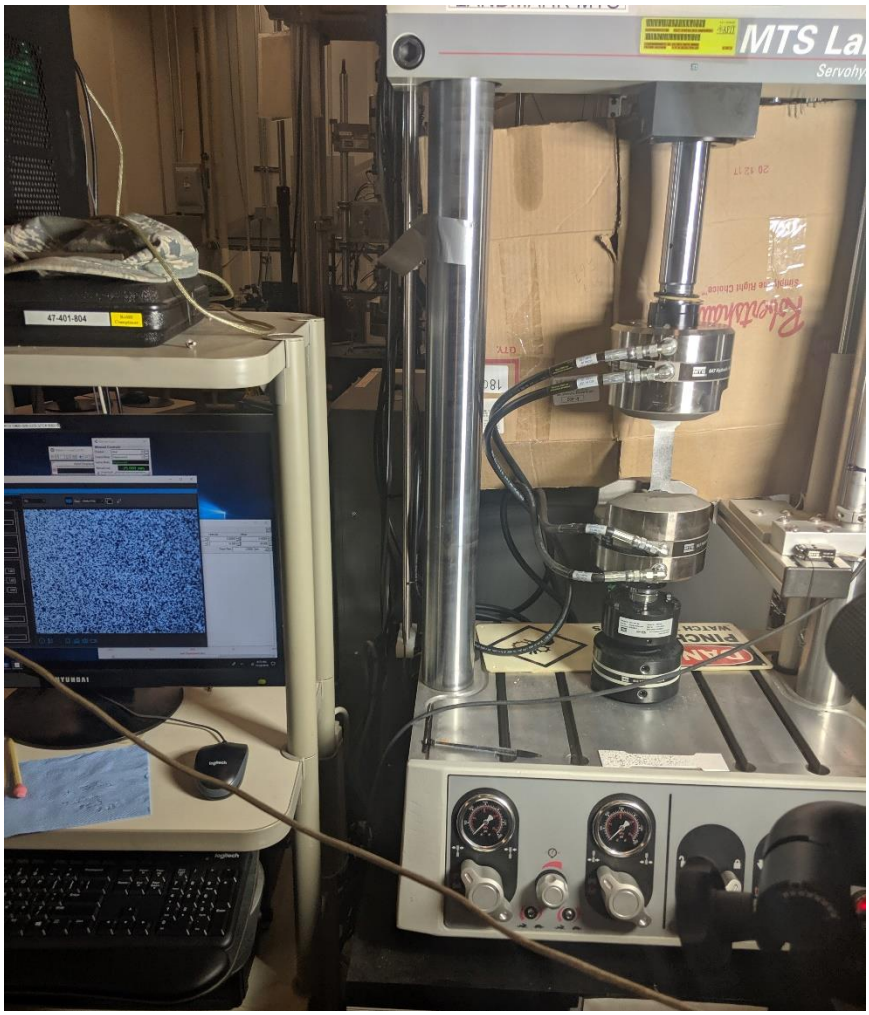

Figure 6: Mechanical Testing System

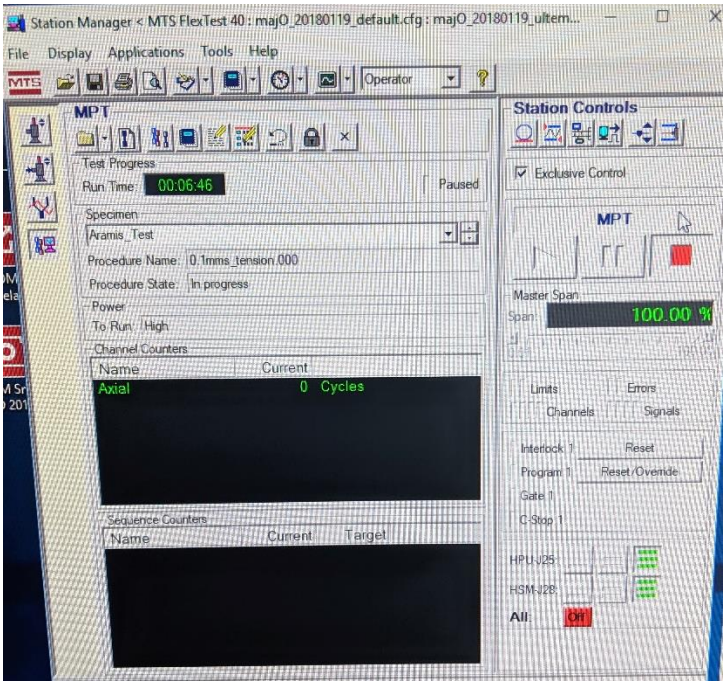

Figure 7: Station Manager for MTS

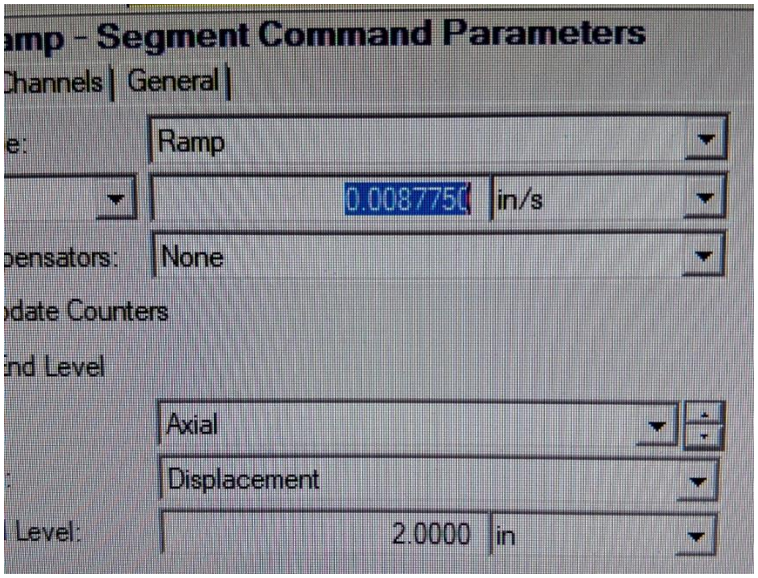

Figure 8: Segment Command Parameters

Table 3: Displacement Rates and Estimated Strain Rates

Displacement Rate $(\frac{in}{s})$	Estimated Strain Rate $(\frac{1}{s})$
0.008775	0.0027
0.0008775	0.00027
0.00043875	0.000135
0.00008775	0.000027

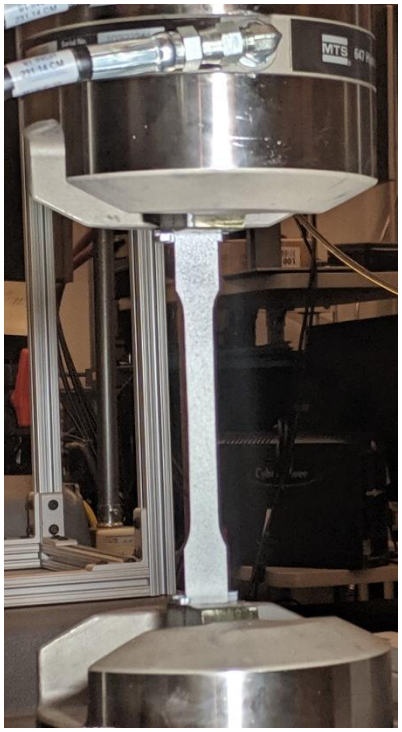

Figure 9: Foil Sample in MTS

Once the specimen was secured in the MTS and the proper procedure had been specified, then the experiment would start. The Machine would pull the specimen until

failure at which point the tester would stop the MTS. All data would be generated by the MTS in the form of load and actuator displacement. The load would be converted into stress based upon material properties and dimensions while the actuator displacement would be converted into strain by Equation XX above. The stress and strain would then be graphed where the yield strength and modulus of elasticity could be derived within a MatLAB code.

Modeling

The basic model of the IM7-977-3 material includes seventeen layers individually made. Nine of those layers are the composite material which were built as follows. A 3.5" x 5.5" rectangle with the hole properly dimensioned as seen in Figure 10 was created using a 3D solid in order to gather individual results for each layer of the model. After building the outline of the model, a thickness of 0.0045 was specified in representation of an individual layer for the IM7-977-3. With a base made for each layer, the next step is to partition the layers according to the fiber direction as stated in Appendix A. After partitioning the four-layer fiber directions, the material definitions for Hashin and Tsai-Wu theory models were defined according to Appendix B.

After specifying the material, each layer received the proper orientation according to the fiber direction using the orientation tool in Abaqus. After the specification of material properties, the mesh for each layer was generated. The mesh was generated using the bottom up mesh tool in Abaqus. The partitioned face was used a basis for the mesh to be generated meaning that the mesh would follow the partition's pattern. Then, one of the edges perpendicular to the partitioned face and along the thickness of the

material would be specified for the mesh to go across. This style of meshing would allow the mesh to be in the same shape as the partitioned face throughout the whole layer. The information for the materials' mesh are depicted in Appendix C. Once the base layers for the IM7-977-3 were created, the cohesive elements came next. Creating a separate cohesive layer allows the model to depict debonding and show whether there is stress occurring across the thickness of the material. These elements were generated using the same technique as the composite layers above with the exception that the thickness is 0.0005".

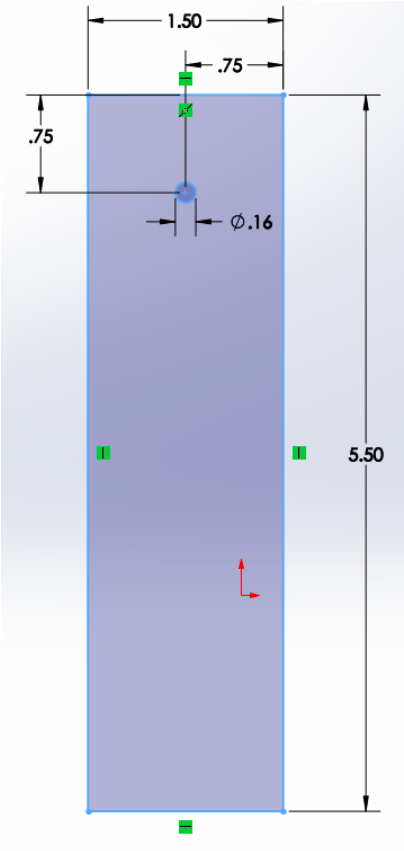

Figure 10: Dimensions of Object

A simple pin was made next for use in the model to represent the pin in experimentation for single-shear experimentation. The pin is depicted in Figure 11 for reference. The center circle of the pin was made slightly smaller than the hole of the model for there not to be issues of interference when the model runs. The length of the inner portion of the pin was designed to be the exact thickness of the entire model. The ends are large circles to ensure no movement in the pin when the model runs. The materials used for the pin are in Appendix B and the elements are specified in Appendix C. The mesh for the pin was generated by Abaqus by using the mesh option and the automatic options picked for a normal mesh.

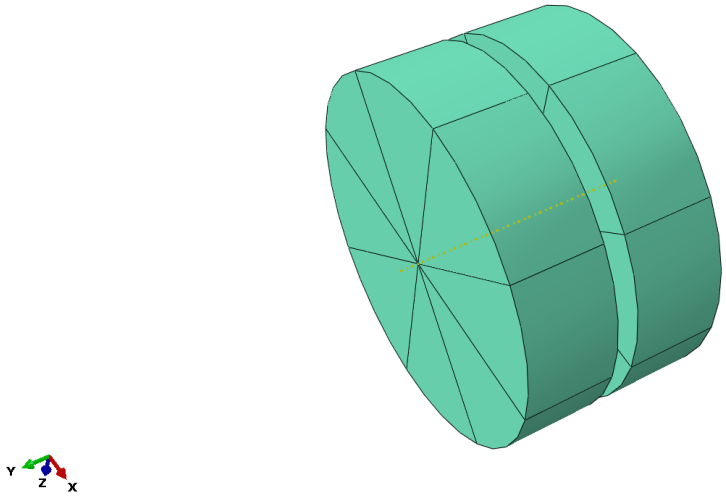

Figure 11: Pin Used in Modeling

Generating the steel foils into the design came next. The steel foil partitions followed the same design as the cohesive element. Material properties were specified using the information gathered from the experimentation of the foil specimen. Two different foil layers were made: one for the combination with the 90-degree layer and the other for the -45-degree layer. New 90- and -45-degree layer bases needed to be made for

the modeling with foils. The new base layers were made in the same fashion but with the new dimensions needed.

After the initial portion of designing the layers themselves, the model needed to be put together. This was done by generating instances of every layer according to the lay-up of the entire object: [45/0/-45/0/90]s. The nine layers were created into instances along with eight instances of the cohesive layer. Using the coincident point tool, each layer was put in the proper order with a cohesive element in-between to ensure the layers are directly next to each other. Incorporating the pin into the model came next. The instance for the pin was generated and put into the proper place using the coincidence plane and concentric circle tools in Abaqus.

The next steps were to ensure each instance was tied together as one object. A contact was generated using the specified information in Appendix D. Then each layer was tied to one another using the tie constraint tool in Abaqus. The back of one layer would be tied to the proceeding front portion of the cohesive element and then the cohesive element would be tied to the following composite layer. The models with the steel foil would have additional ties connecting the bottom of the steel foil to the top of the composite layer below it. Then both the steel foil and the composite within the same layer were tied to the cohesive layers next to them. The pin would be placed next using the concentric constraint with the hole of the object and the inner, smaller circle of the pin. Then the back of the larger circles would be constrained by the front edge of object ensuring the pin would be in the proper place. A contact was then created between the material and object of the hybrid composite and the pin.

Once the object was tied together, the outer portion of the pin would be encastered to ensure no movement. Then a displacement step was applied to the entire bottom of the object using the information depicted in Appendix E resulting in Figure 12. Next, to ensure the proper information was obtained, the field output request was updated to request information for each specific layer instead of just the entire model. The information requested is defined in Appendix F and used in the subsequent results. Once the entire model was completed, the job would be created and submitted for analysis.

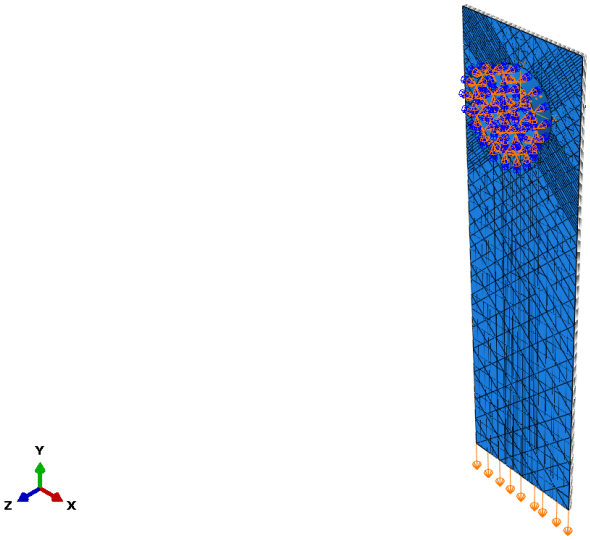

Figure 12: Completed Model in Abaqus

Chapter 4

IV. Analysis and Results

Steel Foil

The steel foils' loads and displacements were run through a MatLAB code in order to transform the load into stress using the equation below:

$$\sigma = \frac{F}{A} \tag{31}$$

Where F is the axial force and A is the cross-sectional area of the specimen. Then the strain was calculated by using the generic strain formula below

$$\varepsilon = \frac{\delta}{L_o} \tag{32}$$

Once the stress and strains were calculated, then the stress-strain curves would be graphed using the values calculated. Overall, twelve tests were performed and separated based upon the estimated strain rate of the test. The stress-strain curves calculated from the load-displacement information were graphed in order to show the difference between each test. Figure 13 shows all four test curves for 0.0027 $\frac{\mathbf{1}}{\boldsymbol{s}}$ strain rate. The initial test subject ran longer than the last three test specimen. Figure 14 shows the three test result curves for 0.00027 $\frac{\mathbf{1}}{\boldsymbol{s}}$, while Figure 15 shows the three test result curves for 0.000135 $\frac{\mathbf{1}}{\boldsymbol{s}}$. Then the final set of tests are shown in Figure 16 for 0.000027 $\frac{\mathbf{1}}{\boldsymbol{s}}$. All four figures show that the test results for each strain rate did not vary a lot. The modulus of elasticity was almost identical between the different tests which can be verified by the slope of each test specimen.

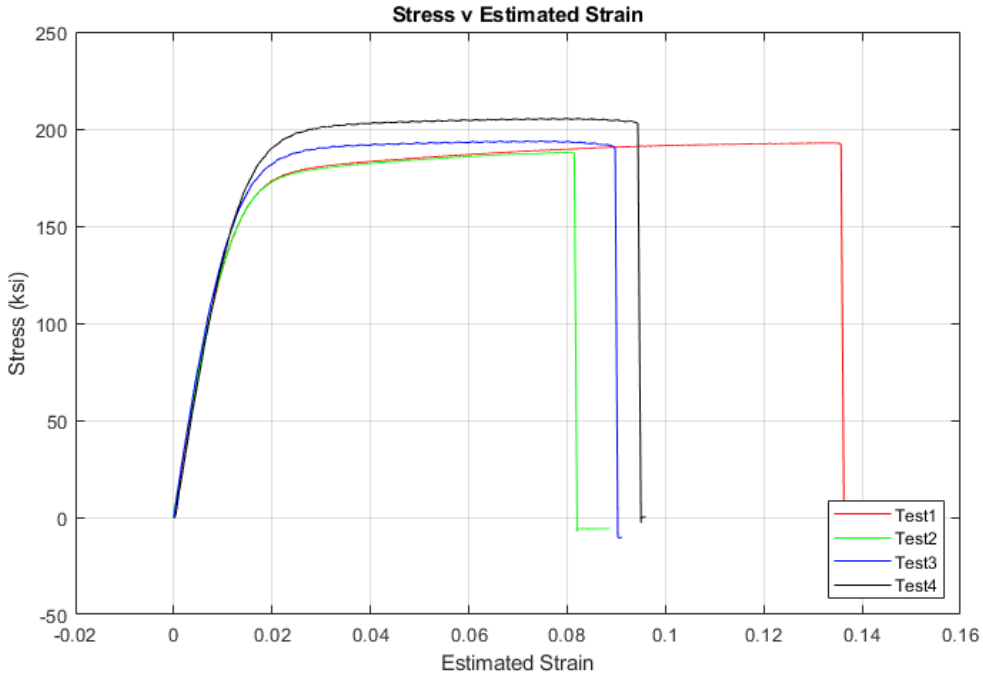

Figure 13: Stress-strain Curve for 0.0027 $\frac{1}{s}$ Estimated Strain Rate

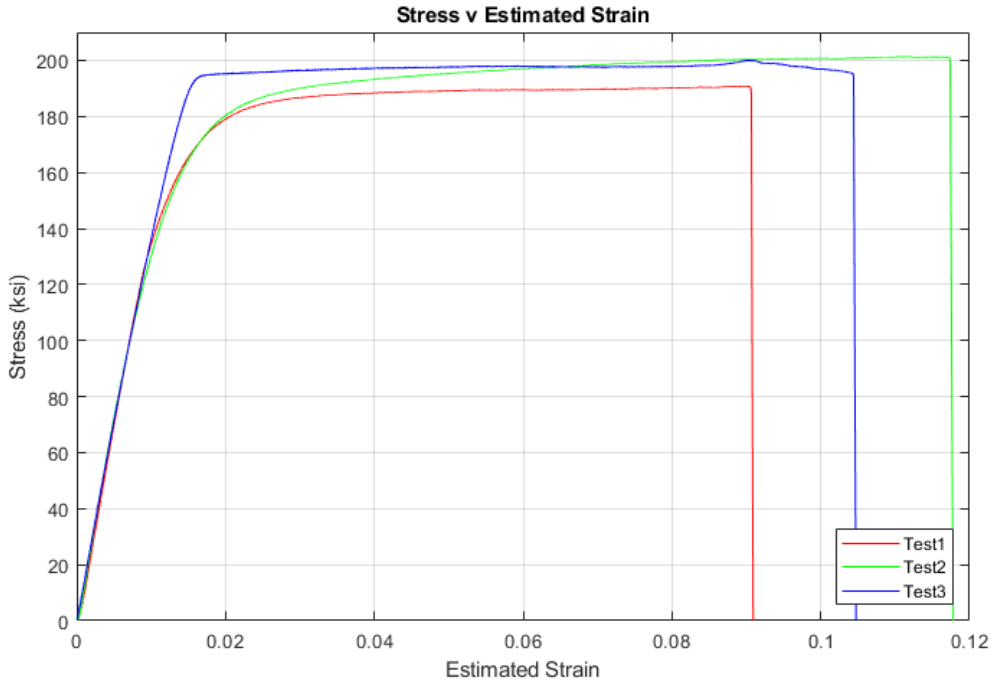

Figure 14: Stress-strain Curve for 0.00027 $\frac{1}{s}$ Estimated Strain Rate

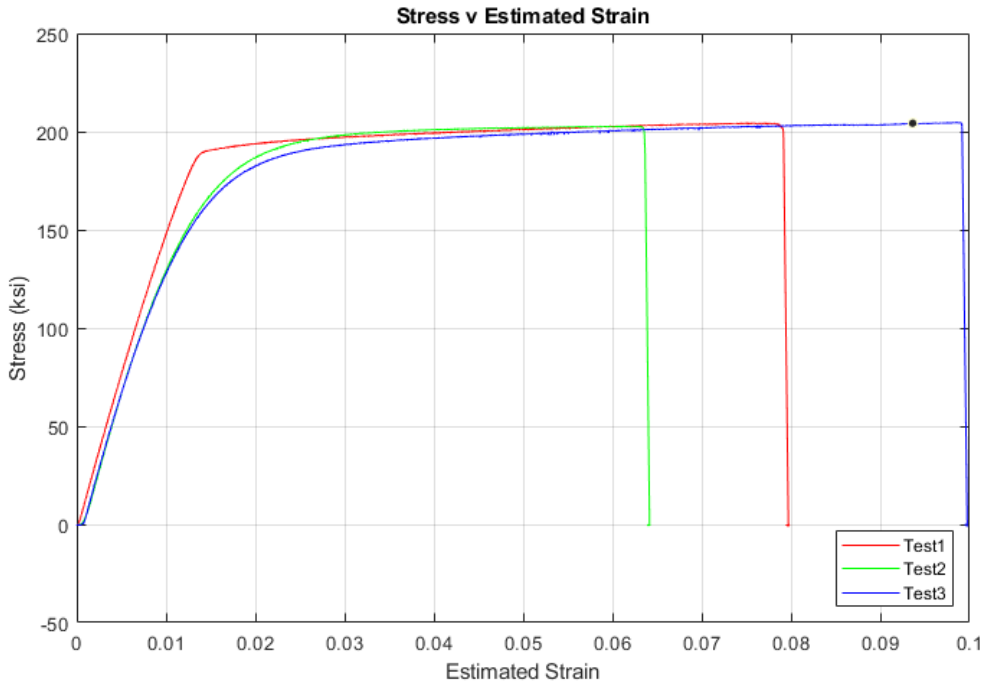

Figure 15: Stress-strain Curve for 0.000135 $\frac{1}{s}$ Estimated Strain Rate

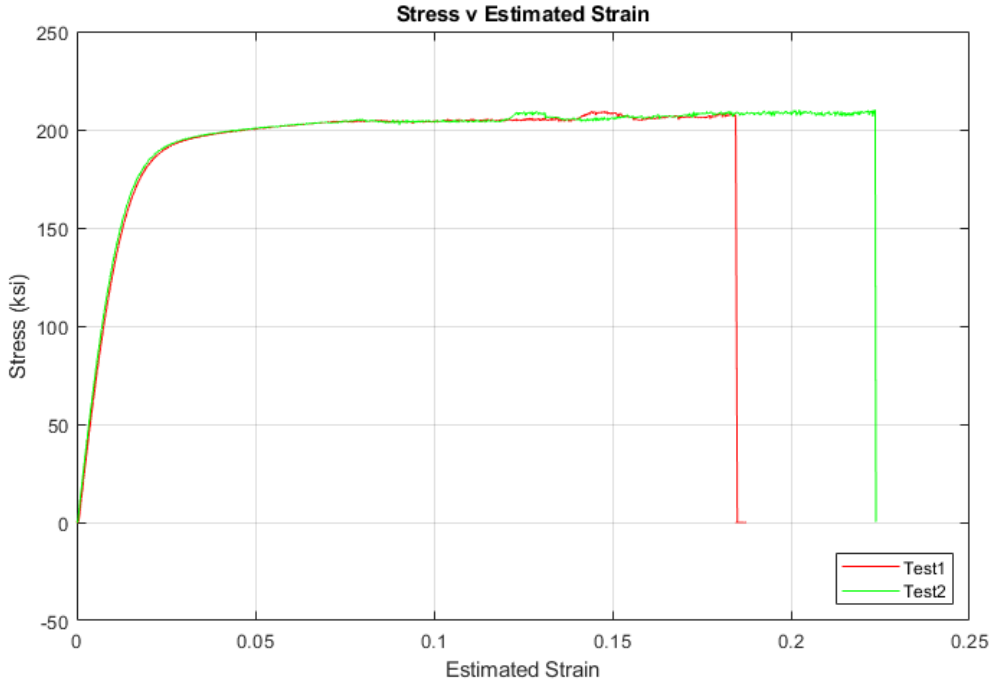

Figure 16: Stress-strain Curve for 0.000027 $\frac{1}{s}$ Estimated Strain Rate

The resulting yield stresses from the various tests at different estimated strain rates are depicted in Table 4. The yield stress was determined from the 0.02% offset line in each graph shown in Appendix G. The slope for each test calculation was determined by taking two points of the most linear portion of the graph and averaging the slope between them. The average from all results was 155.33 ksi, which was then used in the model for the plasticity property of the steel foils.

Table 4: Yield Stress (ksi)

Test	0.0027 $(\frac{1}{s})$	0.00027 $(\frac{1}{s})$	0.000135 $(\frac{1}{s})$	0.000027 $(\frac{1}{s})$
1	142.137	154.1751	189.2742	147.2133
2	141.412	147.2133	150.8392	149.3889
3	147.2133	190.4345	149.3889	
4	155.9156			

The Modulus of Elasticity from each of the tests is shown in Table 5. The average Modulus of Elasticity calculated from all the tests is 14840.5514 ksi, which was used in the foil layers of the model.

Table 5: Modulus of Elasticity (ksi)

Test	0.0027 $(\frac{1}{s})$	0.00027 $(\frac{1}{s})$	0.000135 $(\frac{1}{s})$	0.000027 $(\frac{1}{s})$
1	14293.469	14967.8945	15765.6021	14424.003
2	14357.286	14909.8794	15562.5493	14663.3153
3	14953.3908	14268.813	15040.4134	
4	14880.8719			

The average stress-strain curve for each estimated strain rate was determined and graphed for better comparison in Figure 17. Overall the stress-strain curves follow a typical stress-strain curve for metal properties. The slope varied little between the

different tests. While the yield stress did vary between the different tests, the difference was not extreme and far apart.

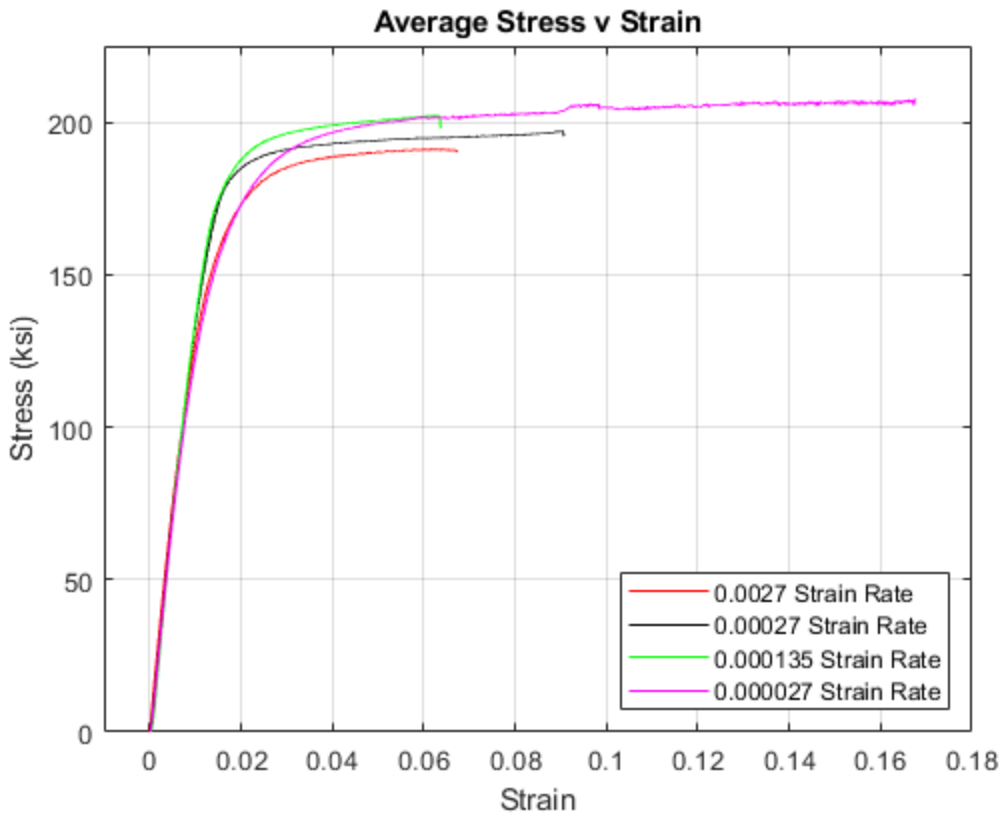

Figure 17: Average Stress-Strain Curve for All Estimated Strain Rates

Hashin Model without Steel Foil

The models without the steel foil used the ply layup of [45/0/-45/0/90]s with a cohesive layer in between the composite layers of the model. Before getting into the composite layers of the first model, an important layer to note is what happens to the cohesive element within the model. Figure 18 shows that the cohesive layer in-between the first and second layer of the model does experience stress. Specifically, the cohesive

element feels stress in the σ_{13} plane which indicates that the cohesive element carries stress through the thickness of the model.

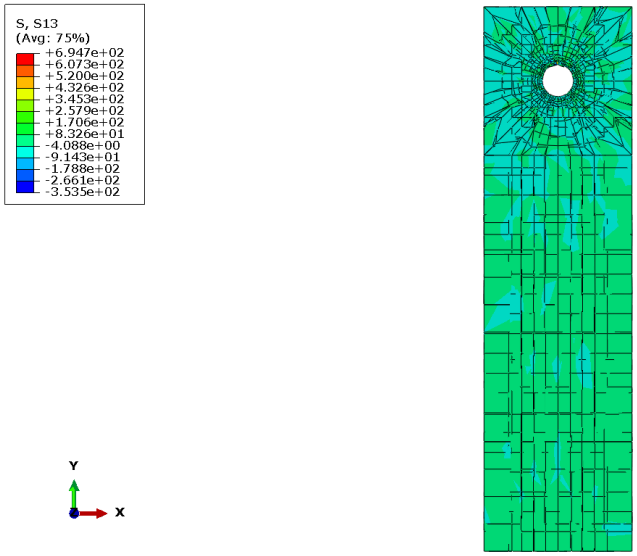

Figure 18: Cohesive Layer in-between Layer 1 and Layer 2

For graphing the results of the different layers within the model, there were five different paths generated depending on which direction the fibers were orientated. Each line shown in the following figures start at the hole and go towards the edge of the layer and used the nodes at each point along the lines. Figure 19 shows the two paths which were used on the 45- and -45-degree fiber orientated layers. The two lines were chosen to depict the longitudinal fiber direction and transverse to the fiber direction. For the 45-degree, the line pictured on the left depicts the longitudinal fiber direction while the second line is transverse to the fiber direction. The -45-degree layer is a mirror image of the 45-degree layer with the line on the right side being in the longitudinal fiber direction.

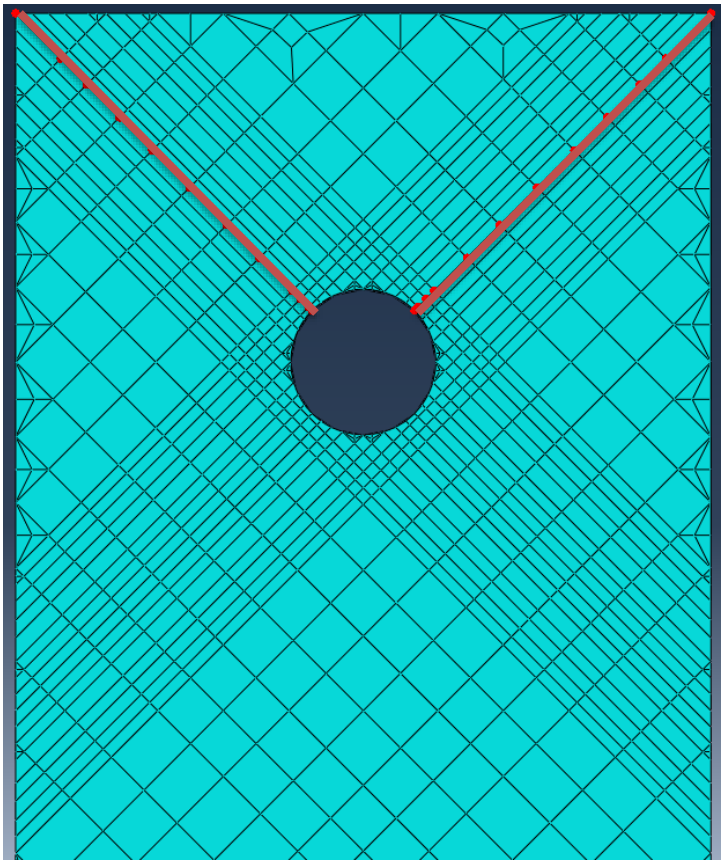

Figure 19: Paths for 45- and -45-degree Layers

Figure 20, on the other hand, shows the paths used for the 0- and 90-degree layers of the model. For the 0-degree layers, the longitudinal direction is the vertical line depicted in the picture. The other two lines are transverse to the fiber direction and when mentioned are called the right and left side referring the lines on the picture on the right and left in the horizontal direction respectively. The 90-degree layer is just the opposite of the 0-degree layers with two longitudinal fiber direction lines.

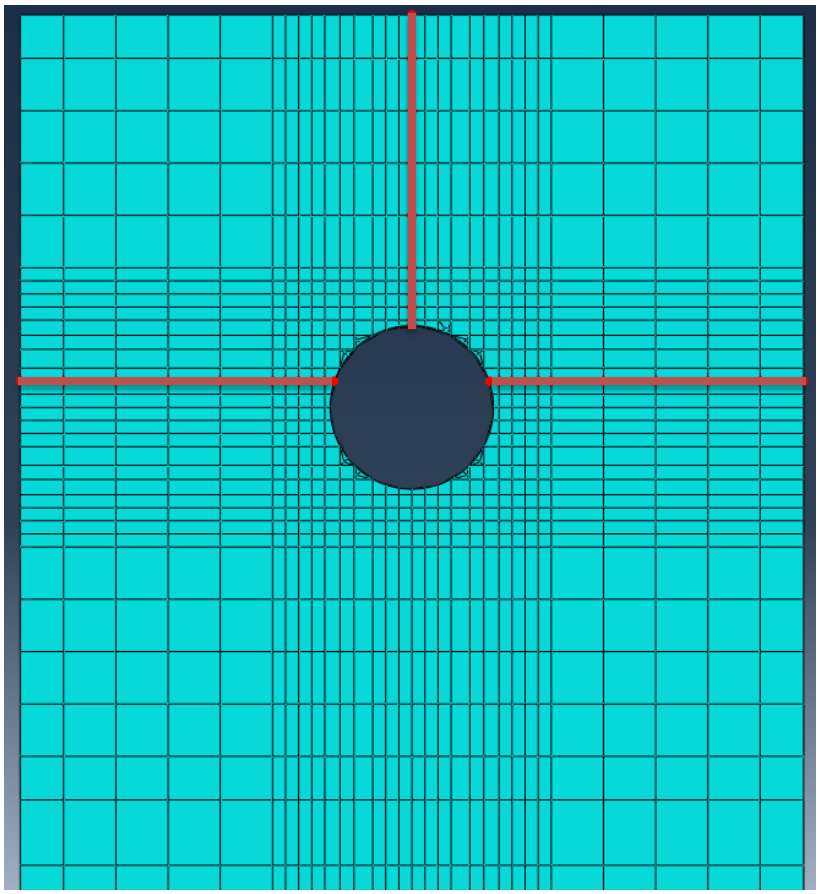

Figure 20: Paths for 0- and 90-degree Fiber Orientations

The Hashin model without the steel foil ran until failure at time 0.067s. Abaqus aborted the model due to a geometrical failure of a cohesive layer. The cohesive layer distorted excessively and therefore the model was considered failed. One element in the cohesive element distorted beyond Abaqus control and made the system abort the model. Each subsequent model time was based upon the Hashin model failure time. Three times were chosen to show the progression of stress over time on each layer: 0.033s, 0.050s, and 0.067s. As time progressed throughout the model, the stress field grew larger and progressed along the specific layer's fiber orientations. As can be seen in Figures 21-23, the von Mises stress in the first layer grows in the 45- and -45-degree directions. The

highest stress points are near the hole and diminishes the farther out the elements are from the hole.

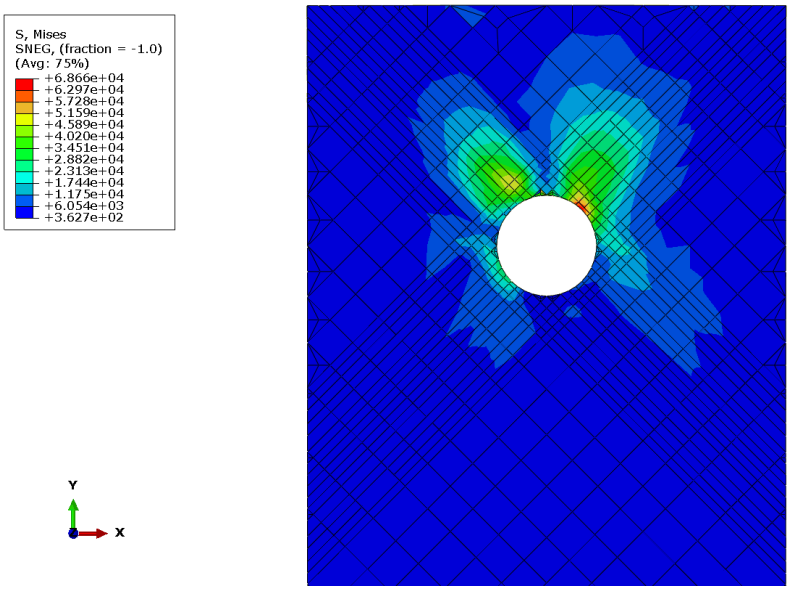

Figure 21: Von Mises Stress in Layer 1 at Time 0.033s

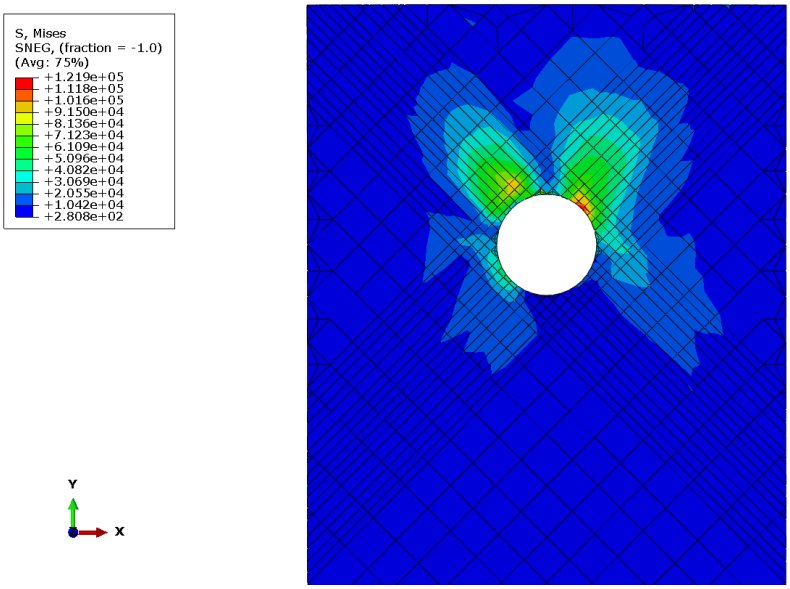

Figure 22: Von Mises Stress in Layer 1 at Time 0.050s

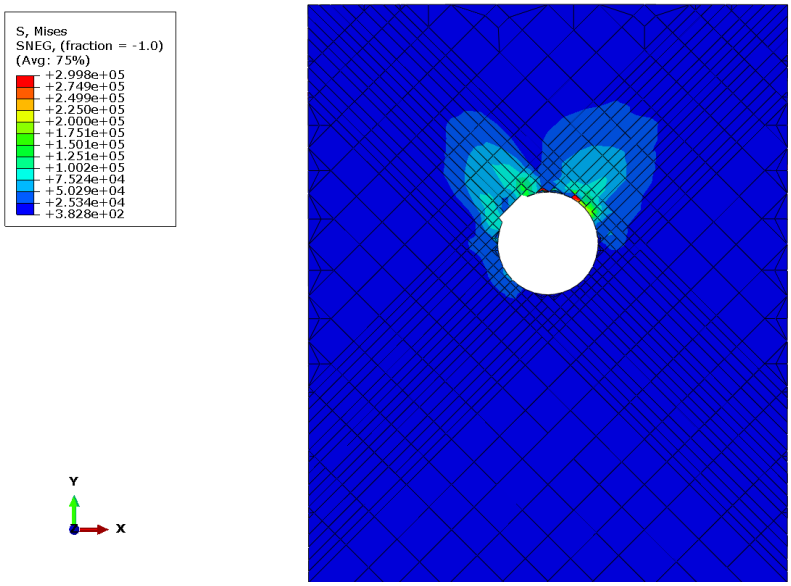

Figure 23: Mises Stress in Layer 1 at Time 0.067s

Due to the nature of composite materials, the stress points were taken along the path according to the fiber directions: longitudinal and transverse. The longitudinal fiber direction stress is determined from the direct direction the fibers lay while the transverse stress measures the stress upon the perpendicular fibers to the fiber direction. Figure 24 shows the stress upon the longitudinal fibers in the first layer. The figures show that the fibers experience compression instead of tension. At time 0.067s, the graphs as shows initial stress of zero which can be understood from the fact that looking back at Figure 23, some of the elements in the longitudinal direction have failed and been deleted.

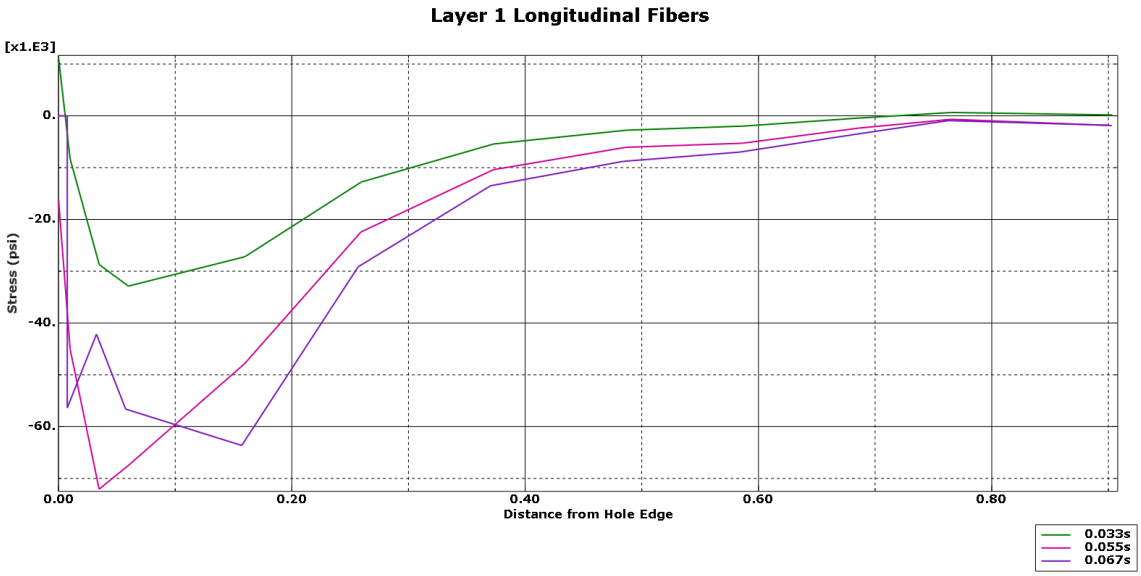

Figure 24: σ_{11} for Layer 1 45-Degree Longitudinal Fiber Direction

Figure 25 shows the stress in the transverse direction. Initially the stress starts as tension, but the compression grows as the material experiences more of the load placed upon the object. With the failure of some elements in the longitudinal direction, the transverse direction turns from tension to compression. Looking back at Figure 23, there are some elements deleted from failure in the longitudinal direction. At the same point these elements are deleted, time 0.067s, the stress in Figure 25 turns from tension to compression. The matrix, which is transverse to the fiber direction, overall takes less stress in the material than the longitudinal fibers.

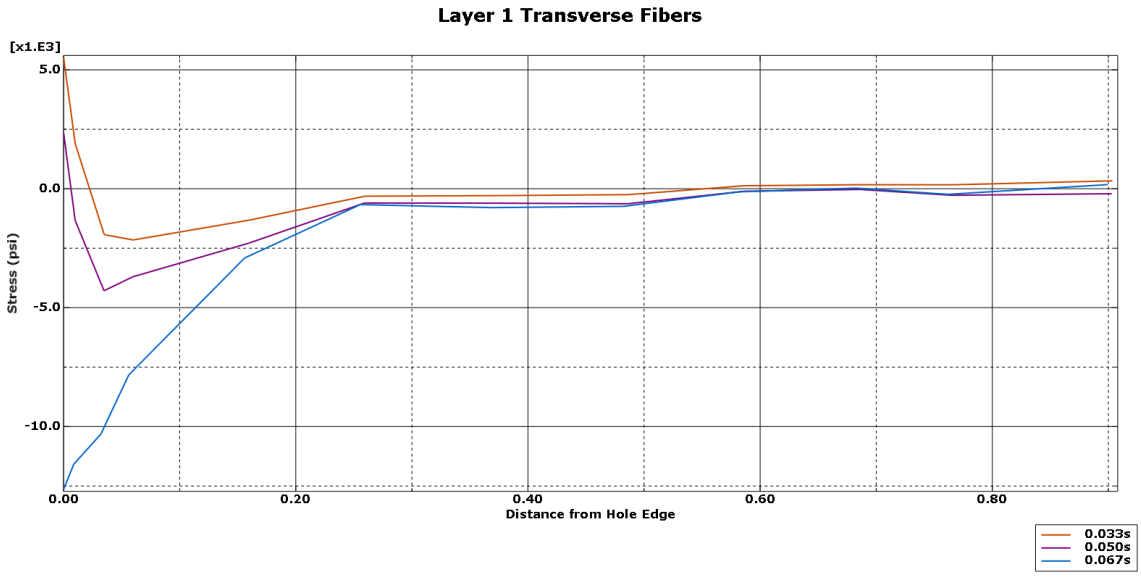

Figure 25: σ_{22} for Layer 1 45-Degree Transverse to the Fiber Direction

The fibers take on most of the stress, but Figure 26 shows the damage taken by the fibers themselves according to Hashin's failure criterion. Figure 26 (b) shows the tension experienced by the fibers and Figure 26 (a) shows the compression failure of the fibers. Tension is seen more in the transverse direction while the longitudinal fibers experience more compression.

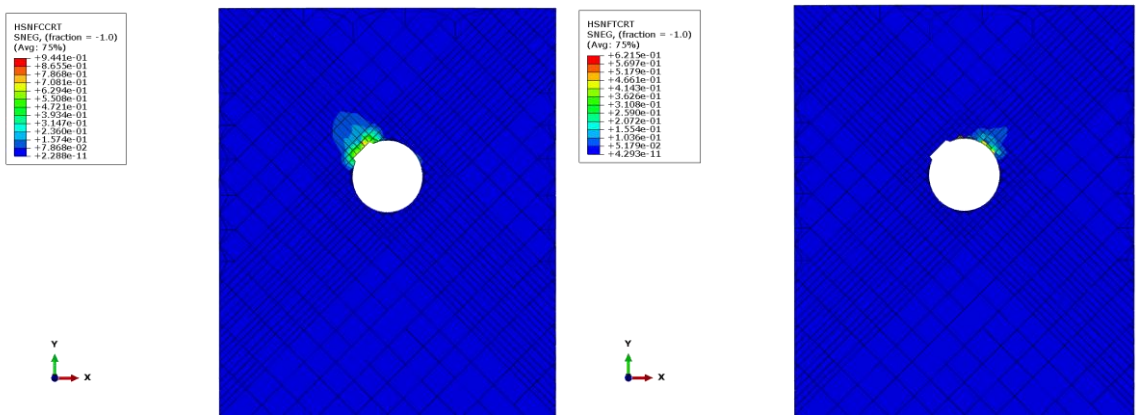

(a) (b)

Figure 26: Fiber Failure in (a) Compression and (b) Tension

Hashin also expresses the failure the matrix feels with the layer. Figure 27 (a) shows the matrix compression failure which occurs primarily around the top half portion of the hole and does not spread much farther. Tension is shown in Figure 27 (b) and primarily occurs in the fiber direction where the fibers are failing due to compression.

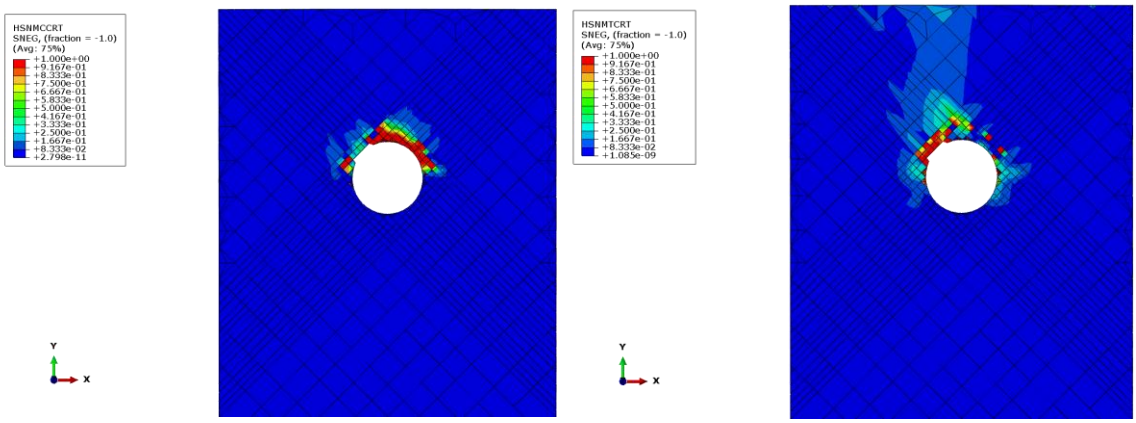

(a) (b)

Figure 27: Layer 1 Matrix Failure in (a) Compression and (b) Tension

The second layer in the composite shows similar failures and stress trends as the first layer even though the fiber direction is different. Figures 28-30 show the progression of stress in the second layer of the model. As time goes on, the model's stress increases but occurs along the longitudinal and transverse fiber direction. The highest stress points also occur at the points closest to the hole and diminishes the further away an element becomes from the hole. The stress in the second layer also traverses downward along the entire layer from the side edges of the hole.

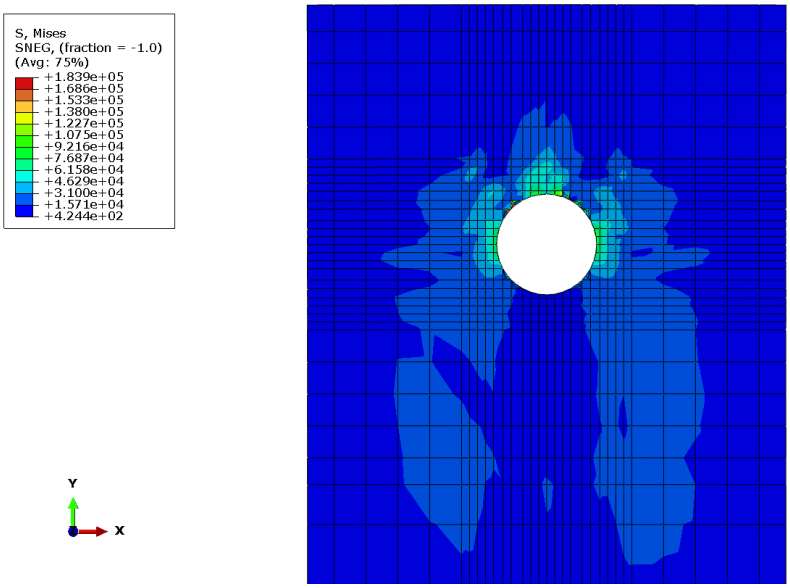

Figure 28: Von Mises Stress for Layer 2 at Time 0.033s

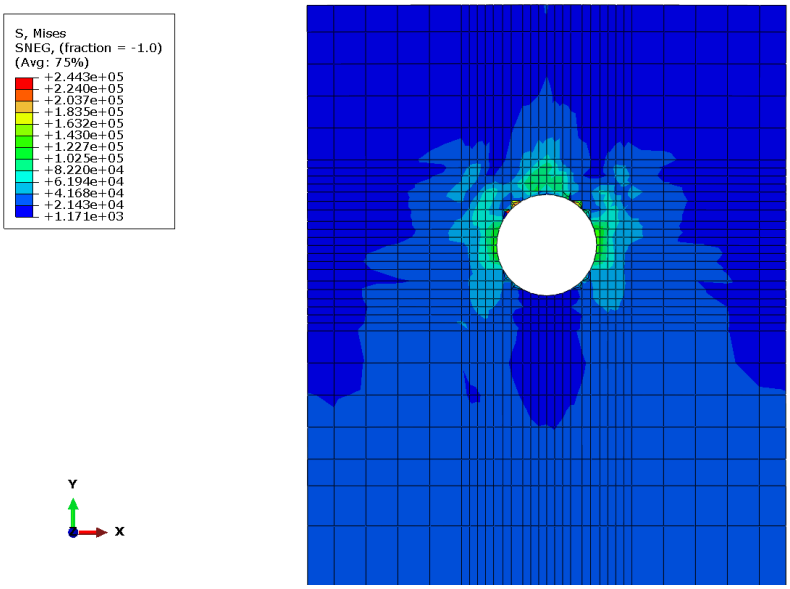

Figure 29: Von Mises Stress in Layer 2 at Time 0.050s

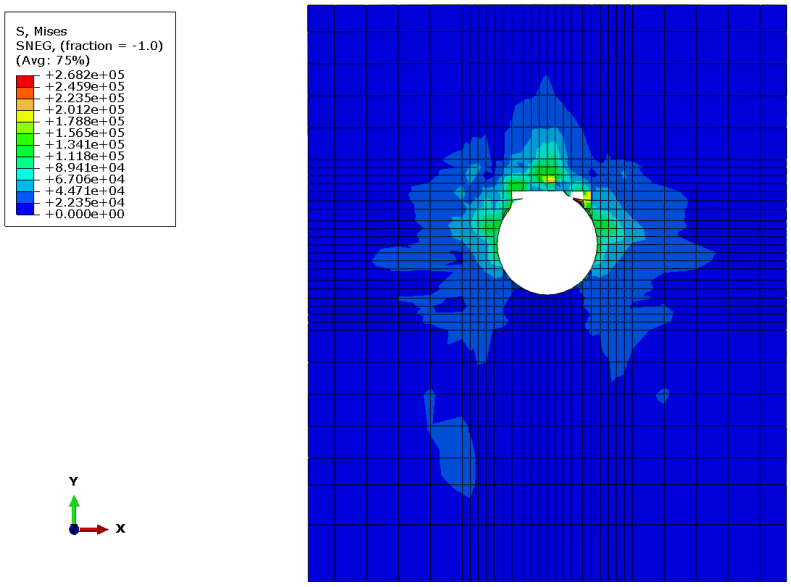

Figure 30: Von Mises Stress in Layer 2 at time 0.067s

The longitudinal fibers experience compression as time goes on for the model as can be seen in Figure 31. Again, at time 0.067s, the initial stress of the hole is zero where Figure 30 shows that the elements surrounding the hole in the longitudinal direction have failed and been subsequently deleted. The graphs also shows that at time 0.067s there is an anomaly in the stress of the material. Approximately 0.03” from the edge of the hole, the stress line turns vertical. Since the stress at the nodes are taken from the elements connected by the node, the four stress values considered are averaged by Abaqus. The vertical line shows that there was an error happening in that Abaqus did not condense the stress values but kept them active, and this vertical line also happens where there are elements that have been deleted due to failure causing an imbalance in calculating the average stress at the proper node.

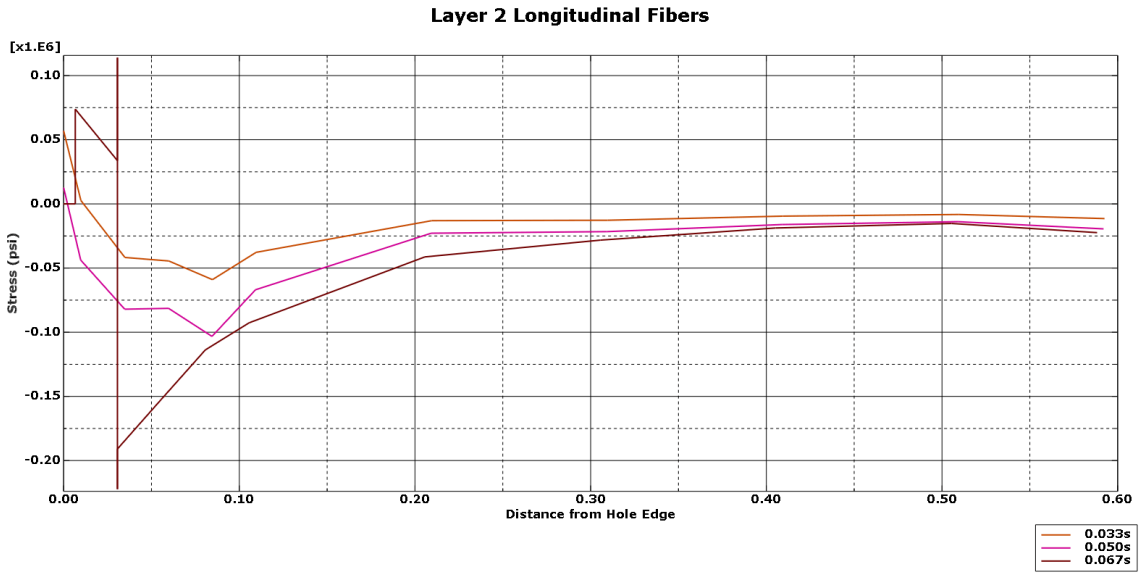

Figure 31: σ_{11} for Layer 2 0-Degree Longitudinal Fiber Direction

Figure 32 shows the stress in the transverse to the fiber direction. The graph shows two sides to the transverse to the fiber direction since the second layer is in the 0-degree fiber orientation. Initially the fibers experience tension but as time wears on in the model, the stress lessens to almost zero. The further away an element is from the circle, the less stress seen by that element.

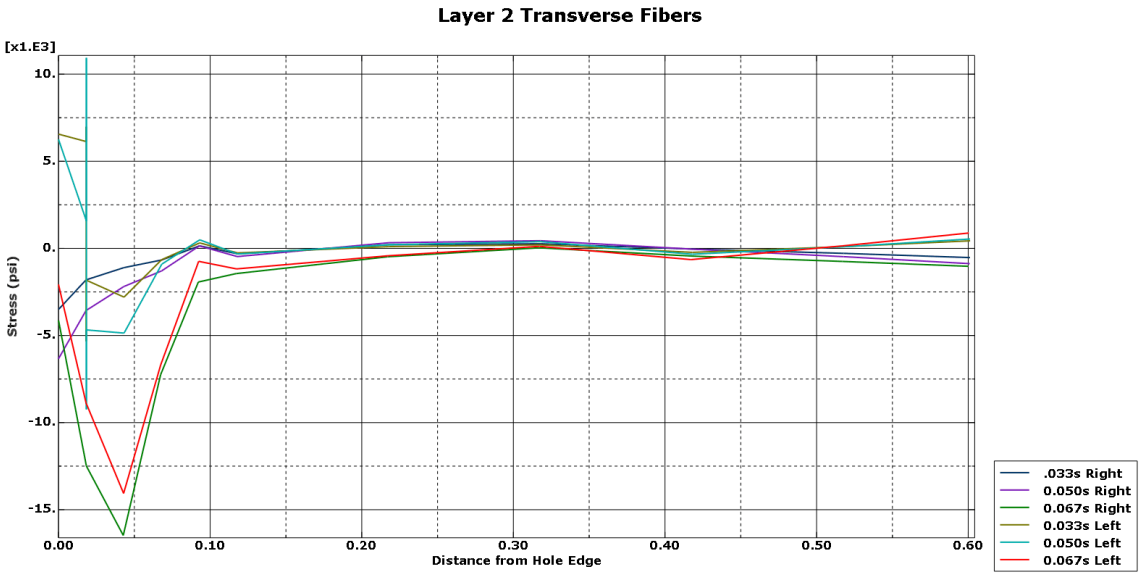

Figure 32: σ_{22} for Layer 2 0-Degree Transverse to the Fiber Direction

The fiber tension and compression failure for the second layer are shown in Figure 33. Fiber compression failure, depicted in Figure 33 (a), experience more failure than fiber tension failure shown in Figure 33 (b). The 0-degree layers experience more fiber compression than tension. Compression also happens directly at the top of the hole in the fiber orientation where some elements experienced complete failure.

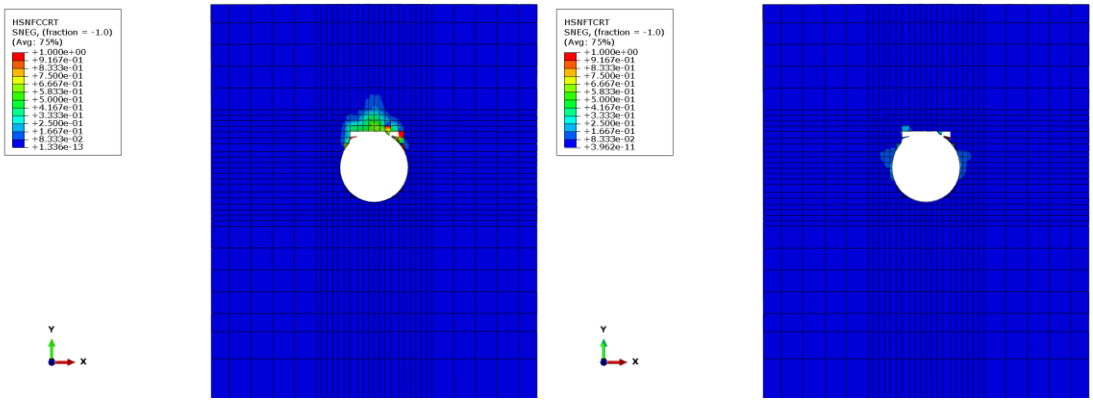

(a) (b)

Figure 33: Layer 2 Fiber Failure in (a) Compression and (b) Tension

The matrix in the second layer experiences more failure than the fibers. Figure 34 shows the matrix failure in both tension and compression. Matrix tension, depicted in Figure 34 (b), shows matrix tension failure from the start of the hole in the fiber direction until the edge of the object. Figure 34 (b) shows that the matrix compression failure, while great, is not as intensive or widespread as the matrix tension failure.

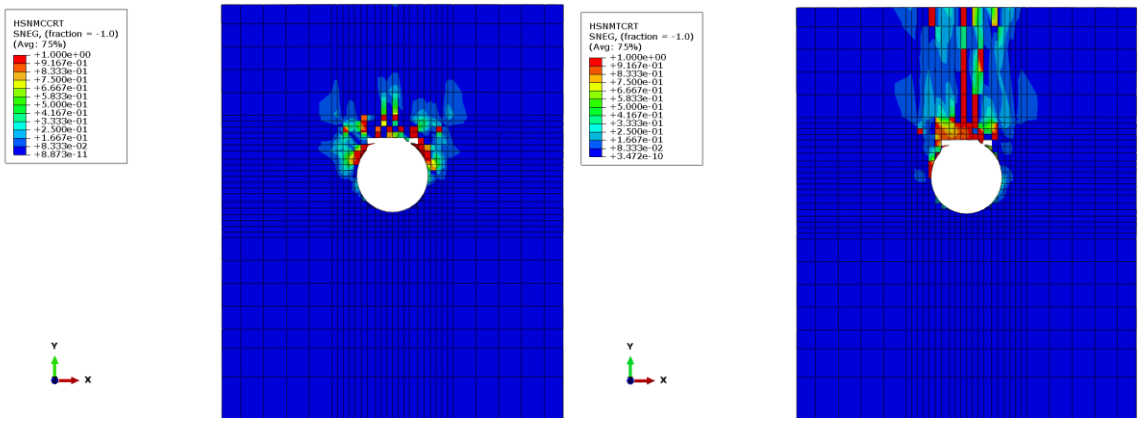

(a) (b)

Figure 34: Layer 2 Matrix Failure in (a) Compression and (b) Tension

The third layer of the object reacts and shows similar numbers and responses to the first layer except in a mirror image. Figures 35-36 shows the evolution of the von Mises stress in the third layer for a -45-degree layer. The results resemble the mirror image of Figures 21-23.

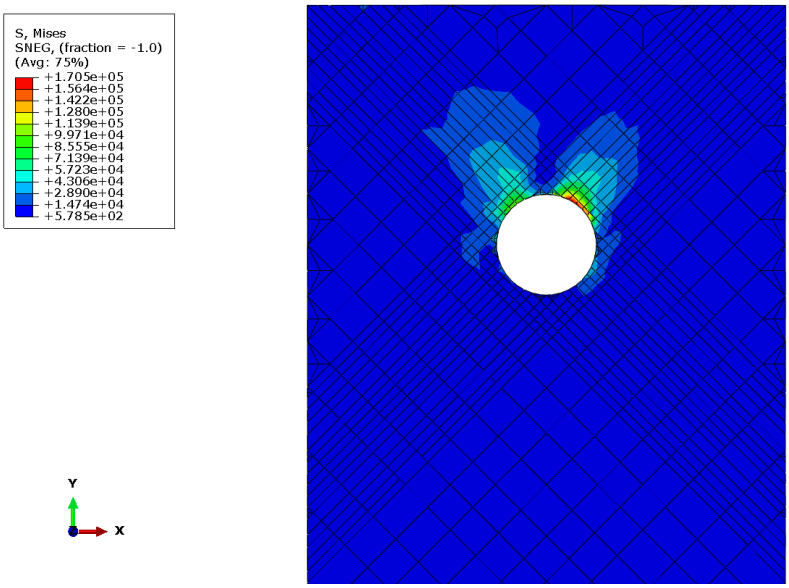

Figure 35: Von Mises Stress in Layer 3 at Time 0.033s

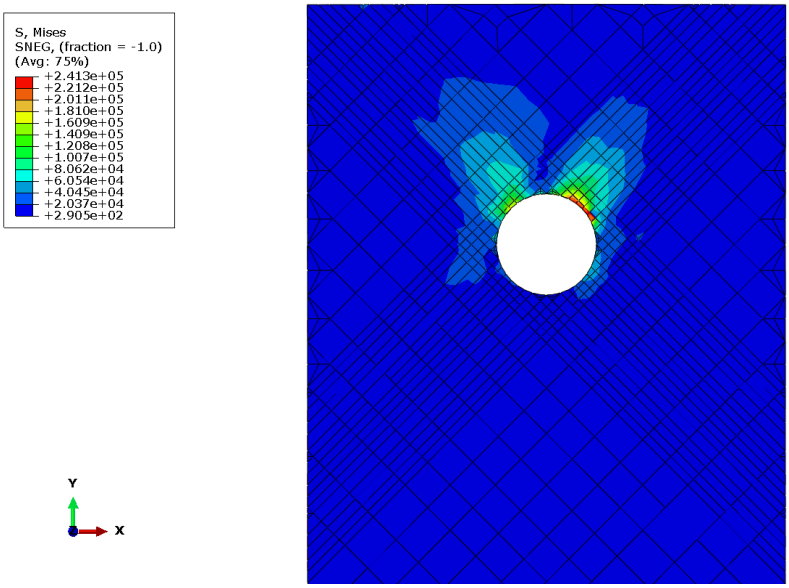

Figure 36: Von Mises Stress in Layer 3 at Time 0.050s

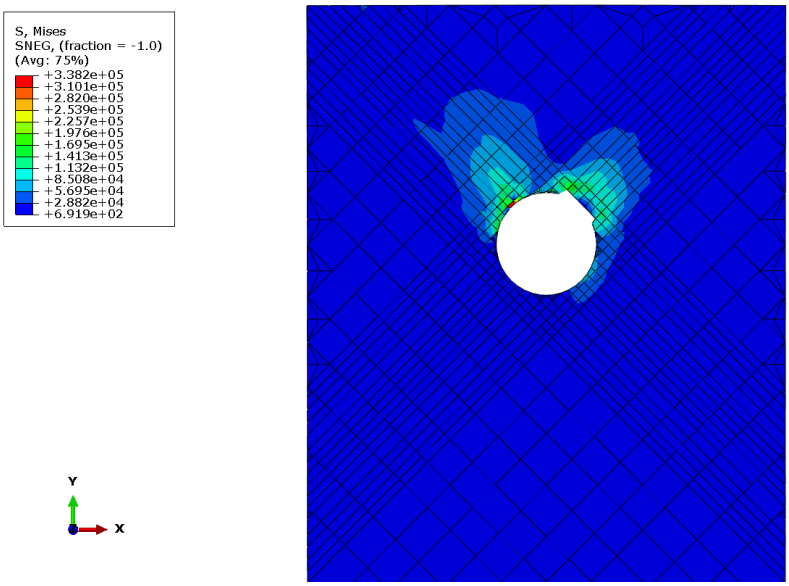

Figure 37: Von Mises Stress in Layer 3 at Time 0.067s

Figure 38 shows the stress seen by the longitudinal fibers of the third layer. The stress experienced by the longitudinal fibers is less than the stress seen in the longitudinal fibers of the first layer. Initial elements in the longitudinal direction have also been deleted in this element due to failure. The stress transverse to the fiber direction is less than the longitudinal fiber stress as depicted in Figure 39.

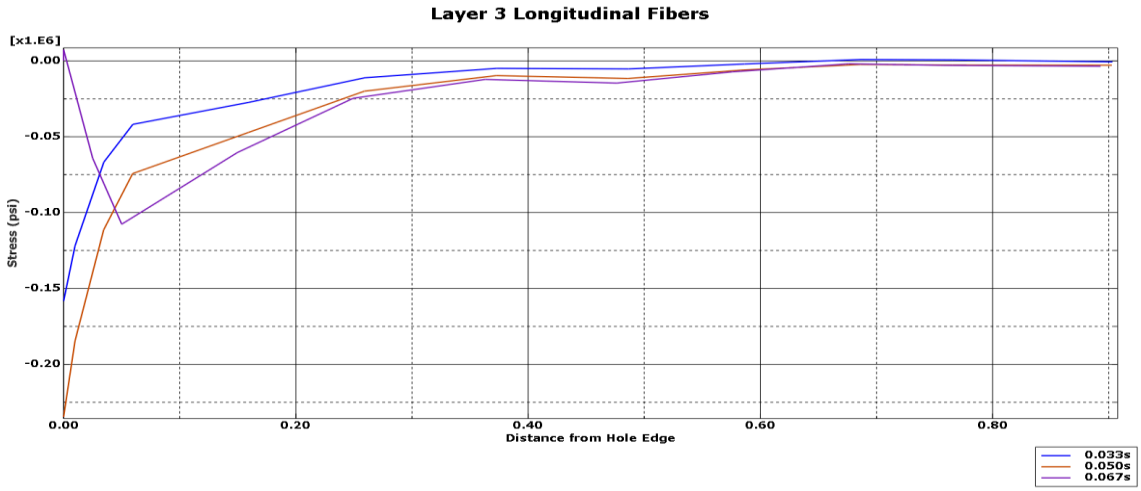

Figure 38: σ_{11} for Layer 3 -45-Degree Longitudinal Fiber Direction

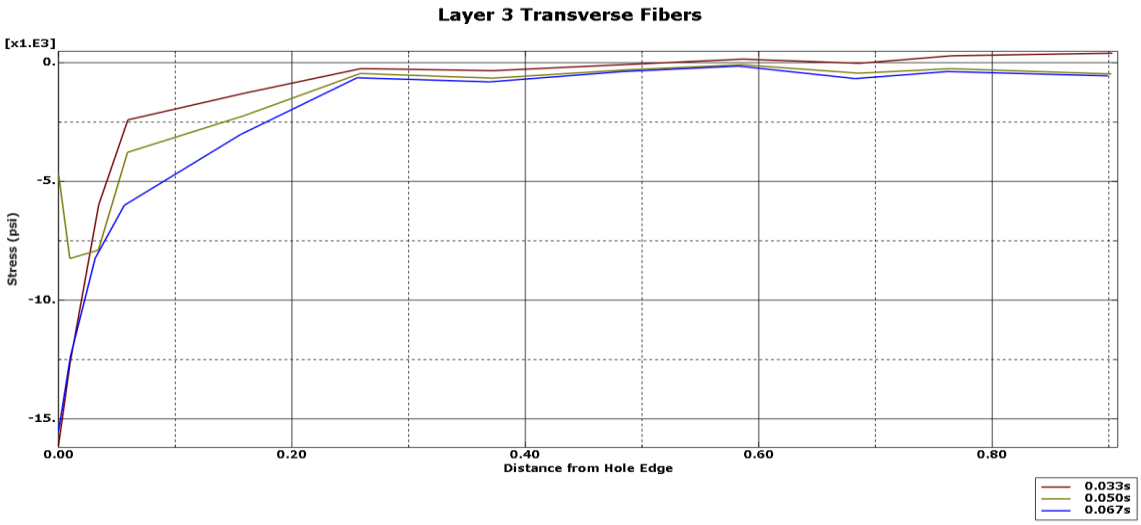

Figure 39: σ_{22} for Layer 3 -45-Degree Transverse to the Fiber Direction

Figure 40 shows that the fibers experience more compression failure than tension failure. The compression failure is also experienced along the longitudinal fiber direction and expands outward along the same direction.

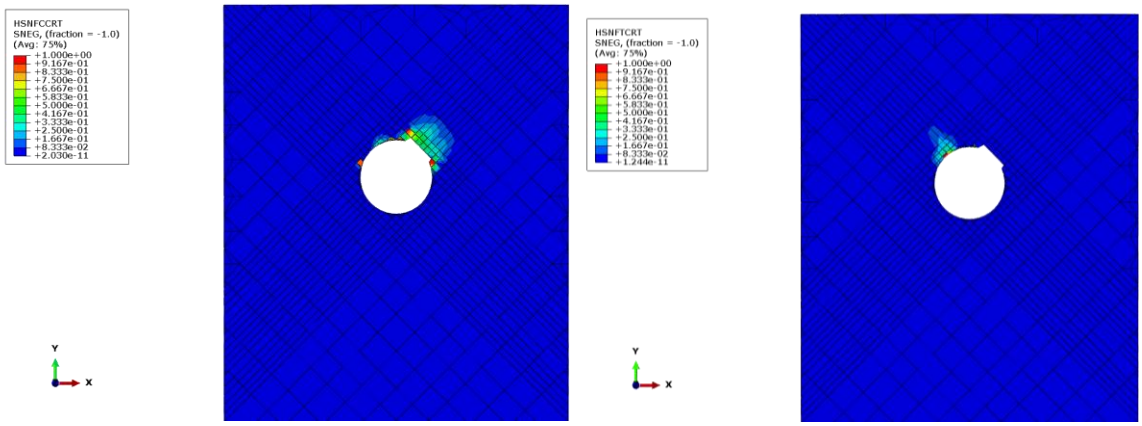

(a) (b)

Figure 40: Layer 2 Fiber Failure in (a) Compression and (b) Tension

The matrix failure that the third layer experiences is shown in Figure 41. Matrix compression covers the top portion of the hole primarily along the transverse fiber direction, while matrix tension failure is experienced by the longitudinal fiber orientation.

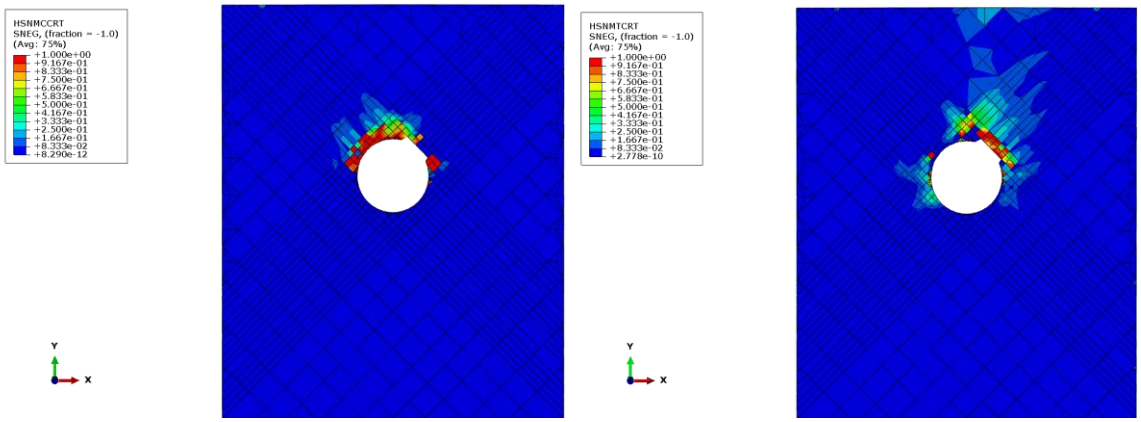

(a) (b)

Figure 41: Layer 3 Matrix Failure in (a) Compression and (b) Tension

The stress experienced in the fifth layer expands over time as shown in Figures 42-44. Like the second layer, the stress field seen by the fifth layer spreads across the longitudinal fiber and transverse to the fiber directions in the fiber orientated mesh.

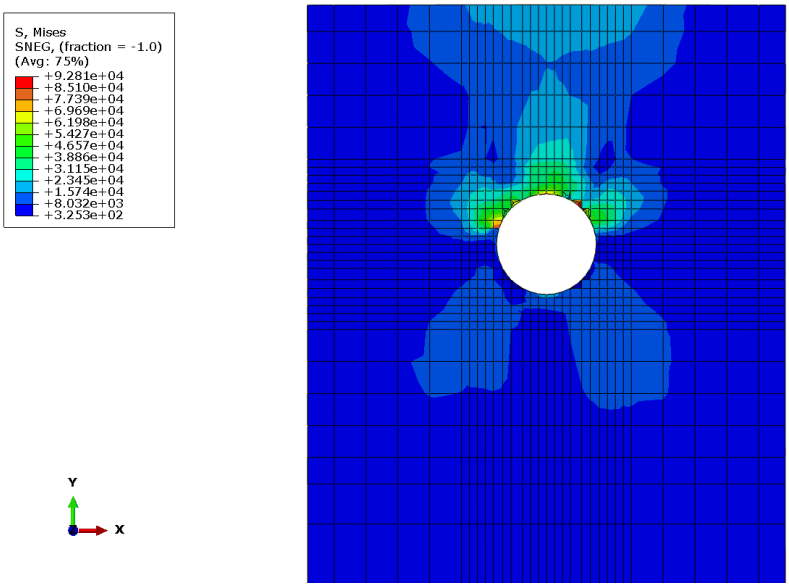

Figure 42: Von Mises Stress in Layer 5 at Time 0.033s

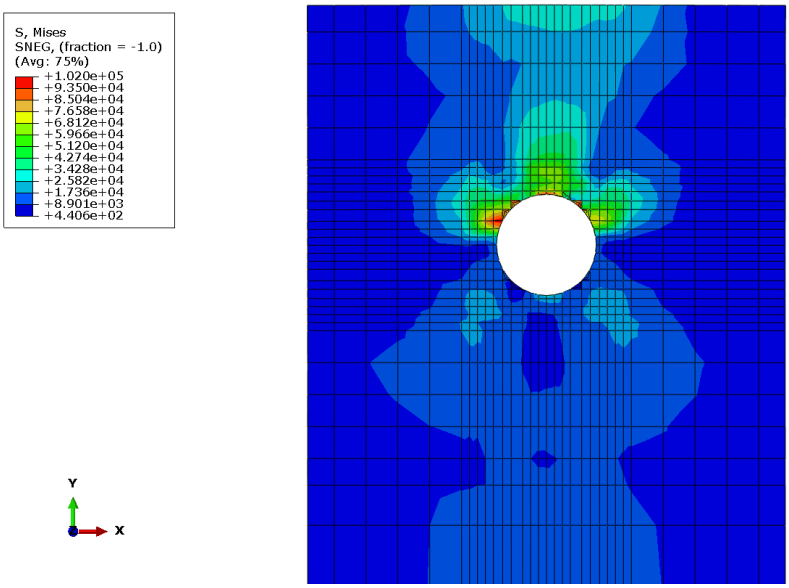

Figure 43: Von Mises Stress in Layer 5 at Time 0.050s

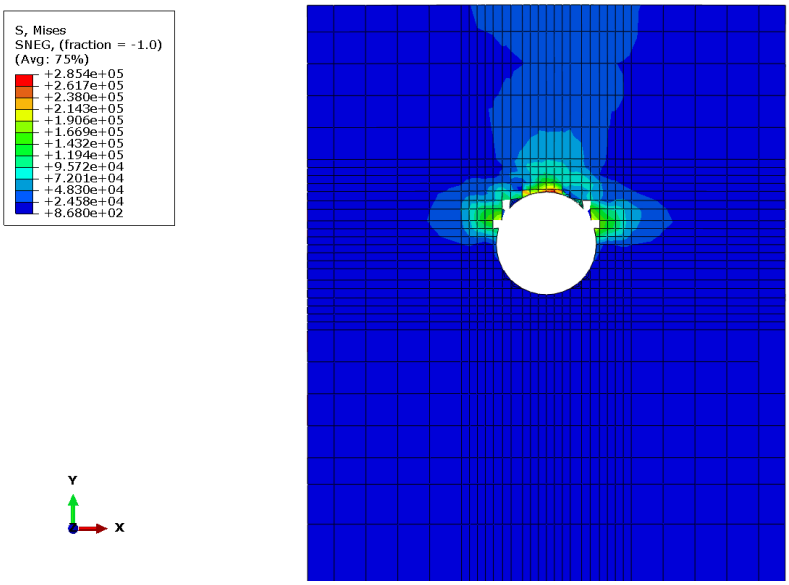

Figure 44: Von Mises Stress in Layer 5 at Time 0.067s

Figure 45 shows the longitudinal fiber stress seen by the fifth layer. The graph shows both the longitudinal fibers on the left side and right side of the hole. While the actual stress is slightly different between the two sides, the stress follows the same trend and pattern for both sides.

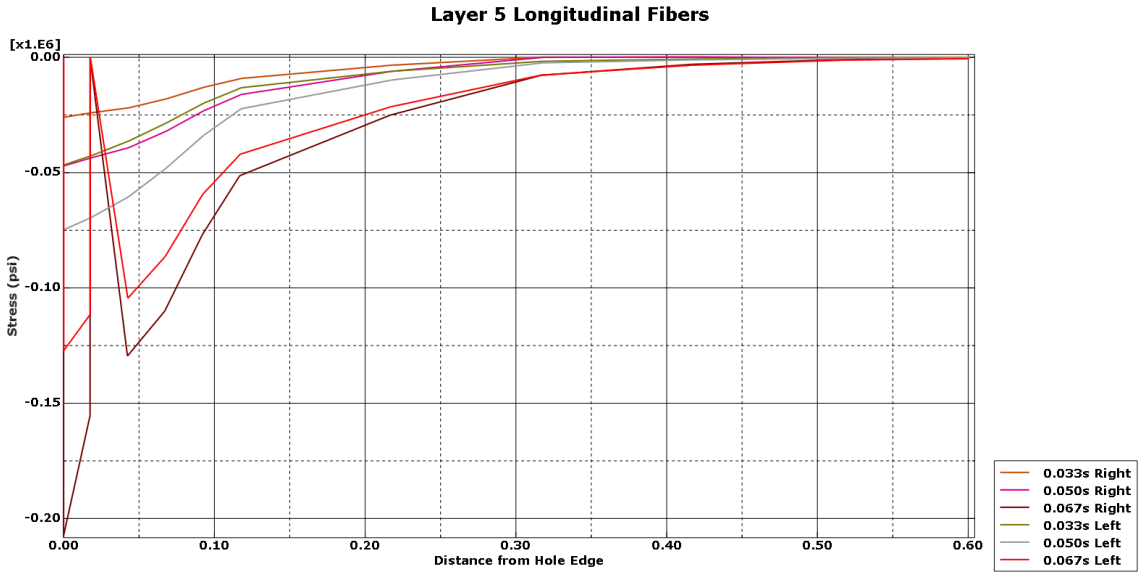

Figure 45: σ_{11} for Layer 5 90-Degree Longitudinal Fiber Direction

The transverse to the fiber direction in the fifth layer, as seen in Figure 46, experience approximately the same stress as the longitudinal fibers. Unlike the other layers shown so far, the fifth layer's transverse to the fiber direction experience almost an equal amount of the stress. As the elements get further away from the hole, nearly no stress can be seen by the layer.

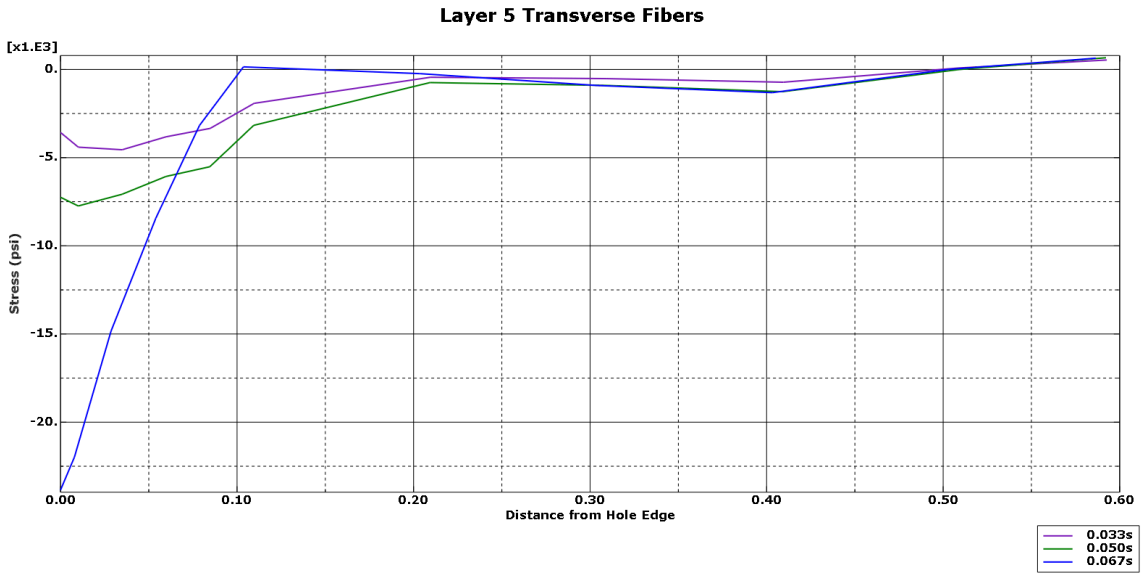

Figure 46: σ_{22} for Layer 5 90-Degree Transverse to the Fiber Direction

The fiber failure for the fifth ply is depicted in Figure 47. Layer 5 experiences little fiber tension failure, but the fiber compression failure is more prominent. The same trend seen in the previous layers also applies to the fifth layer: the fiber compression happens along the longitudinal fiber direction while the fiber tension is experienced transverse to the fiber direction.

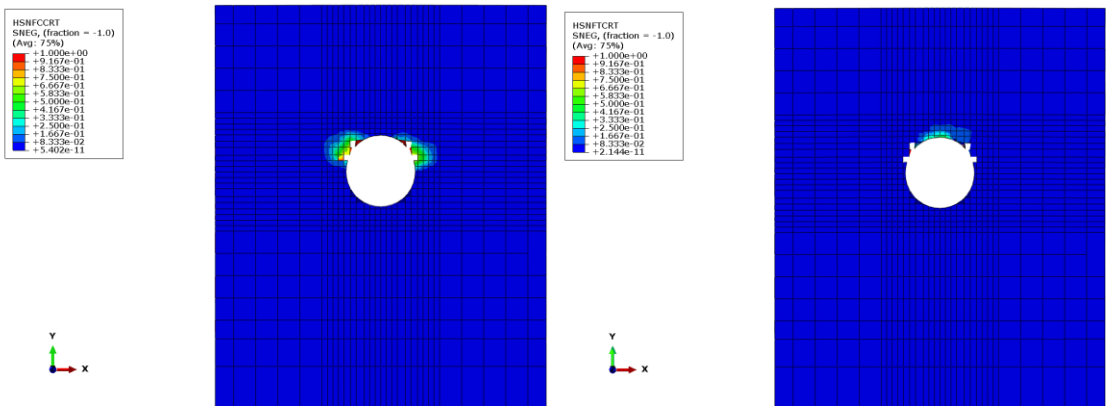

(a) (b)

Figure 47: Layer 5 Fiber Failure in (a) Compression and (b) Tension

Matrix failure follows the opposite pattern of fiber failure. In the longitudinal direction, as depicted in Figure 48 (b), the matrix experiences tension failure. Figure 48 (a) shows that the transverse direction encounters matrix compression failure.

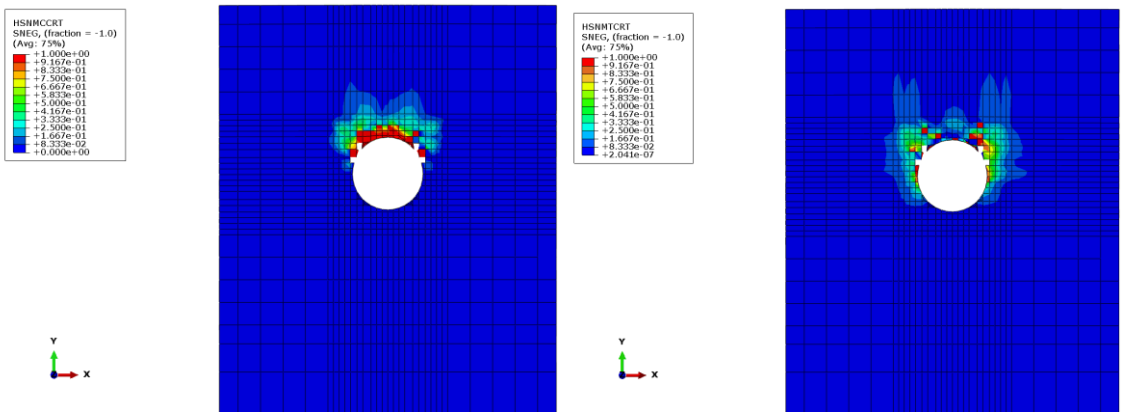

(a) (b)

Figure 48: Layer 5 Matrix Failure in (a) Compression and (b) Tension

Since the model is symmetric with multiple layers containing the 45-, 0-, and -45-degree fiber orientation with similar reactions and patterns, only one representation of each layer was shown. Each individual layer's information may be found in Appendix H.

For a comparison of the different layers and to determine if there was a significant difference, the different layer orientations were graphed together with their respective longitudinal and transverse fiber stress.

Figure 49 shows the 45- degree layers' longitudinal stress. While the two layers experience a similar trend in stress, layer 9 encounters a greater maximum stress. The transverse to the fiber direction, depicted in Figure 50, show a similar pattern. While the two layers feel similar stress at the same areas, there is a consistent small difference between the two layers at the same fiber orientation.

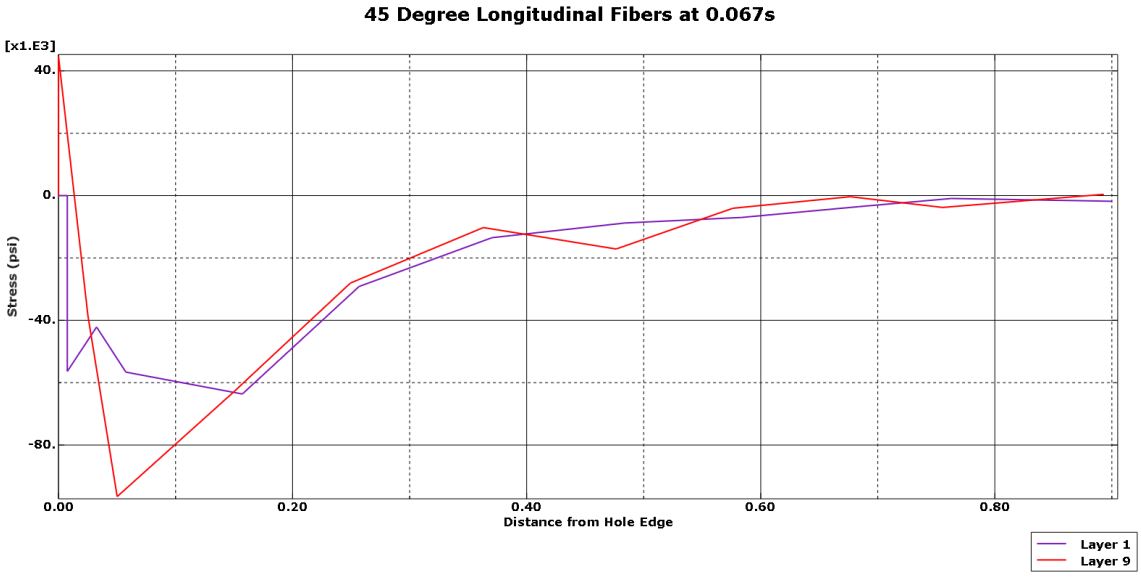

Figure 49: σ_{11} for 45-Degree Layers in the Longitudinal Fiber Direction

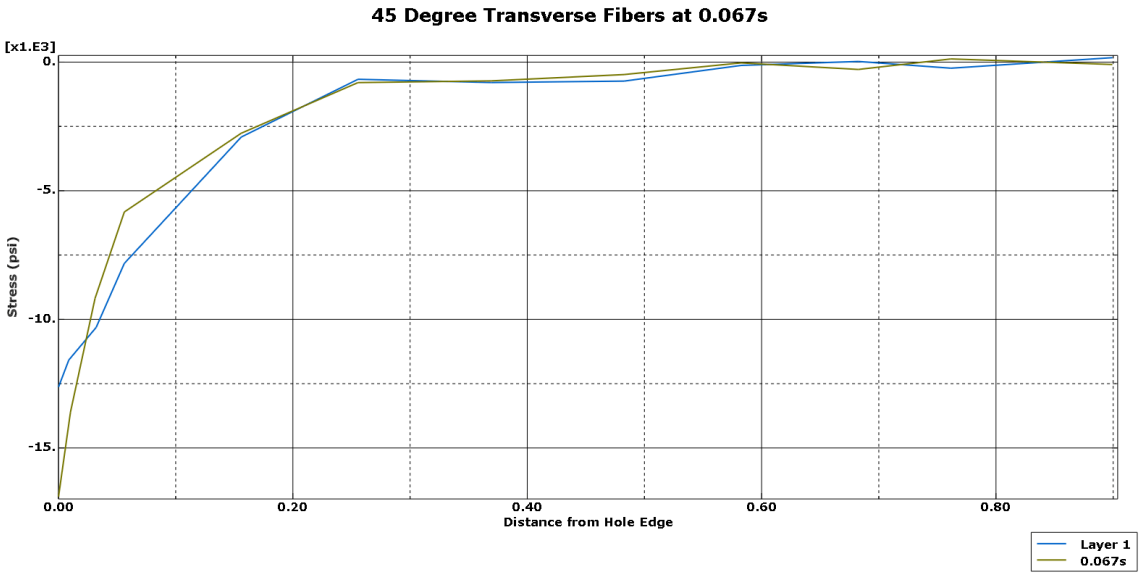

Figure 50: σ_{22} for 45-Degree Layers Transverse to the Fiber Direction

The -45-degree fibers show a similar trend as the 45-degree fibers. Figure 51 shows that the longitudinal fibers experience the same pattern for stress at the same area, but that the maximum stress encountered different between the two layers. Figure 52, however, shows that the transverse stress is almost identical between the two layers.

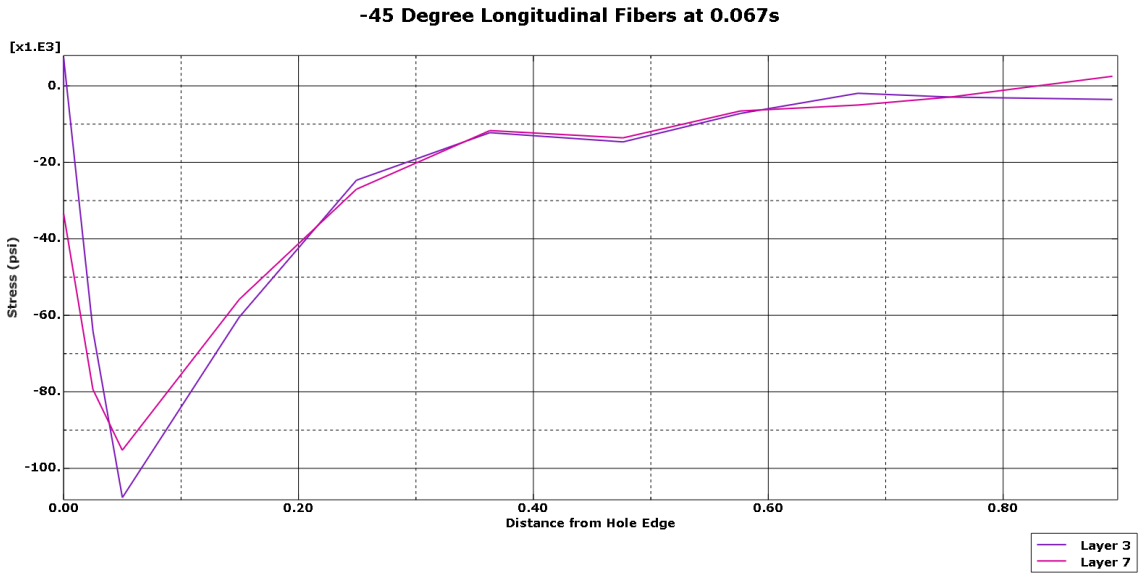

Figure 51: σ_{11} for -45-Degree Layers in the Longitudinal Fiber Direction

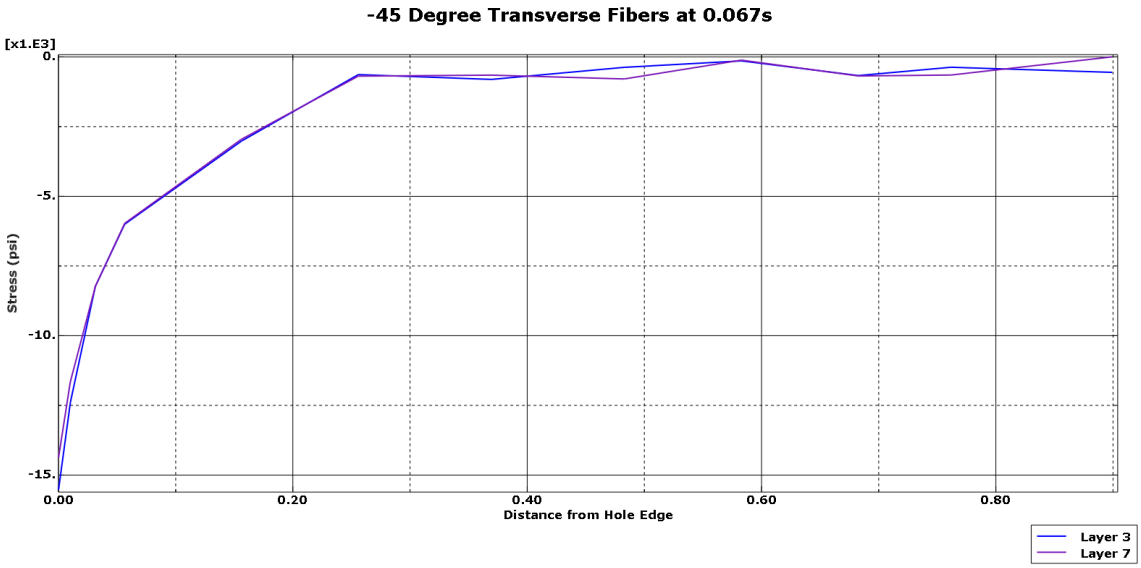

Figure 52: σ_{22} for -45-Degree Layers Transverse to the Fiber Direction

The four 0-degree layers follow the same trend as the previous two fiber orientations. Figure 53 shows that the fibers experience various stresses closer to the hole, but as the elements get further away, then the stress seen between the different layers appears to become almost equivalent. Transverse to the fiber direction, shown in Figure 54, also experience unique stress values from one another.

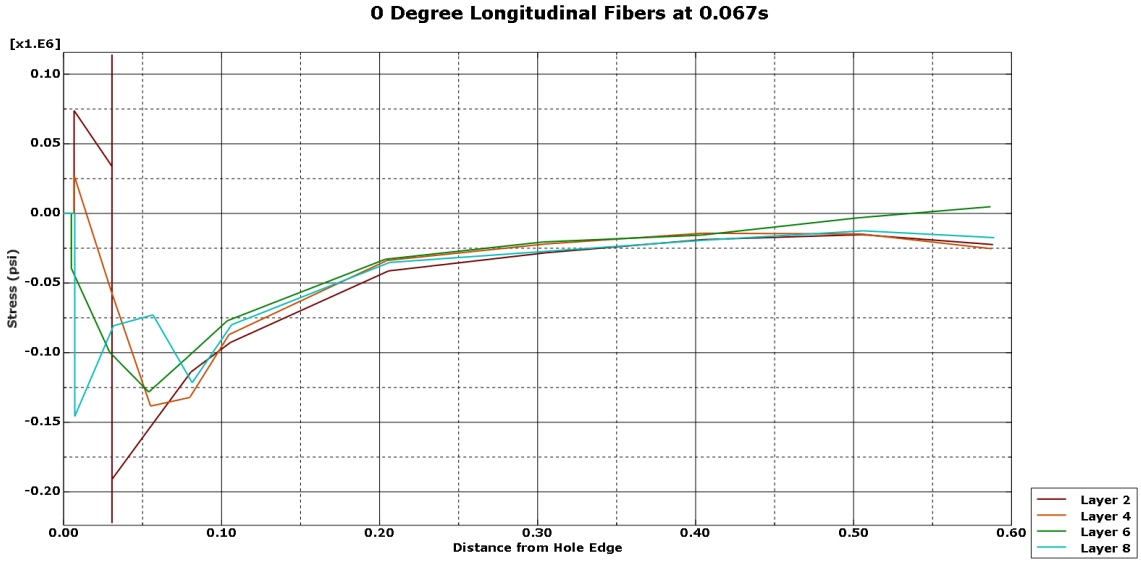

Figure 53: σ_{11} for 0-Degree Layers in the Longitudinal Fiber Direction

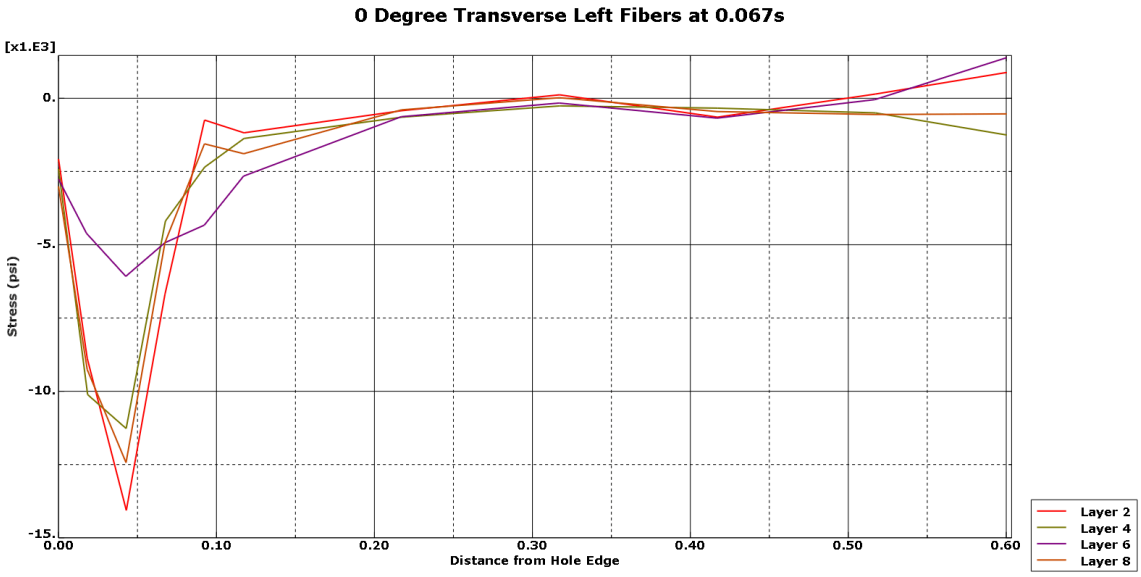

Figure 54: σ_{22} for 0-Degree Layers Transverse to the Fiber Direction

Tsai-Wu Model without Steel Foil

The Tsai-Wu model cohesive elements also show stress occurring through the thickness of the material. As seen in Figure 55, the cohesive elements experiences stress in the x_1x_3 plane. The stress shown reinforces that the cohesive element in the Tsai-Wu model also experiences stress throughout the entire model and that the thickness impacts the stress seen by each individual layer of the model.

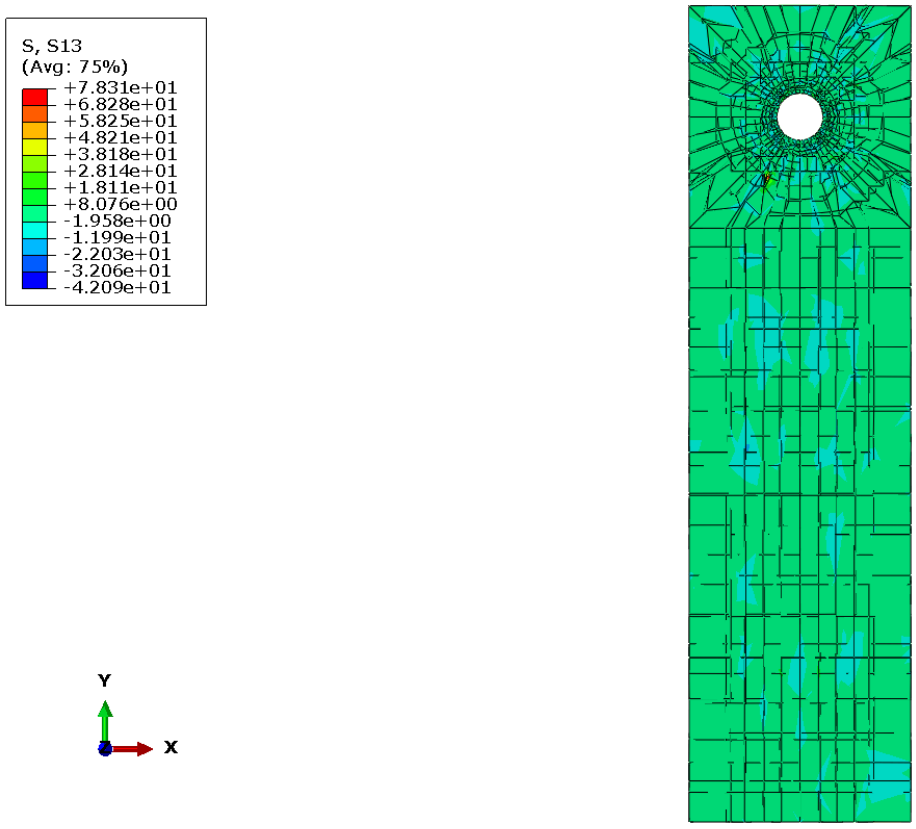

Figure 55: Cohesive Layer in-between Layer 1 and 2

The Tsai-Wu model showed approximately double the values in stress than the Hashin model. Figures 56-58 show the first layer in the Tsai-Wu model at times 0.033s, 0.050s, and 0,067s. The stress in the model extends in the fiber orientated directions with the highest stress occurring at the hole's edge. As the time progresses, the stress becomes more concentrated around the circle. Yet, no sign of failure shows on any of the models below. None of the elements were deleted or distorted excessively in the Tsai-Wu model without a steel foil.

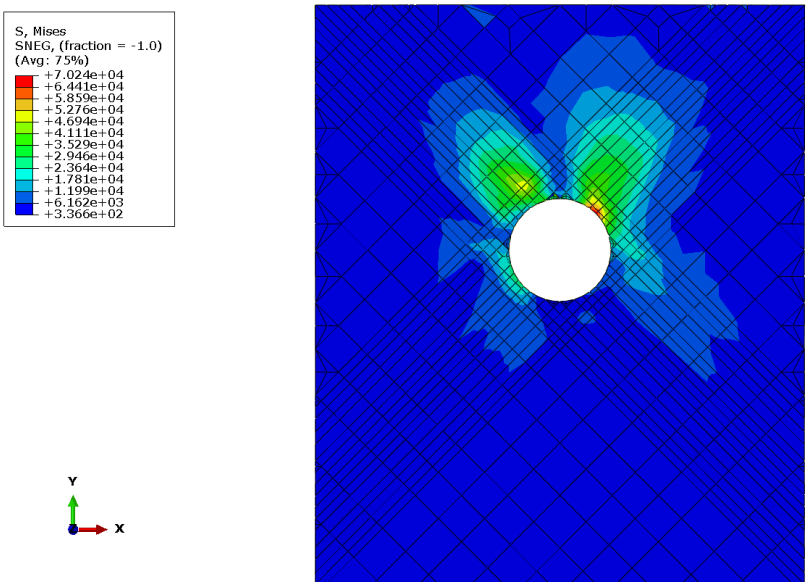

Figure 56: Von Mises Stress in Layer 1 at Time 0.033s

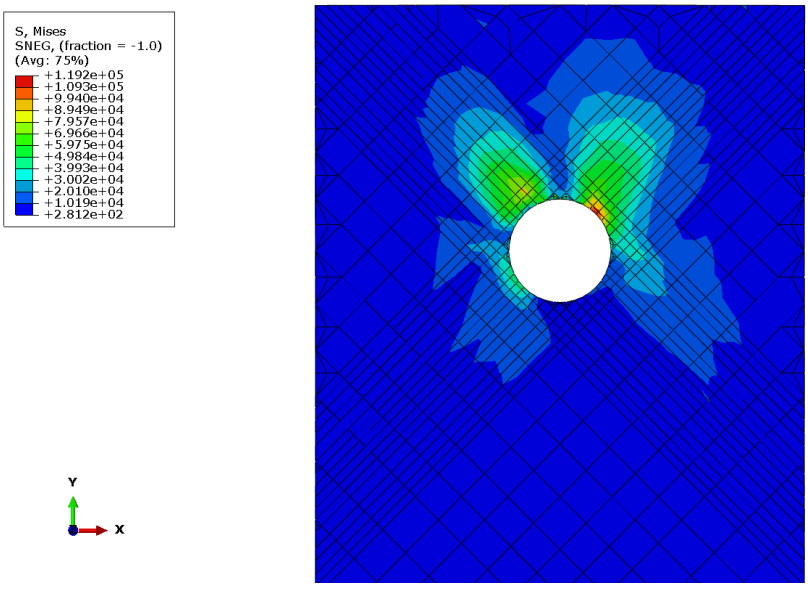

Figure 57: Von Mises Stress in Layer 1 at Time 0.050s

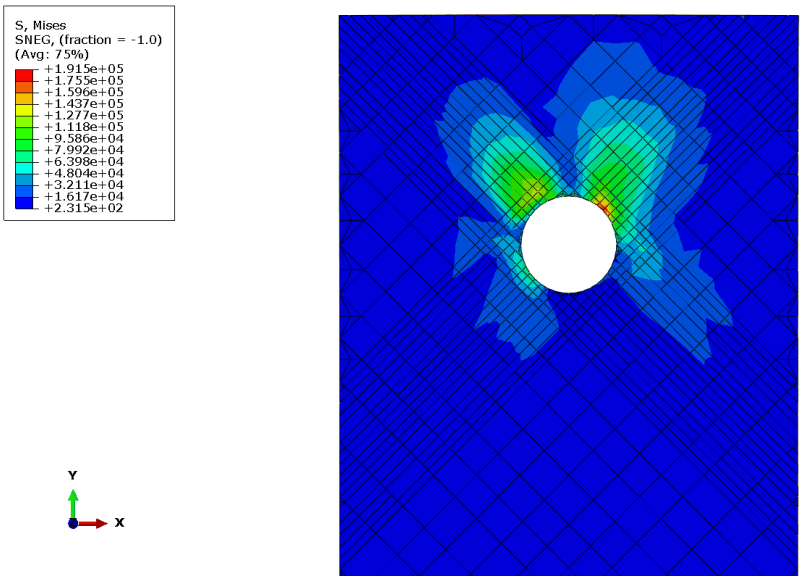

Figure 58: Von Mises Stress in Layer 1 at Time 0.067s

Figure 59 shows a graph of the longitudinal fibers' stress in the first layer of the model. As time progresses, the pattern of the stress seen by the fibers stays the same. The difference between the different times is that the maximum stress becomes greater as time goes on. The further away from the hole's edge, the more similar the stress values.

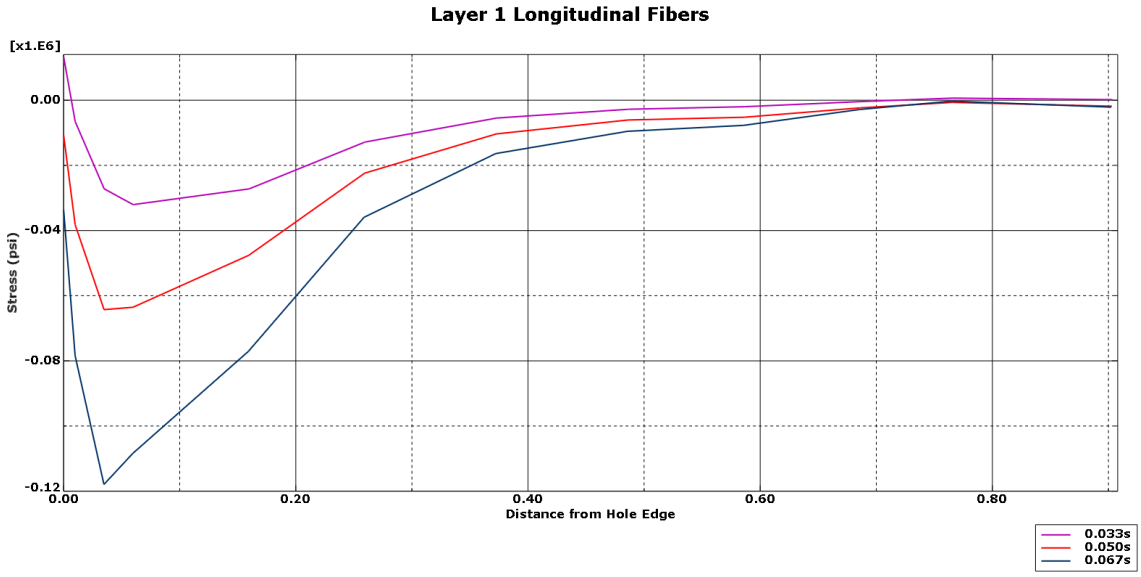

Figure 59: σ_{11} for Layer 1 45-Degree Longitudinal Fibers

The transverse to the fiber direction' stress show a similar pattern in the first layer as the longitudinal fibers' stress. Figure 60 depicts a graph of the transverse to the fiber direction' stress. Initially the fibers experienced tension whereas as time went on, the fibers encounter compression. Still, the stress field maintains the same shape throughout the model, but the maximum values grow larger. The further away from the hole's edge the element is located, the closer the stress values are to zero.

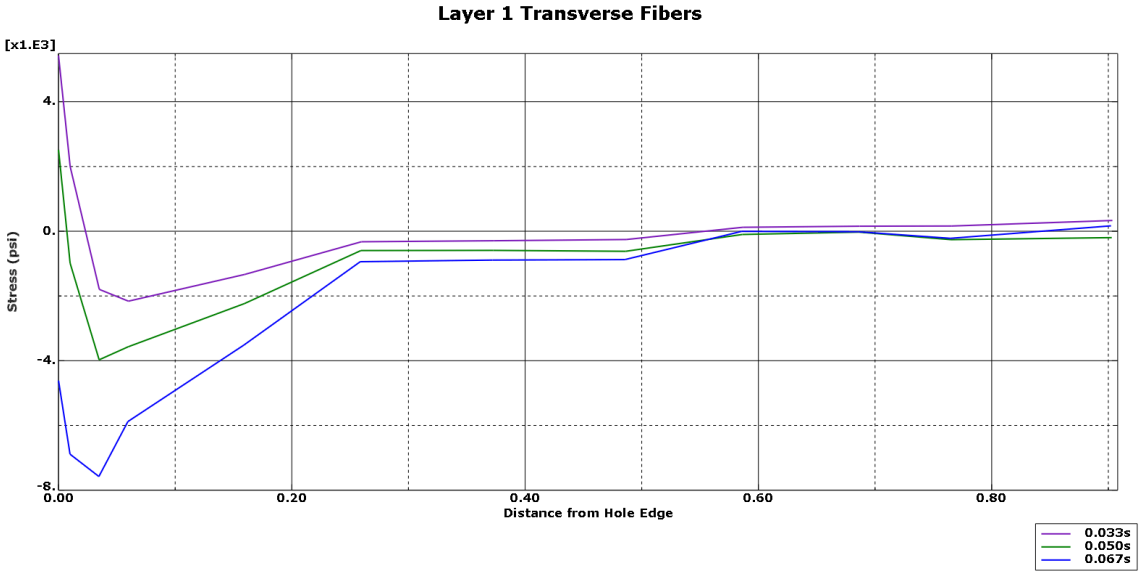

Figure 60: σ_{22} for Layer 1 45-Degree Transverse to the Fiber Direction

The second layer shows the same patterns depicted in the first layer. Stress occurs along the fiber directions as depicted in Figures 61-63. The stress field extends out along the fibers' longitudinal and transverse directions. As time wears on in the model, the stress field stays in the same shape but extends farther out into the material and down along the object.

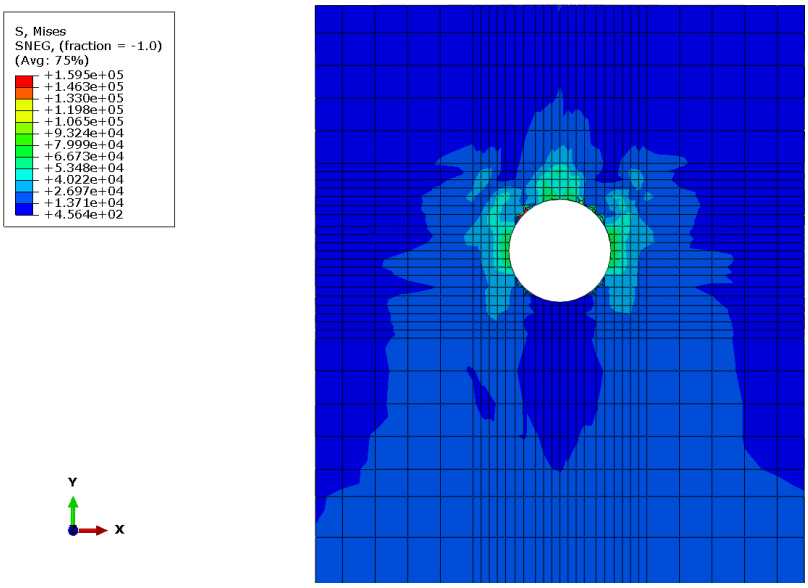

Figure 61: Von Mises Stress in Layer 2 at Time 0.033s

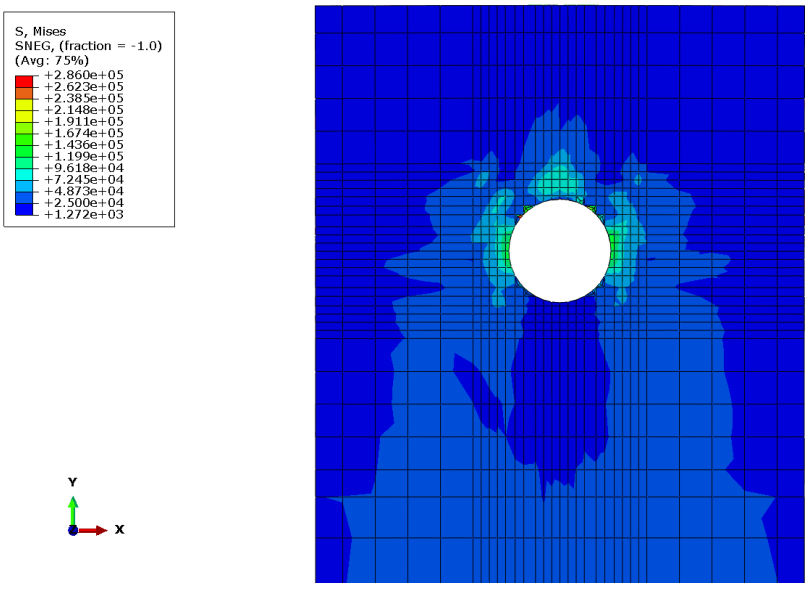

Figure 62: Von Mises Stress in Layer 2 at Time 0.050s

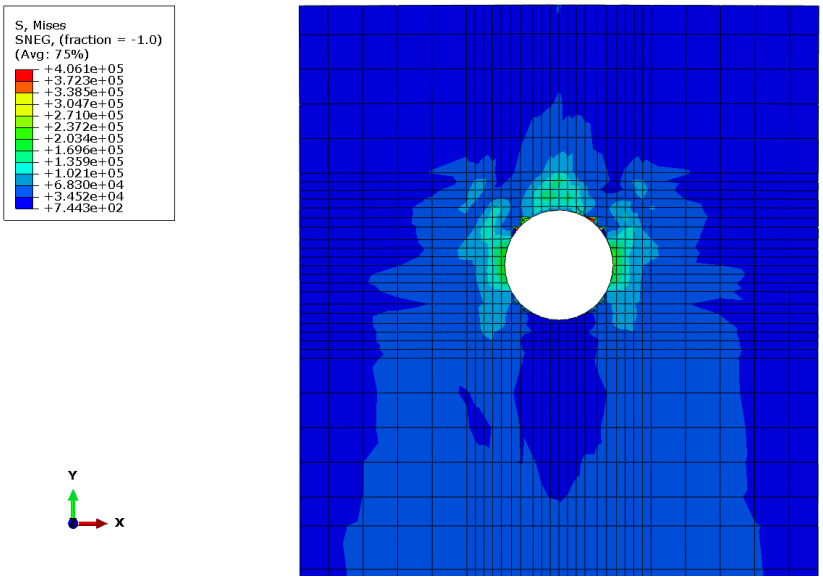

Figure 63: Von Mises Stress in Layer 2 at Time 0.067s

Initially the fibers in the longitudinal direction experienced tension, but the tension quickly changed to compression and continued to grow. Figure 64 shows that the stress possesses the same pattern throughout the model but grows larger as time wears on.

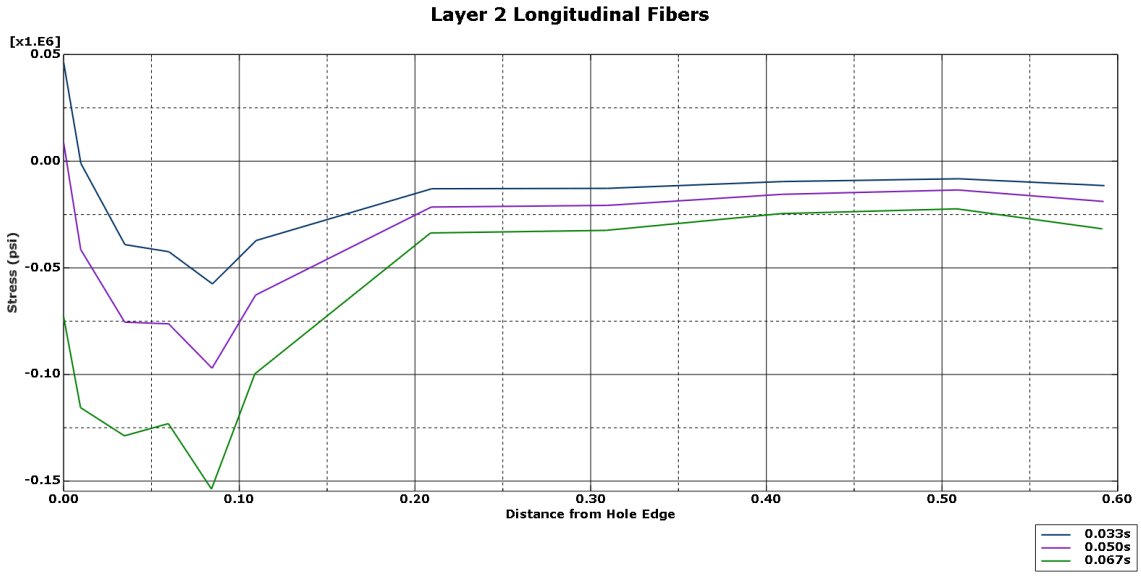

Figure 64: σ_{11} for Layer 2 0-Degree Longitudinal Fibers

Figure 65 shows the stress in the transverse fiber direction. Initially the fibers on the right side of the hole experience compression while the fibers on the left side of the hole encounter tension. Quickly, however, all sides converge upon similar values in stress about 0.09” from the edge of the hole.

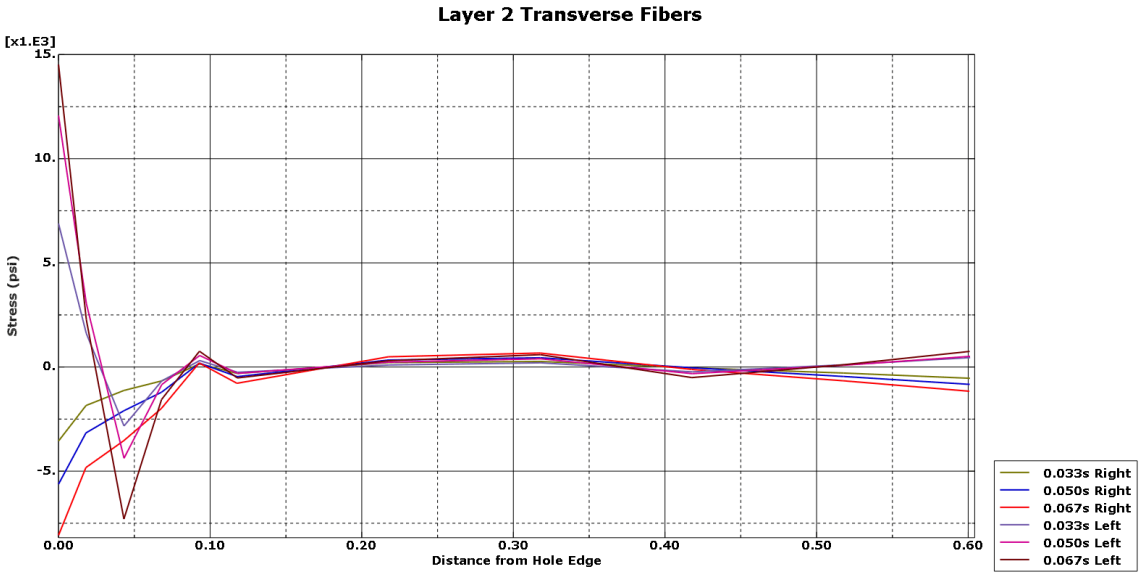

Figure 65: σ_{22} for Layer 2 0-Degree Transverse to the Fiber Direction

The third layer follows a similar trend of the first layer. As seen in Figures 66-68, the stress field around the hole extends out in the 45- and -45-degree fiber direction. The further away an element is on the model, the less stress that element sees. The third layer shows more stress by von Mises than the other layers pictured.

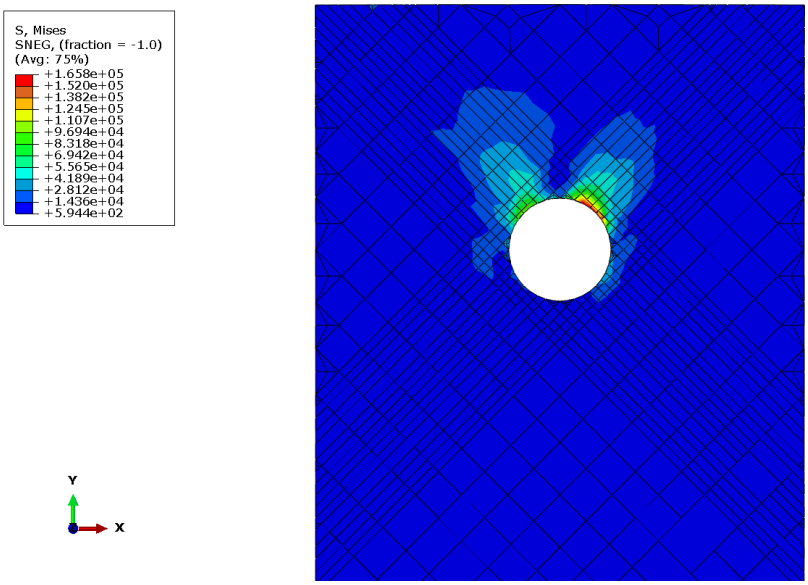

Figure 66: Von Mises Stress in Layer 3 at Time 0.033s

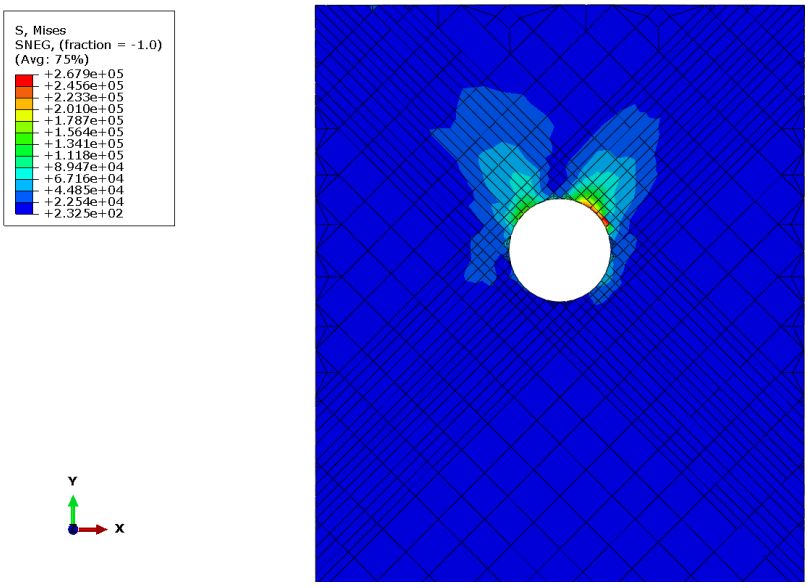

Figure 67: Von Mises Stress in Layer 3 at Time 0.050s

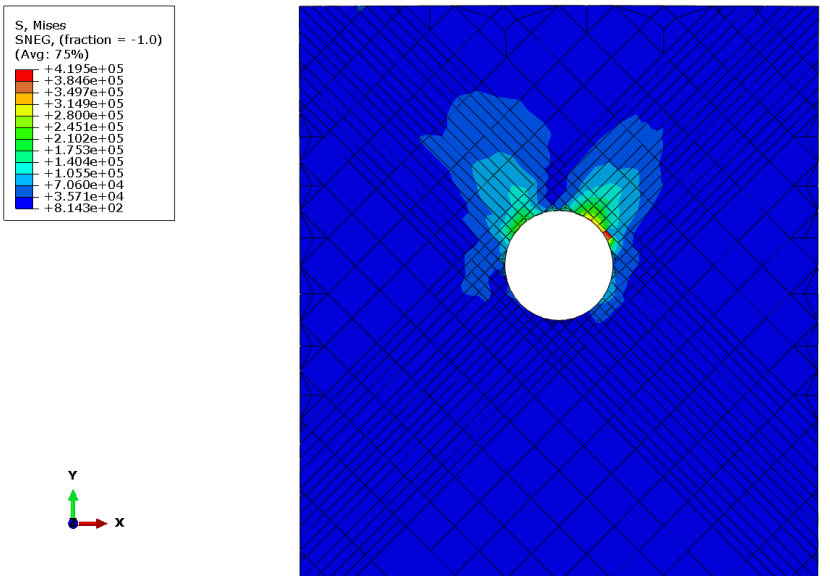

Figure 68: Von Mises Stress in Layer 3 at Time 0.067s

Depicted in Figure 69 is a graph of the stress seen in the longitudinal direction of the fibers in the third layer. Once again, the stress maintains the same pattern but only grows larger as time goes on for the model. As the distance from the hole grows larger, the stress seen by the layer decreases.

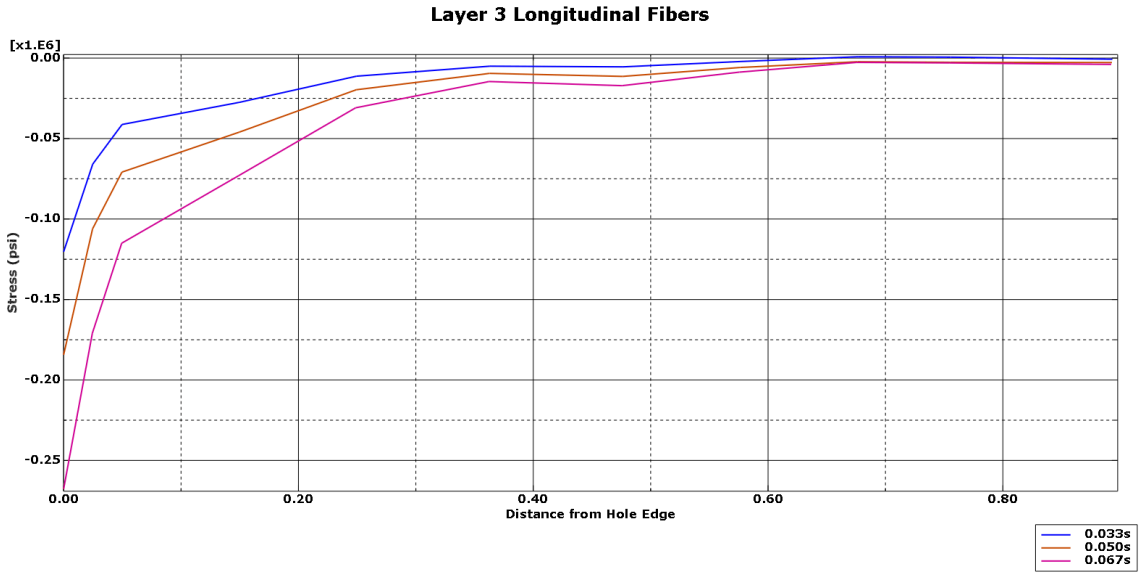

Figure 69: σ_{11} for Layer 3 -45-Degree Longitudinal Fibers

The transverse to the fiber direction experience less stress than the longitudinal fibers. Figure 70 shows the stress transverse to the fiber direction. The graph indicates that the stress in the transverse to the fiber direction are extremely similar throughout the model's time.

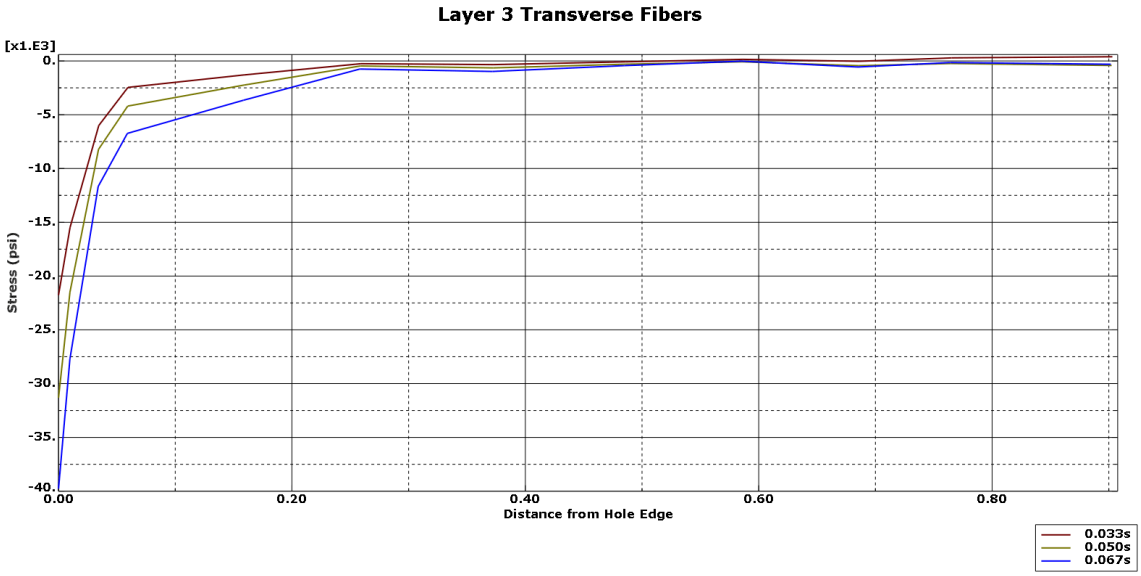

Figure 70: σ_{22} for Layer 3 -45-Degree Transverse to the Fiber Direction

Figures 71-73 show the stress field progression in the fifth layer over times 0.033s, 0.050s, and 0.067s. The stress field is like the one seen by the second layer with the exception that the fifth layer shows more stress above the hole near the top of the layer, and the field is located along the fibers' orientation.

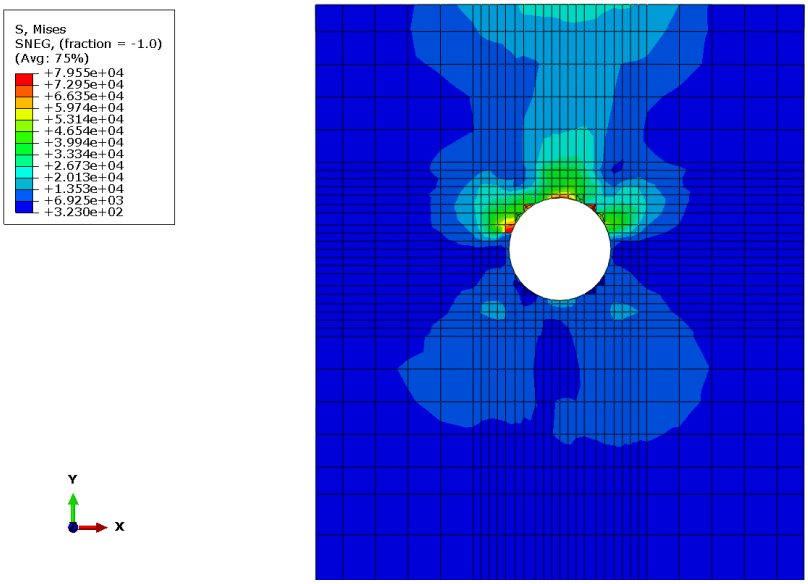

Figure 71: Von Mises Stress in Layer 5 at Time 0.033s

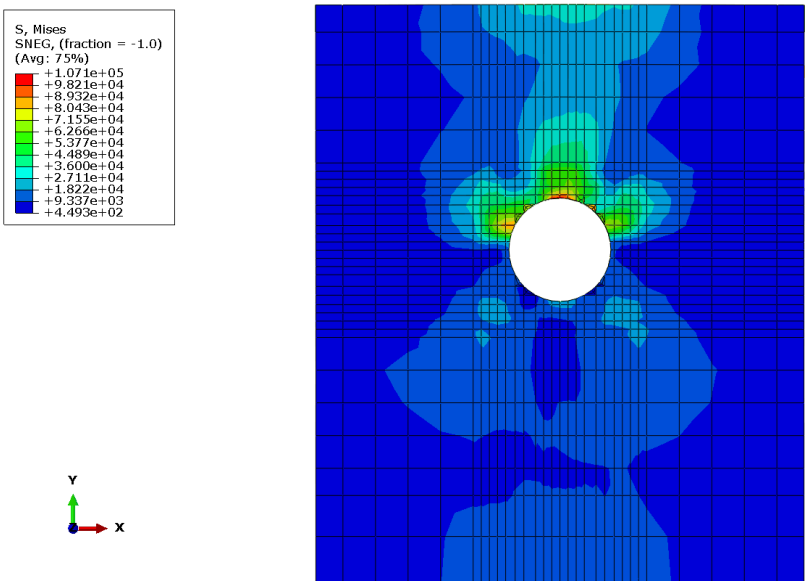

Figure 72: Von Mises Stress in Layer 5 at Time 0.050s

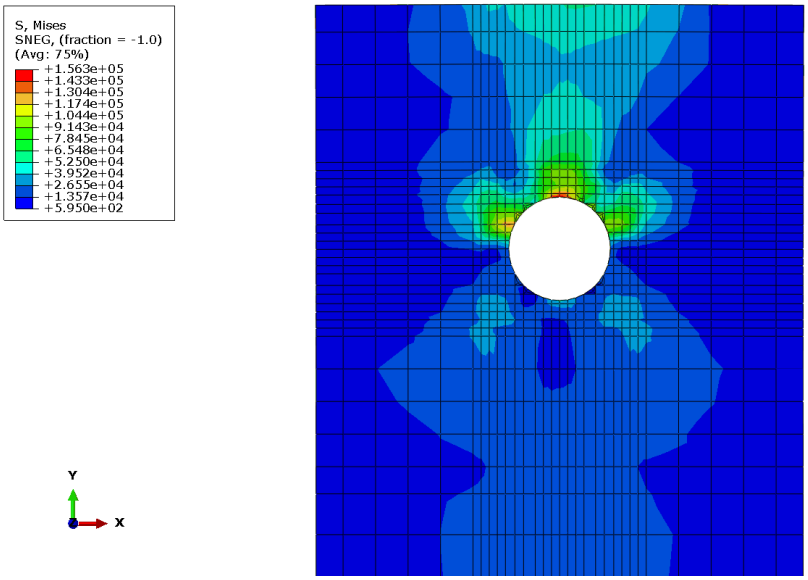

Figure 73: Von Mises Stress in Layer 5 at Time 0.067s

Every portion of the longitudinal fibers, according to Figure 74, experiences compression. The left side of the hole in the longitudinal direction encounters slightly more stress than the right side of the hole. Each stress line shows a similar pattern between the left and right side of the hole and across the different times.

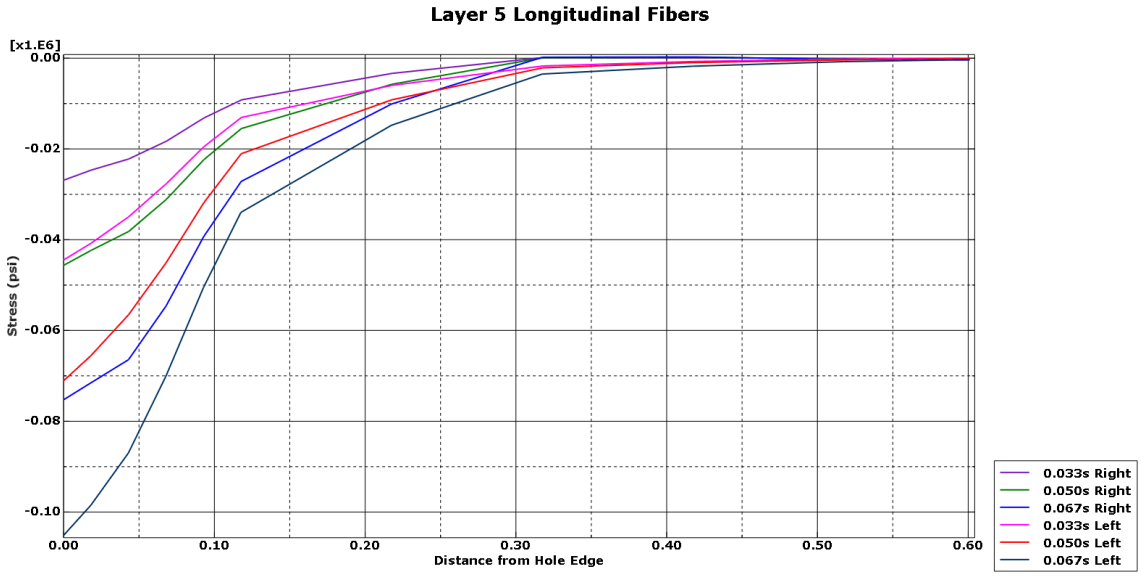

Figure 74: σ_{11} for Layer 5 90-Degree Longitudinal Fibers

The transverse to the fiber direction experience less stress than the longitudinal fibers in the fifth layer. Figure 75 shows that the stress pattern for the fifth layer stays similar as time goes on during the model. The outside edge of model experiences tension while the stress closer to the hole's edge is in compression.

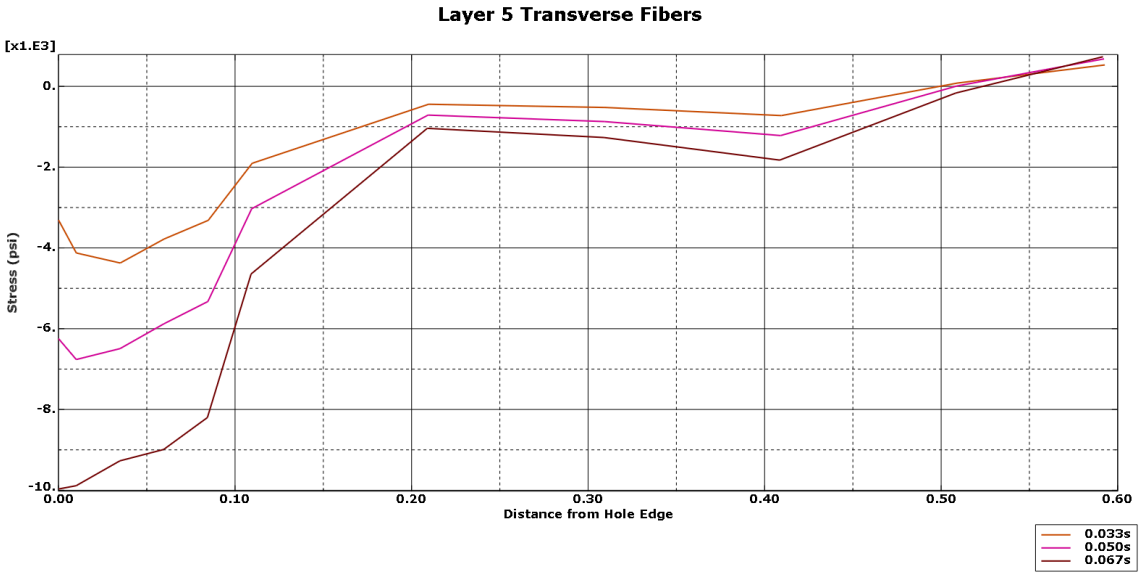

Figure 75: σ_{22} for Layer 5 90-Degree Transverse to the Fiber Direction

The stress between the different layers that are the same fiber orientation is distinct. Figure 76 shows that layer 1 experiences less initial stress than layer 9. At 0.15" the two layers start to see similar stress values and follow an extremely similar pattern with little difference between the two layers' stress. Figure 77 also shows the same pattern in the 45-Degree fiber orientation for transverse to the fiber direction.

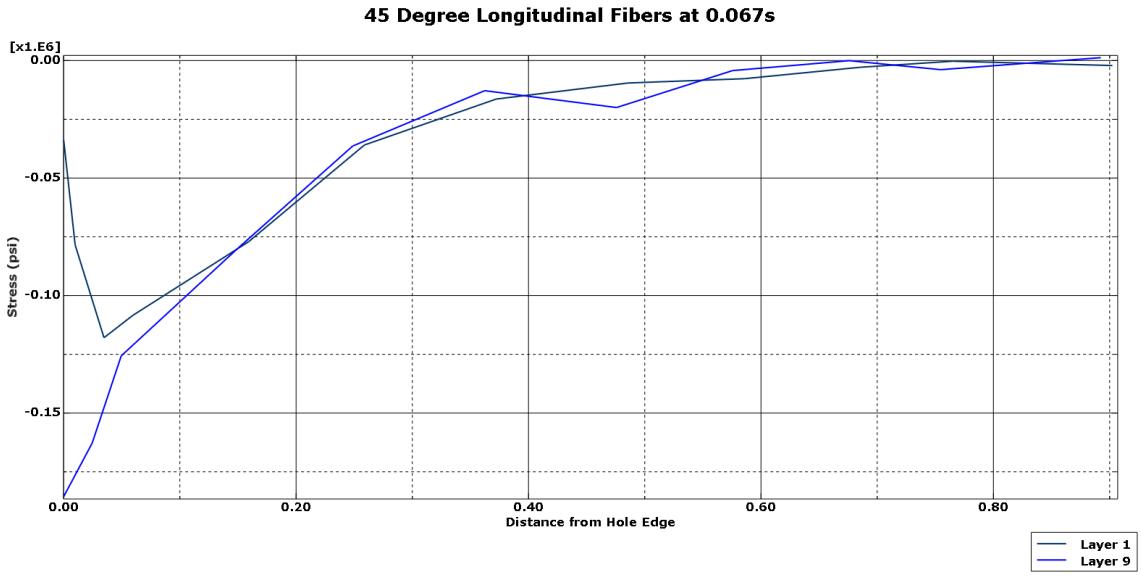

Figure 76: σ_{11} for 45-Degree Layers Longitudinal Fibers

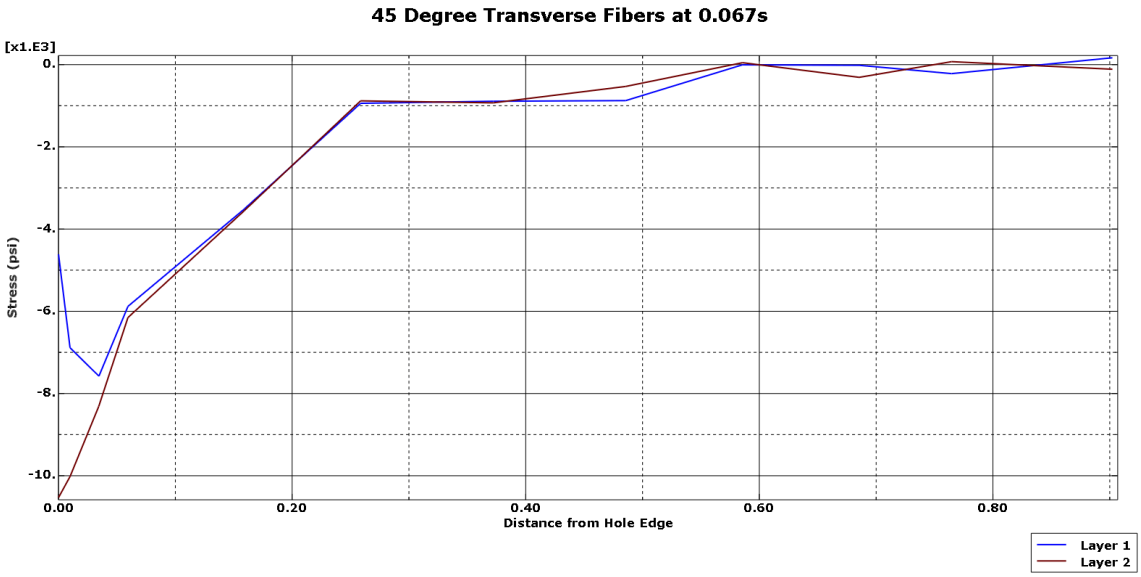

Figure 77: σ_{22} for 45-Degree Layers Transverse to the Fiber Direction

Figures 78 and 79 show that the -45-degree layers experience almost the same stress after 0.05” from the edge of the hole. The two layers in -45-degree direction show initial stress at the hole is where the main difference lies between them.

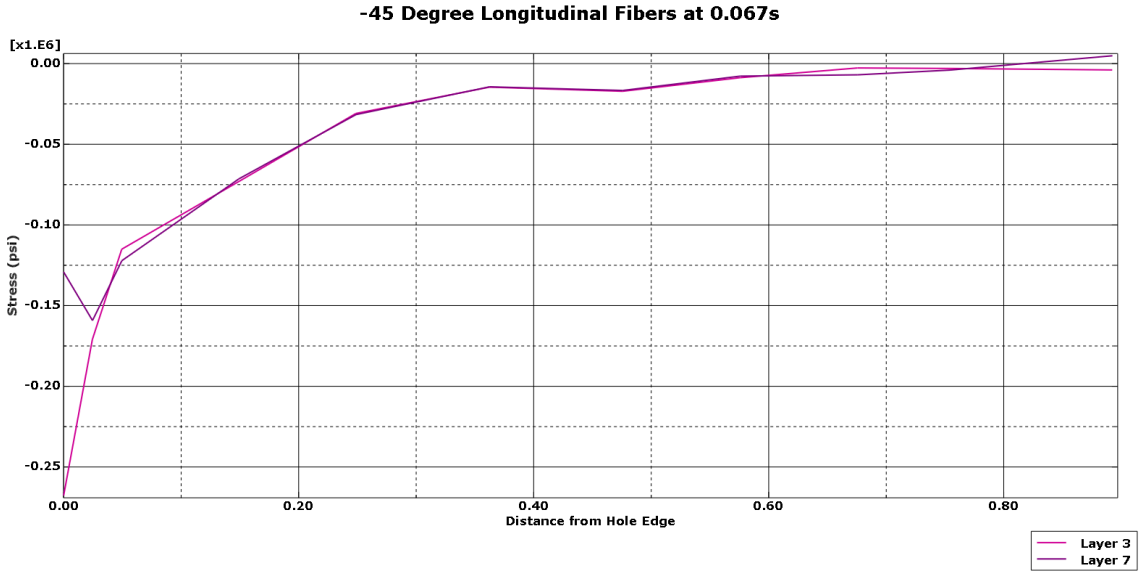

Figure 78: σ_{11} for -45-Degree Layers Longitudinal Fibers

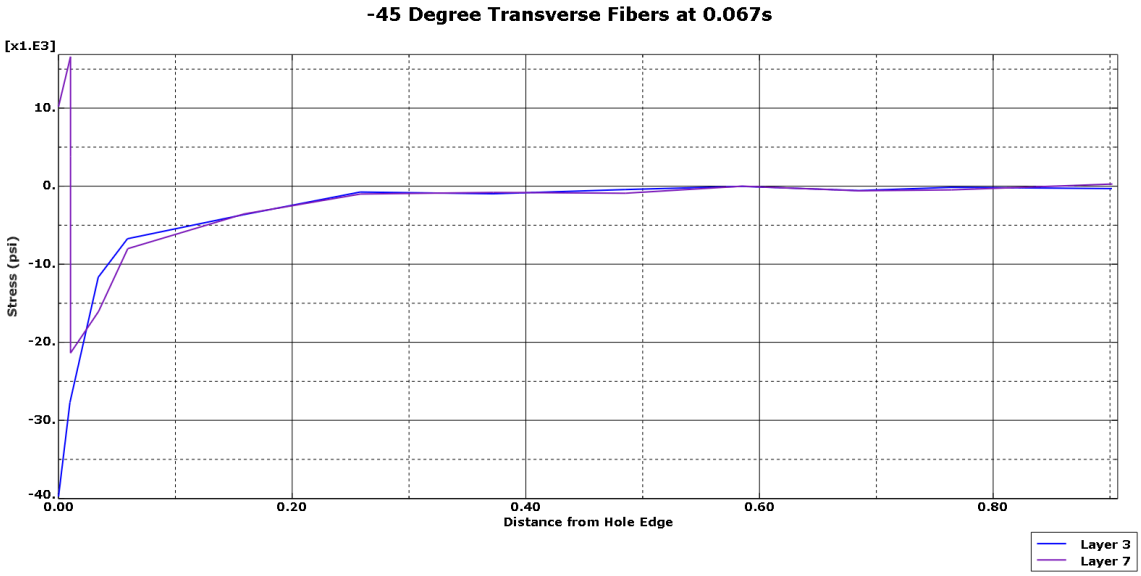

Figure 79: σ_{22} for -45-Degree Layers Transverse to the Fiber Direction

The 0-degree orientation layers experienced similar stress values except for the initial values. Layer 2 and 4 experience less stress initially than layers 6 and 8. Figure 80 shows that the longitudinal fiber directions converge upon almost identical stress 0.20" away from the hole's edge. The initial stress is the same between the two layers that are in the first half of the model, while the two layers in the second half of the model experience similar stress.

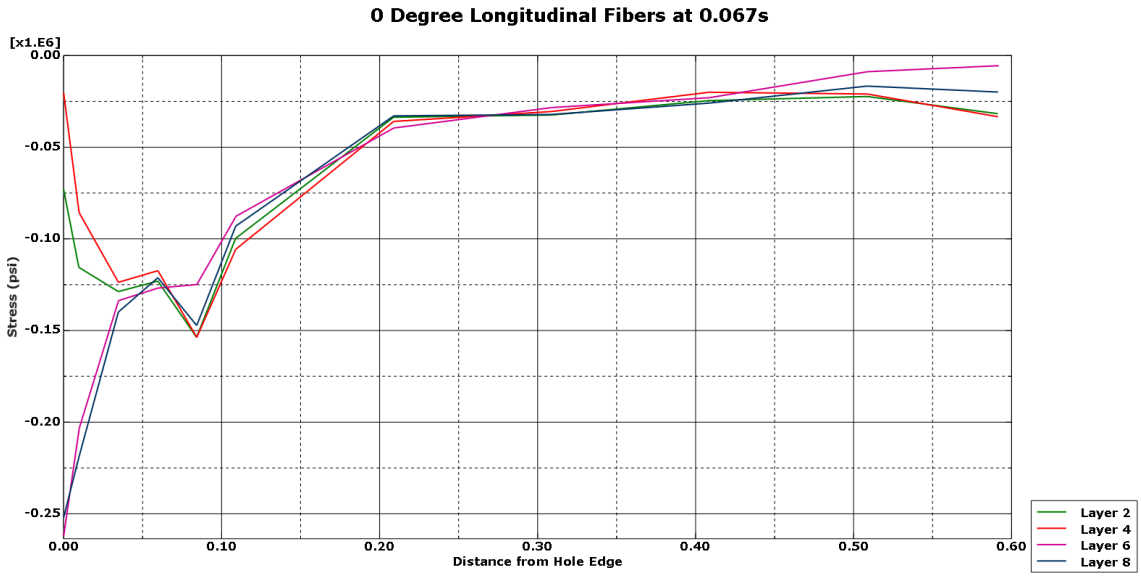

Figure 80: σ_{11} for 0-Degree Layers Longitudinal Fibers

Figure 81 shows that the stress across the layers that are 0-degree orientation experience different stress, but the graph also shows that the stress is not like the pattern pictured in Figured 80. The graph in Figure 81 shows that layer 2 and layer 8 encounter exact opposite stress in the transverse fiber direction. Layer 2 is in tension while layer 8 is in compression. Meanwhile layers 4 and 6 experience comparable stress values through the whole distance from the hole's edge.

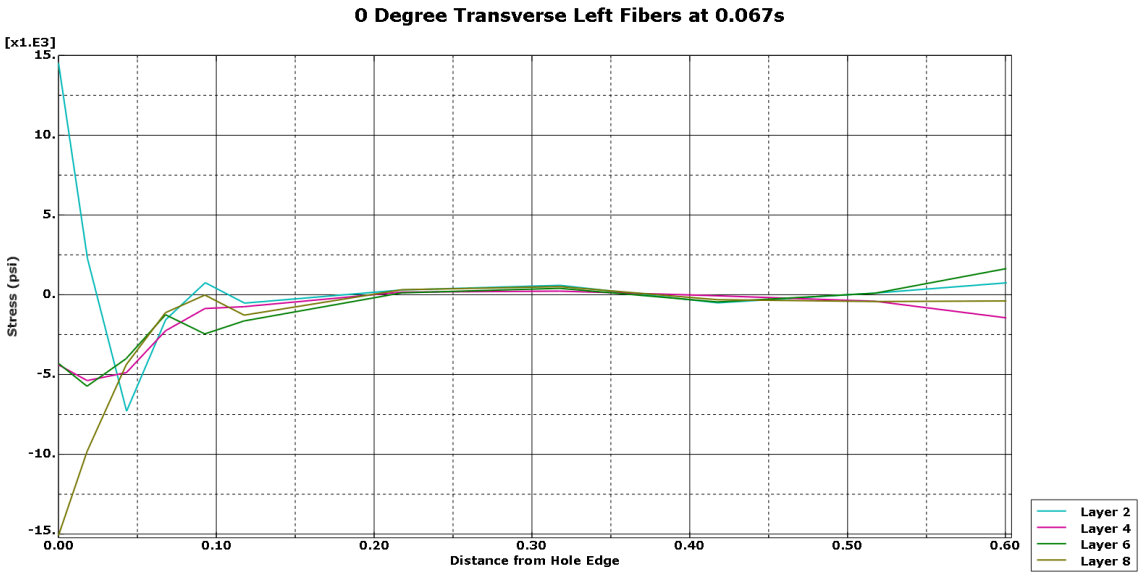

Figure 81: σ_{22} for 0-Degree Layers Transverse to the Fiber Direction

Hashin Model with Steel Foil

Once again, just like the previous two models shown, the cohesive element experiences stress through the thickness. As seen in Figure 82, there is stress in the x_1x_2 plane which shows that the thickness of the material still plays a role in the model.

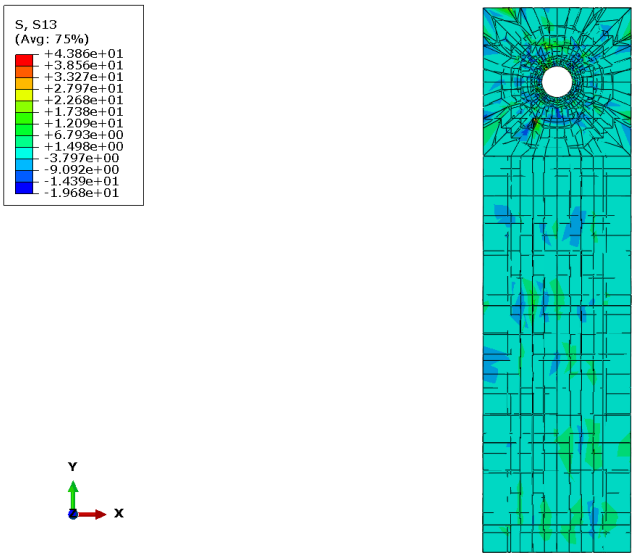

Figure 82: Cohesive Element in-between Layer 1 and 2

The models including the steel foil behaved in a similar manner to the models without foils. Stress expanded primarily in the fiber direction, and the longitudinal fibers experienced a greater amount of stress than the transverse to the fiber direction. Figures 83-85 show the progression of the von Mises stress field around the hole as time progressed in the model. Once again, the stress is concentrated around the top half of the hole in the object and expands primarily in the upwards direction along the fibers. As time progresses, the stress stays along the fibers orientation and only grows in number. An important item to note is that in Figure 85, there are no failed elements around the edge of the circle unlike the model's counterpart without a foil.

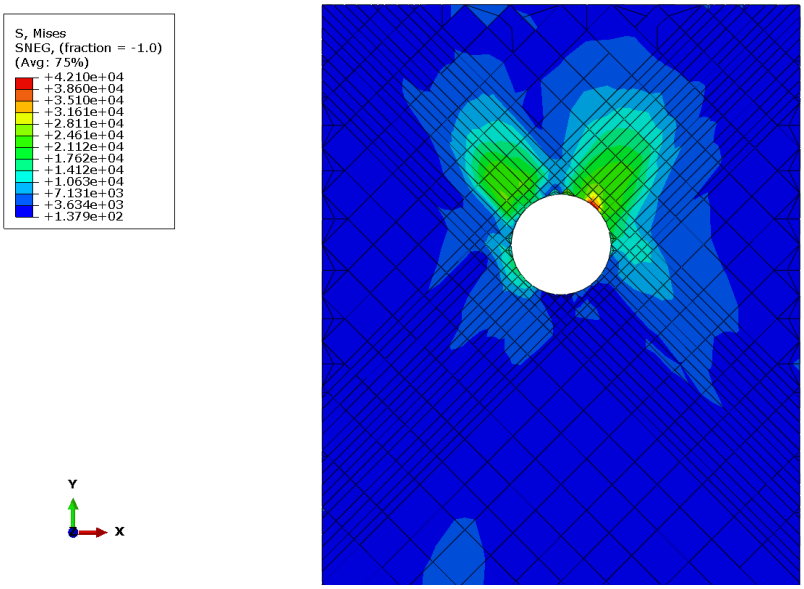

Figure 83: Von Mises Stress in Layer 1 at Time 0.033s

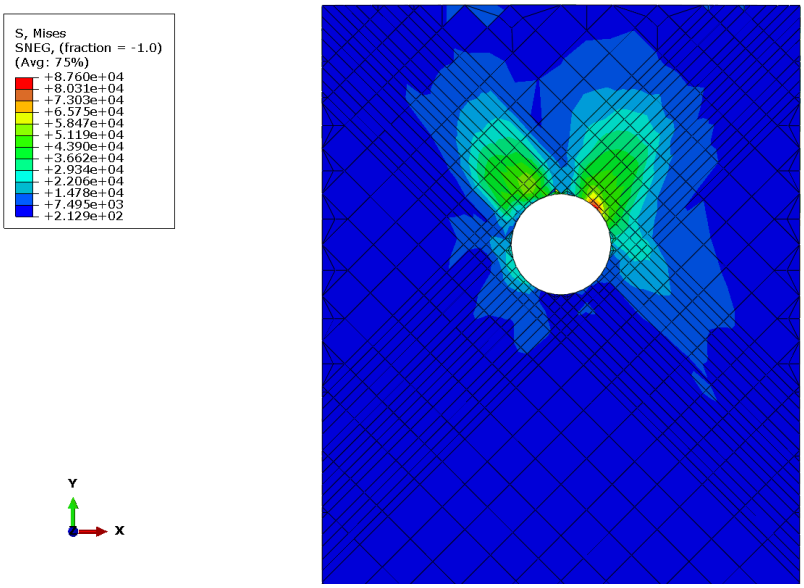

Figure 84: Von Mises Stress in Layer 1 at Time 0.050s

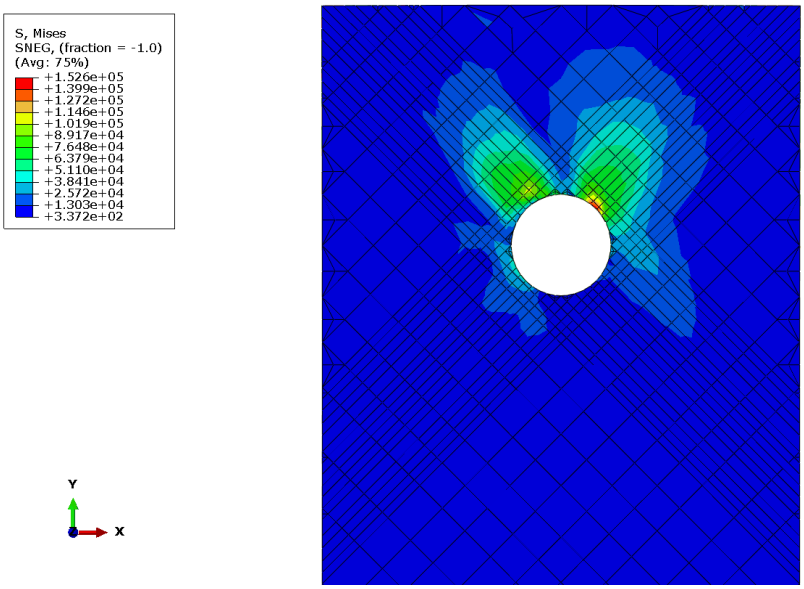

Figure 85: Von Mises Stress in Layer 1 at Time 0.067s

Without failed elements surrounding the hole's edge, the failure criterion of Hashin should note that there are less fibers and matrix elements failing in the model. Figure 86 shows little fiber failure occurring at time 0.067s. The fibers encounter little

tension, Figure 86 (b), but do experience some compression, Figure 86 (a). The failure spreads along the fibers' orientation.

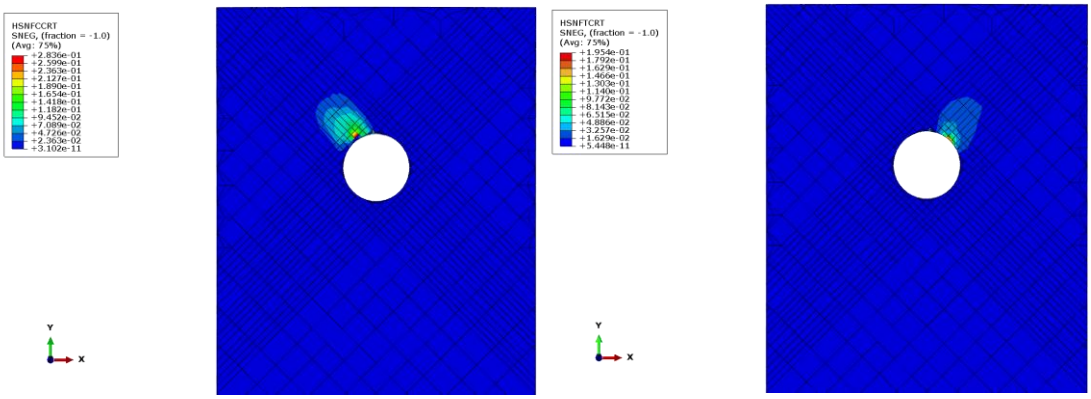

(a) (b)

Figure 86: Layer 1 Fiber Failure in (a) Compression and (b) Tension

According to Hashin, the matrix shows more failure than the fibers. Figure 87 depicts the matrix failure occurring in the first layer. Opposite to how the fibers experience their failure, the matrix experience tension failure along the longitudinal fiber direction and compression. The greater failure for the fibers and matrix occurs on the longitudinal fiber direction meaning that is where the first failure of the model can be expected to happen.

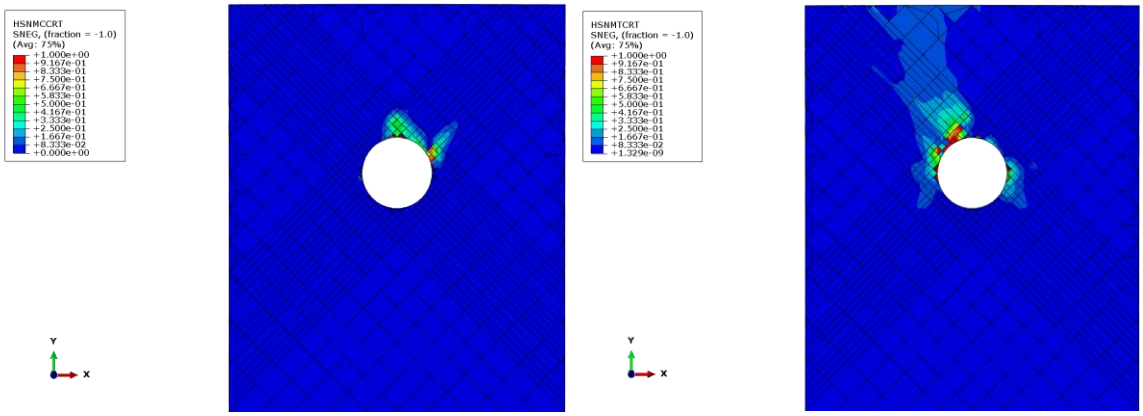

(a) (b)

Figure 87: Layer 1 Matrix Failure in (a) Compression and (b) Tension

Since the longitudinal fibers see more failure than the transverse fibers, the stress in them should be greater than the transverse to the fiber direction. Figures 88 and 89 graph the stress seen along the longitudinal and transverse fiber direction respectively. Initial stress is the main variance between the different times recorded, but each line maintains a similar pattern 0.05” from hole’s edge. The stress appears to converge about 0.60” from the hole and head towards possessing zero stress in the layer.

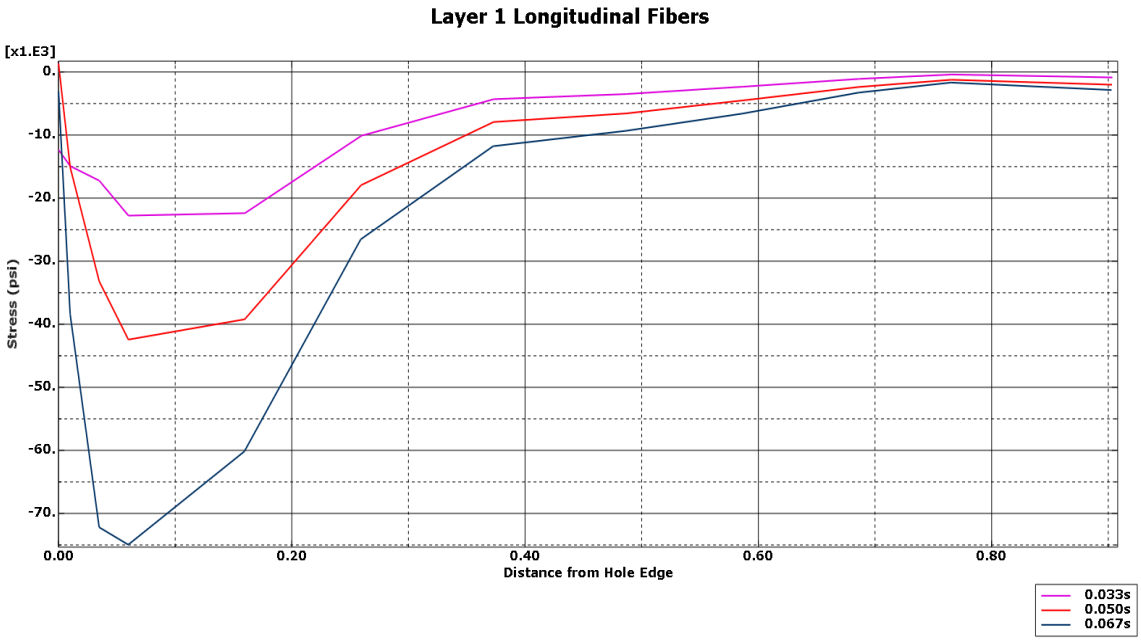

Figure 88: σ_{11} for Layer 1 45-Degree Longitudinal Fibers

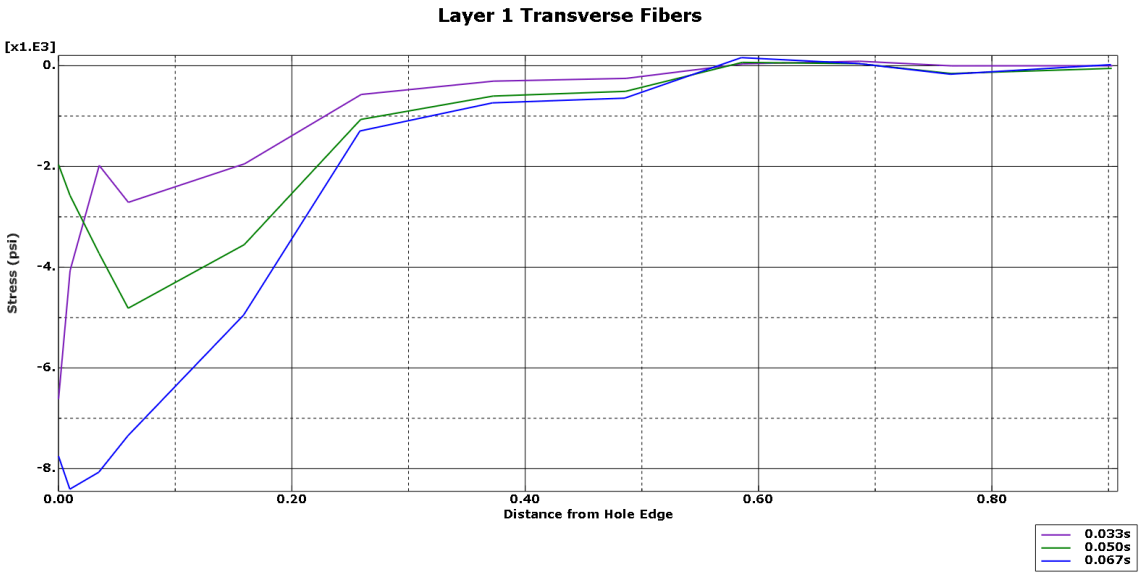

Figure 89: σ_{22} for Layer 1 45-Degree Transverse to the Fiber Direction

The second layer in the model still follows the same pattern of expanding the stress along the fiber direction, but this layer experiences greater stress than the first layer and its counterpart layer in the model without a foil. Figures 90-92 depict the progression of von Mises stress in the second layer. Figure 92 shows that the layer encounters a higher stress than depicted in other layers.

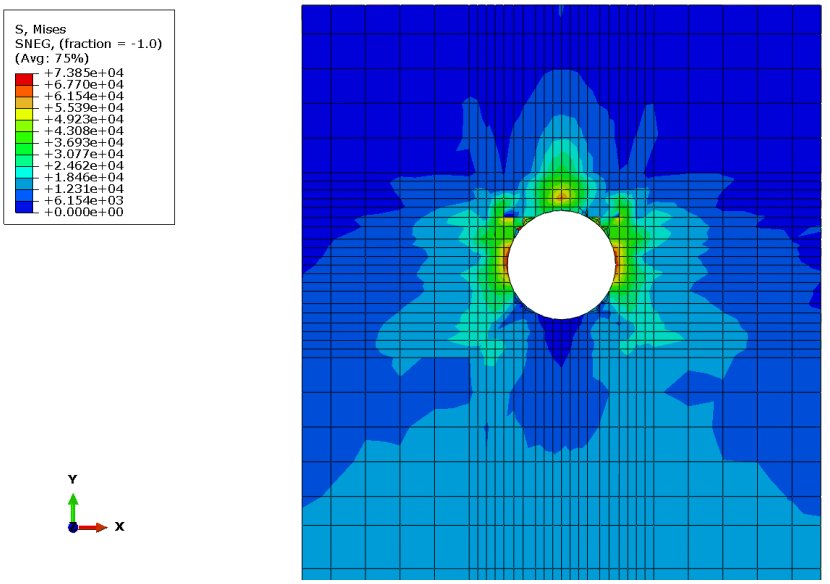

Figure 90: Von Mises Stress in Layer 2 at Time 0.033s

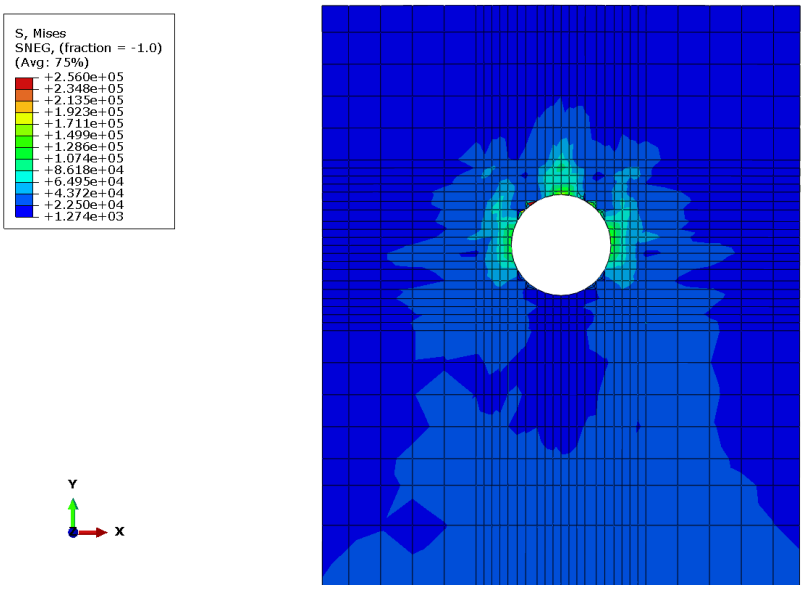

Figure 91: Von Mises Stress in Layer 2 at Time 0.050s

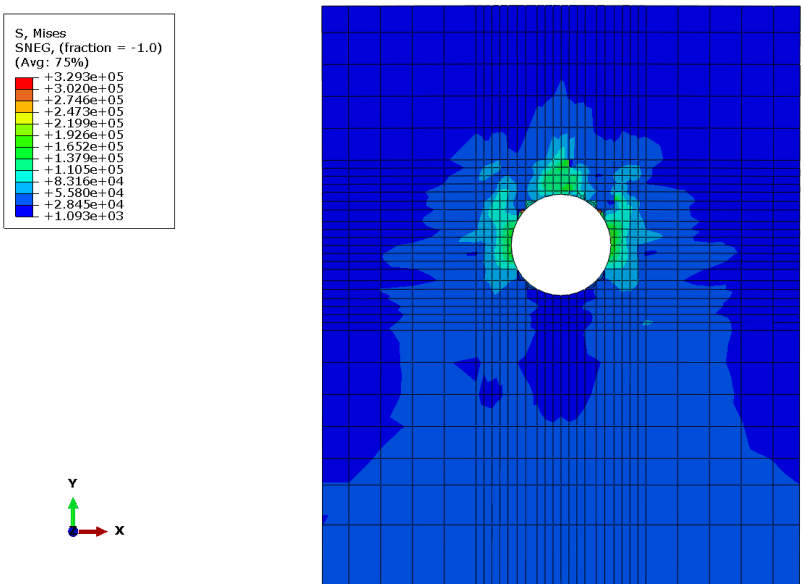

Figure 92: Von Mises Stress in Layer 2 at Time 0.067s

The failures occurring in the second layer are minimal. Figure 93 depicts that the fibers experience little failure throughout the model around the hole. The highest failure can be seen in Figure 93 (a) with fiber compression failure along the longitudinal fiber direction.

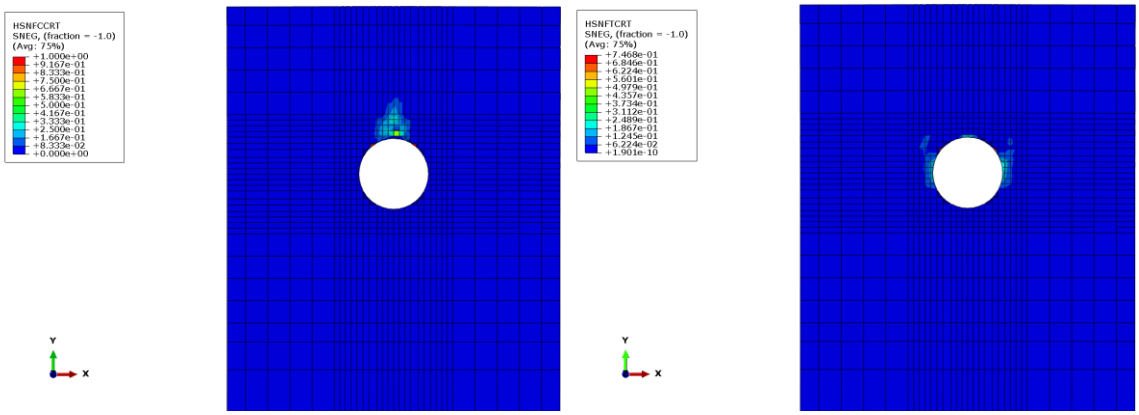

(a) (b)

Figure 93: Layer 2 Fiber Failure in (a) Compression and (b) Tension

The matrix, however, experiences more failure than the fibers. Figure 94 shows that the matrix in tension encounters the most failure, and that this failure spreads to the top of the object from the hole.

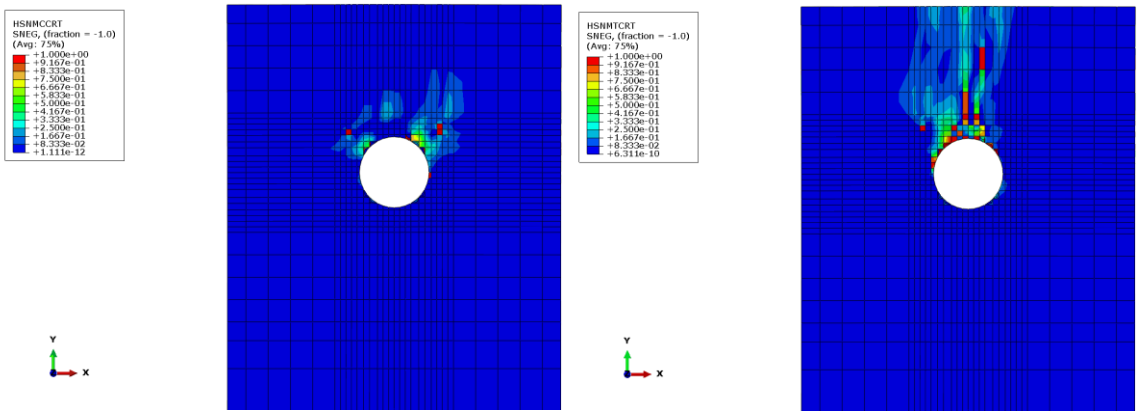

(a) (b)

Figure 94: Layer 2 Matrix Failure in (a) Compression and (b) Tension

Figure 95 graphs the stress observed by the longitudinal fibers in the second layer. The pattern of the stress field stays consistent and grows as time progresses for the model. Figure 96 graphs the stress experienced by the transverse to the fiber direction in the second layer. The transverse to the fiber direction on the right side of the hole appear to feel tension at first while the left side only shows compression. At time 0.067s both sides of the hole depict compression happening.

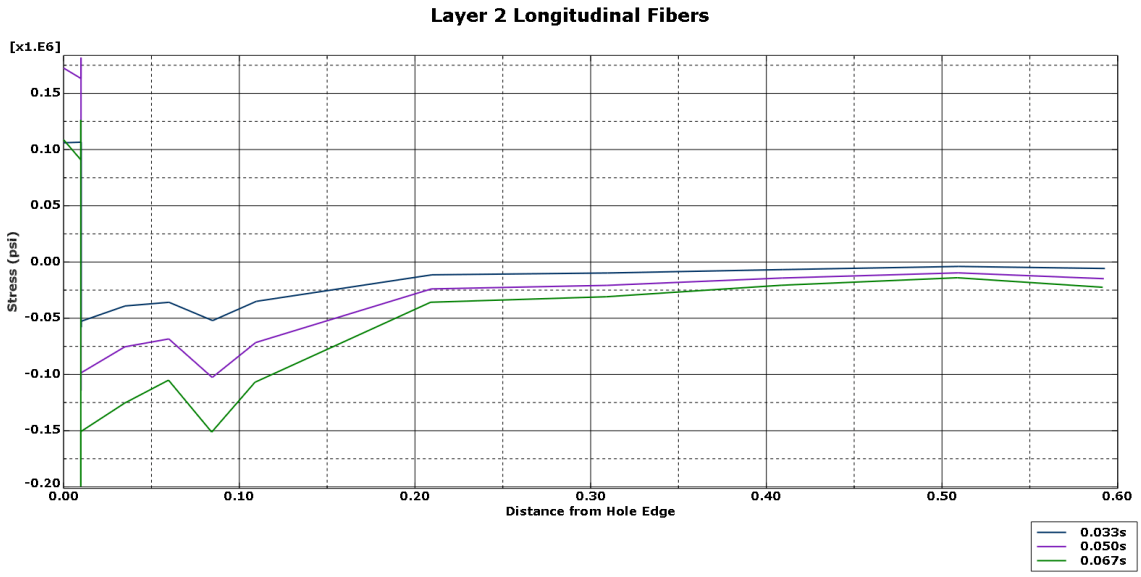

Figure 95: σ_{11} for Layer 2 0-Degree Longitudinal Fibers

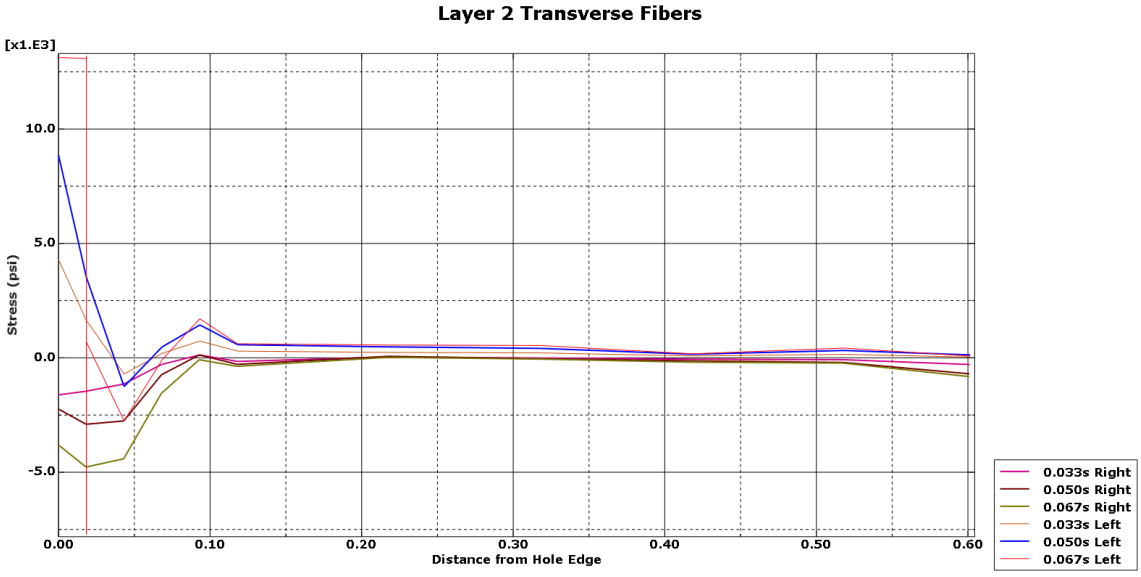

Figure 96: σ_{22} for Layer 2 0-Degree Transverse to the Fiber Direction

The two different length steel foils each matched with a different fiber orientation. The shorter foil length pair with the -45-degree fiber direction, while the other steel foil matched with the 90-degree fiber orientation. Stress shown for each foil is dependent

upon the counterpart composite layer in the models with the steel foils. The stress lines are equivalent to the ones calculated on the composite only model. Figures 97-99 show layer 3, a -45-degree layer in the previous models, von mises stress over time. Unlike how the composites stress fields followed a certain pattern, the stress field surrounding the foil spreads out in all directions from where the hole meets the pin in the model.

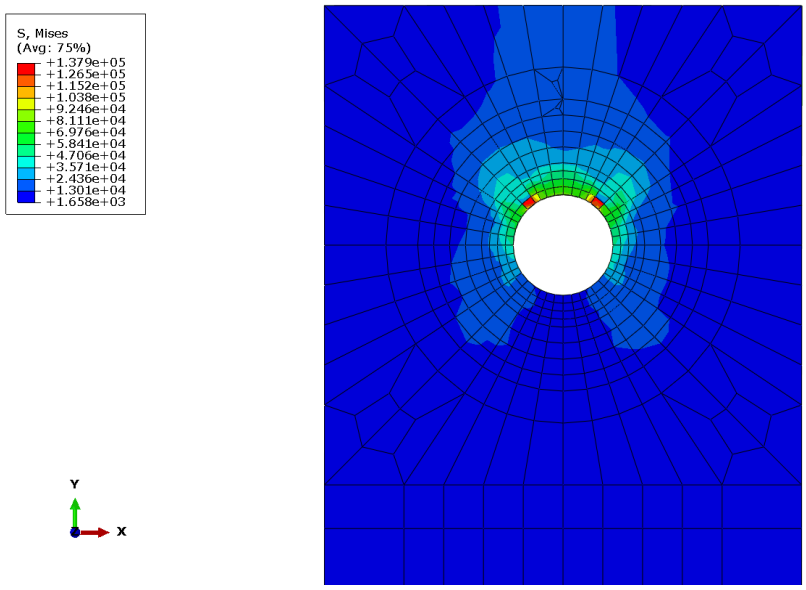

Figure 97: Von Mises Stress in Layer 3 Short Foil at Time 0.033s

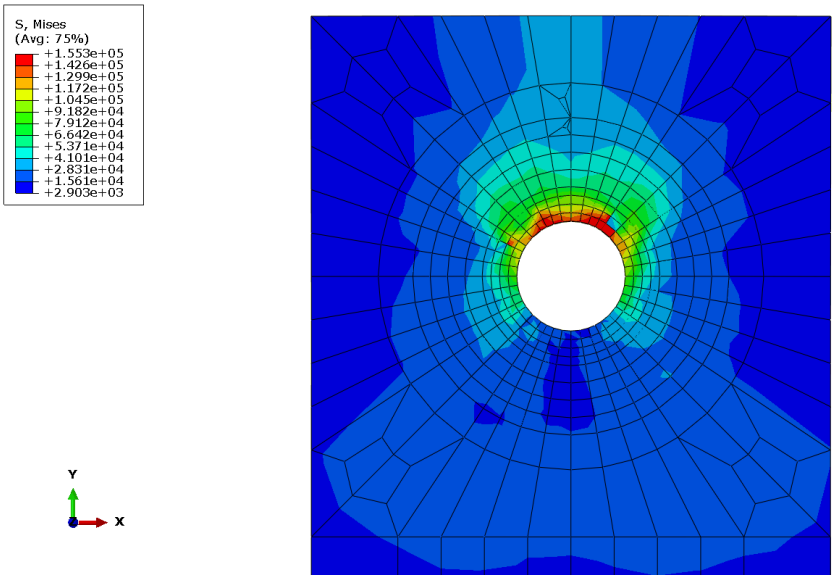

Figure 98: Von Mises Stress in Layer 3 Short Foil at Time 0.050s

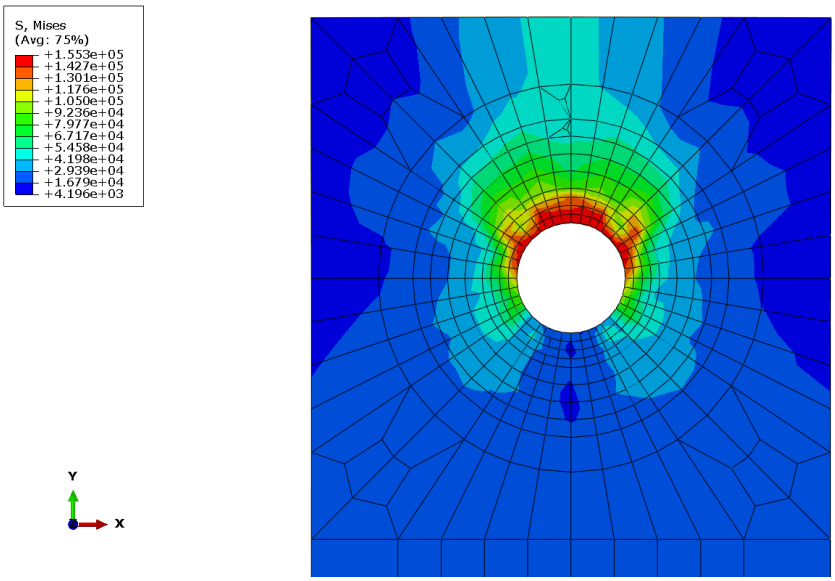

Figure 99: Von Mises Stress in Layer 3 Short Foil at Time 0.067s

The stress concentration for the foil is highest around the hole's edge. As depicted in Figure 100, the graph shows the stress that each 45-degree angle of stress from the center of the hole experiences. The overall stress seen on each side are comparable to one

another unlike the composite. The two differing sides, while showing S_{11} and S_{22} respectively for left and right, still possess similar stress. Figure 100 also shows that the stress field stays consistent when progressing in time of the model but that the stress does get larger. The stress for all portions of the foil converge at 0.72" away from hole at zero stress.

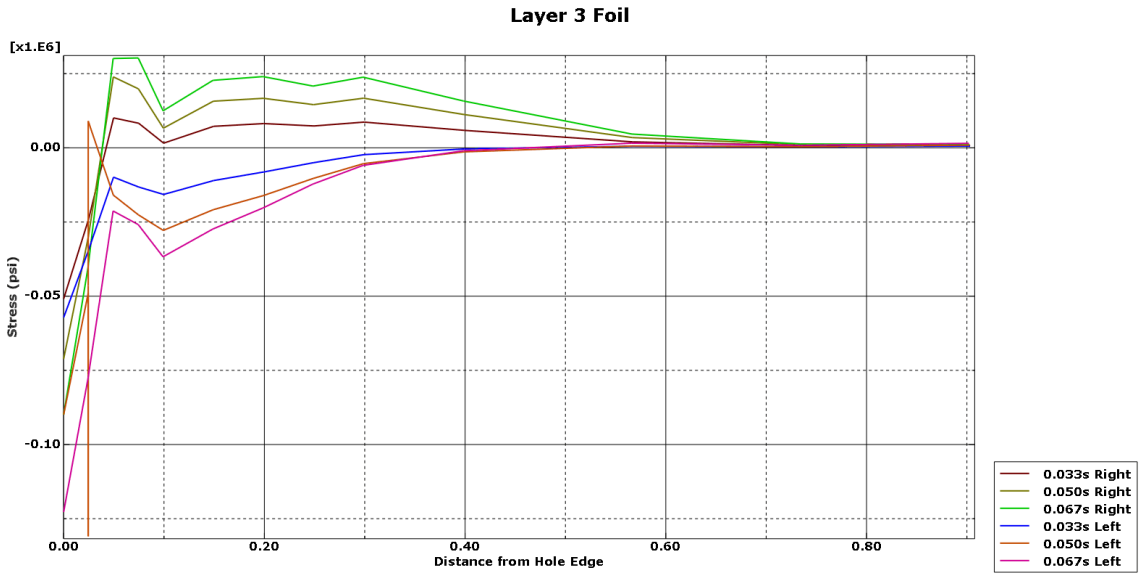

Figure 100: σ_{11} and σ_{22} Layer 3 Foil

The center foil, which replaces the 90-Degree layer, exhibits the same patterns seen in the third layer of the model. Figures 101-103 bear the same stress field shapes and the same stresses as seen in Figure 97-99. The stress field grows as time progresses, and it encompasses the top half of the circle where the pin is located. The highest stress is shown to be at the top of the hole's edge in the entire upper half.

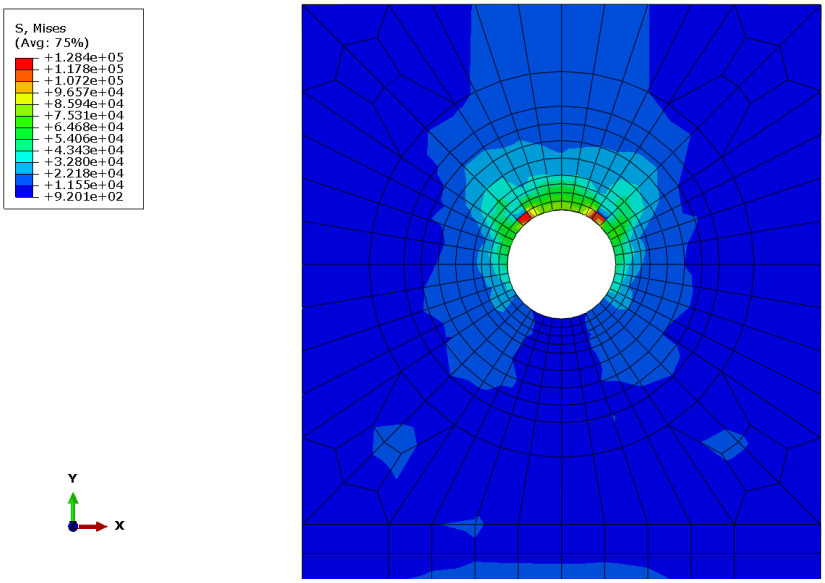

Figure 101: Von Mises Stress in Layer 5 Long Foil at Time 0.033s

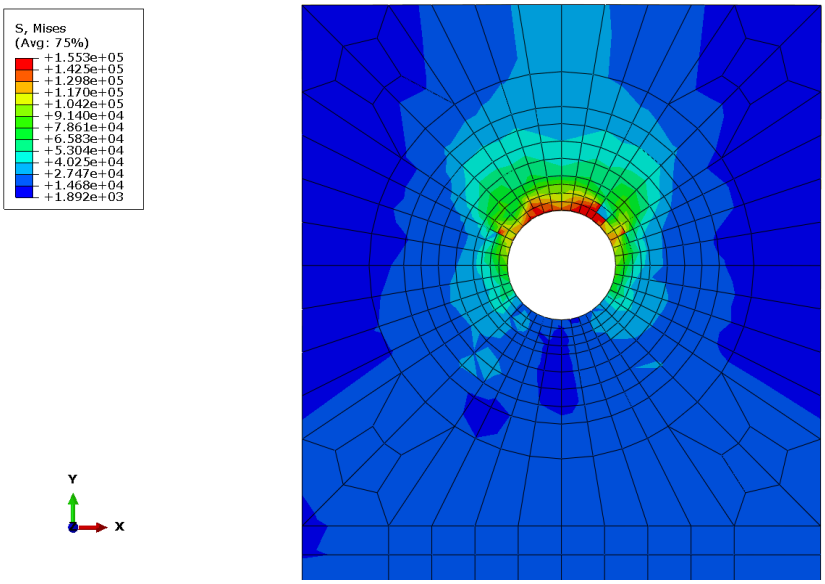

Figure 102: Von Mises Stress in Layer 5 Long Foil at Time 0.050s

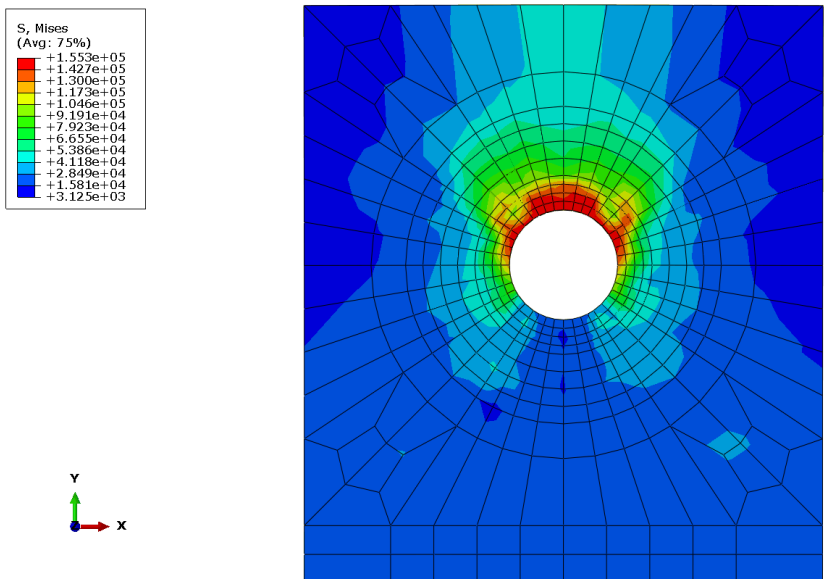

Figure 103: Von Mises Stress in Layer 5 Long Foil at Time 0.067s

The area depicted on the graph in Figure 104 is a line in the transverse fiber direction of a 90-degree layer. Figure 104 shows that the foil in layer 5 exhibits the same pattern as previous layers. The stress field stays consistent in shape but growth in magnitude. Layer 5 is also in compression the entire time during the model.

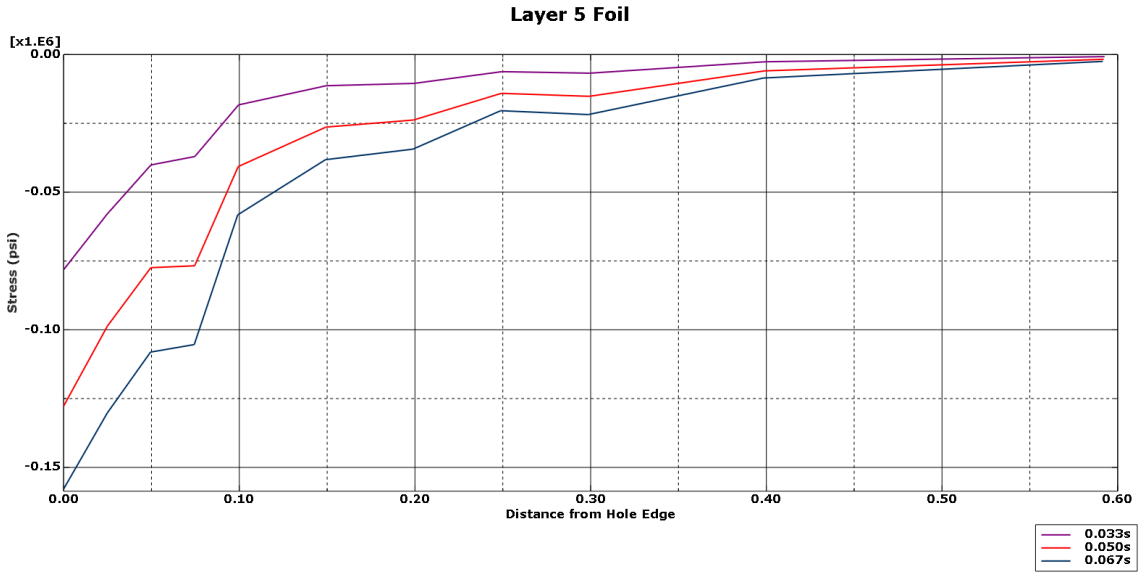

Figure 104: σ_{11} and σ_{22} for Layer 5 Foil

Despite different layers possessing identical fiber orientation, each layer shows distinct stress values during the model, especially near the hole's edge. Figures 105 and 106 graph the longitudinal and transverse to the fiber direction respectively and their stress values. At 0.15" from the edge of the hole, the stress experienced by the longitudinal fibers follow similar paths. Initially layer 9 shows more stress but the two layers' stress values tend toward zero the closer to the edge of the material. The transverse to the fiber direction, which experience less stress, converge upon0.05: from the edge of the hole; these transverse to the fiber direction in the 45-degree layers are closer in numbers to each other than the longitudinal fibers.

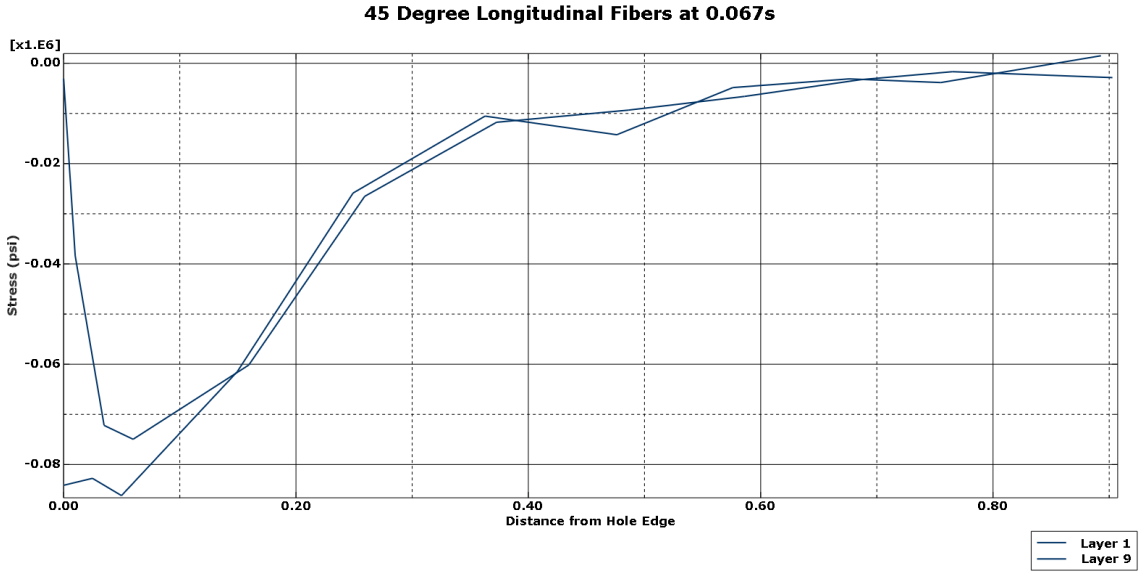

Figure 105: σ_{11} for 45-Degree Layers Longitudinal Fibers

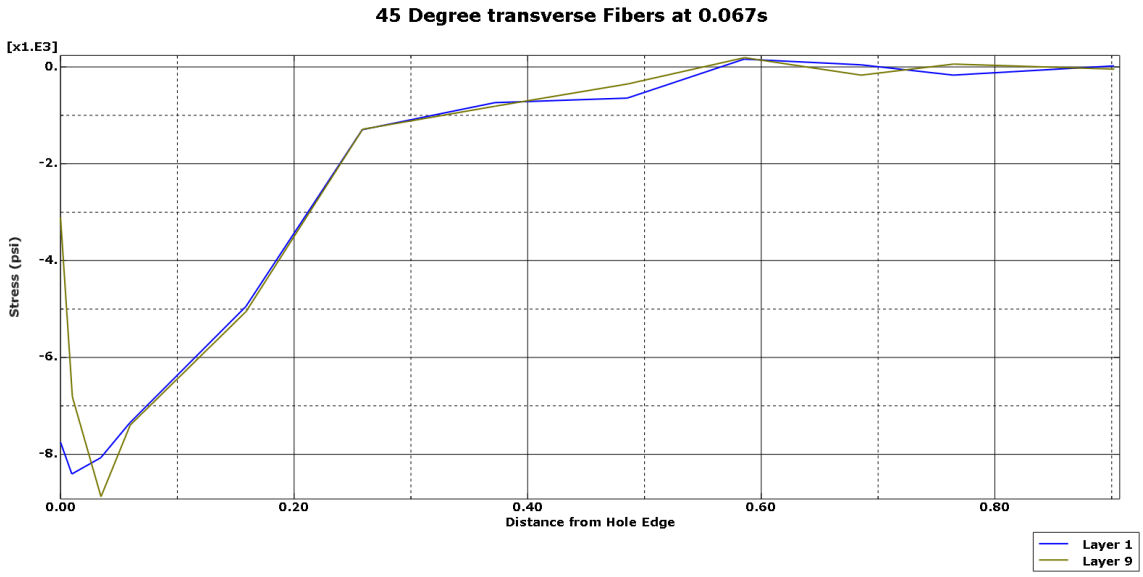

Figure 106: σ_{22} for 45-Degree Layers Transverse to the Fiber Direction

The 0-degree layers stress relations between the layers are closer than the models without steel foils. In Figure 107, the stress in the longitudinal fibers' direction converges quickly with one another and tend towards zero. The initial values of the layers are where the most distinct values occur. Layer 2 starts out in tension while the other three layers experience compression from the start. Immediately, the second layer drops to compression in stress, but the other layer exhibiting different behavior is the sixth layer. Layer 6 experiences a greater amount of compression than the other three layers initially. Figure 108, however, shows that the transverse layers experience almost the opposite effect of the longitudinal fibers. The various layers in the transverse direction experience the same stress field but the layers diverge instead of converging. Approximately 0.50" from the edge of the hole, the four layers go in different directions: layer 2 gains more compression, layer 4 stays around zero, layer 6 gains stress in tension, and layer 8 stress turns into higher tension.

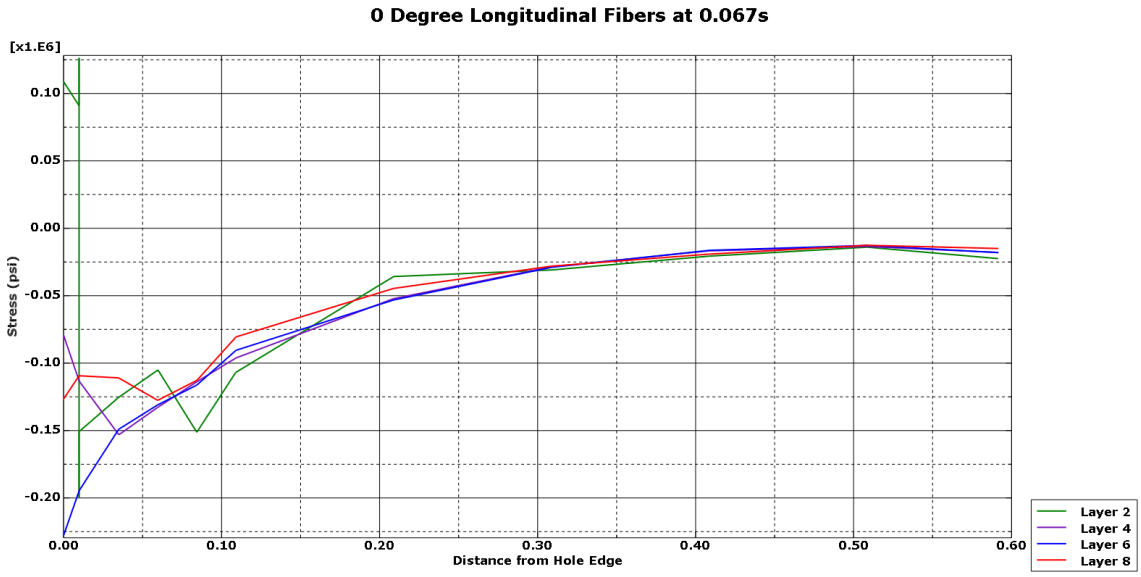

Figure 107: σ_{11} for 0-Degree Layers Longitudinal Fibers

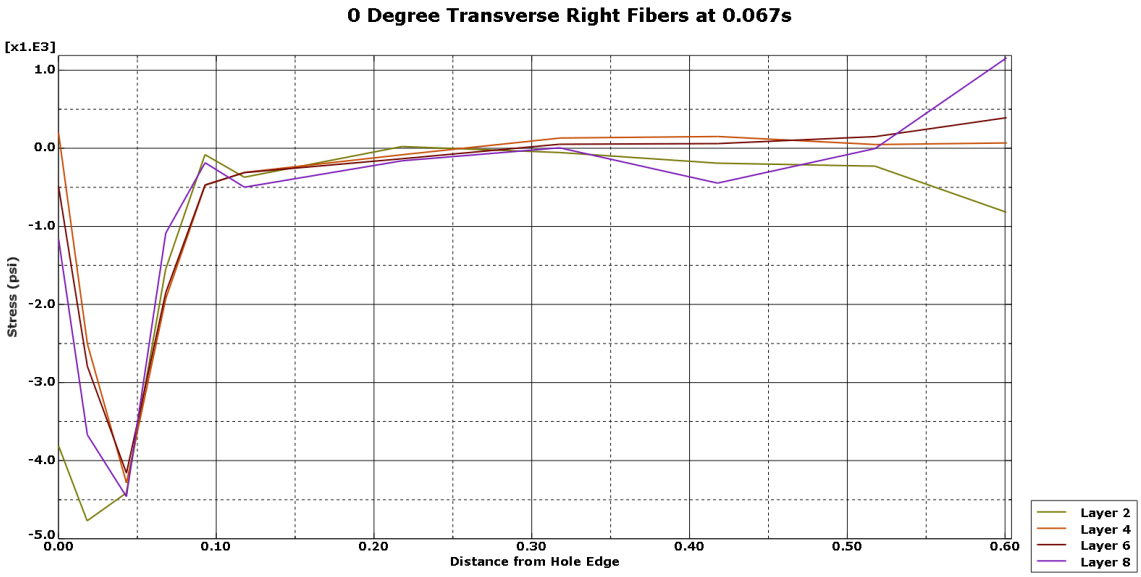

Figure 108: σ_{22} for 0-Degree Layers Transverse to the Fiber Direction

The two steel foil layers connected to the -45-degree ply are completely identical in stress. Figure 109 shows that despite being in two different layers, layer 3 and layer 7 containing the foil experience completely identical stress values.

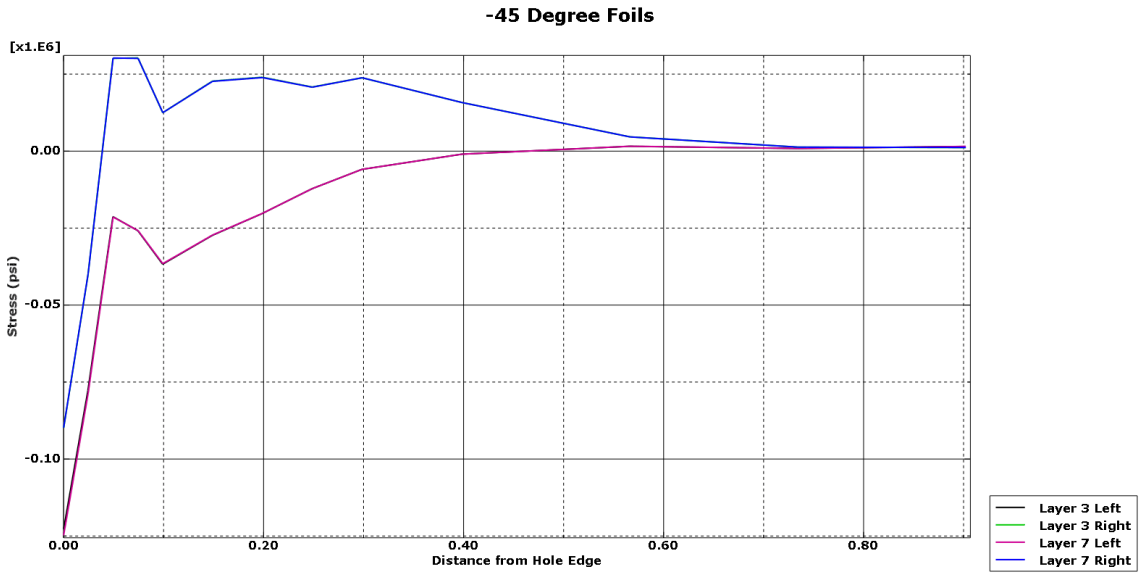

Figure 109: σ_{11} and σ_{22} for -45-Degree Foils

Tsai-Wu Model with Steel Foil

The final model also shows that the cohesive element experiences stress through the thickness. Figure 110 shows that the stress occurs through the model in the x_1x_3 plane.

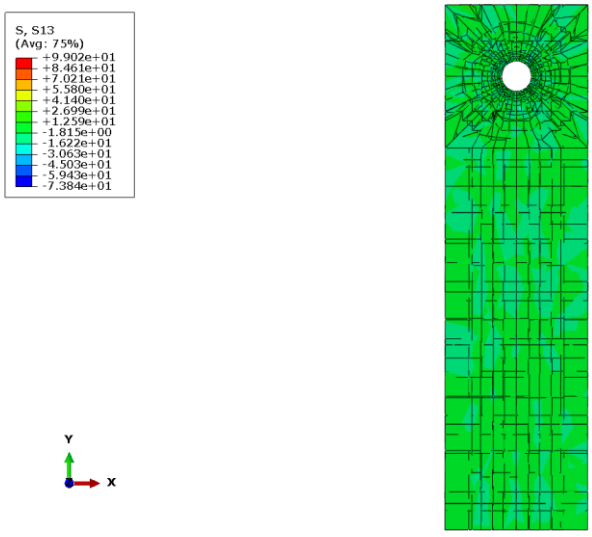

Figure 110: Cohesive Element in-between Layer 1 and 2

The Tsai-Wu model with a steel foil follows the same patterns as the model without steel foils with the exception that the model with steel foils experiences less stress. Figures 111-113 show the progression of the von Mises stress field on the first layer in the Tsai-Wu with a steel foil model. The field extends out along the fibers' direction. As time goes on in the model, the stress increases especially around the hole. A portion of the stress in this model extends downward in the fiber direction too unlike in previous models where the stress was primarily dedicated to the top half of the hole.

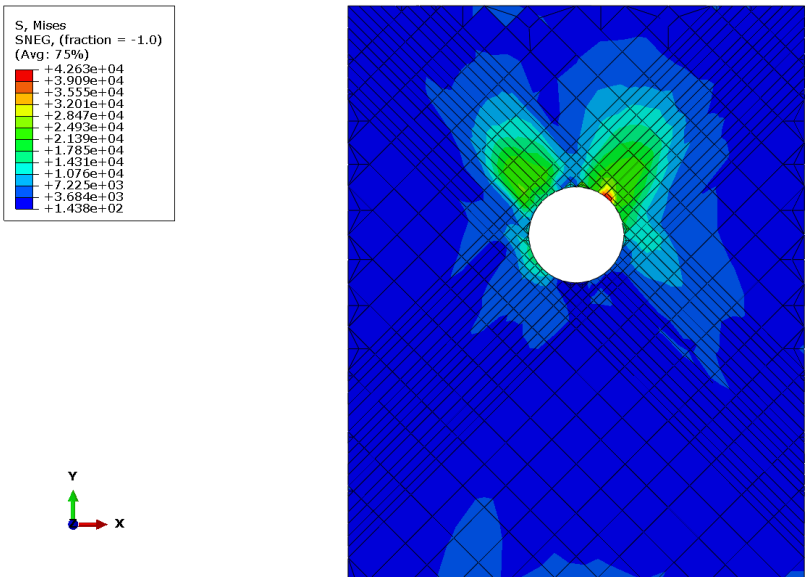

Figure 111: Von Mises Stress in Layer 1 at Time 0.033s

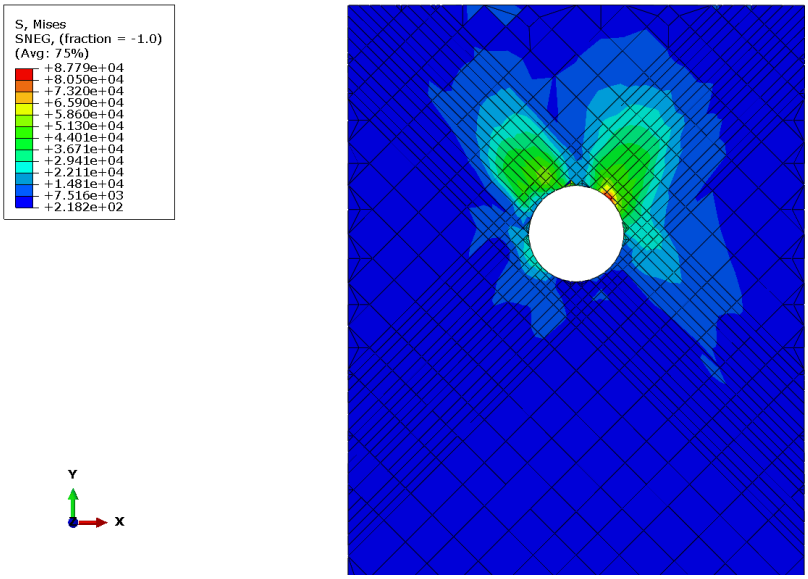

Figure 112: Von Mises Stress in Layer 1 at Time 0.050s

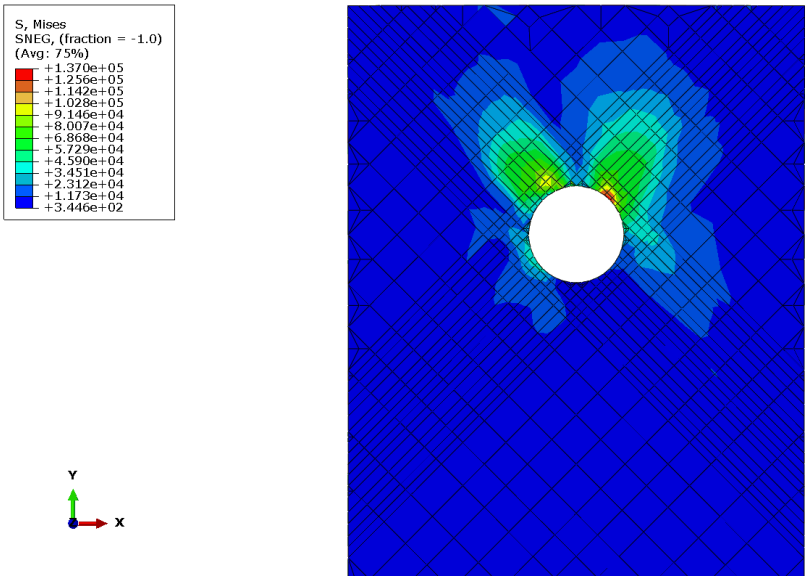

Figure 113: Von Mises Stress in Layer 1 at Time 0.067s

The first layer shows the same pattern dictated in the previous models where the stress field remains consistent and only grows in compression as time progresses. Figure

114 graphs the stress versus distance in the longitudinal fiber direction. The graph shows that the fibers around the hole experience compression.

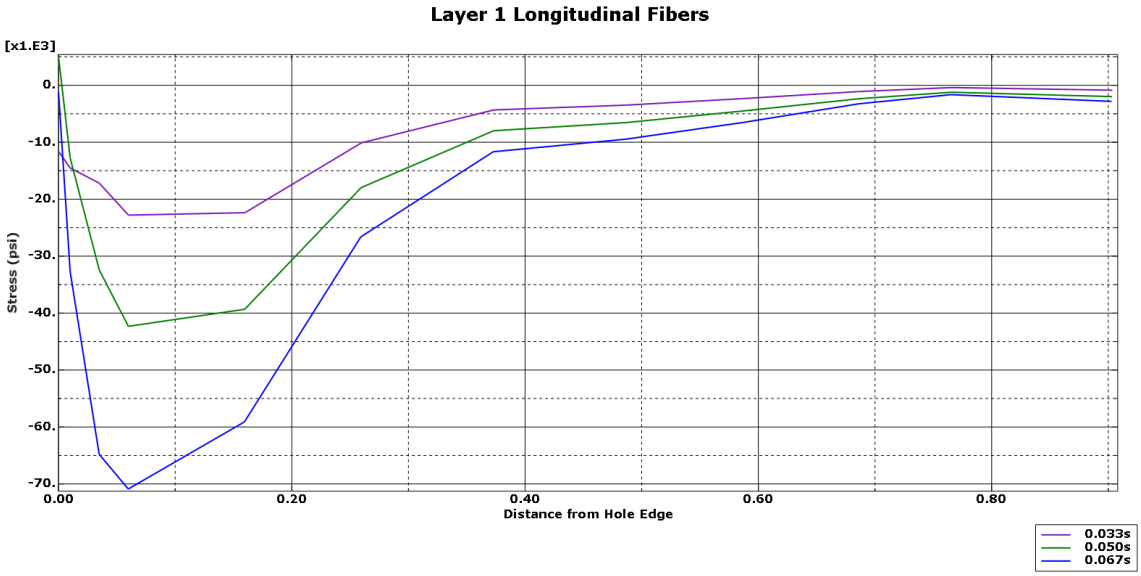

Figure 114: σ_{11} for Layer 1 45-Degree Longitudinal Fibers

In the transverse fiber direction, depicted in Figure 115, the main difference between previous models is that the first layer experiences that greatest compression initially rather than later in the time of the model. At 0.05" from the hole's edge, the pattern of the stress field becomes equivalent, except for values, across the material.

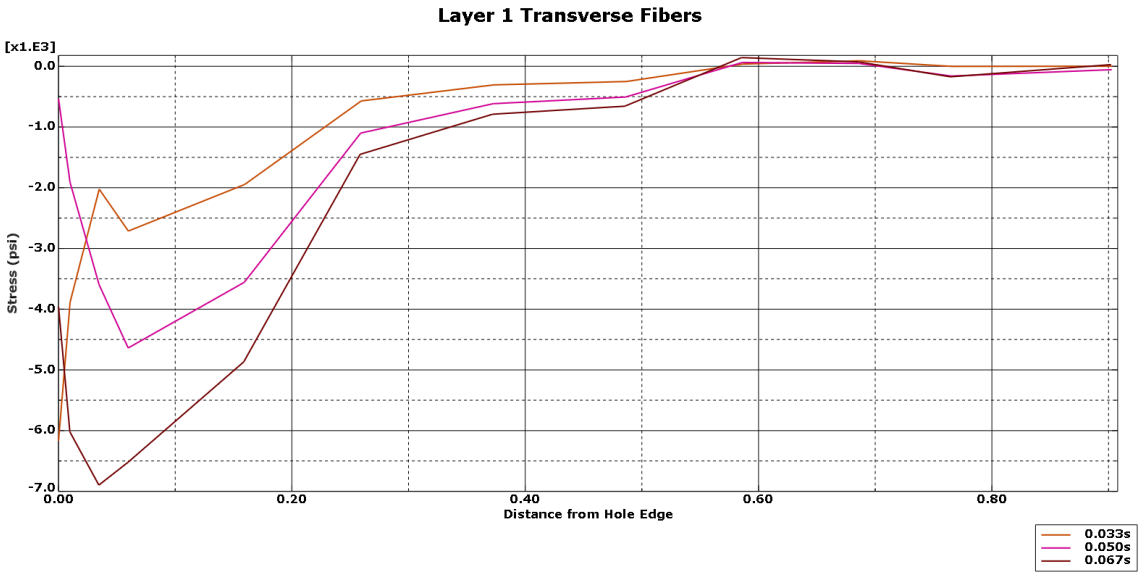

Figure 115: σ_{22} for Layer 1 45-Degree Transverse to the Fiber Direction

Figures 116-118 shows the stress field progression as time advances. The same pattern is depicted in layer 2 as with the other models. The stress field primarily extends in the direction of the fibers with the stress extending downward along the material towards the axial load upon the object.

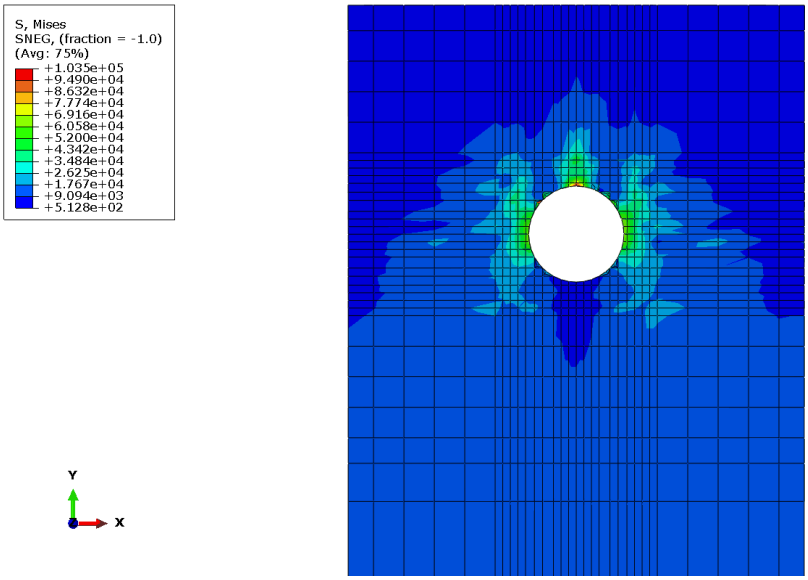

Figure 116: Von Mises Stress in Layer 2 at Time 0.033s

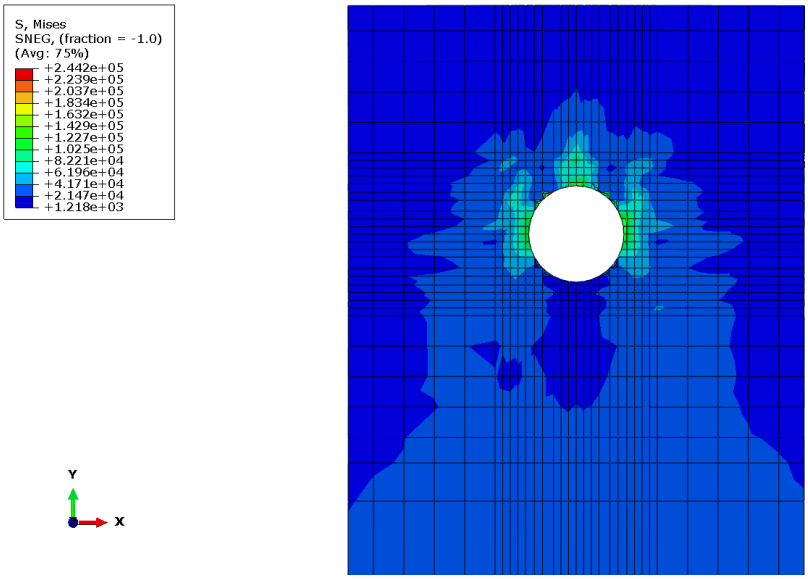

Figure 117: Von Mises Stress in Layer 2 at Time 0.050s

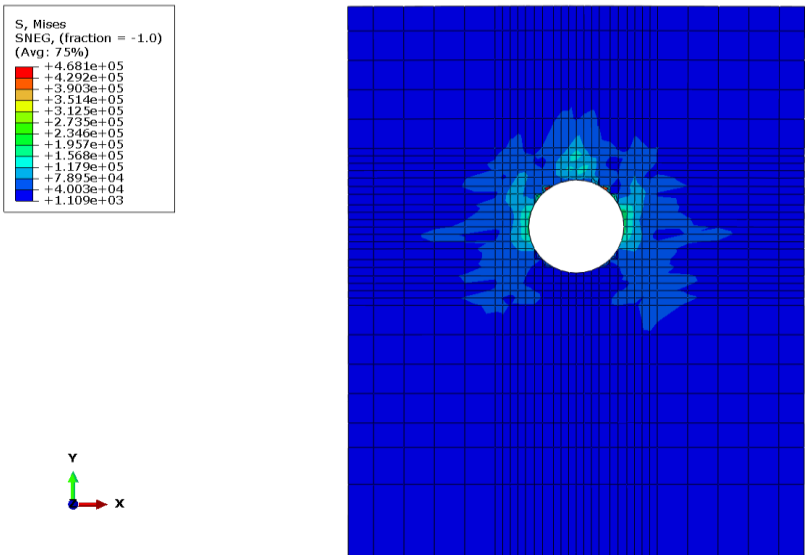

Figure 118: Von Mises Stress in Layer 2 at Time 0.067s

The biggest difference in the second layer of the model is the initial stress occurring at the hole's edge. Figure 119 depicts the stress occurring on the longitudinal fibers. The stress field stays pretty consistent and converges approximately 0.21" away

from the edge of the hole. Initially the fibers experienced tension but the tension quickly turned into compression.

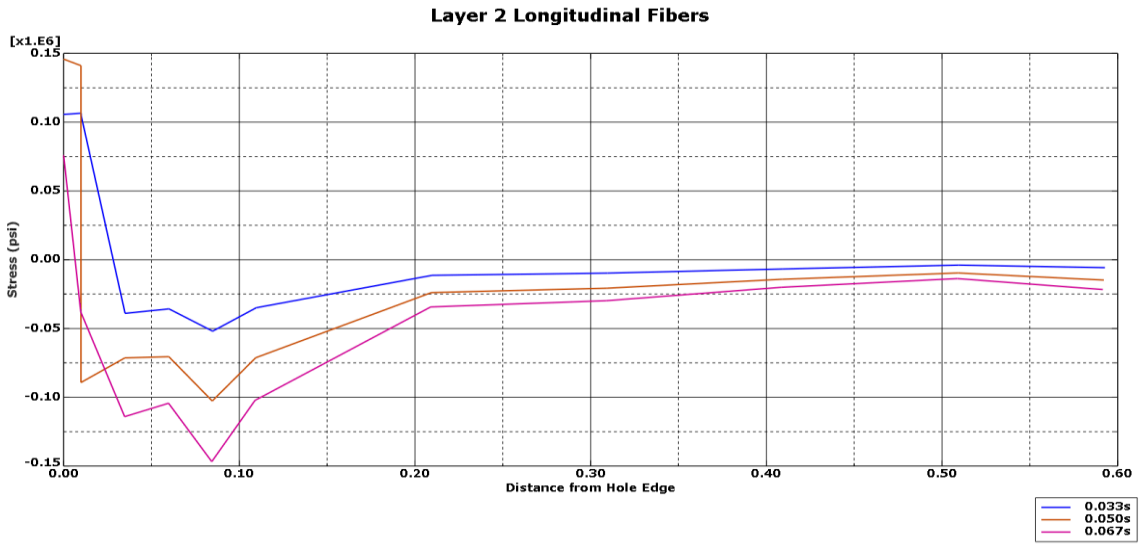

Figure 119: σ_{11} for Layer 2 0-Degree Longitudinal Fibers

The fibers in the transverse direction experience less stress, but half of the layer is in tension while the other half is in compression. Figure 120 depicts the stress seen by the transverse to the fiber direction in the second layer. The right side of the hole of the transverse to the fiber direction is in tension while the left side is in compression. At 0.05” away from the hole, all of the stress in the fibers begins to converse at zero.

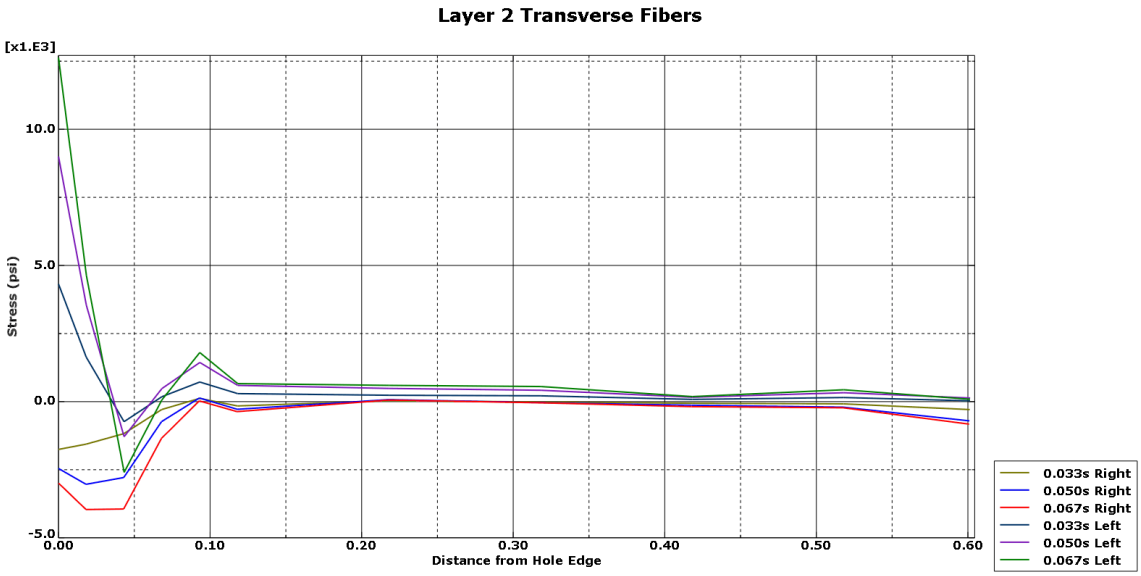

Figure 120: σ_{22} for Layer 2 0-Degree Transverse to the Fiber Direction

Figures 121-123 depicts the von Mises stress at various times of the third layer. The third layer in this model is the steel foil connected to the -45-degree fiber orientated layer. The stress in the foil spreads out from around the hole with the highest concentration of stress occurring in the top half of the hole.

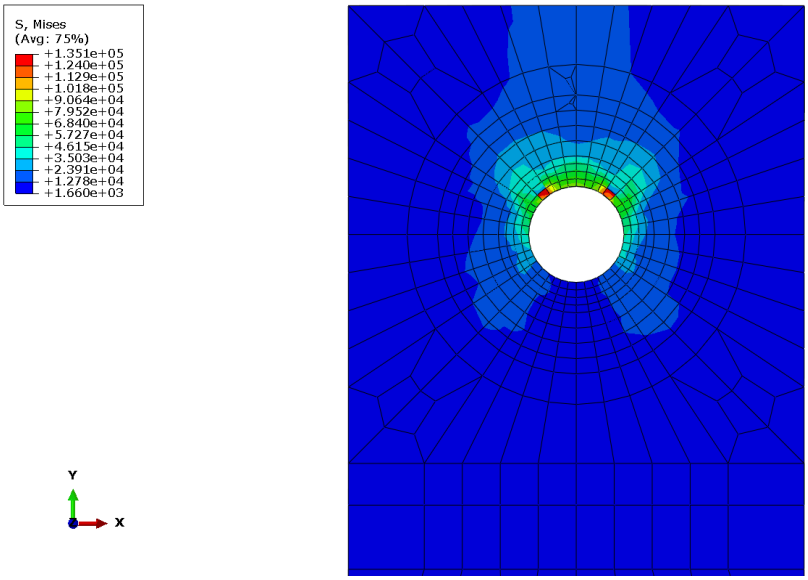

Figure 121: Von Mises Stress in Layer 3 at Time 0.033s

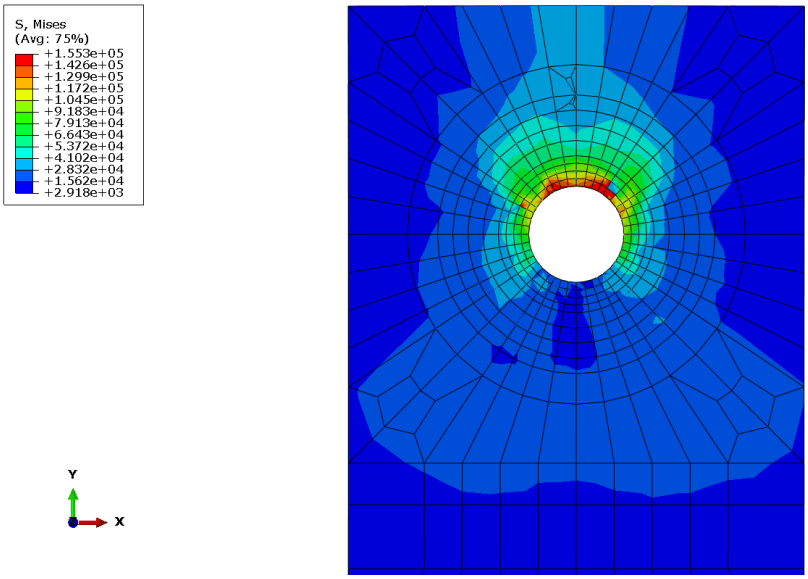

Figure 122: Von Mises Stress in Layer 3 at Time 0.050s

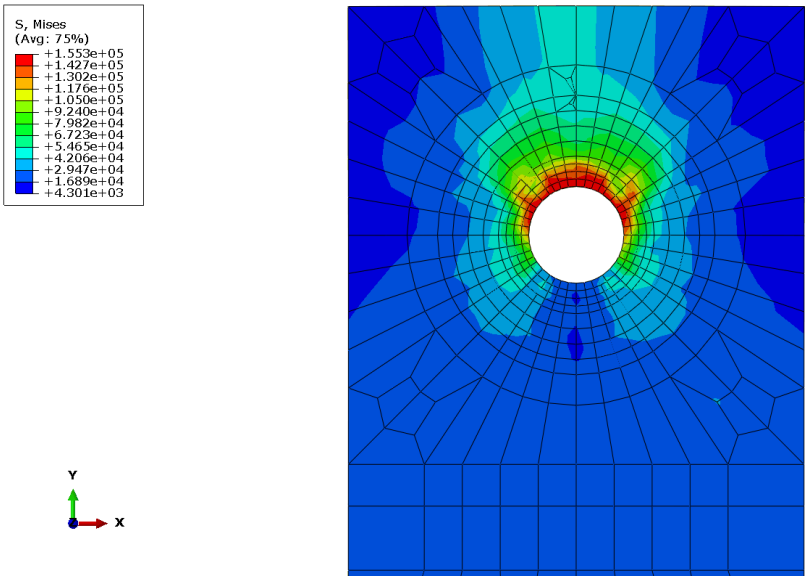

Figure 123: Von Mises Stress in Layer 3 at Time 0.067s

The stress in the third layer, depicted in the graph in Figure 124, follows the same trend of possessing similar stress patterns but only differing in value. For this foil, the two lines were drawn as if the steel foil was in the -45-degree fiber direction. Therefore,

the two sides depicted are in the 45- and -45-degree direction from the hole. The stress coming from the left side of the foil are initially in compression but quickly turn to tension. All of the stresses, however, converge at approximately 0.65” from the edge of the hole upon zero.

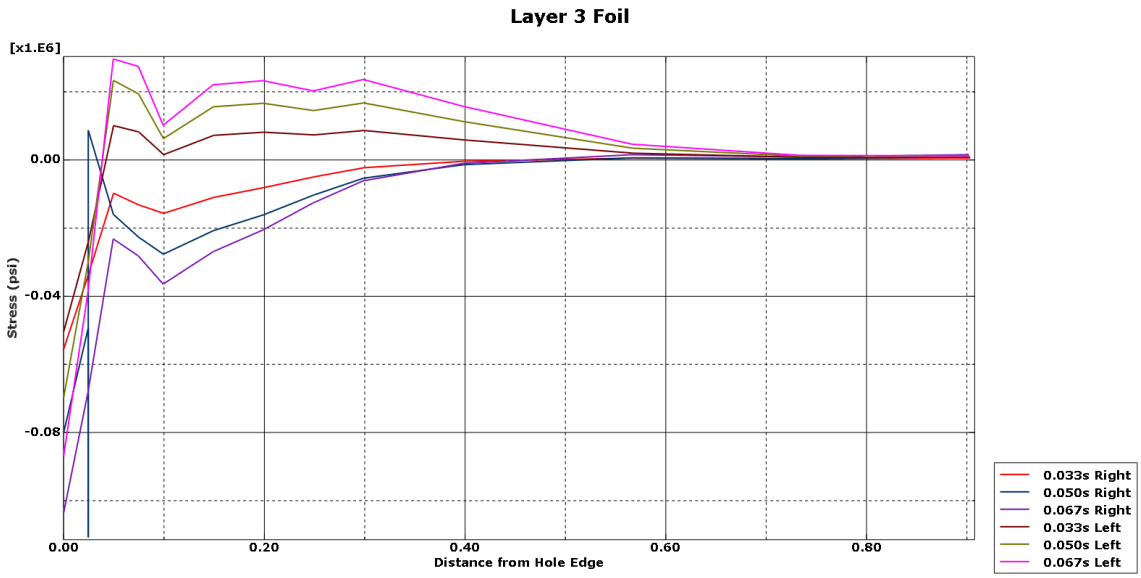

Figure 124: σ_{11} and σ_{22} for Layer 3 Foil

The stress field located on the foil in the fifth layer is almost identical to the stress field presented earlier in layer 3. The fields look identical but possess different stress values. Layer 5 is not as extreme in stress as the third layer. The field spreads out from the hole with the highest concentration occurring on the top half of the hole’s edge as depicted in Figures 125-127.

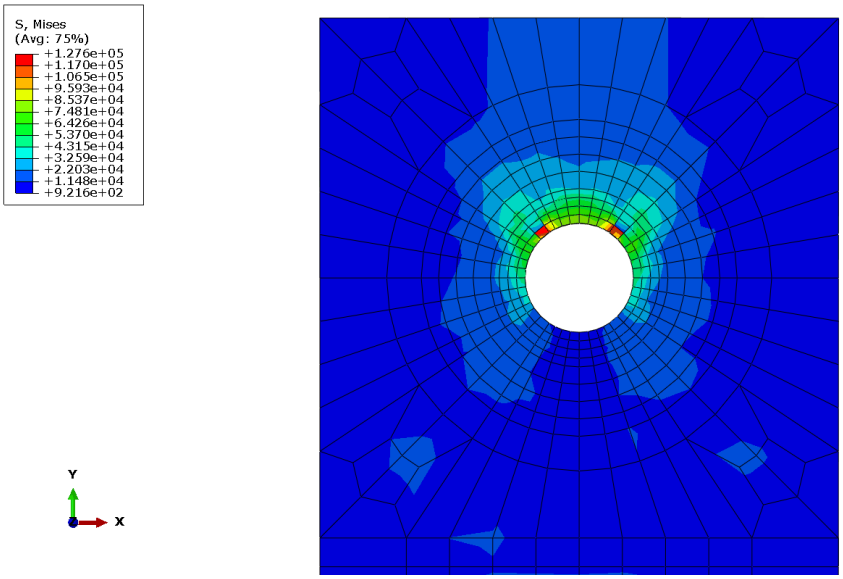

Figure 125: Von Mises Stress in Layer 5 at Time 0.033s

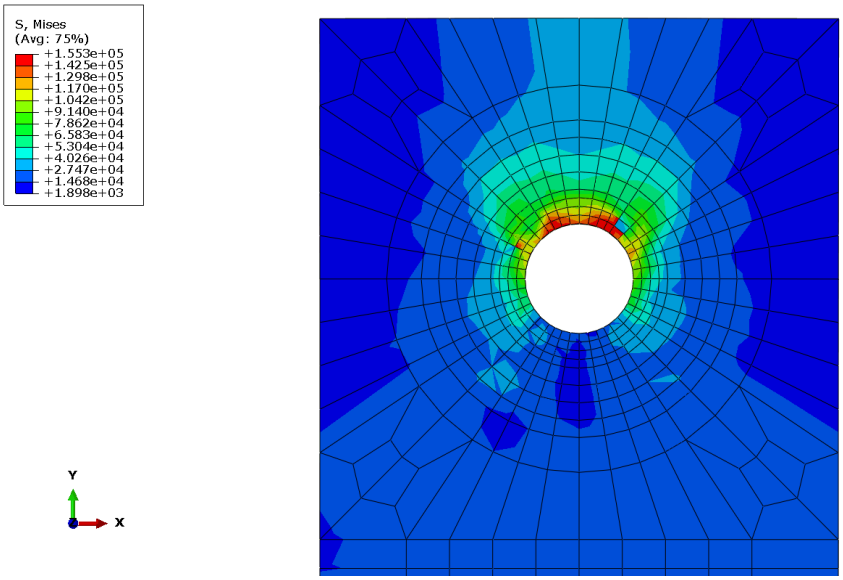

Figure 126: Von Mises Stress in Layer 5 at Time 0.050s

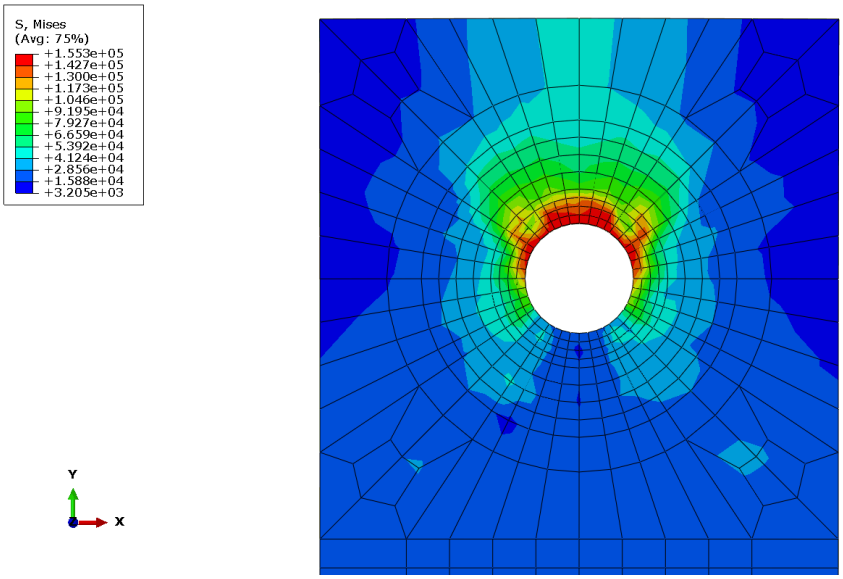

Figure 127: Von Mises Stress in Layer 5 at Time 0.067s

Figure 128 graphs the stress seen by the fifth layer of the model which is another foil; this foil, however, replaces and is connected to a 90-degree fiber orientated composite. Therefore, the distance depicted in the graph of Figure 128 is the transverse fiber direction of a 90-degree fiber orientated layer. The stress exhibited in the fifth layer follows a pattern throughout the entire time of the model. As time progresses, the foil experiences more compression.

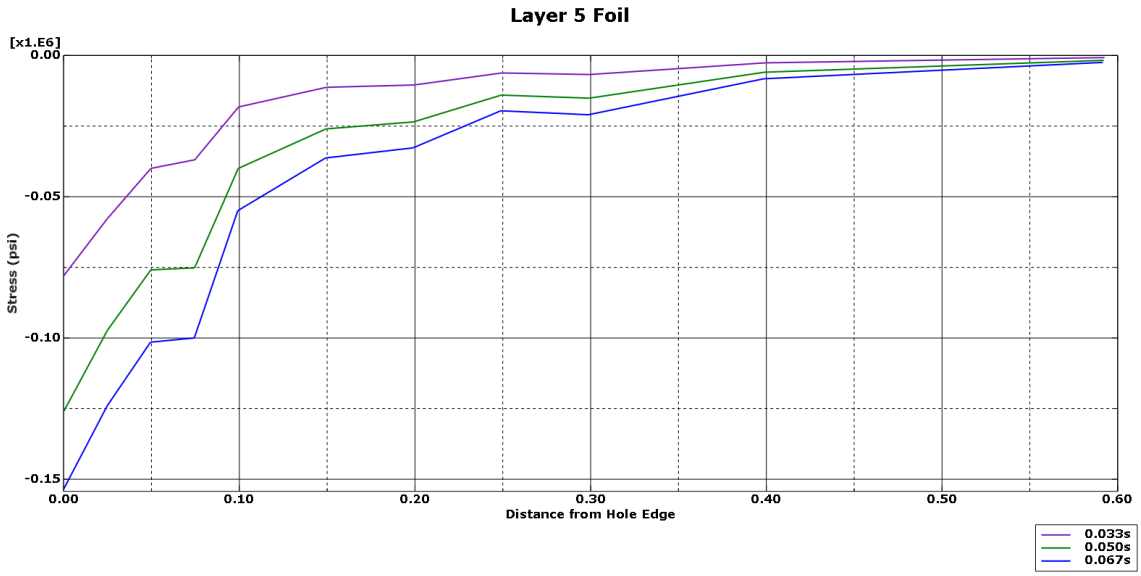

Figure 128: σ_{11} and σ_{22} for Layer 5 Foil

Figures 129-130 depict the stress experienced by the 45-degree layers. Initially there is a difference between the two layers, but the two layers quickly converge upon one another and follow the same pattern with slight variation. Layer 9 in both graphs experience a greater maximum compression than Layer 1. Both fiber directions converge upon zero stress.

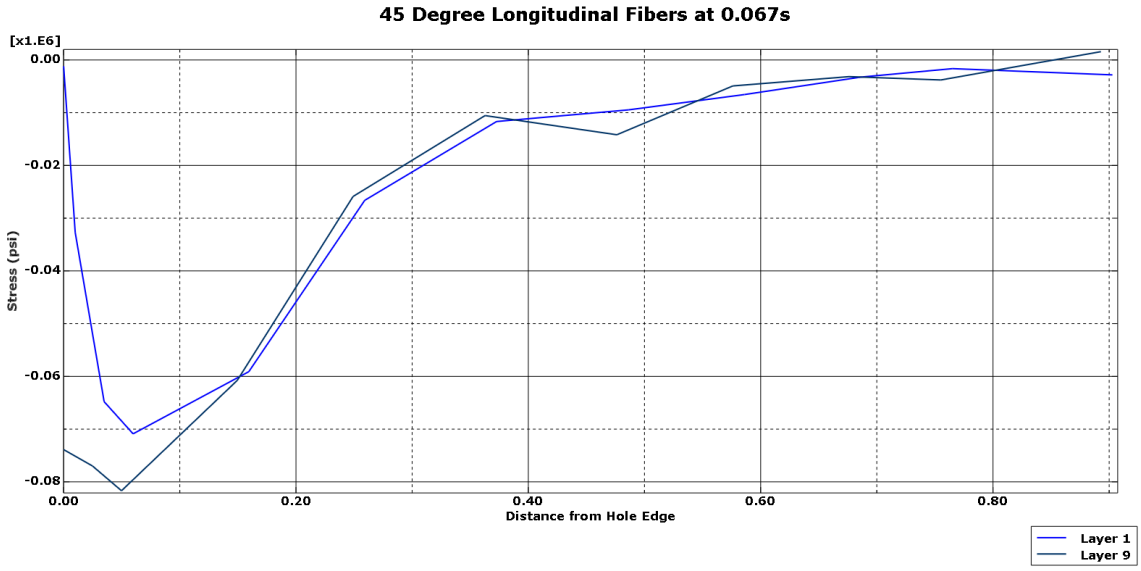

Figure 129: σ_{11} for 45-Degree Layers Longitudinal Fibers

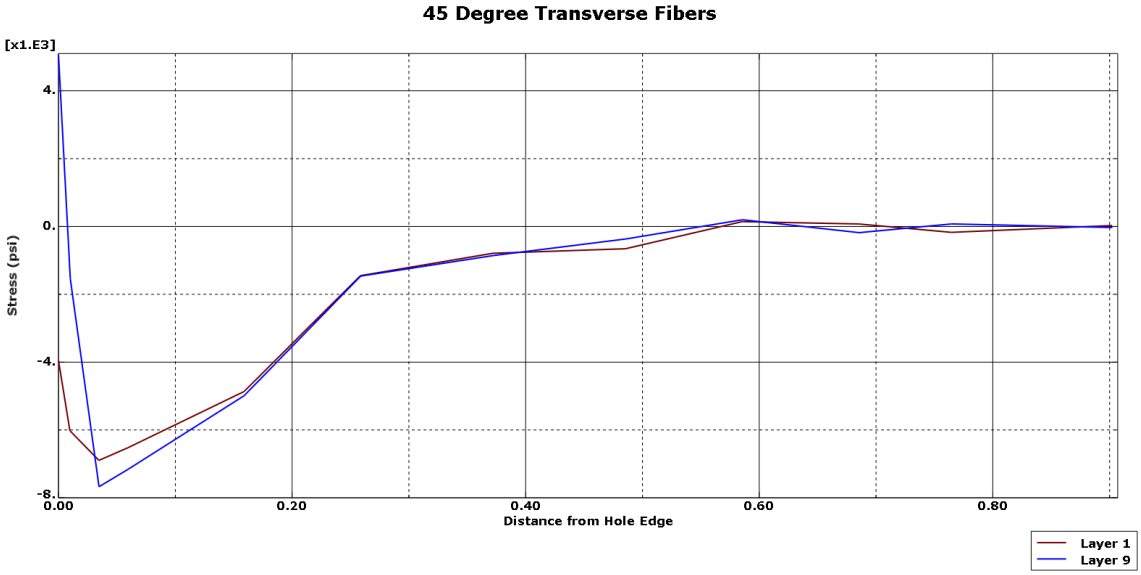

Figure 130: σ_{22} for 45-Degree Layers Transverse to the Fiber Direction

The 0-degree fiber orientated layers exhibit similar behaviors seen before. The longitudinal fibers' stress, depicted in Figure 131, initially starts out between tension and compression. Layers 2 and 4 start out in tension while layers 6 and 8 start out in

compression. The stress values quickly converge together around 0.10” and all layers tend towards zero stress.

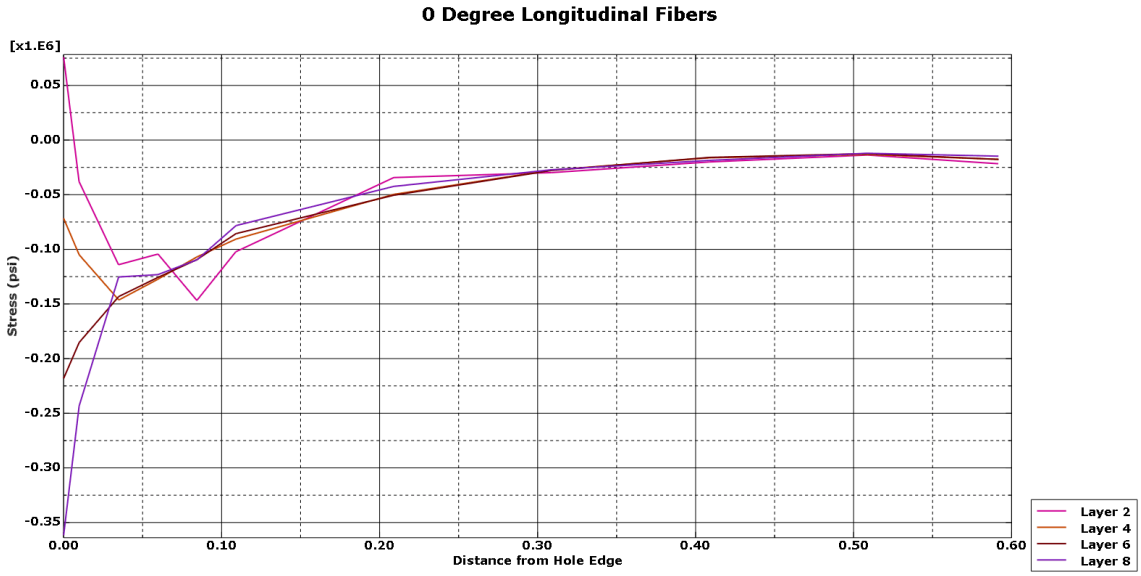

Figure 131: σ_{11} for 0-Degree Layers Longitudinal Fibers

The stress in the transverse fiber direction does not converge but rather diverges at 0.50” from the edge of the hole as shown in Figure 132. Before that moment, the stress is close in values and follow the same trends.

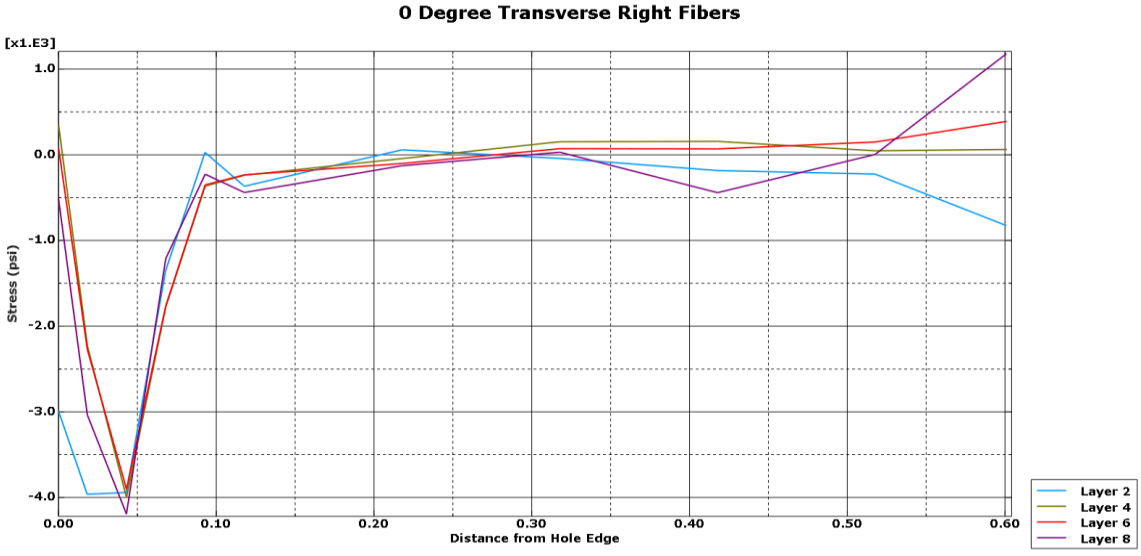

Figure 132: σ_{22} for 0-Degree Layers Transverse to the Fiber Direction

Figure 133 shows that the foils, like the foils in the Hashin model, experience identical stress values. Despite the difference in positioning of the layers, and unlike the composite layers, the foils stay consistent in their stress values throughout the thickness.

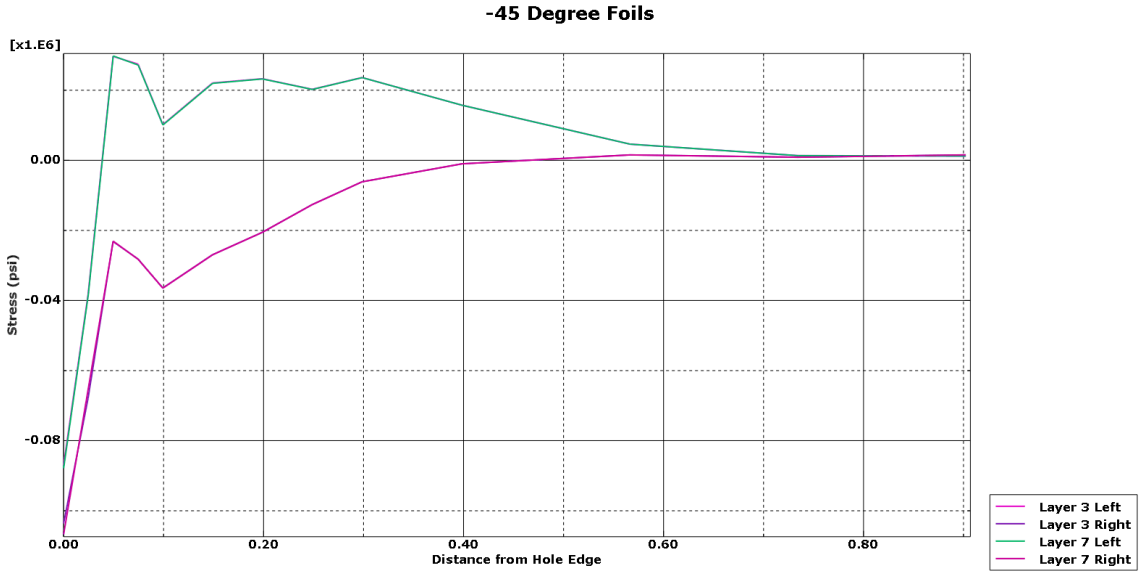

Figure 133: σ_{11} and σ_{22} -45-Degree Foils

Review

The four different models showed different stress values but similar stress fields within them. Table 6 shows the maximum von Mises stress value seen by each layer of the models. Each layer experiences a different maximum stress value. The models without foils experienced greater stress than the two models with foils. The models with foils show a closer range of stress values between the Hashin and Tsai-Wu failure criterion models. The Hashin models experienced less stress overall than the Tsai-Wu models except for the 0-degree layers. Typically the 0-degree layers saw greater stress values in the Tsai-Wu model for both the model with and without a foil. The steel foils

experienced the exact same stress values throughout both models and all layers containing the steel foil.

Table 6: Maximum Stress in Each Layer for Each Model

	Hashin Without Foil	Hashin With Foil	Tsai-Wu Without Foil	Tsai-Wu With Foil
Layer 1	299,800	152,600	191,500	137,000
Layer 2	268,200	329,300	406,100	468,100
Layer 3	338,200	155,300	419,500	155,300
Layer 4	228,000	238,600	479,500	216,800
Layer 5	285,400	155,300	156,300	155,300
Layer 6	189,600	255,800	405,200	377,400
Layer 7	280,700	155,300	219,300	155,300
Layer 8	321,700	247,600	916,500	504,400
Layer 9	371,400	254,800	300,800	221,000

Only one model indicated failure occurring within the composite layers: the Hashin model without steel foils. Each layer within the Hashin model without steel foils showed at least 4 elements having failed within each ply. The 0-degree fiber orientated layers showed the most failures and deleted elements.

Table 7: Element Deletion Within Each Layer for Each Model

	Hashin Without Foil	Hashin With Foil	Tsai-Wu Without Foil	Tsai-Wu With Foil
Layer 1	4	0	0	0
Layer 2	13	0	0	0
Layer 3	5	0	0	0
Layer 4	14	0	0	0
Layer 5	10	0	0	0
Layer 6	15	0	0	0
Layer 7	10	0	0	0
Layer 8	13	0	0	0
Layer 9	4	0	0	0

Chapter 5

V. Conclusions and Recommendations

Conclusions of Research

Despite the differing estimated strain rates, the steel foil specimen show similar material properties. As can be seen in Figure 17, the Modulus of Elasticity for the averages of the tests are extremely close and show little-to-no difference. This shows that under quasi-static loading, the steel foil shows elasticity with almost identical Modulus of

Elasticity for each test. The maximum difference between the different Modulus of Elasticity is -3.7% to 6.2%. The average for the overall experimental tests, therefore, is reasonable to use in the modeling of the steel foils and shows accuracy of the steel foil layers.

All four models show stress occurring along the fiber directions. The fiber-orientated mesh design is important when modeling composite materials. The initial failure for the Hashin models occurs along the longitudinal fiber direction. Each layer within the model fails in a different portion around the circle, but the common factor is that the failure occurs along the fiber direction which the fiber-orientated mesh shows. Failure also occurs around the top half of the hole, which was to be expected. The top portion of the hole sees the most stress from the load placed upon the object. With the pin being short and therefore less malleable, the top half of the hole in the material feels compression from the load pulling down the object.

The Hashin model without the steel foil shows failure occurring through the deletion of elements by time 0.067s. Varying stress throughout the layers show that the thickness plays a role in the model. Complete failure and deletion of the elements occurs from the fiber and matrix feeling failure from the stress. The matrix fails before the fibers, but when the fibers start to fail is when complete failure of the element occurs. Matrix compression failure occurs along the transverse fiber direction with fiber tension while matrix tension fails along the longitudinal fiber direction with fiber compression. The matrix is in tension when the fibers are in compression and in compression when the fibers are in tension.

The Tsai-Wu model stress across the layers shows an interesting trend. Initially at the hole, the layers experience opposing stress: tension and compression. The varying stress values show that the thickness once again plays a role in a 3D model of a composite. Unfortunately, Abaqus does not specifically show matrix or fiber information for Tsai-Wu modeling information. However, the stress occurring in each model without steel foils shows more of the difference in the two modeling types. The difference comes from how the two models are initially set up. Hashin failure criterion assumes a four-function piece-wise formula while Tsai-Wu simplifies the equation into one formula for a fit all case. However, composite materials fail in four different ways depending on the matrix and fibers. The Tsai-Wu model does not specify individual failure modes meaning that complete failure needs to occur before element deletion.

The stress from each layer in the Hashin and Tsai-Wu model show similar patterns and loads. The von Mises stress of the Tsai-Wu model is almost double the amount of the stress the Hashin model meaning that there are extreme differences between the two failure criterion, however the real issue is determining failure. While Tsai-Wu failure criterion shows stress, the failure criterion is not perfect at showing compression failure within a composite. According to the Hashin model, the layers fail according to fiber compression and matrix tension, while the Tsai-Wu model does not indicate any sort of failure occurring at the same point in time.

Adding the steel foil into the model changed the results. The steel foil strengthened the material overall. Whereas by time 0.067s the Hashin model without the steel foil failed, the other Hashin model with a steel foil only showed the fibers and matrix beginning to see failure. The steel foil strengthened the material by allowing the

object to experience a greater stress and helping the material fail later. The layers adjacent to the steel foil experienced greater stress without failing.

Summary

The Hashin and Tsai-Wu model are different in their approaches to determining failure in a composite material. Hashin's failure criterion is based upon the fail in both the fibers and matric in either tension or compression; this gives four different equations to evaluate while Tsai-Wu failure criterion uses one equation to fit all scenarios. The Hashin model depicts compression failure better than the Tsai-Wu failure criterion for this model. Adding the steel foil into the model made the layers beside the model stronger and fail later than the earlier models. The steel enhanced the model while the Hashin model better predicted whether the material would start to fail.

Appendix A

Fiber-orientated Mesh

The primary goal of partitioning each layer according its degree of rotation is so that the mesh will align with the fibers and provide more accurate results. In order to generate a mesh along the fibers of the specific layer, one face of the layer needs to be partitioned according to the fiber directions. An important factor to remember when partitioning an object in Abaqus along the fiber direction is how Abaqus deals with circles. Abaqus does not generate a perfect circle but rather creates a mutli-faceted polygon as depicted in Figure 134 and 135 below.

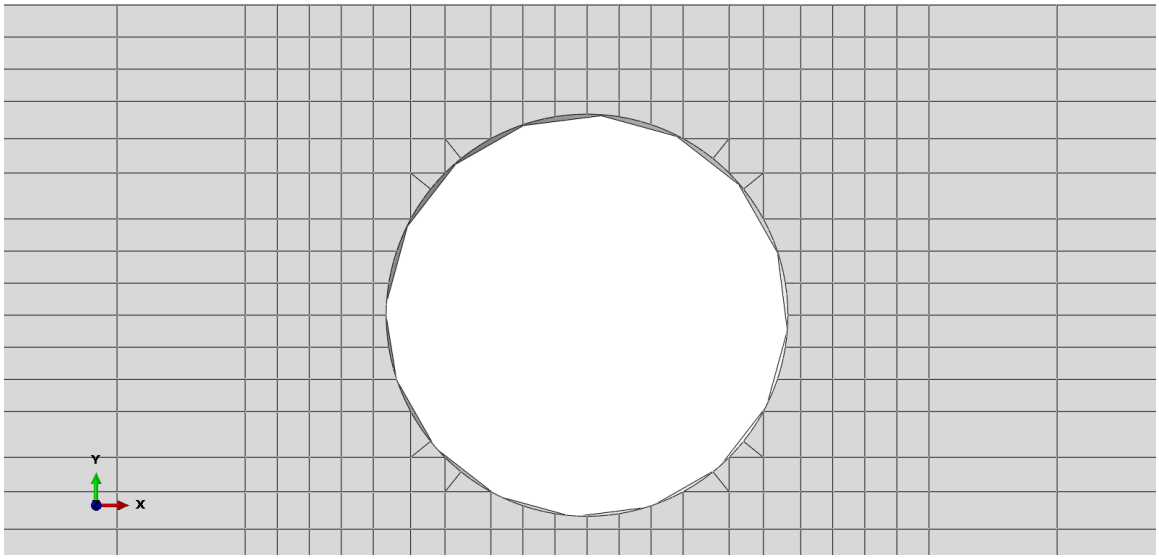

Figure 134: Close-up of 0- and 90-Degree Fiber Mesh

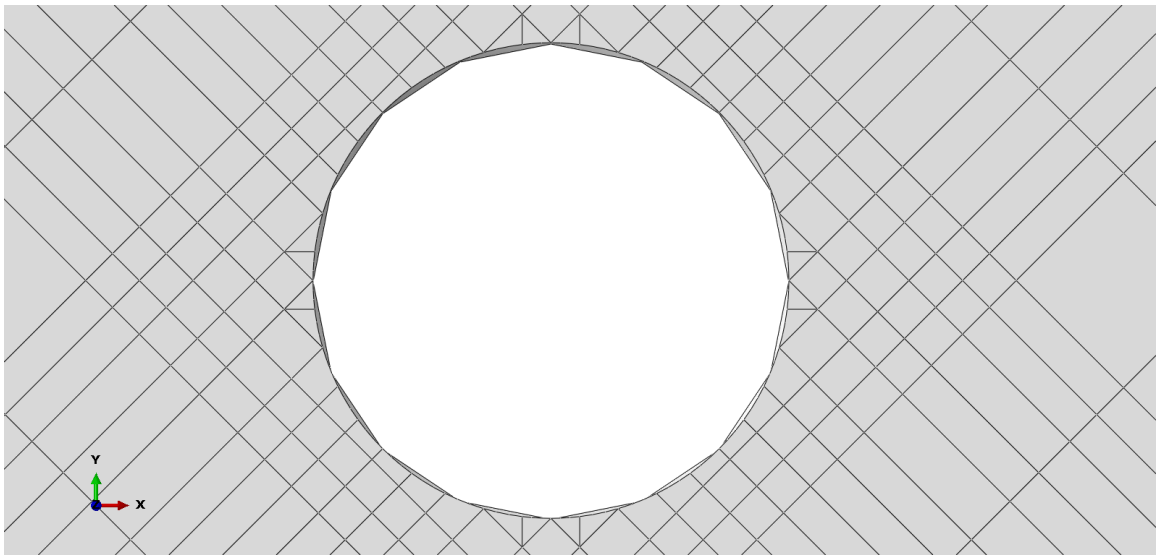

Figure 135: Close-up of 45- and -45-Degree Fiber Mesh

The placement of the lines around the circle are the most crucial portion of the partition. Four of the line placements depend on where the user specified the size of the circle. In the two above Figures 134 and 135, the circle was specified at the exact top so four lines were designated at the top, bottom and perpendicular to the straight line going up generating four points on the circle in which the partition needed to cover.

Starting with the 0- and 90-degree orientation plys, one line would be designed in the 0-degree direction in which the rest of the partition would start. From that initial line, more could be copied and drawn. Starting with either the right of left half of the model, the lines drawn closely around the circle need to be placed in such a way as to avoid distorted elements when the model runs. The lines should be placed as to either directly intersect the polygon points or intersect the edges in approximately the middle. In the case of distorted elements still occurring in the model, the partition may be able to fix the problem by splitting the element in the partition in half. Once that portion of the partition is completed, the rest of the partition may be finished by using the mirror command. The

mirror command would ensure the resulting lines are parallel, symmetrical, and perpendicular. The finished result is depicted in Figure 136 below.

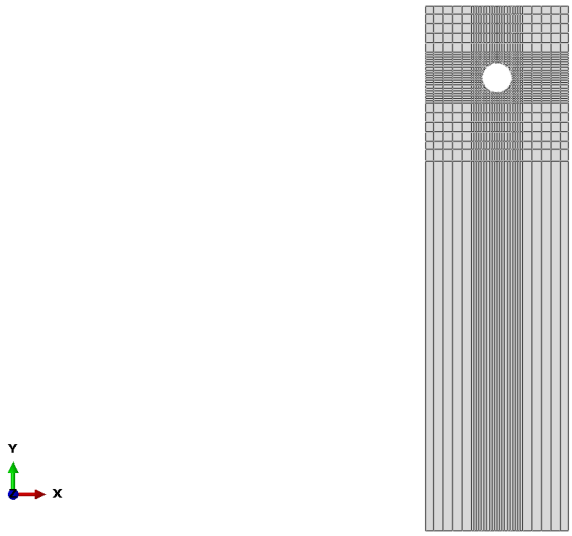

Figure 136: 0- and 90-Degree Partitioned Layer

The 45- and -45-degree plys are made in the same way as the 0- and 90-degree ply model with the exception that the initial line is drawn bisecting the hole at the top in a 45-degree direction. The subsequent lines drawn are made parallel using the parallel constraint tool in Abaqus. This tool ensures that the new lines drawn are at the exact same angle as the first line. Again, the mirror tool in Abaqus may be utilized to ensure the lines are symmetrical about the hole centered. The finished product is depicted in Figure 137 below.

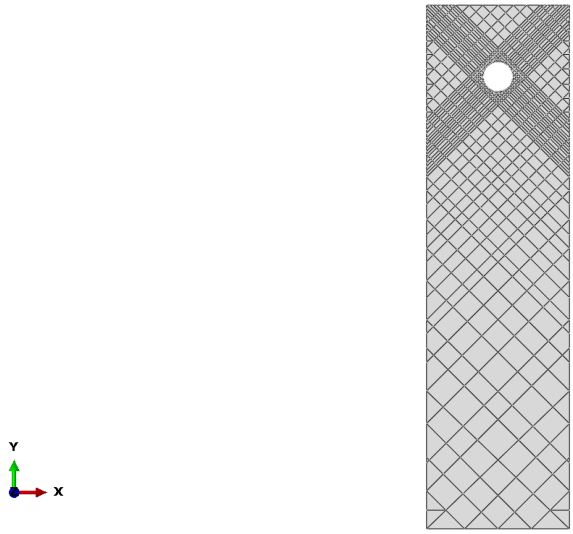

Figure 137: 45- and -45-Degree Partitioned Layer

Steel Foils

For the model with steel foils incorporated, new -45- and 90-degree ply layers needed to be built. The partition was degenerated in the same method as mentioned previously, but the size of these two layers and their partition is depicted in Figure 138 and 139 below. The -45-degree and 90-degree were also redone to incorporate the steel foil in connection with them.

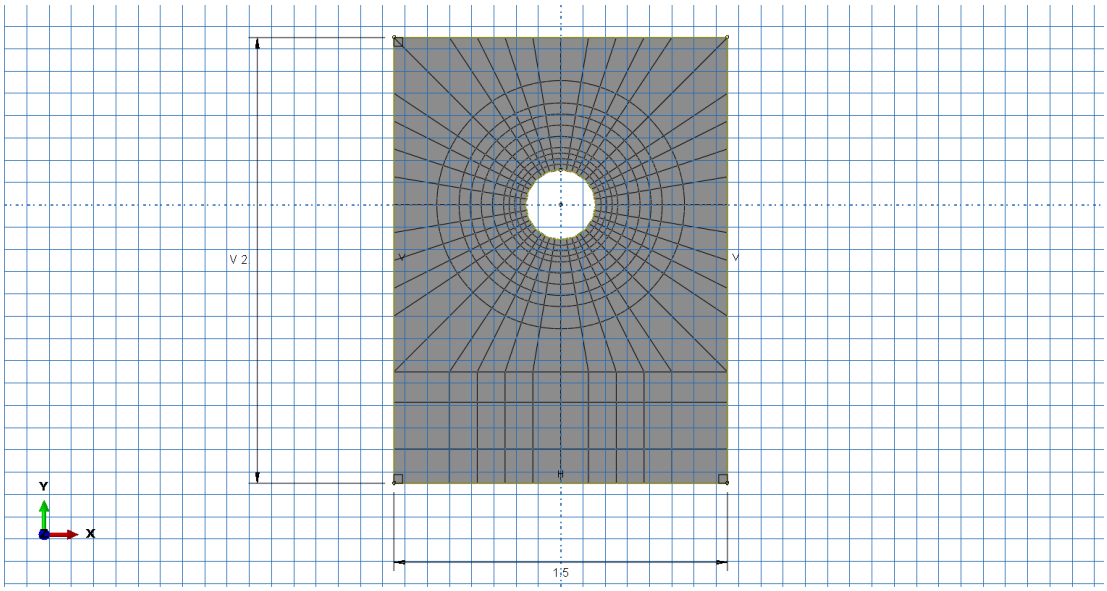

Figure 138: Steel Foil Connected to -45-Degree Fibers

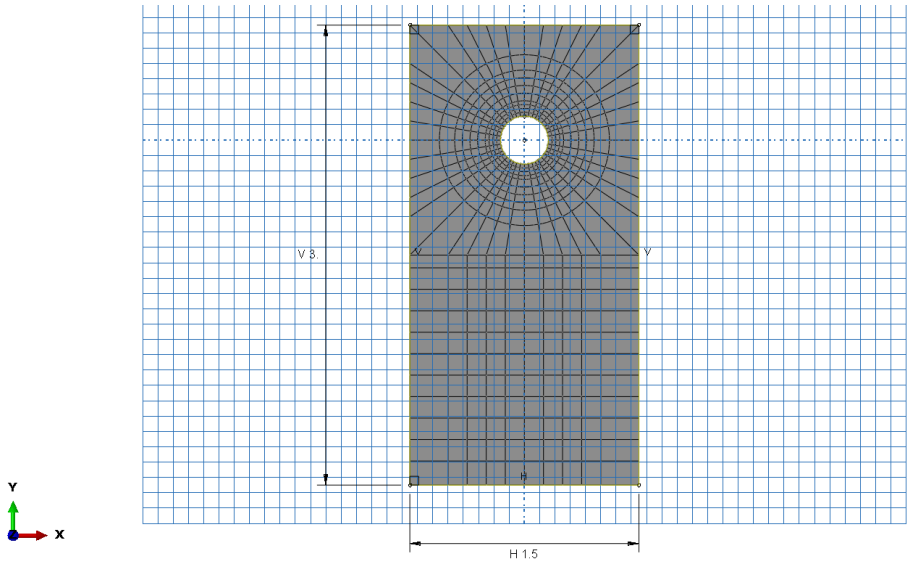

Figure 139: Steel Foil Connected to 90-Degree Fibers

Cohesive Layer

The cohesive partition involved a slightly different technique than the composite layers. Instead of focusing on partitioning the model according to fiber orientation, the

cohesive model was partitioned with multiple circles surrounding the hole and lines going out in all directions. The resulting partition is depicted below in Figure 140.

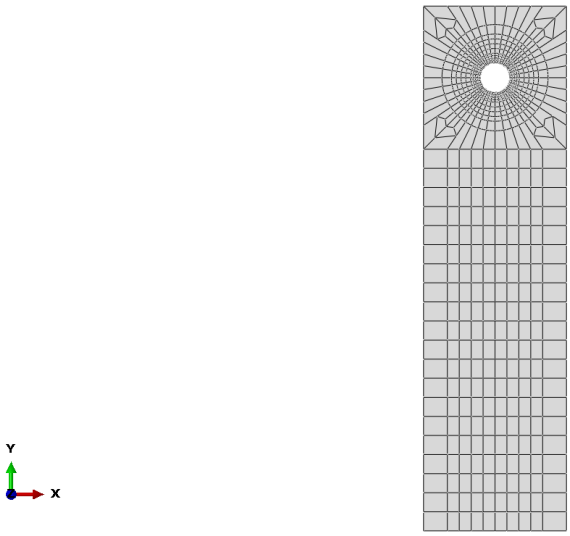

Figure 140: Cohesive Layer

Appendix B

The following tables show the material properties used for each layer in the model. IM7-977-3 material properties are defined in two ways depending on if the model used Hashin or Tsai-Wu failure criterion. Hashin failure material properties were defined using the Hashin Damage material property option with the Damage Evolution sub option using the information in Table 8. The elastic portion of the material properties was defined by the Elastic option with the specification that the material is a lamina type.

Table 8: IM7-977-3 Material Properties

Longitudinal Tensile Strength	392450 psi
Longitudinal Compressive Strength	256060 psi
Transverse Tensile Strength	13880 psi
Transverse Compressive Strength	34330 psi
Longitudinal Shear Strength	17110 psi
Transverse Shear Strength	17110 psi
E_1	18910000 psi
E_2	1260000 psi
ν_{12}	0.32
G_{12}	824000 psi
G_{13}	824000 psi
G_{23}	432000 psi
Density	0.0643 lbs/in^3

The cohesive element material property is defined with a traction separation and the properties defined in Table 9. The Maxe Damage option with the sub option of Damage Evolution selected. Additional information for the cohesive layer is Quads Damage option with the Damage Evolution sub option.

Table 9: Cohesive Material Properties

Nominal Strain Normal-only Mode	0.5
Nominal Strain Shear-only mode First Direction	0.5
Nominal Strain Shear-only mode Second Direction	0.5
Nominal Stress Normal-only Mode	13880 psi
Nominal Stress First Direction	17110 psi
Nominal Stress Second Direction	17110 psi
Density	0.0643 lbs/in^3

The pin made within the model used the steel material definitions in Table 10 with the plastic strain information used in Table 11.

Table 10: Steel Material Properties

Density	0.284 lbs/in^3
Young's Modulus	28500000 psi
Poisson's Ratio	0.272
Fracture Strain	0.1073
Stress Triaxiality	1
Strain Rate	1

Table 11: Pin Plastic Strain

Yield Stress	Plastic Strain
110000 psi	0
168000	0.1073

Appendix C

Each material of different portions of the model used specific elements and properties for mesh. The IM7-977-3 material and cohesive layers used the explicit option in the element library. The family was specified as a continuum shell with no second-order accuracy. Hourglass control uses the default method, but element deletion is specified to happen with a max degradation of 0.9 under element controls. Table 12 shows the different elements, number of nodes, and number of elements used for each type of material and layer built within the model.

Due to the difference in material properties of the steel foil and composite portion of the model, the steel foil used the same elements as the pin. The explicit option in the element library is also selected, but the family is specified as 3d stress. The default options for element controls is used with no modification. These selected options result in the C3D10M element being selected and used for the mesh in the steel foil and pin.

Table 12: Mesh Information

Layer Type	Element Type	# of Nodes	# of Elements
45-Degree	SC8R/SC6R	2,178	1,071
0-Degree	SC8R/SC6R	2,738	1,290
-45-Degree	SC8R/SC6R	2,178	1,071
90-Degree	SC8R/SC6R	2,738	1,290

Cohesive	COH3D8/COH3D6	1,572	728
Foil Short	C3D8R	1,006	460
-45-Degree Short	SC8R	1,032	462
Foil Long	C3D8R	1,170	534
90-Degree Short	SC8R	714	320
Pin	C3D10M	95,027	65,732

Appendix D

The contact information was made from a tangential behavior and normal behavior. The tangential behavior included penalty friction formula with isotropic directionality with a friction coefficient of 0.1, while the normal behavior defined a hard contact.

Appendix E

The displacement loading of the model is placed along the entire bottom of the material. An amplitude as specified in Table 13 is used for the load placed upon the model.

Table 13: Load

Time/Frequency	Amplitude
0	0
0.5	1

The explicit information used for the model is described in Table 14.

Table 14: Non-linear Analysis Parameters

Incrementation Type	Automatic
Stable Increment Estimator	Global
Time Increment	0.001
Linear Bulk Viscosity Parameter	0.06
Quadratic Bulk Viscosity Parameter	1.2

Appendix F

The field output results specified for the material depended on whether that model used the Hashin or Tsai-Wu material properties. For Hashin material properties, the damage information for the fiber and matrix of each layer is requested. The entire layer for each portion of the model was specified back when creating the base layers. The set, which contains the entire layer, is specified when requesting the information. Otherwise, all layers requested the stress and magnitude of displacement. The cohesive layer also requested the tie information to see if the cohesive layer stays connected to the respective tied composite or steel foil layers.

Appendix G

The following figures show the graphed test calculations for each test specimen in order to calculate the Modulus of Elasticity and Yield Stress. These graphs also show the shifted line for the curve of the experimental data.

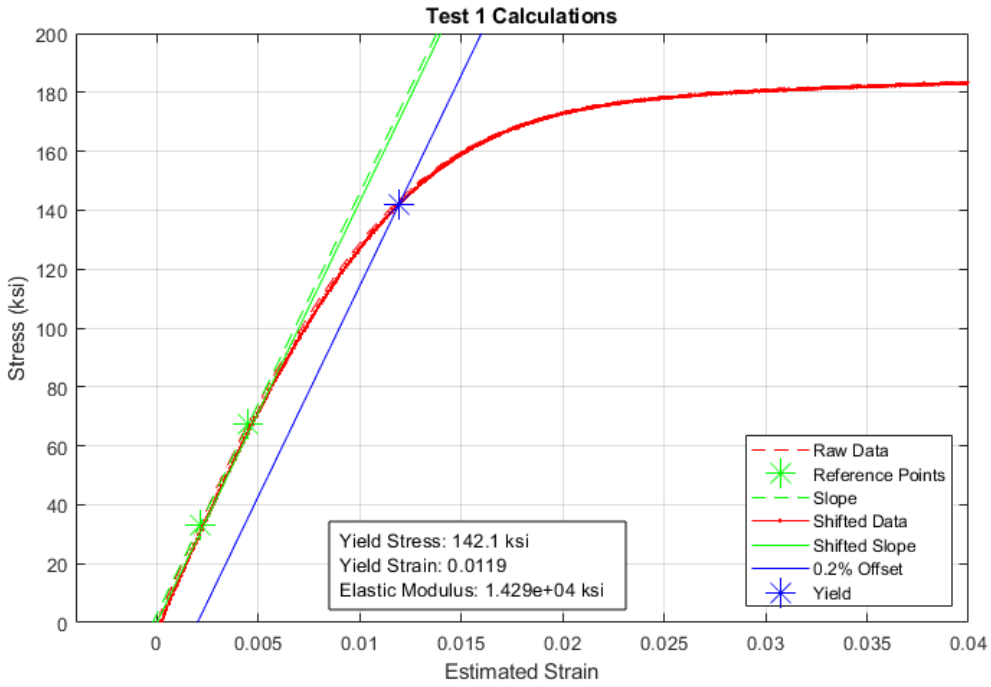

Figure 141: Test 1 Calculations for 0.0027 1/s Estimated Strain Rate

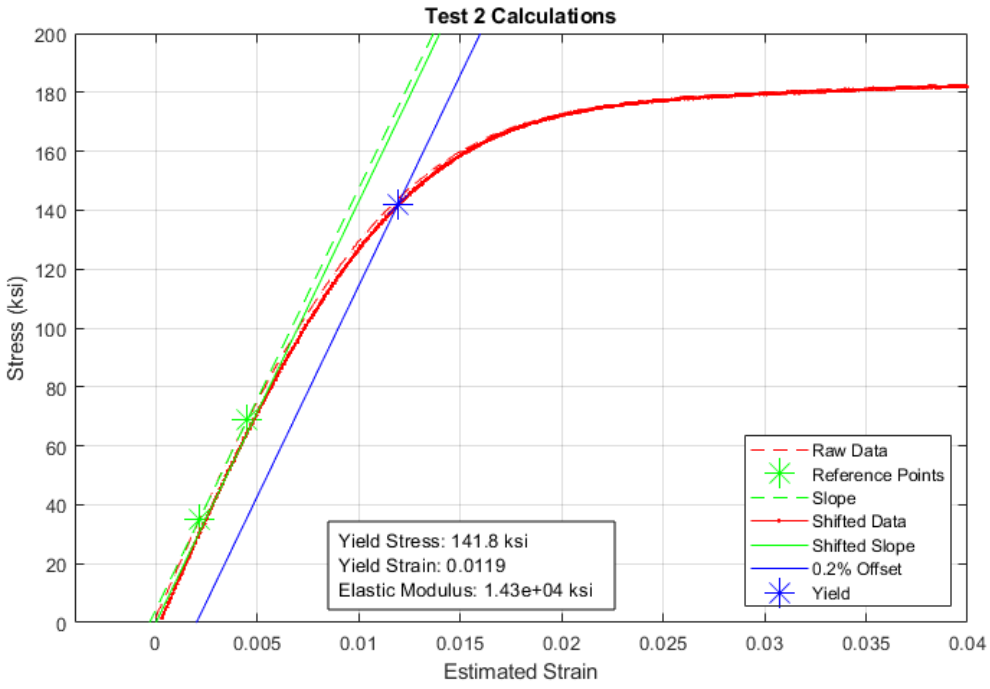

Figure 142: Test 2 Calculations for 0.0027 1/s Estimated Strain Rate

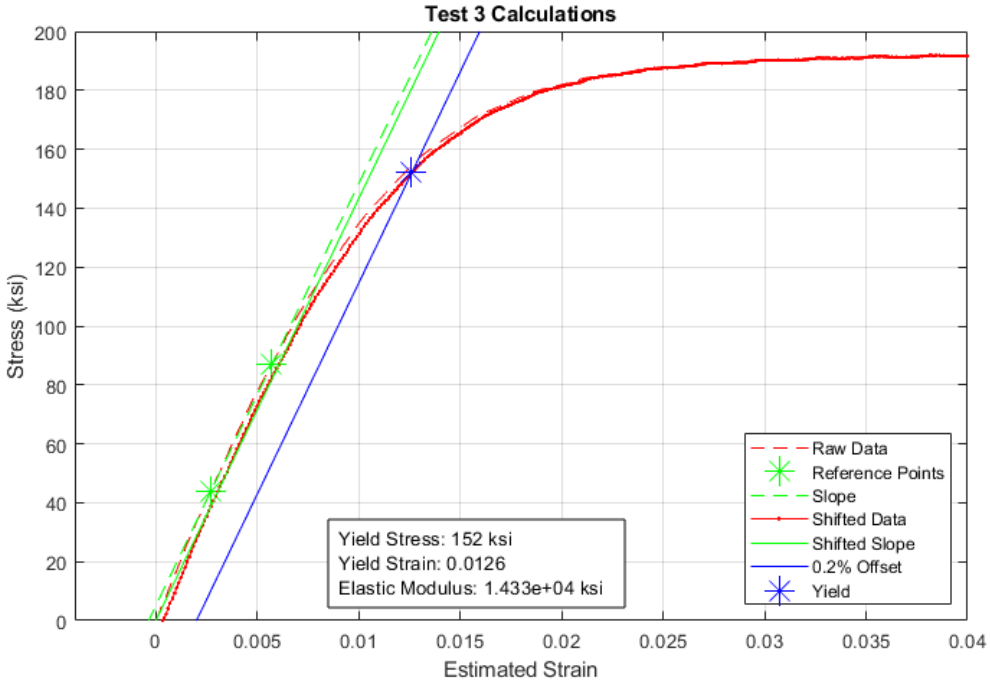

Figure 143: Test 3 Calculations for 0.0027 1/s Estimated Strain Rate

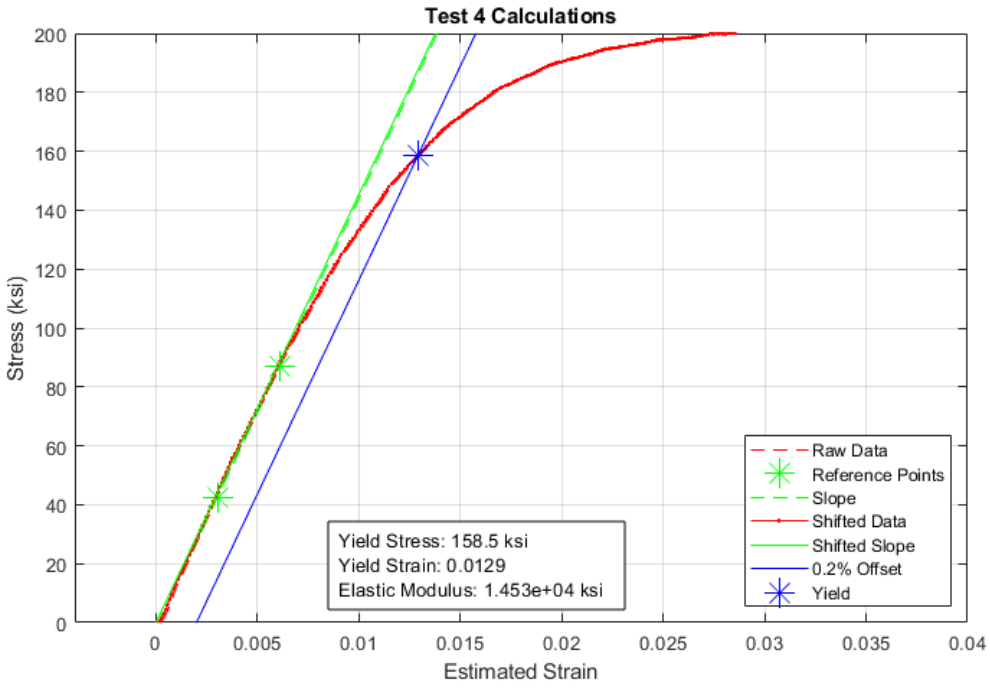

Figure 144: Test 4 Calculations for 0.0027 1/s Estimated Strain Rate

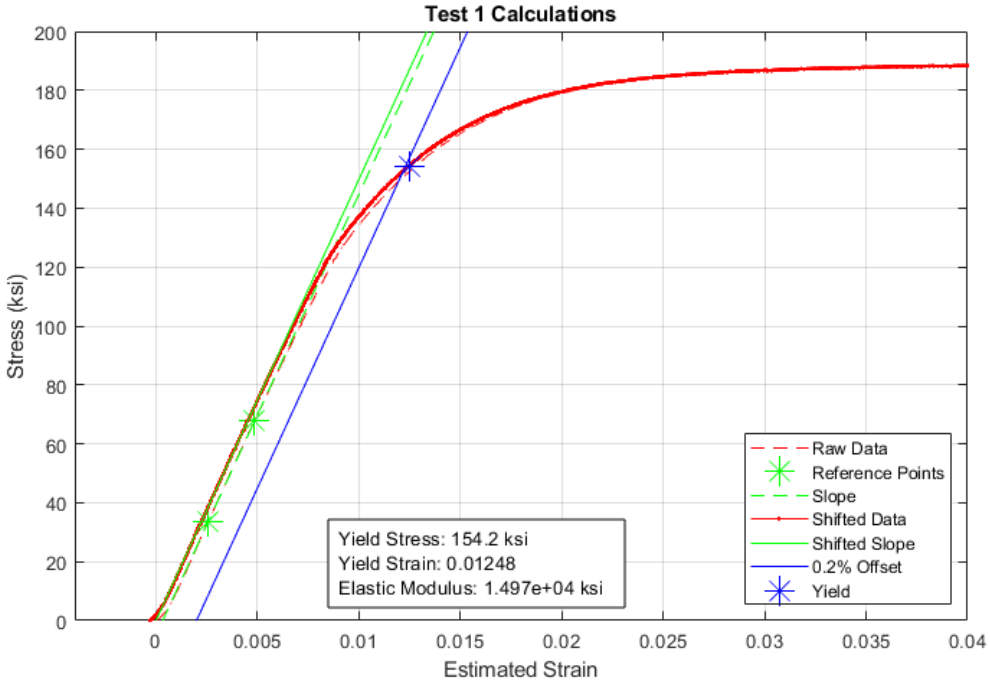

Figure 145: Test 1 Calculations for 0.00027 1/s Estimated Strain Rate

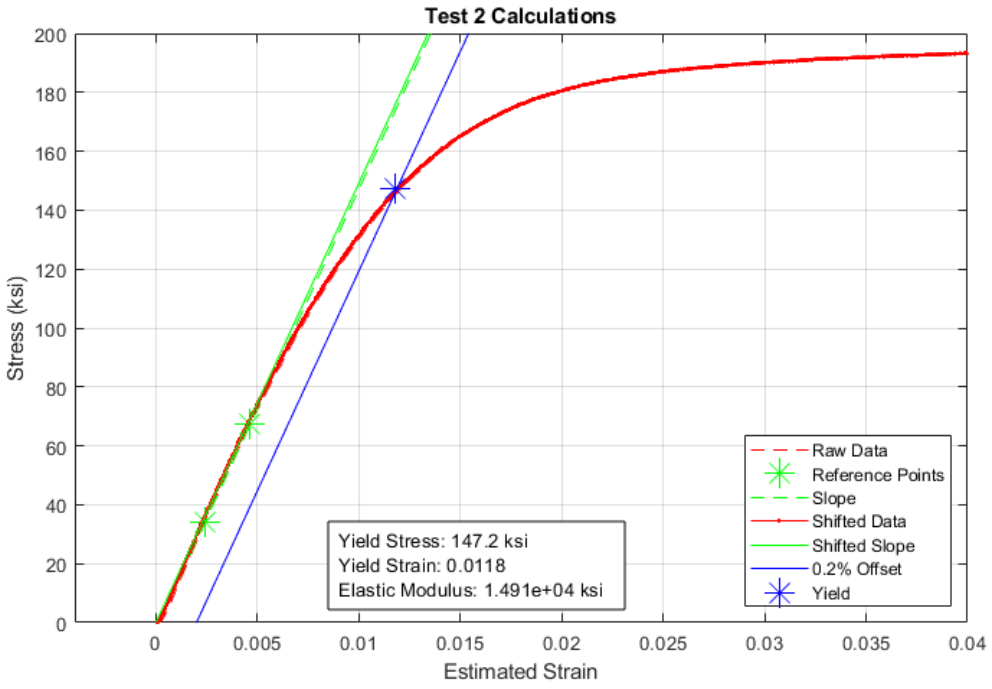

Figure 146: Test 2 Calculations for 0.00027 1/s Estimated Strain Rate

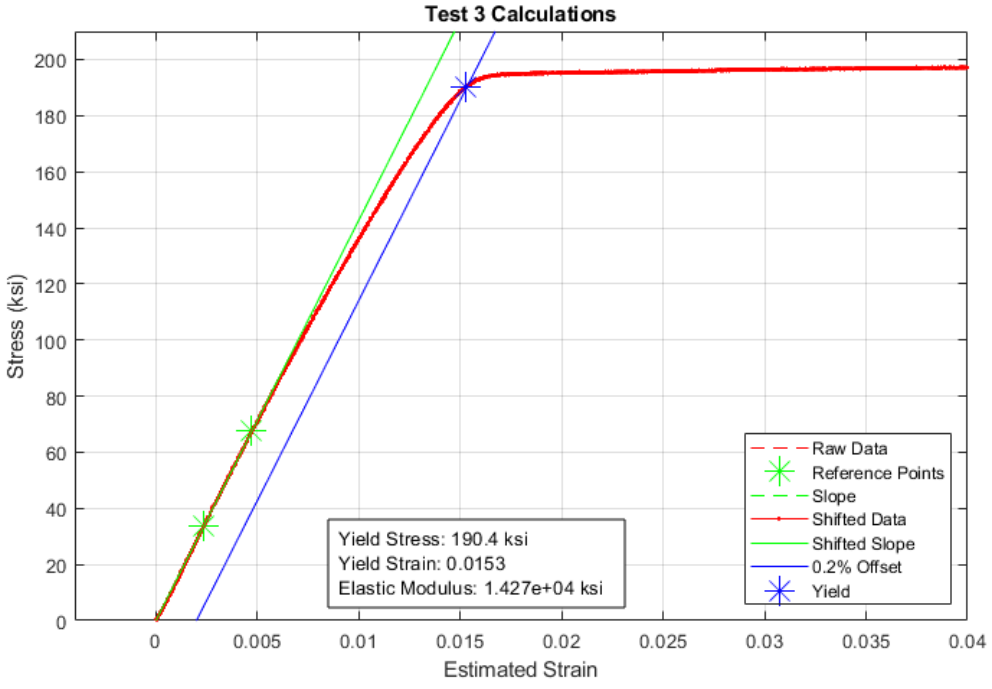

Figure 147: Test 3 Calculations for 0.00027 1/s Estimated Strain Rate

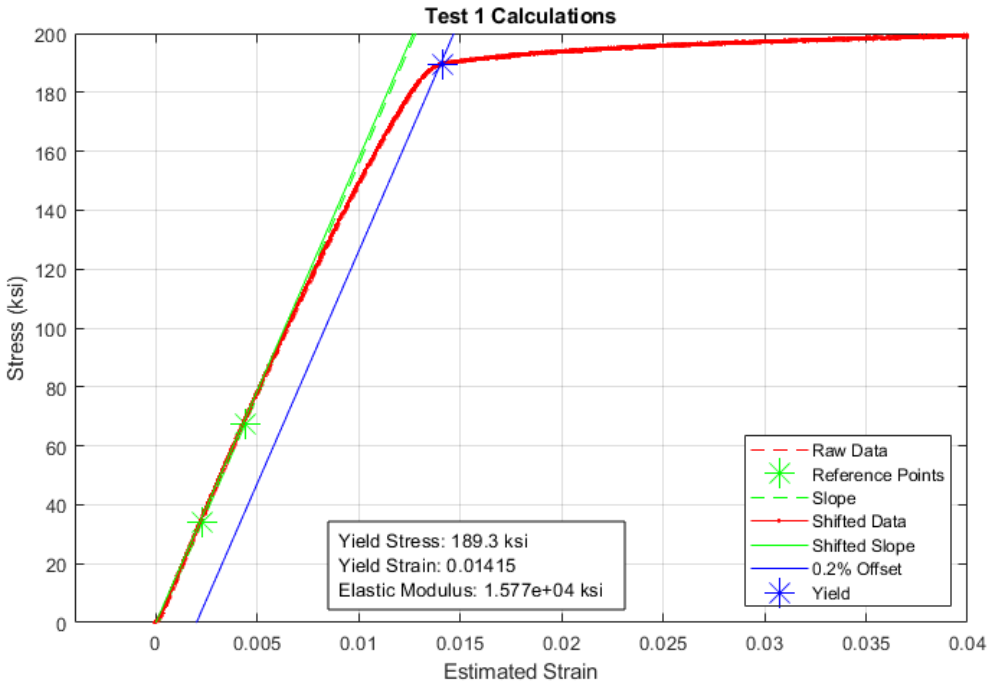

Figure 148: Test 1 Calculations for 0.000135 1/s Estimated Strain Rate

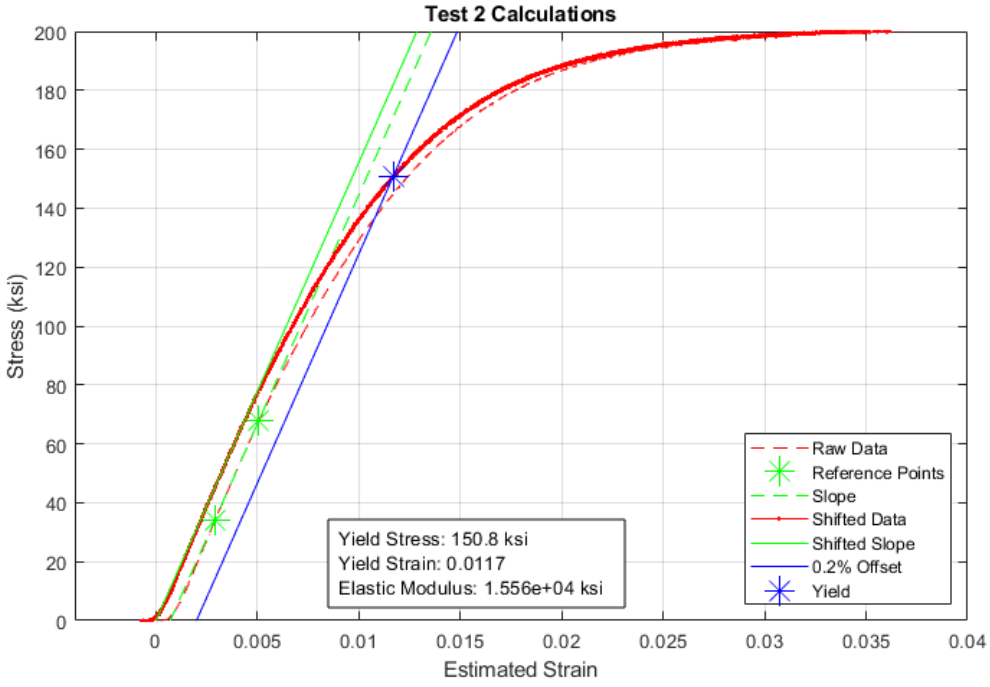

Figure 149: Test 2 Calculations for 0.000135 1/s Estimated Strain Rate

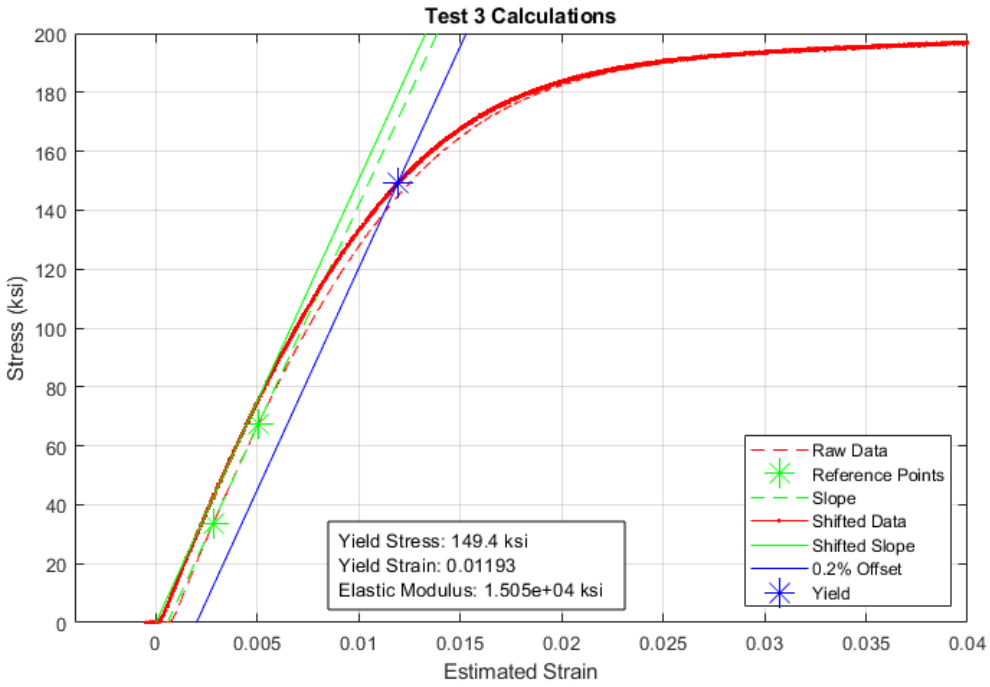

Figure 150: Test 3 Calculations for 0.000135 1/s Estimated Strain Rate

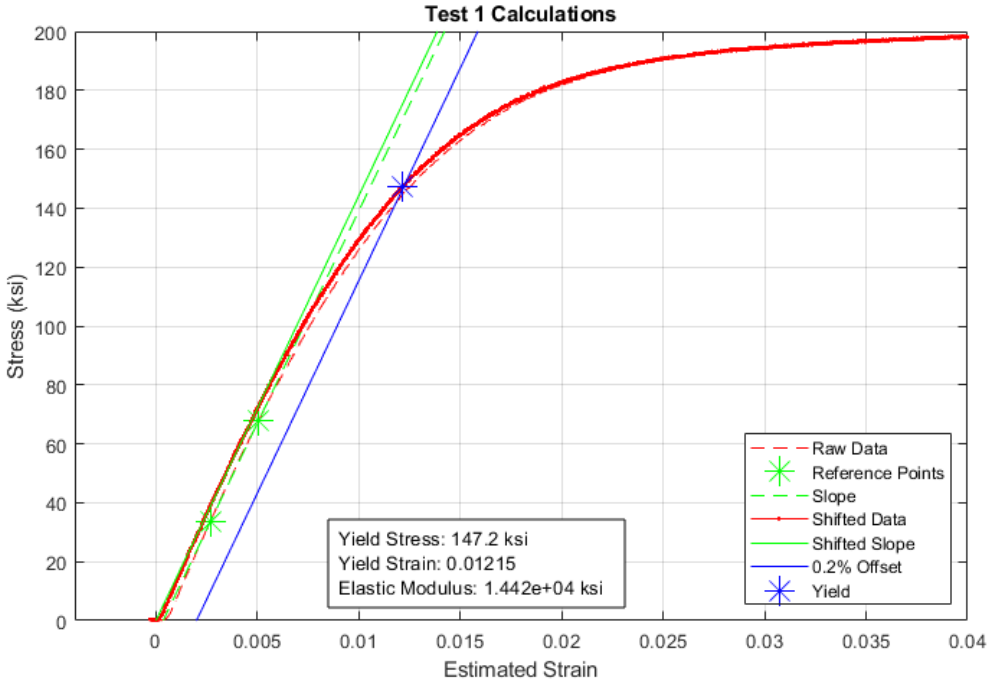

Figure 151: Test 1 Calculations for 0.000027 1/s Estimated Strain Rate

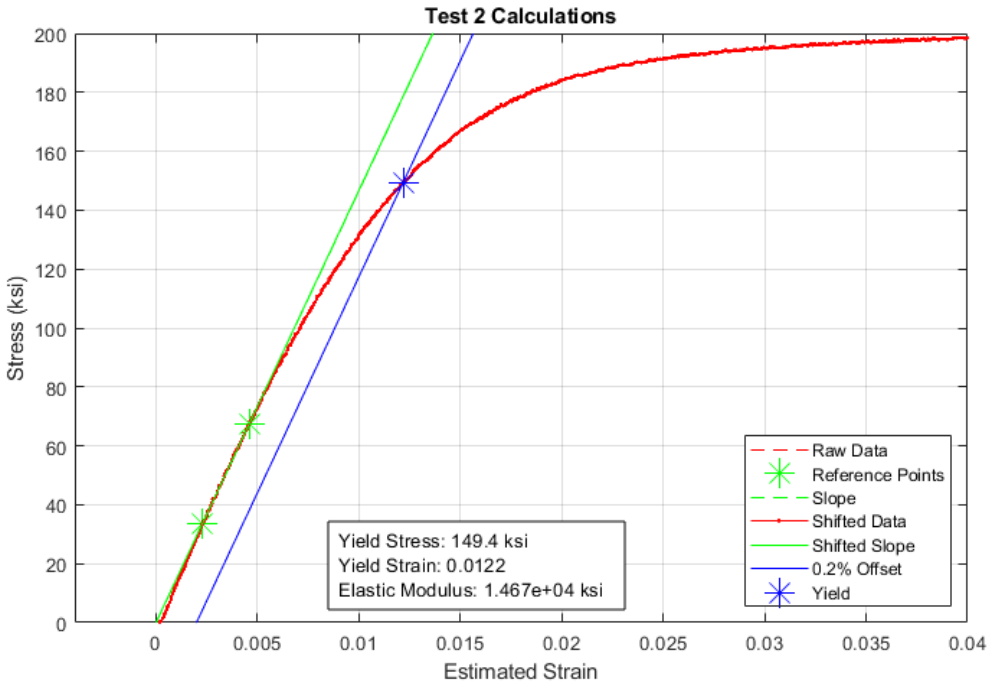

Figure 152: Test 2 Calculations for 0.000027 1/s Estimated Strain Rate

Appendix H

The following graphs show the stress versus distance curves for the other layers at 0.033s, 0.050s, and 0.067s for the Hashin model without a steel foil.

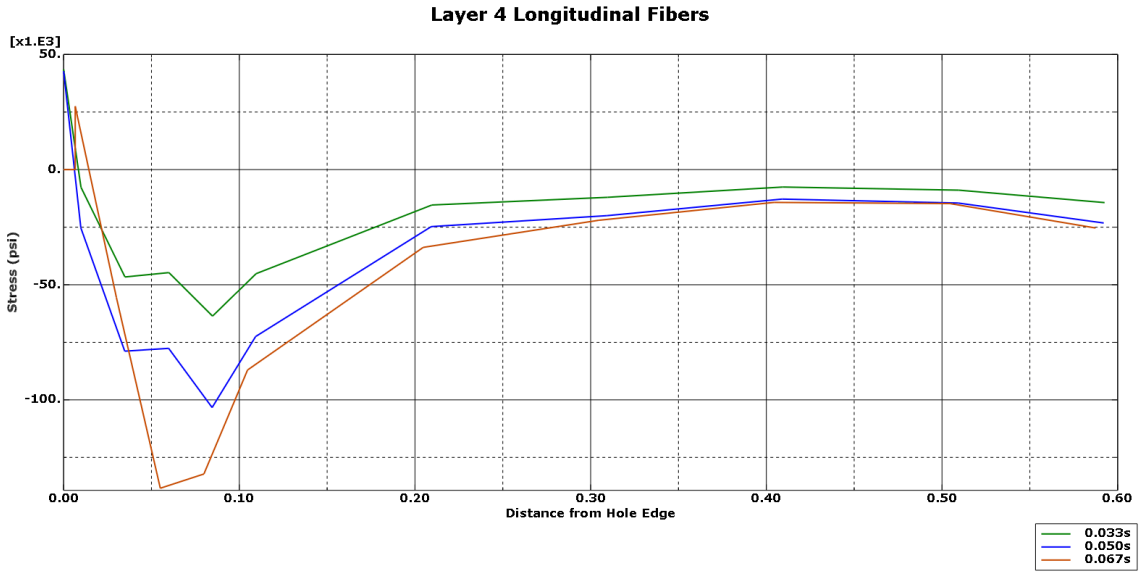

Figure 153: σ_{11} for Layer 4 0-Degree Longitudinal Fibers

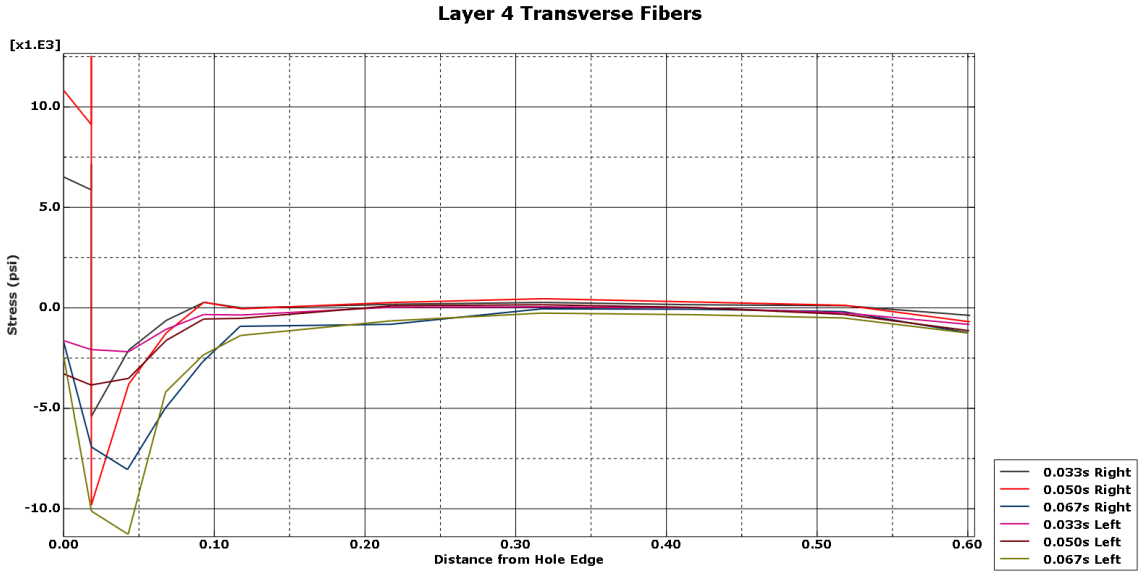

Figure 154: σ_{22} for Layer 4 0-Degree Transverse to the Fiber Direction

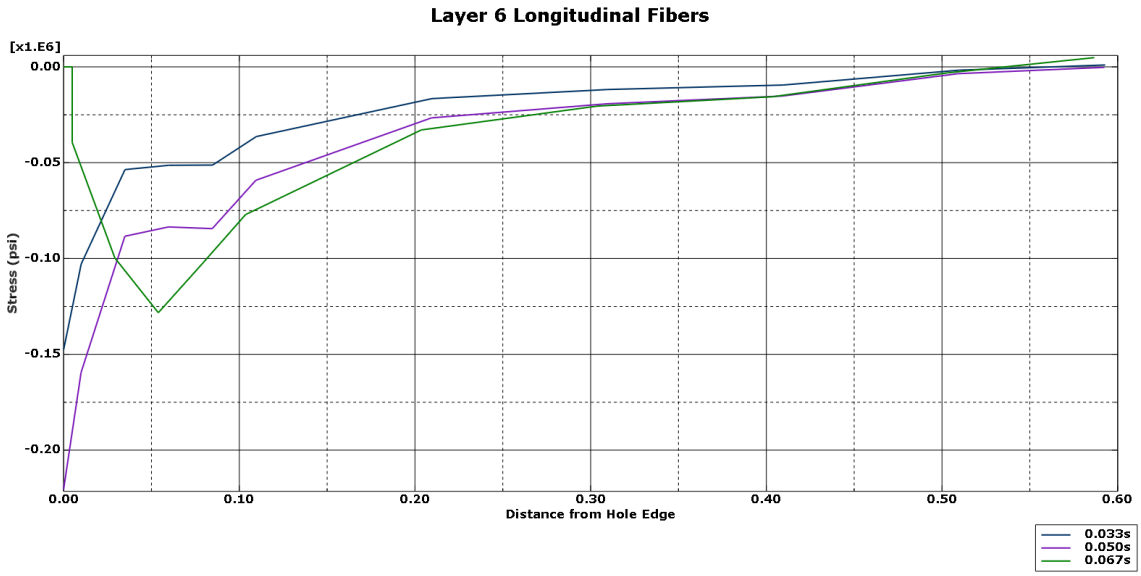

Figure 155: σ_{11} for Layer 6 0-Degree Longitudinal Fibers

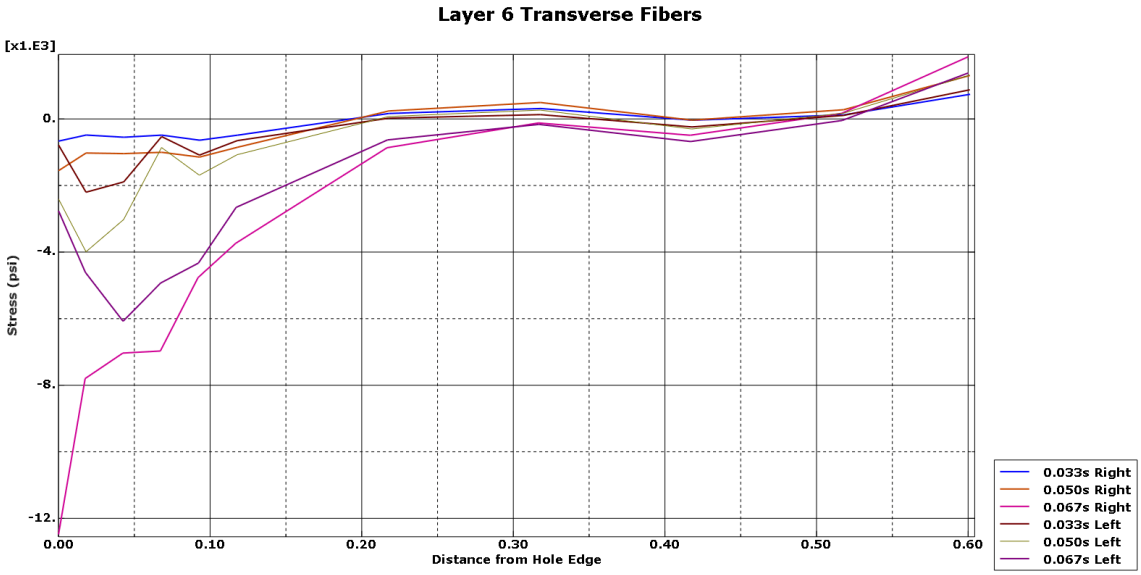

Figure 156: σ_{22} for Layer 6 0-Degree Transverse to the Fiber Direction

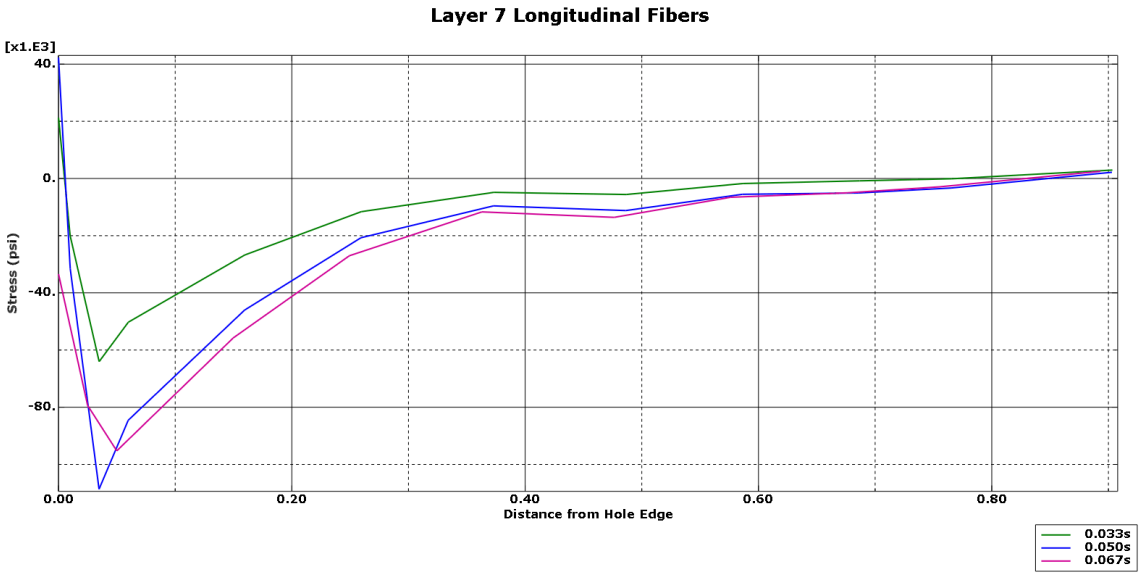

Figure 157: σ_{11} for Layer 7 -45-Degree Longitudinal Fibers

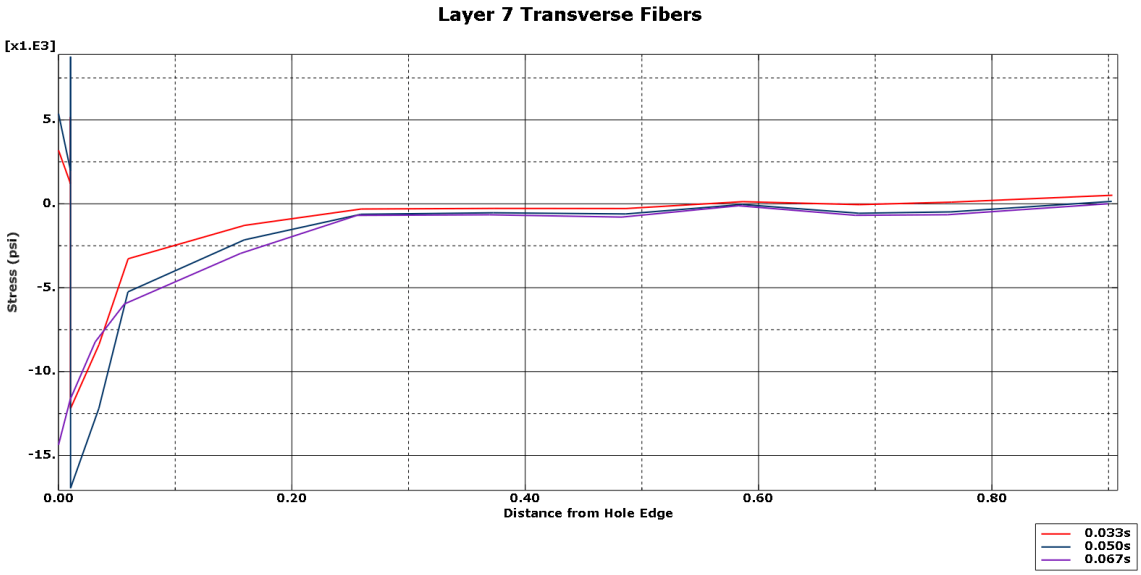

Figure 158: σ_{22} for Layer 7 -45-Degree Transverse to the Fiber Direction

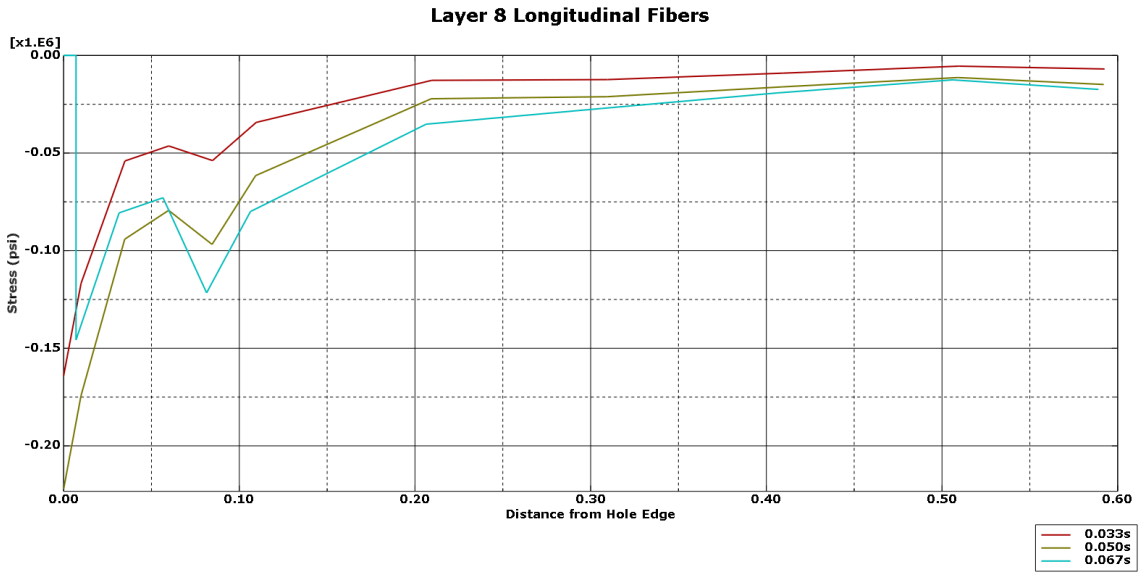

Figure 159: σ_{11} for Layer 8 0-Degree Longitudinal Fibers

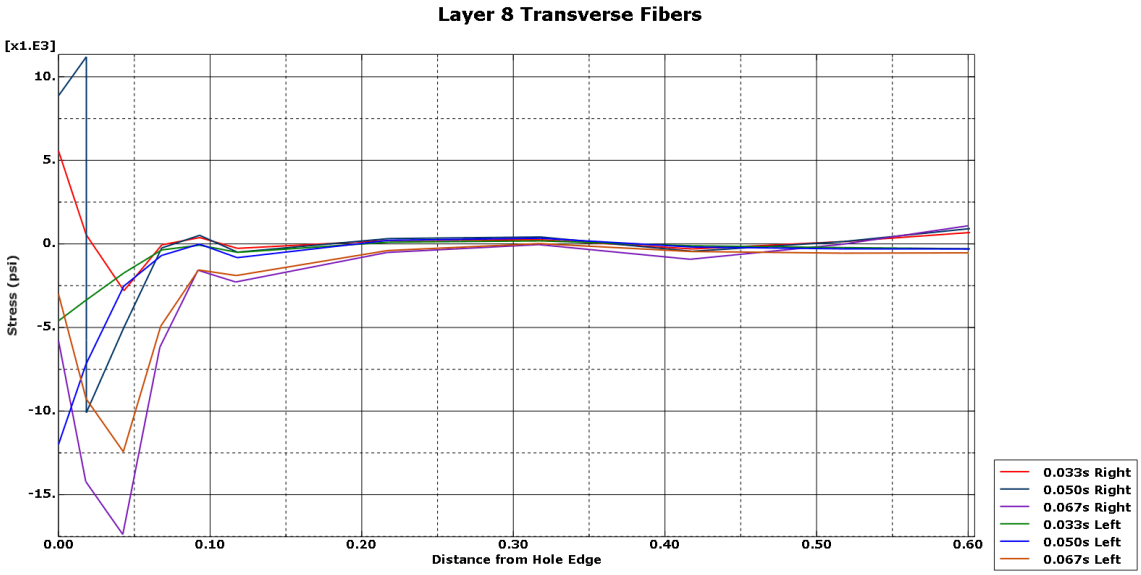

Figure 160: σ_{22} for Layer 8 0-Degree Transverse to the Fiber Direction

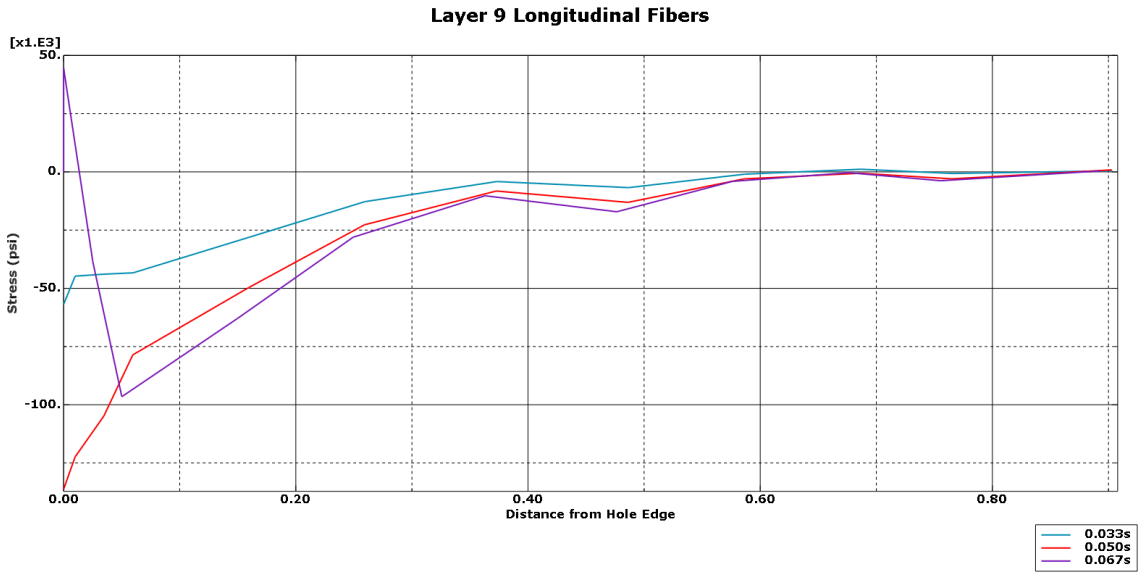

Figure 161: σ_{11} for Layer 9 45-Degree Longitudinal Fibers

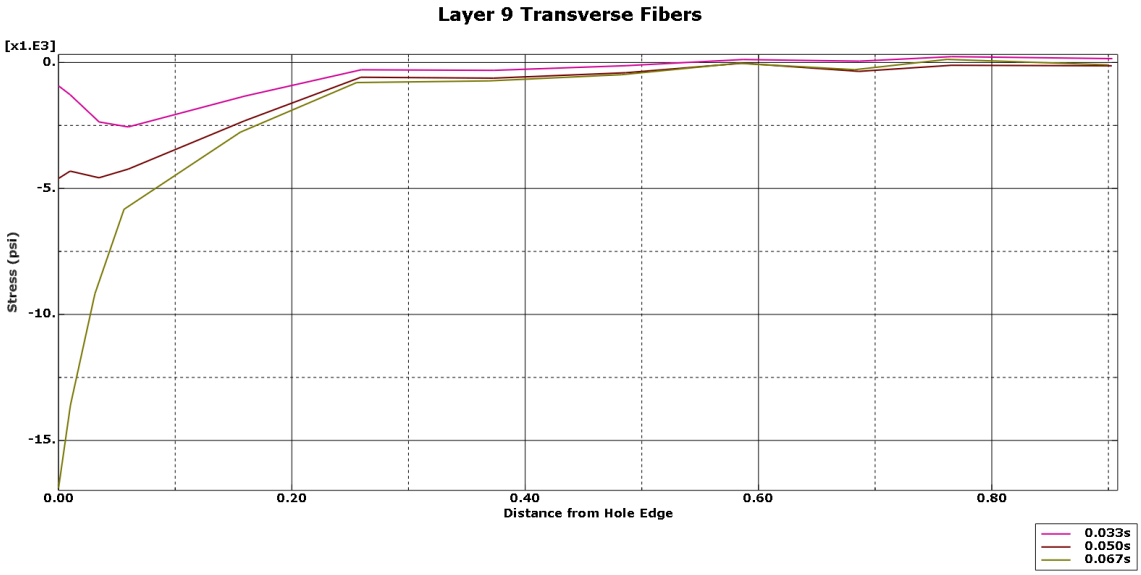

Figure 162: σ_{22} for Layer 9 45-Degree Transverse to the Fiber Direction

The following graphs show the stress versus distance curves for the other layers at 0.033s, 0.050s, and 0.067s for the Tsai-Wu model without a steel foil.

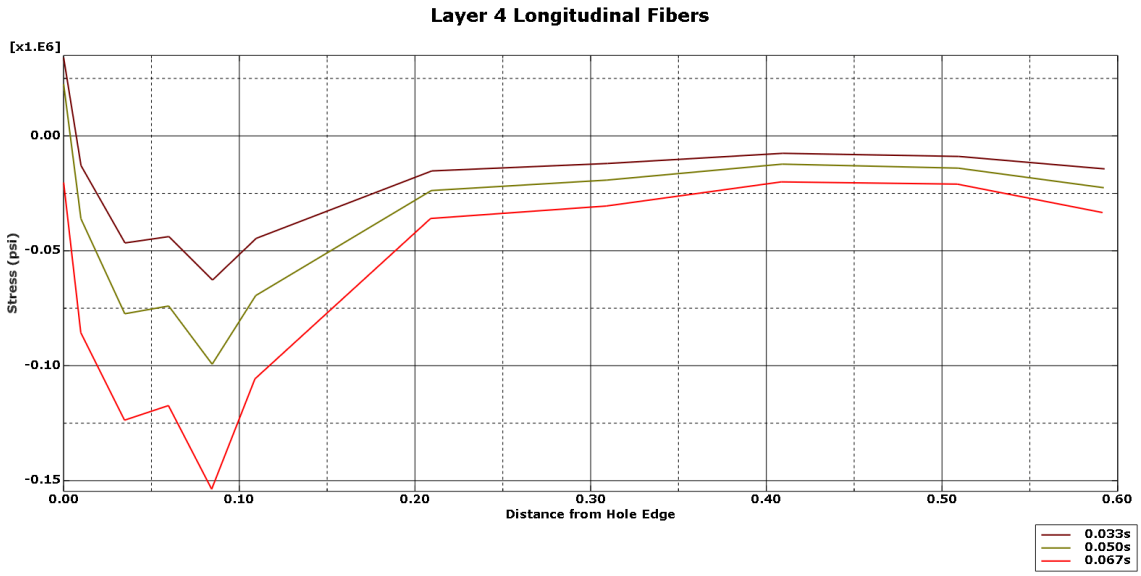

Figure 163: σ_{11} for Layer 4 0-Degree Longitudinal Fibers

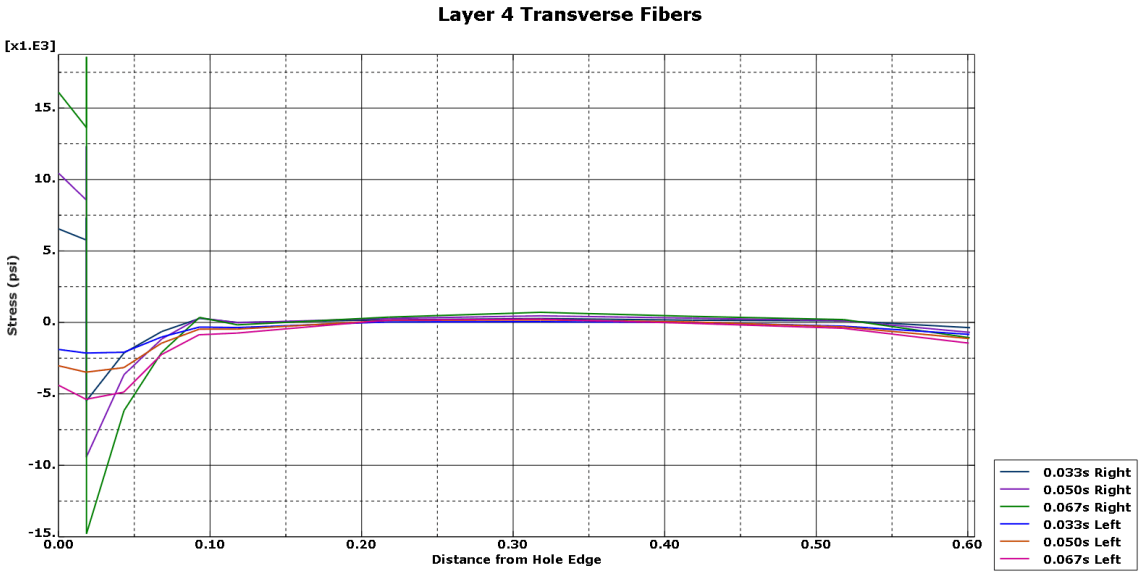

Figure 164: σ_{22} for Layer 4 0-Degree Transverse to the Fiber Direction

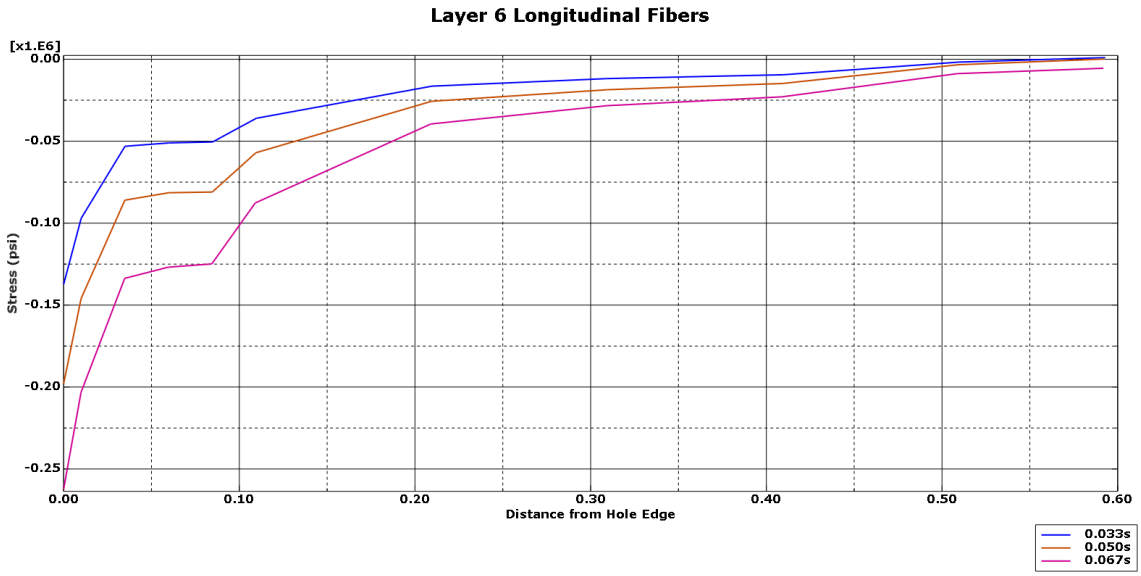

Figure 165: σ_{11} for Layer 6 0-Degree Longitudinal Fibers

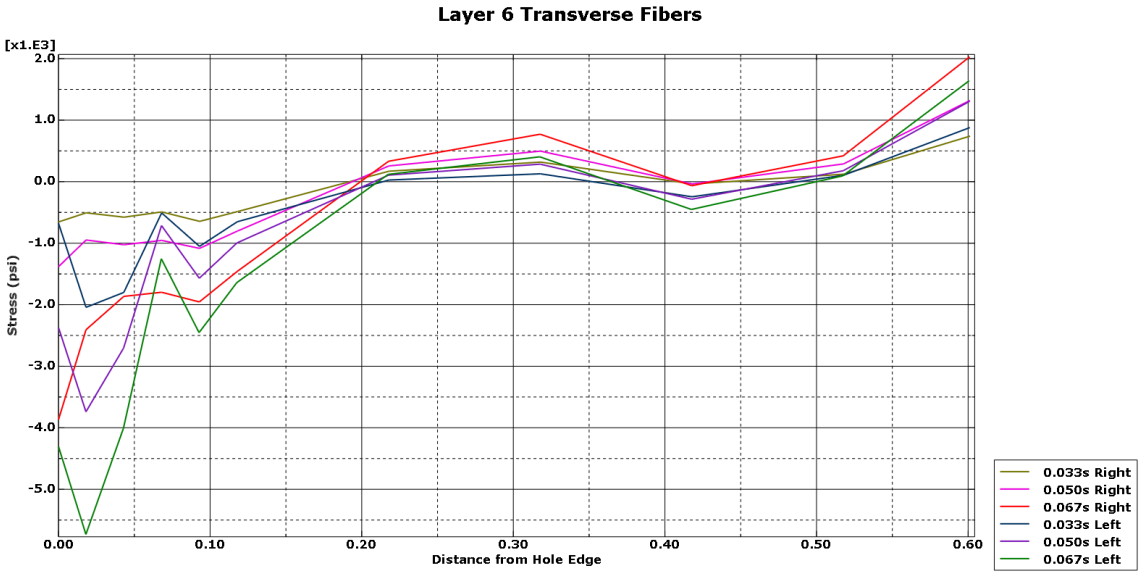

Figure 166: σ_{22} for Layer 6 0-Degree Transverse to the Fiber Direction

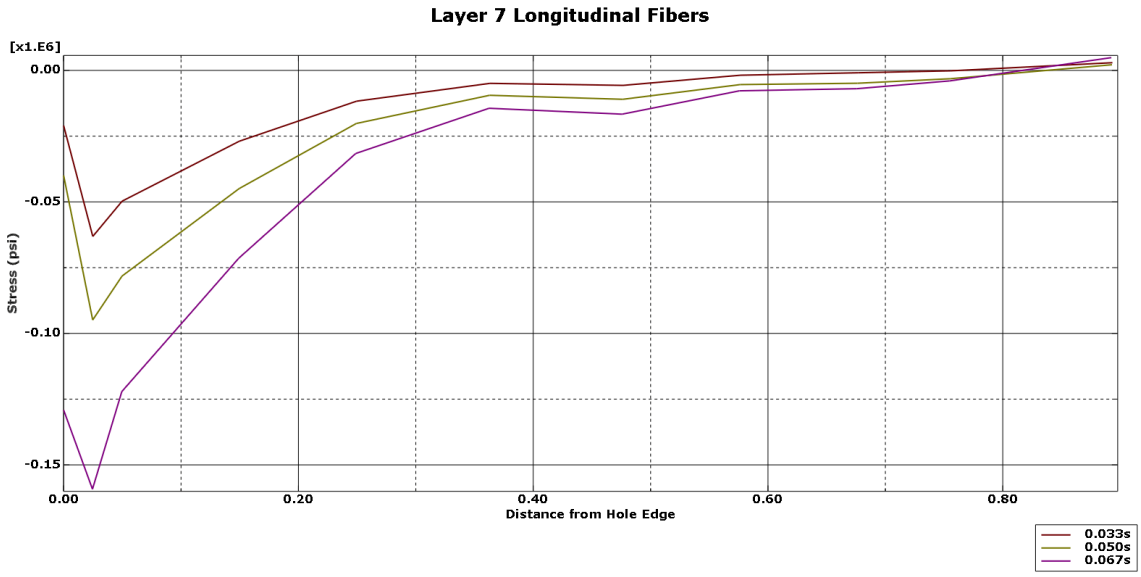

Figure 167: σ_{11} for Layer 7 -45-Degree Longitudinal Fibers

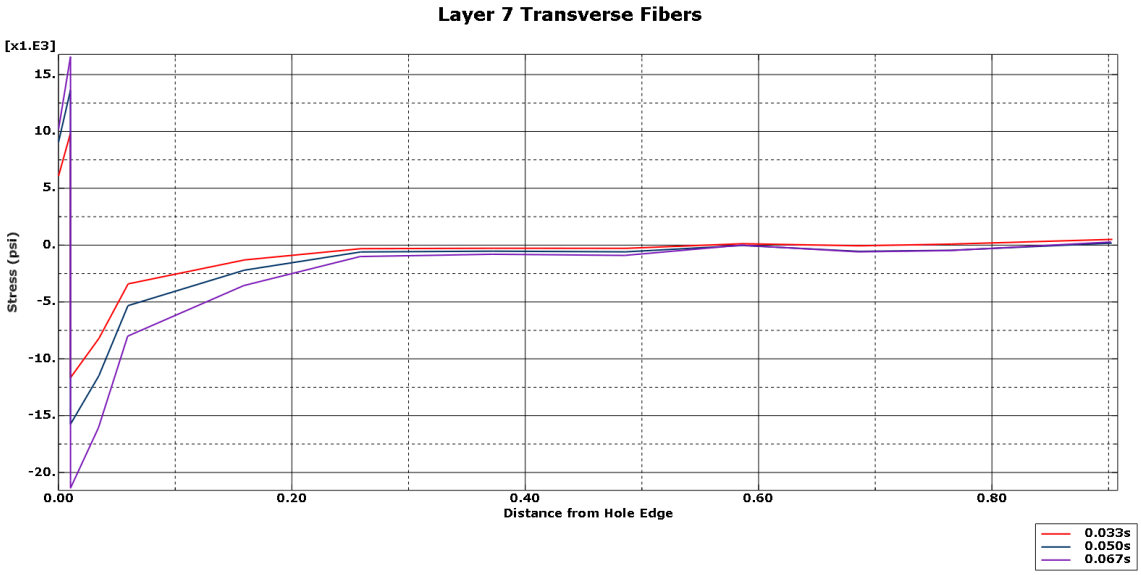

Figure 168: σ_{22} for Layer 7 -45-Degree Transverse to the Fiber Direction

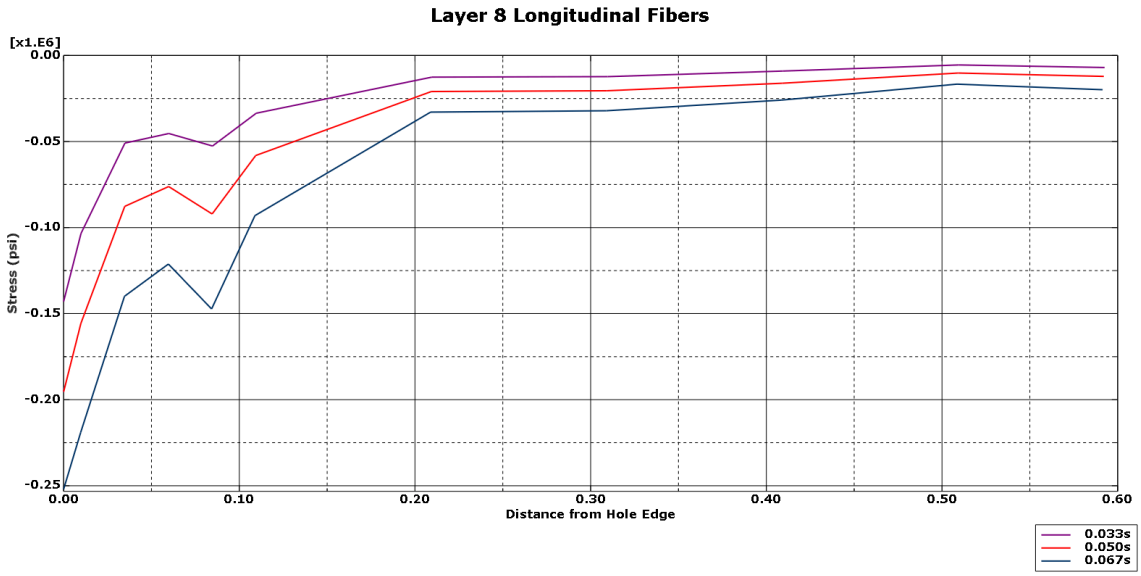

Figure 169: σ_{11} for Layer 8 0-Degree Longitudinal Fibers

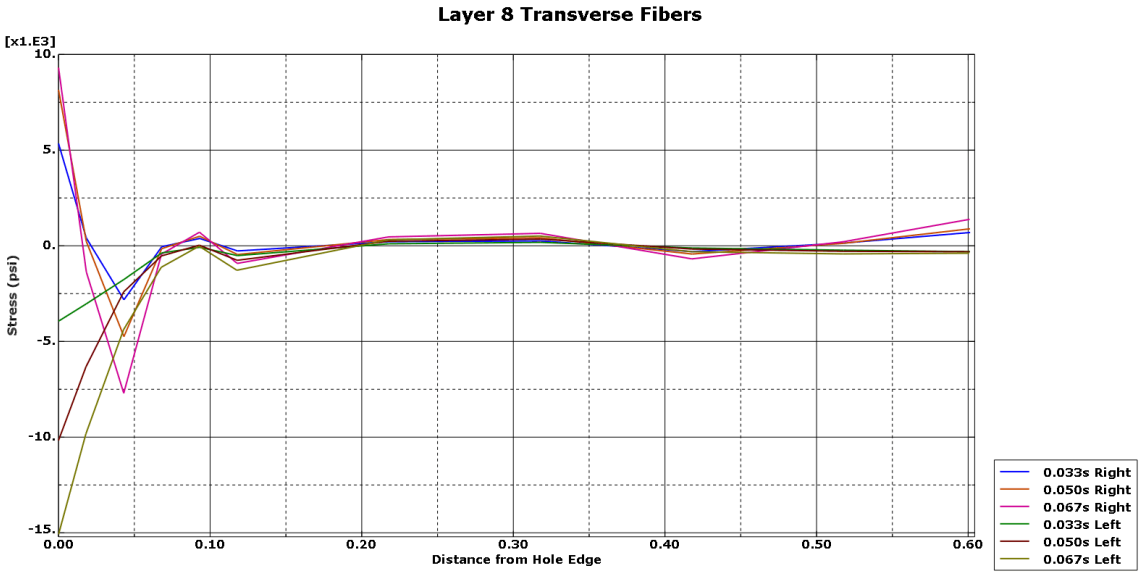

Figure 170: σ_{22} for Layer 8 0-Degree Transverse to the Fiber Direction

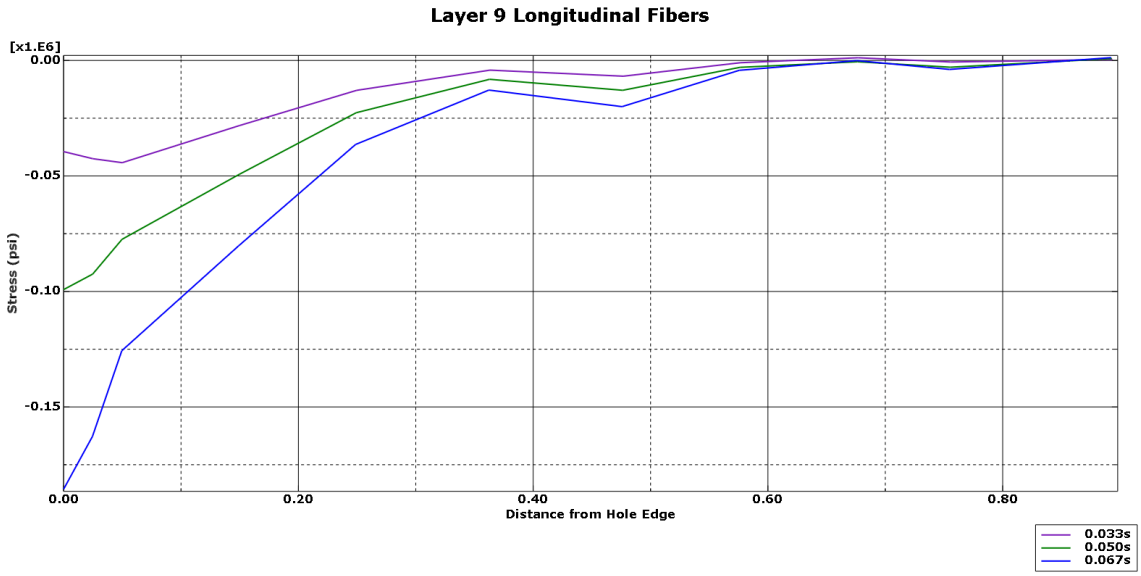

Figure 171: σ_{11} for Layer 9 45-Degree Longitudinal Fibers

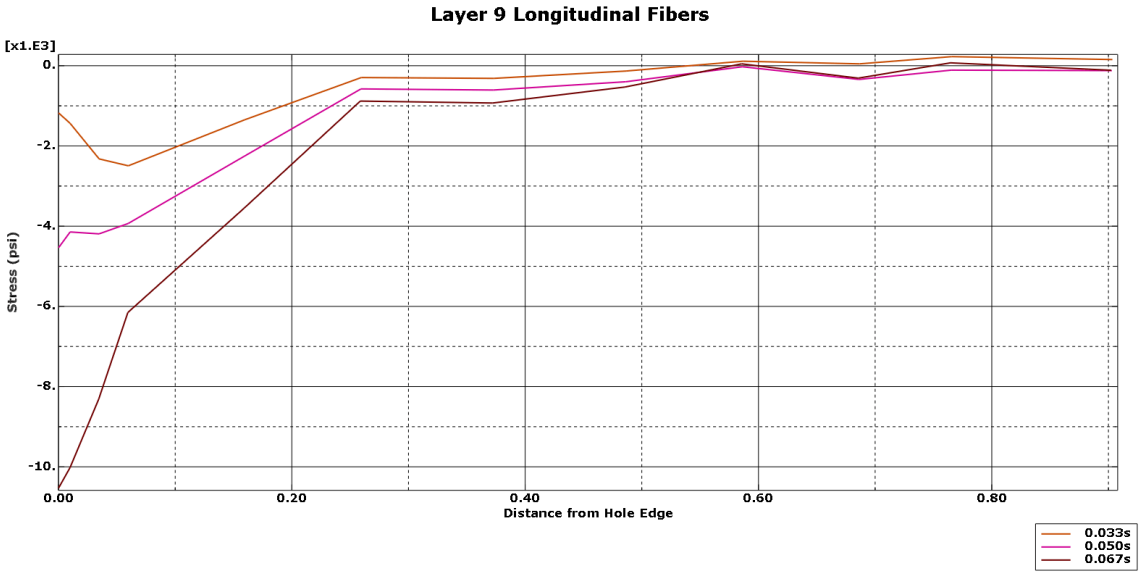

Figure 172: σ_{22} for Layer 9 45-Degree Transverse to the Fiber Direction

The following graphs show the stress versus distance curves for the other layers at 0.033s, 0.050s, and 0.067s for the Hashin model with a steel foil.

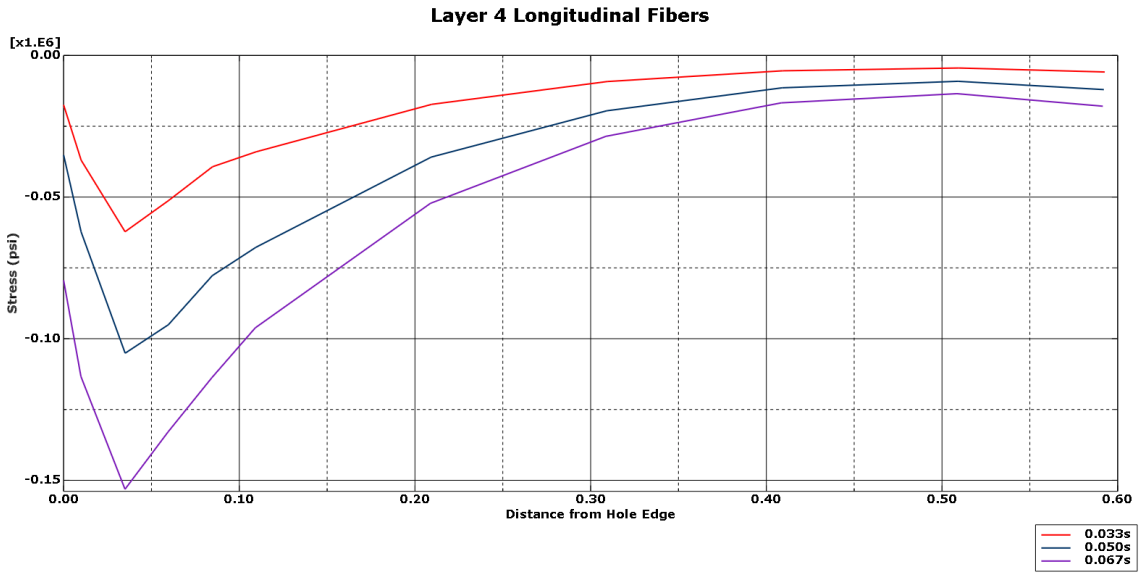

Figure 173: σ_{11} for Layer 4 0-Degree Longitudinal Fibers

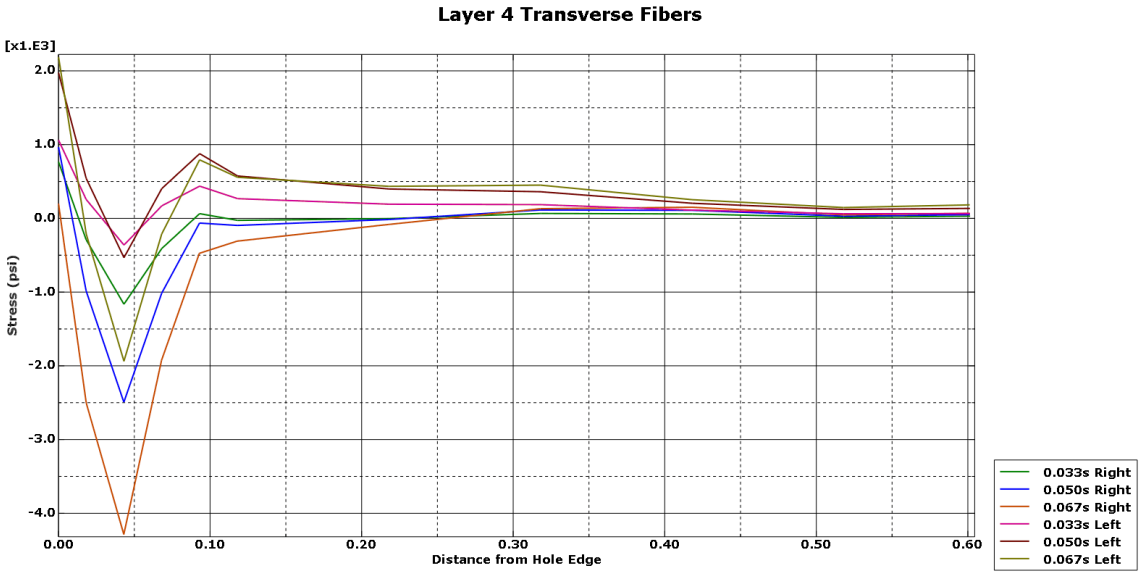

Figure 174: σ_{22} for Layer 4 0-Degree Transverse to the Fiber Direction

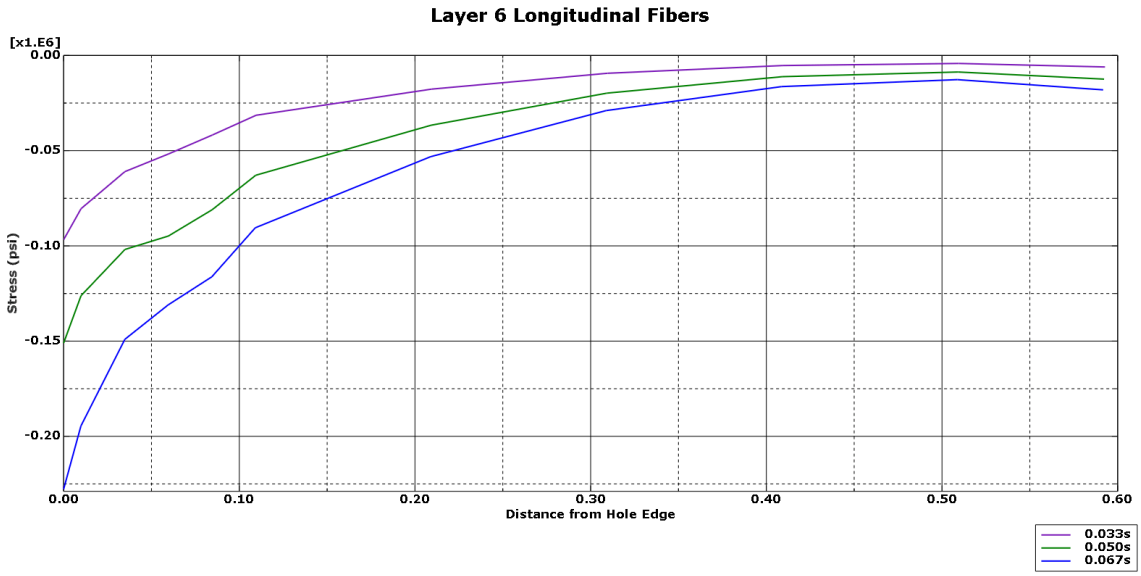

Figure 175: σ_{11} for Layer 6 0-Degree Longitudinal Fibers

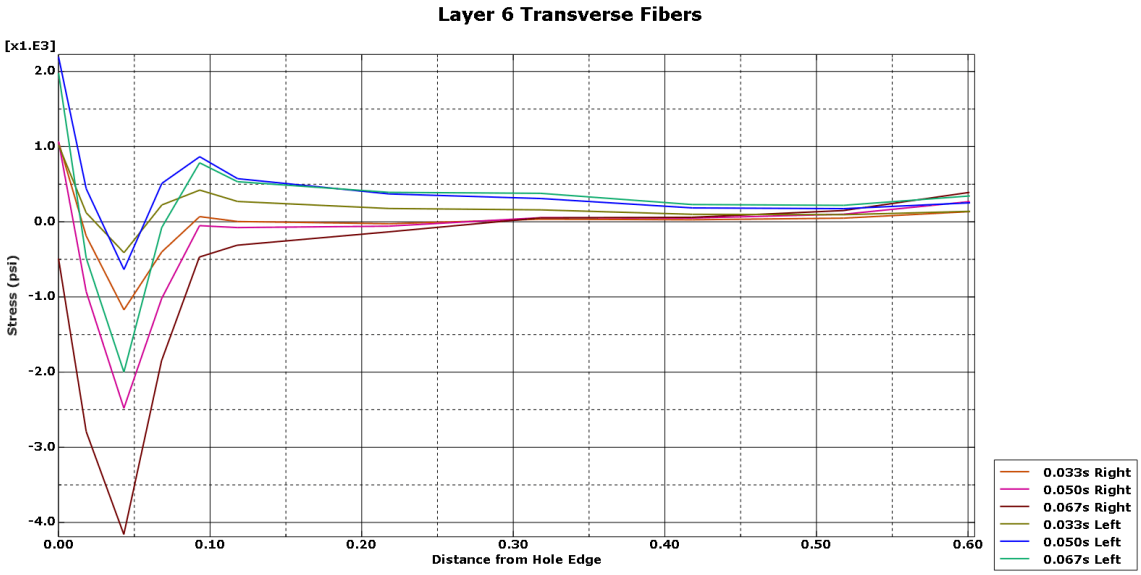

Figure 176:

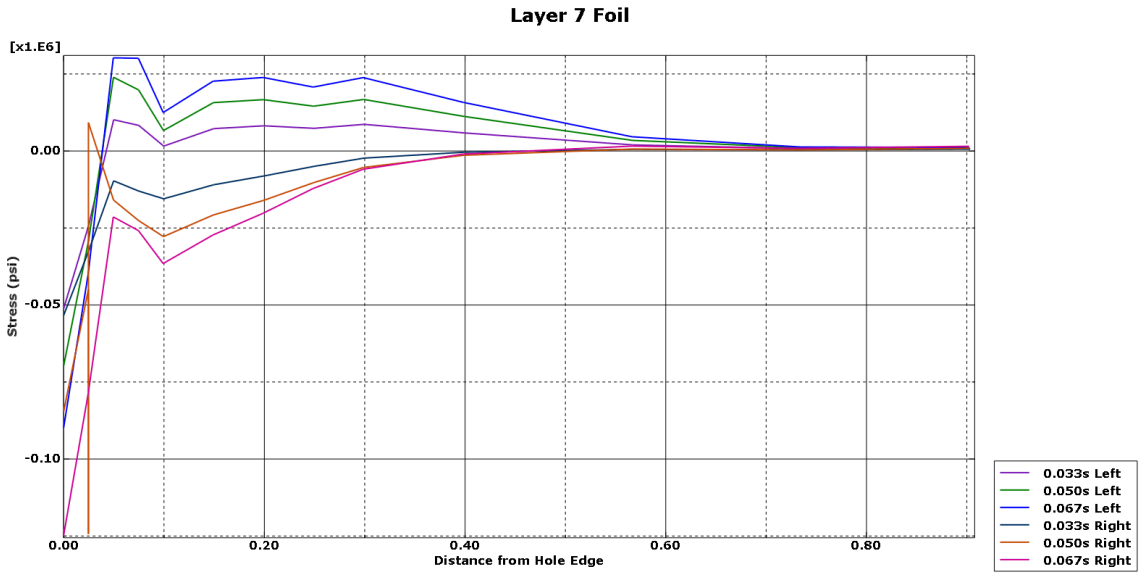

Figure 177: σ_{11} and σ_{22} for Layer 7 Foil

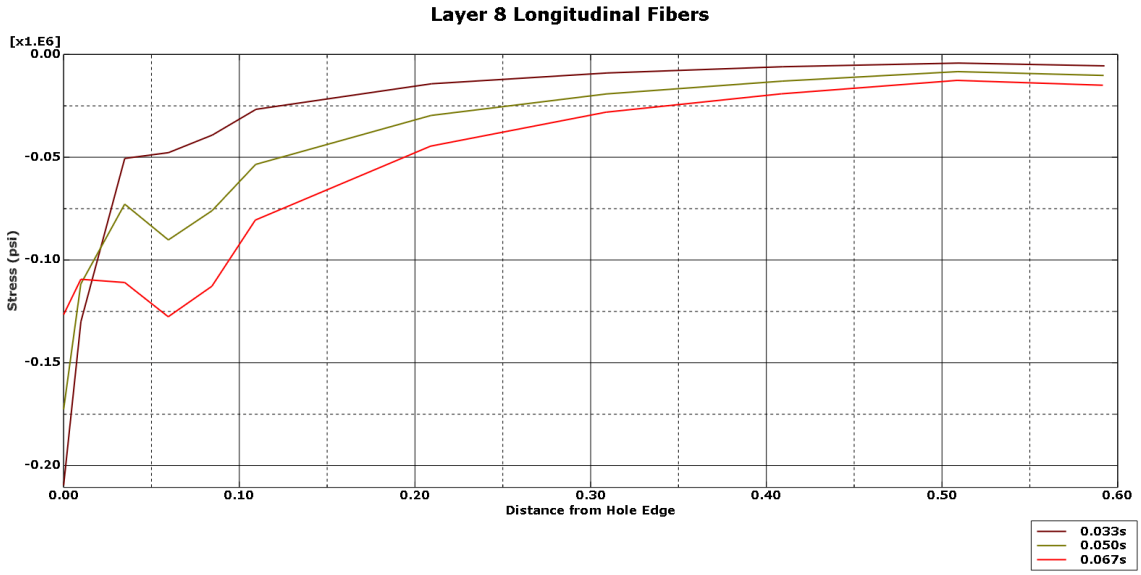

Figure 178: σ_{11} for Layer 8 0-Degree Longitudinal Fibers

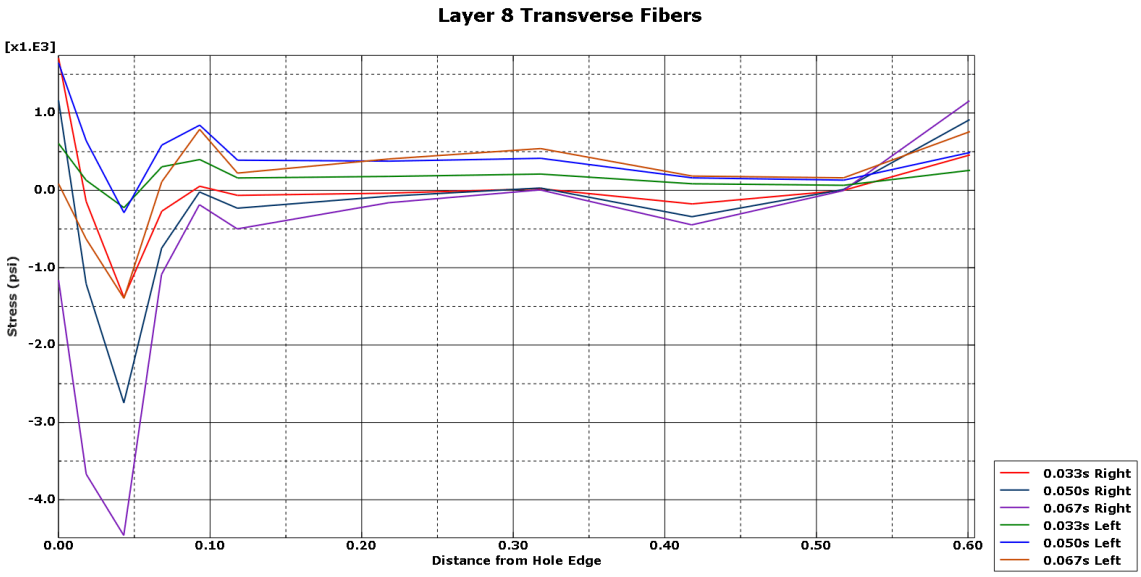

Figure 179: σ_{22} for Layer 8 0-Degree Transverse to the Fiber Direction

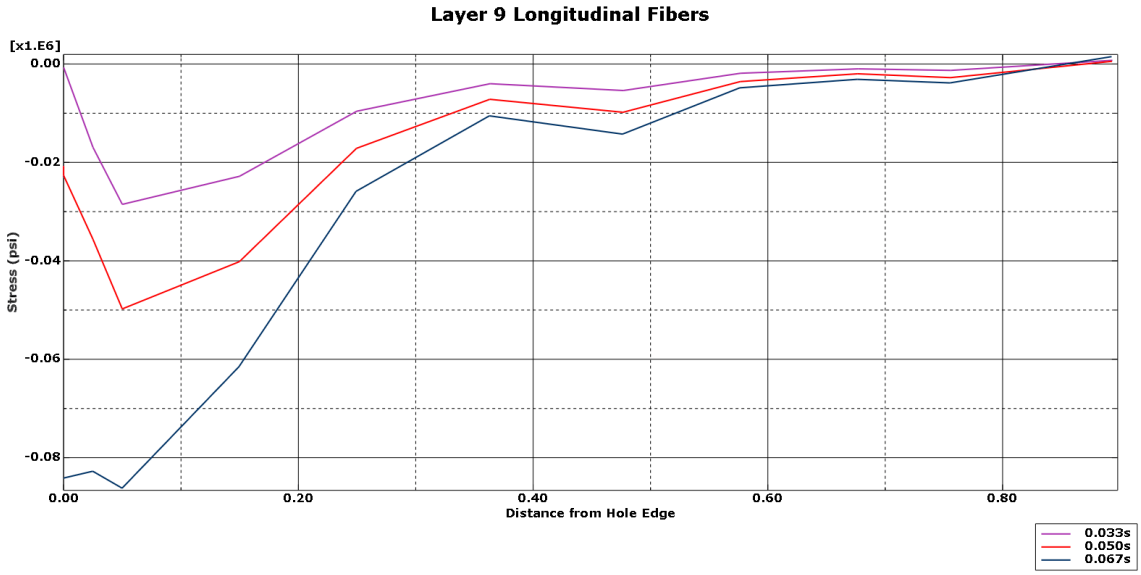

Figure 180: σ_{11} for Layer 9 45-Degree Longitudinal Fibers

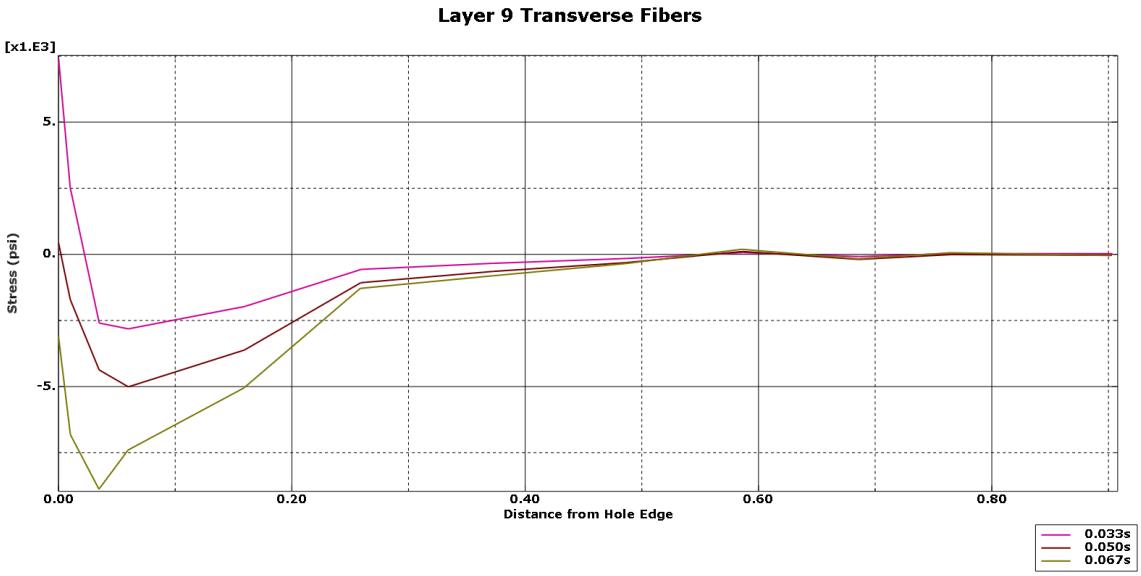

Figure 181: σ_{22} for Layer 9 45-Degree Transverse to the Fiber Direction

The following graphs show the stress versus distance curves for the other layers at 0.033s, 0.050s, and 0.067s for the Tsai-Wu model with a steel foil.

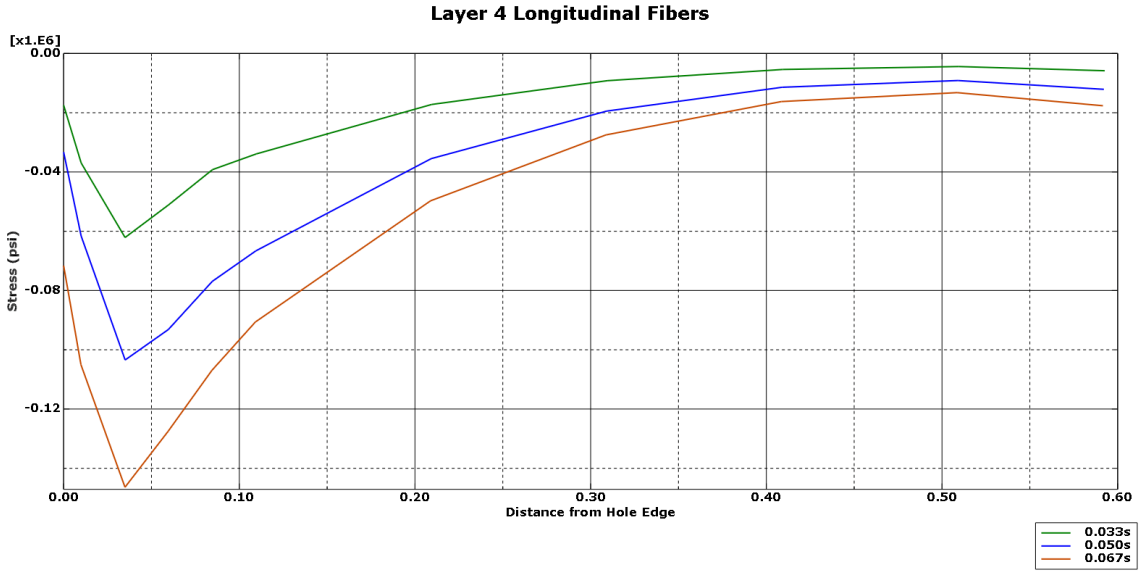

Figure 182: σ_{11} for Layer 4 0-Degree Longitudinal Fibers

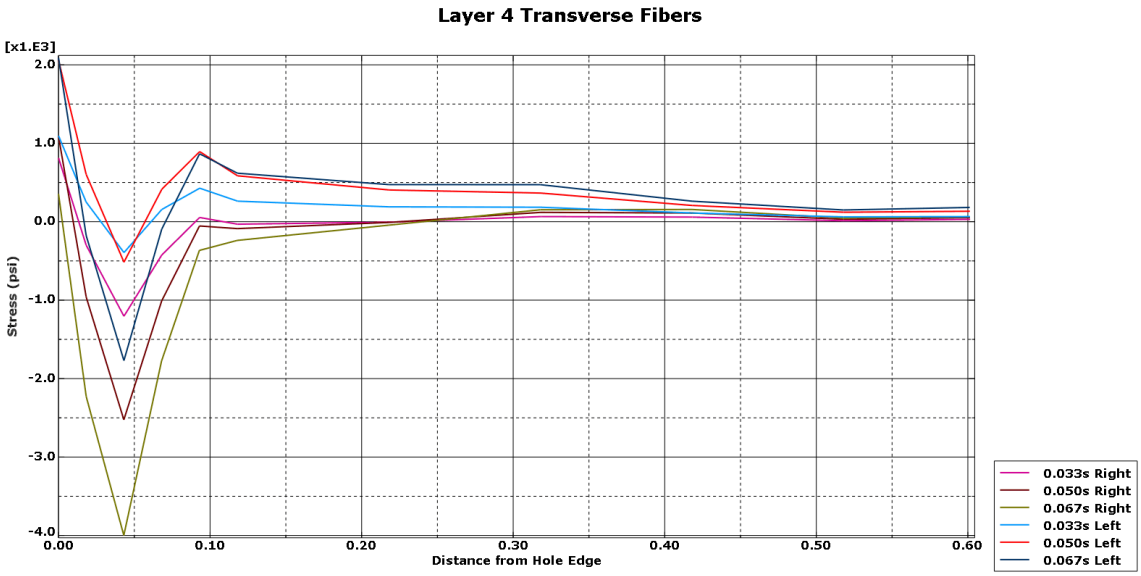

Figure 183: σ_{22} for Layer 4 0-Degree Transverse to the Fiber Direction

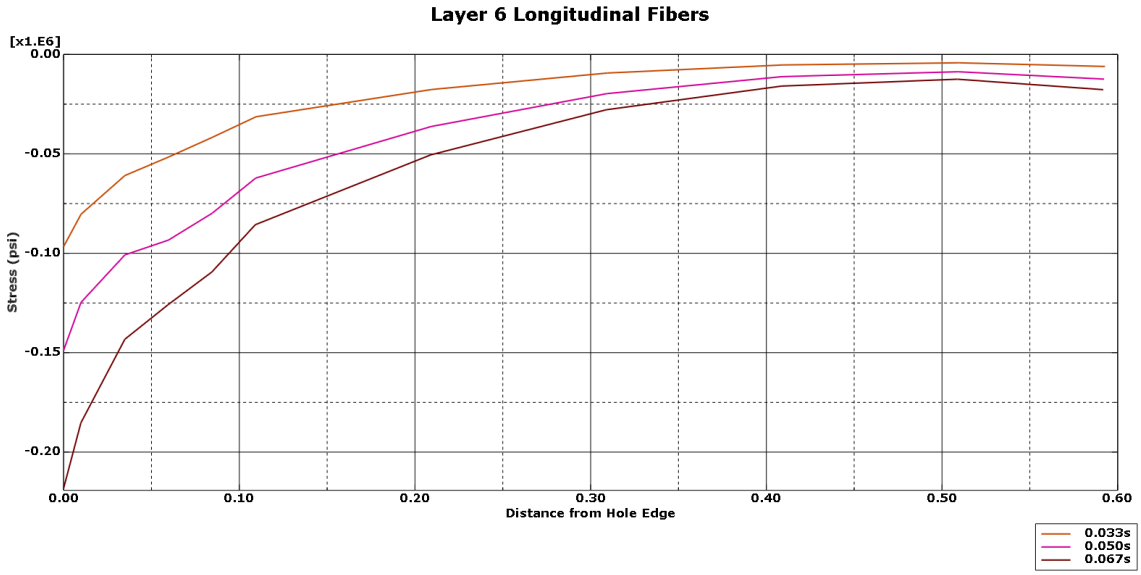

Figure 184: σ_{11} for Layer 6 0-Degree Longitudinal Fibers

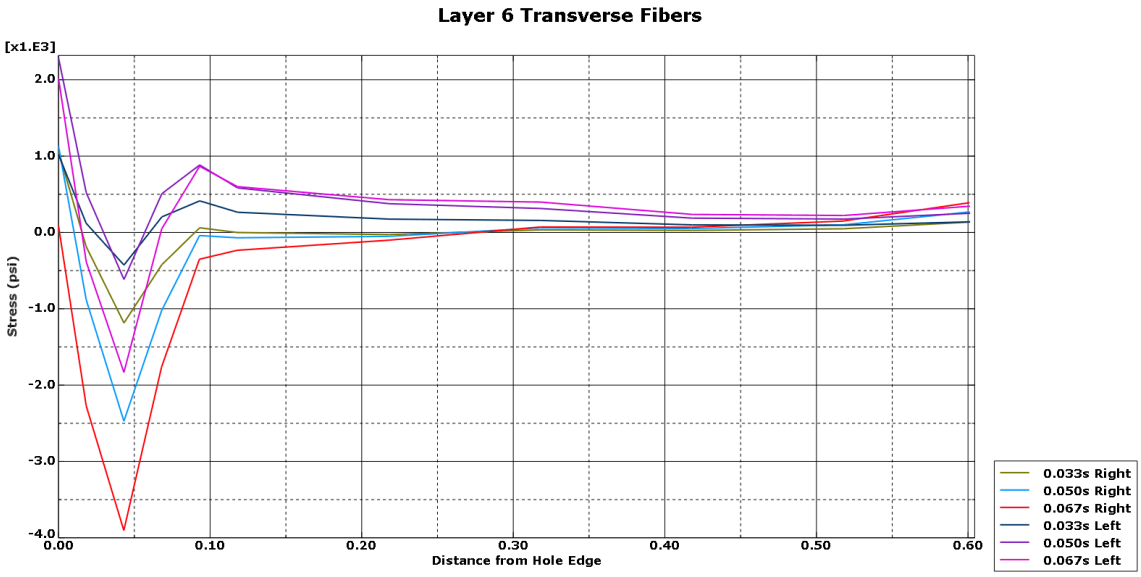

Figure 185: σ_{22} for Layer 6 0-Degree Transverse to the Fiber Direction

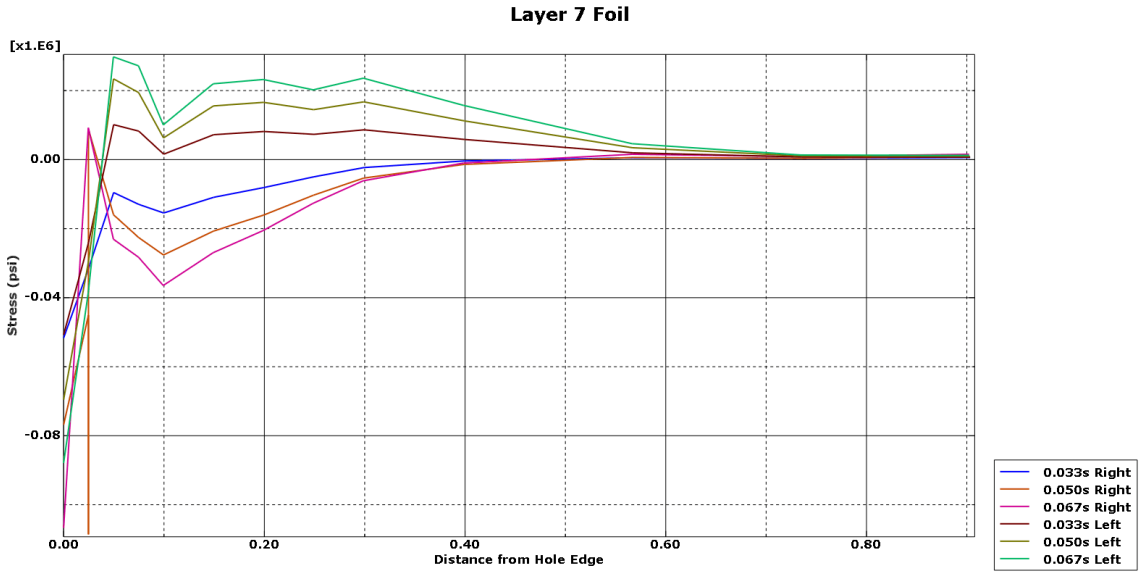

Figure 186: σ_{11} and σ_{22} for Layer 7 Foil

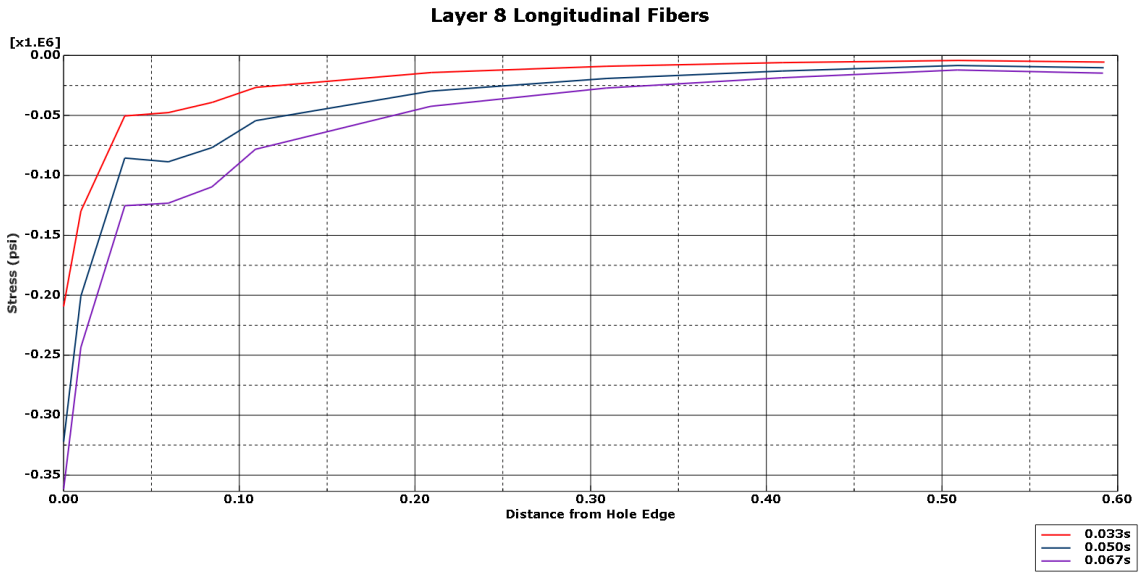

Figure 187: σ_{11} for Layer 8 0-Degree Longitudinal Fibers

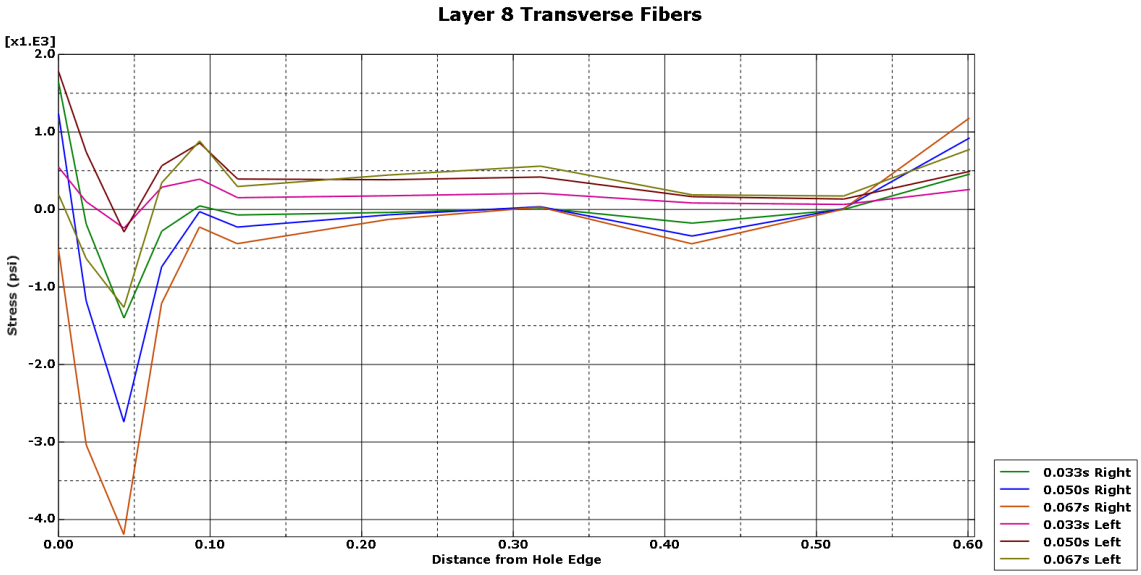

Figure 188: σ_{22} for Layer 8 0-Degree Transverse to the Fiber Direction

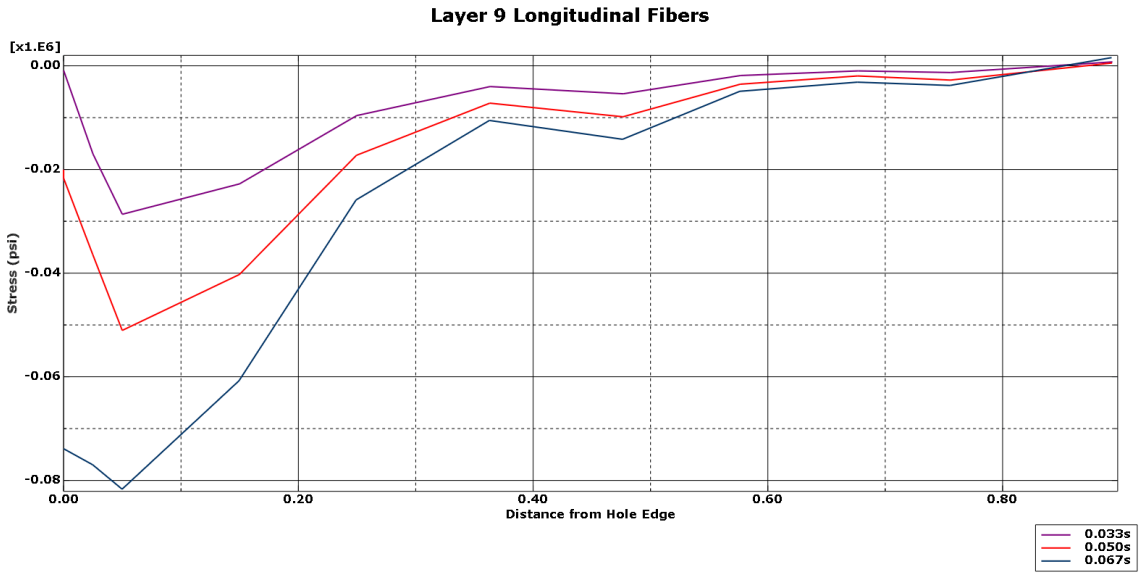

Figure 189: σ_{11} for Layer 9 45-Degree Longitudinal Fibers

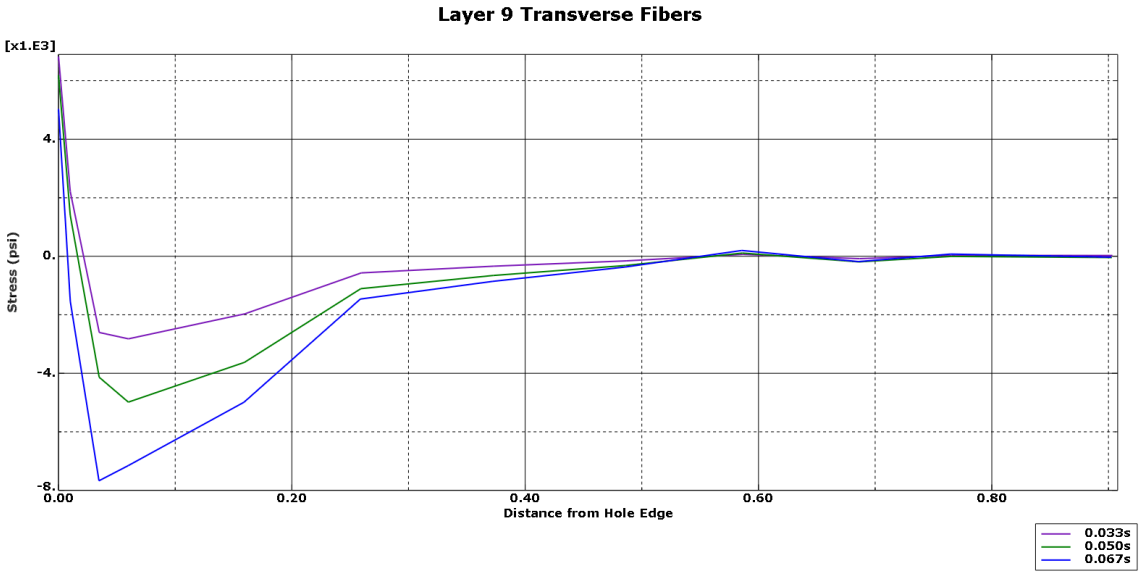

Figure 190: σ_{22} for Layer 9 45-Degree Transverse to the Fiber Direction

Bibliography

[1] American Chemical Society National Historic Chemical Landmarks, “High Performance Carbon Fibers,” https://www.acs.org/content/acs/en/education/whatischemistry/landmarks/carbonfibers.html, 2003

[2] Bumpus, S. R. J., “Experimental Setup and Testing of Fiber Reinforced Composite Structures,” https://dspace.library.uvic.ca/bitstream/handle/1828/585/bumpus_2005.pdf?sequence=1, 2002.

[3] Hessenbruch, A., “Composites Overview,” https://authors.library.caltech.edu/5456/1/hrst.mit.edu/hrs/materials/public/composites/Composites_Overview.htm#4th_generation, 2002.

[4] School of Materials Science and Engineering, “Metal Matrix Composites,” http://www.materials.unsw.edu.au/tutorials/online-tutorials/7-metal-matrix-composites, 2013.

[5] T. W. Clyne, P. W., *An Introduction to Metal Matrix Composites.* 1993.

[6] I. A. Ibrahim, F. A. M. & E. J. L., “Particulate reinforced metal matrix composites,” https://link.springer.com/article/10.1007/BF00544448, 1991.

[7] Encyclopedia of Britannica, “Metal-matrix and ceramic-matrix composites,” https://britannica.com/technology/materials-science/Metal-matrix-and-ceramic-matrix-composites, 2020.

[8] Evans, A. G. & D. B. M., “Failure Mechanisms in Ceramic-Fiber/Ceramic-Matrix Composites,” https://ceramics.onlinelibrary.wiley.com/doi/abs/10.1111/j.1151-2916.1985.tb15313.x, 1985

[9] Glen Mandigo, D. F., “A Primer on CMCs,” http://compositesmanufacturingmagizine.com/2015/02/a-primer-on-ceramic-matrix-composites/, 2015.

[10] Edson Cochieri Botelho, R. A. S., L. C. P., & M. C. R., “A review on the development and properties of continuous fiber/epoxy/aluminum hybrid composites for aircraft structures,” http://www..scielo.br/scielo.php?script=sci_arttext&pid=S1516-14392006000300002, 2006

[11] Baker, C. R., “Assessing Damage in Composite Materials,” https://etd.ohiolink.edu/!etd.send_file?accession=akron1390315001disposition=inline, 2014.

[12] Falugi, M. A., “Hybrid Laminates for Efficient Composite Bolted Joints,” https://arc.aiaa.org/doi/pdfplus/10.2514/6.2017-0432, 2017.

[13] Velmurugan, R., “Composite Materials,” http://www.mcours.net/cours/pdf/info/Composite_Materials.pdf.

[14] “Strength of Aligned Fibre Composites,” http://www.mse.mtu.edu/~drjohn/my4150/compositesdesign/cd2/cd1.html.

[15] “Module 7 Simple Beam Theory,” http://web.mit.edu/16.20/homepage/7_SimpleBeamTheory/SimpleBeamTheory_files/module_7_with_solutions.pdf, 2020.

[16] “316 Stainless Steel,” https://icme.hpc.msstate.edu/mediawiki/index.php/316_Stainless_Steel.

[17] Gotro, J., “Polymer Composites Part 3: Common Reinforcements Used in Composites,” https://polymerinnovationblog.com/polymer-composites-part-3-common-reinforcements-used-composites/, 2016.

[18] Stephen W. Tsai, E. M. W., “A General Theory of Strength for Anisotropic Materials,” *Journal of Composite Materials,* Vol. 5, 1971, pp. 58-80.

[19] Hashin, Z., “Fatigue Failure Criteria for Unidirectional Fiber Composites,” *Journal of Applied Mechanics,* Vol. 47, 1980, pp. 329-334.

[20] Z. Hashin, A. R., “A Fatigue Failure Criterion for Fiber Reinforced Materials,” *Journal of Composite Materials,* Vol. 7, 1973, pp. 448-464.

[21] “Abaqus Version 6.6 Documentation,” https://classes.engineering.wustl.edu/2009/spring/mase5513/abaqus/docs/v6.6/books/stm/default.htm?startat=ch02s04ath19.htm, 2006.

REPORT DOCUMENTATION PAGE

Form Approved
OMB No. 074-0188

1. REPORT DATE *(DD-MM-YYYY)*	**2. REPORT TYPE**	**3. DATES COVERED** *(From – To)*
13-03-2020	Master's Thesis	October 2018 – March 2020

TITLE AND SUBTITLE

MODELING HYBRID COMPOSITES USING TSAI-WU AND HASHIN FAILURE CRITERION

5a. CONTRACT NUMBER

5b. GRANT NUMBER

5c. PROGRAM ELEMENT NUMBER

6. AUTHOR(S)

Roberts, Candice R., Second Lieutenant, USAF

5d. PROJECT NUMBER

5e. TASK NUMBER

5f. WORK UNIT NUMBER

7. PERFORMING ORGANIZATION NAMES(S) AND ADDRESS(S)
Air Force Institute of Technology
Graduate School of Engineering and Management (AFIT/ENY)
2950 Hobson Way, Building 640
WPAFB OH 45433-8865

8. PERFORMING ORGANIZATION REPORT NUMBER

AFIT-ENY-MS-20-M-278

9. SPONSORING/MONITORING AGENCY NAME(S) AND ADDRESS(ES)
Michael G. Gran, AFRL/RQVS
Aerospace Systems Directorate
Air Force Research Laboratory
1950 5th St
Wright-Patterson AFB, OH 45433, USA

10. SPONSOR/MONITOR'S ACRONYM(S)

AFRL/RQVS

11. SPONSOR/MONITOR'S REPORT NUMBER(S)

12. DISTRIBUTION/AVAILABILITY STATEMENT
DISTRUBTION STATEMENT A. APPROVED FOR PUBLIC RELEASE; DISTRIBUTION UNLIMITED.

13. SUPPLEMENTARY NOTES
This material is declared a work of the U.S. Government and is not subject to copyright protection in the United States.

14. ABSTRACT

Hybrid composites require further study and testing for future use in various fields. This study focuses on simulating a Hybrid Composite using IM7-977-3 laminae with steel foils in Abaqus under bolt loading by using Hashin and Tsai-Wu failure criterion. Initial simulations contain only the IM7-977-3 composite with cohesive layers. Foil samples were then tested for accurate material properties from which the simulations were then updated to include steel foils. The two models show that Tsai-Wu failure criterion, while great for anisotropic material in tension, does not prove accuracy around the hole of the composite material which is in compression. Hashin shows failure in compression for the matrix and portions of the fibers for the material long before Tsai-Wu indicates any failure is forthcoming. Each layer is analyzed for differing results between the two failure criterion.

15. SUBJECT TERMS
(Fill in with pertinent terminology related to the topic of your thesis.)

16. SECURITY CLASSIFICATION OF: A			**17. LIMITATION OF ABSTRACT**	**18. NUMBER OF PAGES**	**19a. NAME OF RESPONSIBLE PERSON**
a. REPORT	**b. ABSTRACT**	**c. THIS PAGE**			Palazotto, Anthony, PhD, AFIT/ENY
U	**U**	**U**	**UU**	176	**19b. TELEPHONE NUMBER** *(Include area code)* (937) 255-6565 (NOT DSN) (candice.roberts@afit.edu)

Standard Form 298 (Rev. 8-98)
Prescribed by ANSI Std. Z39-18